UNIVERSITY OF CALIFORNIA

Santa Barbara

Oxide Supported Rh Catalysts in Automotive NO Reduction Chemistry: The Roles of Atomically Dispersed Rh, Support, Water, and Dynamic Restructuring

A dissertation submitted in partial satisfaction of the requirements for

the degree Doctor of Philosophy

by

Chithra Asokan

Committee in charge:

Professor Phillip Christopher, Chair

Professor Susannah Scott

Professor Bradley Chmelka

Professor Horia Metiu

June 2021

The dissertation of Chithra Asokan is approved.

_____

Horia Metiu

_____

Susannah Scott

_____

Bradley Chmelka

_____

Phillip Christopher

March 2021

Oxide Supported Rh Catalysts in Automotive NO Reduction Chemistry: The Roles of Atomically Dispersed Rh, Support, Water, and Dynamic Restructuring

by

Chithra Asokan

ACKNOWLEDGEMENTS

First, I would like to acknowledge my family, especially my mother and father who emphasized the importance of education in my life at an early age and supported me through my pursuit of higher knowledge. Also, I am grateful for my sister Vanitha (Akka) and her family, especially my niece and nephew Indira and George, for their kindness, for their curiosity, and for teaching me understanding in the face of adversity. I would like to acknowledge and thank my advisor Phillip Christopher for everything he has taught me, his patience, his time, and his energy.

Thank you to those who have supported me throughout the various stages of my life, including my peers from Natya, Daniela Valdez, Rebecca Knight, and those who have stayed in touch with me during my graduate school career. Thank you to Ron Kurczak who encouraged me to enjoy life in the moment. Thank you to my classmates and professors at UIC that helped create the foundation of my Chemical Engineering knowledge including Andrew Duffy, Nick Shaskevich, Antonett Madriaga, and My-Lynn Pham. Thank you to Dr. Randall Meyer whose mentorship introduced me to DFT and catalysis, and who also set the bar high for the quality of people I choose to work with. Thank you to my old colleagues at UOP who I had the pleasure to work with and learn from including Candice Swift, Beth Carter, Pelin Cox, Peter Eckels, Bryan Egolf, Laura Lenard, Blaze Arena, Andrea Bozzano, Willie Morrissette, and Emily Harrell.

I would like to acknowledge the support I received from the UC Riverside department of Chemical and Environmental Engineering and the graduate student community including Jill Foster, Thomas Dugger, Sami Corber, Marissa Giroux, Melina Fuentes-Garcia, Deborah Nelson, Sara Vliet, Ece Aytan, Wenny Wong, Nicholas Derimow, Brandon Simmons-Rawls, Sooyoun Yu, Sangavi Pari, and many more. I would also like to acknowledge the UC Santa Barbara department of Chemical Engineering and the graduate students for welcoming me into their community including Candice Swift, Lesley Chan, Julia Fisher, Tsatsral Battsengel, Clark Palmer, Valeria Tamayo, Lucy Hedley, and Wendy Bagnasco.

Importantly, I would like to acknowledge and thank my labmates, past and present, for all they have taught me, their help, and their support over the years. Thank you, Matt Kale and John Matsubu for starting the lab and establishing high standards of productivity and quality. Thank you Talin Avanesian for being a mentor in DFT and life. Thank you, Leo Deritia and Sergei Hanukovich for your leadership in building, establishing protocol, and maintaining the lab, especially during our move to UCSB. Thank you, Leo Deritia for collaborating with me and acting as a mentor in all work related to single atom catalysis. Thank you, Christian Alcaraz for being a labmate and a friend. Thank you to Postdocs Andy Therrien, Hossein Robatjazi, Sujith Ramakrishnan, Insoo Ro, Joaquin Resasco, and Bhogeswararao Seemala for all your help, mentorship and advice. Thank you to my current labmates Ji Qi, Gregory Zakem, Jordan Finzel, Isabel Barraza Alvarez, Emily Schroeder, Justin Marlowe, and Zach Westman for allowing me to learn with you, your continuous help, your support, and the atmosphere you have created for future lab generations to come.

VITA OF Chithra Asokan
February 2020

EDUCATION

University of California – Santa Barbara (UCSB), Santa Barbara, CA
Ph.D., Chemical Engineering, March 2021
Advisor: Phillip Christopher
University of Illinois, Chicago (UIC), College of Engineering
B.S., Chemical Engineering, May 2010

PUBLICATIONS

- Zhang, J.; **Asokan, C.**; Zakem, G.; Christopher, P.; Medlin, J. W. "Enhancing Sintering Resistance of Atomically Dispersed Catalysts in Reducing Environments with Organic Monolayers." *Green Energy & Environment* (2021).
- **Asokan, C.**; Yang, Y.; Dang, A.; Getsoian, A.; Christopher, P. "Low-Temperature NH_3 Production during NO Reduction by CO is due to Atomically Dispersed Rh Active Sites." *ACS Catal.* 2020, 10 (9), 5217-5222
- **Asokan, C.**; Thang, H. V.; Pacchioni, G.; Christopher, P. "Reductant Composition Influences the Coordination of Atomically Dispersed Rh on Anatase TiO_2." *Catal. Sci. Technol.* 2020, 10 (6), 1597−1601.
- Tang, Y.; **Asokan, C.**; Xu, M.; Graham, G. W.; Pan, X.; Christopher, P.; Li, J.; Sautet, P. "Single Atoms on TiO_2 Dynamically Respond to Reaction Conditions by Adapting their Site." *Nat. Com.* 2019, 10(1), 4488.
- **Asokan, C**.; Derita, L.; Christopher, P. "Using Probe Molecule FTIR Spectroscopy to Identify & Characterize Pt Group Metal Based Single Atom Catalysts." *Chinese J. Catal.* 2017, 38 (9), 1473–1480.
- Abbott, H.L.; Aumer, A.; Lei, Y.; **Asokan, C.**; Meyer, R.J.; Sterrer, M.; Shaikhutdinov, S.; Freund, H.J. CO adsorption on monometallic & bimetallic Au− Pd nanoparticles supported on oxide thin films. *The Journal of Physical Chemistry C*, 2010, 114(40), 17099-17104.
- **Asokan C.**; Mingjie X.; Sheng, D.; Pan, X.; Christopher P. "Synthesis of Atomically Dispersed Rh Catalysts on Oxide Supports via Strong Electrostatic Adsorption and Characterization by Cryogenic Infrared Spectroscopy"-*In Prep*-
- **Asokan C.**; Qi, Ji.; Resasco J.; Christopher P. "Support Influence on Atomically Dispersed Metal."-*In Prep*-
- Hoffman, A.; **Asokan, C.**; Getsoian, A.; Christopher, P; Hibbits, D. "Assessing coverages and frequencies on Rh nanoparticles using CO and NO probe molecule FTIR and density functional theory" -*In Prep*-
- **Asokan, C.**; Hoffman, A.; Getsoian, A.; Hibbits, D; Christopher, P. "Identifying the Structure of Atomically Dispersed Rh Active Sites on Al_2O_3 for Automotive NO Reduction." -*In Prep*-

CONFERENCES & PRESENTATIONS

"Low Temperature NH_3 Production during NO reduction by CO is due to Atomically Dispersed Rh Active Sites"
AICHE Annual Meeting (via Zoom) *Presentation* Nov '20
"Low Temperature NH_3 Production during NO reduction by CO is due to Atomically Dispersed Rh Active Sites"
UCSB Catalysis Seminar Series (via Zoom) *Presentation* April '20
"Role of Rh Structure, Support Effects & Dynamics on Automotive NO Reduction Catalysis"
UCSB Graduate Student Symposium, Santa Barbara, CA. *Presentation* September '19
"Synthesizing Atomically Dispersed Rh catalysts on oxide supports." &
"Identifying Unique Characteristics of Atomically Dispersed Rh using CO Probe FTIR"
UCSB Mellichamp Sustainability **Fellowship Recipient** Lecture Series *Presentations* June '18 & July '19
"Synthesis using Strong Electrostatic Adsorption & Cryogenic FTIR Characterization Approach for Oxide Supported Atomically Dispersed Rh Catalysts"- **UCSB Travel Grant Recipient**
NAM (North American Catalysis Society Meeting), Chicago, IL. *Poster* June '19
"Utilizing Electrostatic Adsorption & Cryogenic IR Spectroscopy as a General Synthesis & Characterization Approach for Oxide Supported Atomically Dispersed Rh Catalysts" - **UCSB Travel Grant Recipient**
AICHE Annual Meeting, Pittsburg, PA. *Presentation* Oct '18
"Characterizing Atomic Rh on Oxide Supports" -**Recipient of Best Poster**
UCR CEE Symposium, Riverside, CA. *Poster* Sept '16

ABSTRACT

Oxide Supported Rh Catalysts in Automotive NO Reduction Chemistry: The Roles of Atomically Dispersed Rh, Supports, Water, and Dynamic Restructuring

by Chithra Asokan

At a time when global warming has led to aggressive regulations on emissions control around the world, the demand for automotive pollution-mitigating catalytic converters has grown. The three-way catalyst (TWC) in catalytic converters, composed of platinum group metals, has played a critical role in automotive pollution mitigation. Specifically, rhodium (Rh) is crucial in TWCs to reduce nitrogen oxide (NO_x) emissions produced by burning hydrocarbon fuel. Rh is a distinct catalyst in its ability to reduce NO at high rates with a high selectivity towards N_2, while remaining robust.

Despite extensive investigation, NO reduction mechanisms under automotive conditions remain unclear. Particularly, it is unknown which sites are responsible for the unselective reduction of NO to NH_3 under light-off conditions, or in CO-rich feeds. This is important for further optimization of TWCs as NH_3 is currently an unregulated emission from automobiles, despite it being a strong greenhouse gas. While Rh is highly selective towards N_2 at steady state conditions, the current understanding in literature rarely incorporates realistic automotive operating conditions where large concentrations of CO and H_2O are present. Additionally, most studies have been performed over nanoparticle surfaces at higher weight loadings of Rh, >1%, despite the fact that the actual Rh weight loading in the TWC is lower than ~0.3%, where a mix of nanoparticles, small clusters, and atomically dispersed species are likely to be present.

In this work, we focused on identifying the distinct properties and reactivity of atomically dispersed Rh active sites on oxide supports for NO reduction under automotive

conditions. We developed and optimized approaches to synthesize atomically dispersed Rh catalysts on various oxide supports using principles of strong electrostatic adsorption. Probe molecule Fourier-transform infrared spectroscopy (FTIR) was utilized in correlation with temperature programmed desorption, aberration corrected scanning transmission electron microscopy, and Density Functional Theory calculations to provide insights into the structure and local coordination of the Rh species. Probe molecule FTIR was particularly useful in characterizing the distribution of Rh species in a sample as probe molecules bond with different stoichiometries and vibrational stretching frequencies on different Rh species ranging from atomically dispersed to nanoparticles.

Using a series of well characterized samples with various Rh structures, we observed via light off and kinetic measurements that atomically dispersed Rh active sites result in distinct NO reduction reactivity as compared to Rh nanoparticles. Specifically, under dry environments, NO is reduced by CO at higher rates on Rh nanoparticles as compared to atomically dispersed Rh species. Interestingly, the addition of H_2O to the feed significantly promotes the NO consumption rate for atomically dispersed Rh active sites and results in 100% selectivity to NH_3 at relevant operating temperatures. Alternatively, Rh clusters are less reactive than atomically dispersed species in the presence of H_2O, and the reaction primarily leads to N_2 formation. Thus, Rh structure has strongly affected NO reduction chemistry in catalytic converter conditions, both in terms of NO consumption rate and selectivity. Our results suggest that TWC formulations and emission control strategies should be targeted to avoid the formation of atomically dispersed Rh species to mitigate low temperature NH_3 formation. More broadly, the results highlight the potential role (sometimes negative) of atomically dispersed metal species in industrial catalytic processes.

TABLE OF CONTENTS

LIST OF FIGURES

Chapter 1:

Introduction

1.1 The Background of Catalytic Converter NO_x Reduction

The three-way catalyst (TWC) in catalytic converters has played an essential role in controlling automotive pollution from gasoline burning engines. The catalytic converter was originally invented and patented by the French mechanical engineer Eugene Houdry in 1930 to minimize smog from smokestack and automobile exhaust. [1–6] By the 1950s, he had developed catalytic converters for gasoline engines in cars but this technology would not be implemented broadly for another 25 years because the catalyst was poisoned during operation by tetraethyllead, a common gasoline additive that acted as an anti-knock agent. [1] In 1975, the United States Environmental Protection Agency's (EPA) Clean Air Act required a 75% decrease in chemical emissions in all new vehicle models, so tetraethyllead was removed from gasoline in order for TWCs in catalytic converters to be implemented. [1–6] Today, the demand for emissions control catalysts continues to dramatically rise as the US and other parts of the world (including Europe, India, and China) increase strict toxic chemical control on transportation to comply with environmental and health regulations.[1,7–9] Continuing the development of the TWC in catalytic converters found in gasoline powered vehicles is required to prevent the ongoing negative effects brought on by global transportation demands. Improvement to the process includes mitigation of unregulated pollutants, such as NH_3 and N_2O, or optimizing operation at low temperature start up, when the most toxins are released.[4,7–10]

After fuel is burned in vehicle engines through combustion with air, the exhaust gas flows to catalytic converters where "three" pertinent reactions occur over the TWC, hence the name. These "three" reactions are the reduction of nitrogen oxides (NO_X) into molecular nitrogen (N_2), the oxidation of carbon monoxide (CO) to carbon dioxide (CO_2), and the oxidation of residual hydrocarbons into CO_2 and water (H_2O).[6,10,11] These reactions are

critical because the toxic pollutants released without the presence of the TWC can create smog that affects human health, and adverse environmental consequences such as acid rain and damaged water quality.[8,9,12,13]

Combustion effluent that flows into the catalytic converter and over the TWC is commonly composed of CO (< 1%), H_2 (< 1%,), O_2 (< 1%), CO_2 (~14%), H_2O (~13%), hydrocarbons (~1000 ppm), and NO_x (~1000 ppm) (figure 1.1).[10,11] Automobiles release a majority of toxic emissions in the first minute of operation because, unlike industrial catalytic processes that are brought on stream in a controlled manner, the catalytic converter is forced to start heating up rapidly from ambient temperature (cold start), where the catalyst is inactive, to operating temperatures where desired conversion is achieved.[4,14] The conversion of reactants as temperature increases over the catalyst from ambient temperature, mimicking the start-up of a car, can be referred to as a "light off curve" as seen in figure 1.1. Notably, NO and CO light off (convert) at the same temperature, then the conversion of hydrocarbons follows, suggesting that NO reduction to N_2 primarily occurs via reactions with CO.

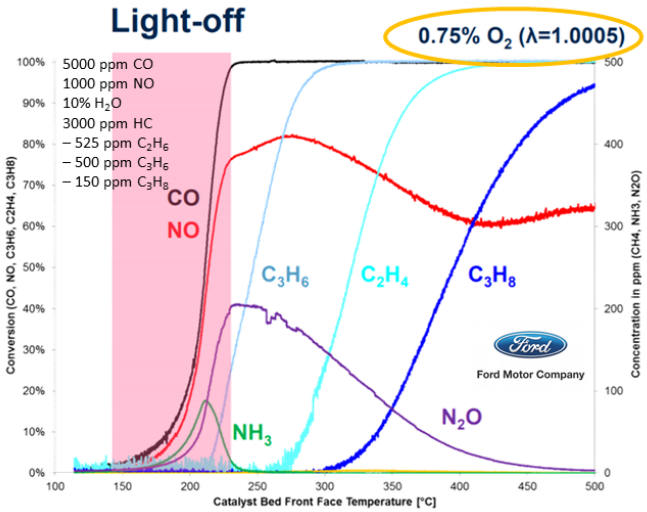

Figure 1.1: a) Conversion of typical exhaust gas composition flowing over TWC versus temperature. Temperature is increased 5 °C/min at 0.75% O_2 atmosphere (**λ**=1.0005). (courtesy of Bean Getsoian at Ford Motor Company)

The catalytic converter is a honeycomb structure composed of a ceramic monolith that is mechanically and chemical stable at high temperature and is encased by a metal housing with thermally insulating layers. This honeycomb interior has thin wall channels and is wash coated with porous oxides (CeO_2/Al_2O_3) to maximize the surface area where catalytically active metals are deposited, and catalytic reactions occur. The TWC in catalytic converters typically contains a combination of 3 reactive noble metals (or sometimes only 2) that are impregnated on the oxide layer wash coat; Pt, Pd, and Rh. Rh is considered the most viable noble metal for NO_x reduction because it exhibits higher NO_x conversion rates and selectivity to N_2 compared to Pd or Pt.[4,10,15,16] Ru, Ir, and Os have also been considered for NO_x reduction chemistry, but these precious metals form volatile oxides that are unstable in automotive conditions.

NO_x is detrimental to human health, causing respiratory infections, lung disease, and possibly cancer.[9,12] In certain areas of the world, NO_x can be noticed by a brownish haze in the atmosphere and creates acid rain when NO_x reacts with water in the atmosphere to form acids.[17,18] Other nitrogen containing pollutants that are released from automobiles due to unoptimized catalyst selectivity include N_2O (laughing gas), and NH_3 (ammonia). These species are most often seen at low temperature, during light off. N_2O is a potent greenhouse gas, and atmospheric NH_3 can cause airborne poisonous particulate formation, water source contamination from ground water runoff, and plant-life eradication.[17,19–21] To guide the formulation and operation of TWCs to minimize NH_3 and N_2O formation, while maintaining maximal control over NO_x emissions, deeper understanding of the mechanisms of NO_x reduction on TWCs is required. Even under simplified conditions, mechanistic understanding of NO reduction by CO on Rh single crystals is inconsistent with results obtained on supported Rh particles. This shows the need for understanding structure-function

relationships between Rh catalysts and NO reduction, where specific catalytic behavior is connected to specific active sites.[22–27]

The reaction mechanism for NO reduction by CO on Rh has been widely studied and is still debated. Grounding a deeper understanding of this mechanism could lead to a more sustainable catalyst design, especially if small clusters or atomically dispersed Rh may serve as the active species.[28–30] The dynamic shifts in the reactant composition from oxidizing and reducing (figure 1.1, **λ**) can cause Rh restructuring that may result in differences in catalyst reactivity.[6] Insights into relationships between Rh active site structure and catalytic functionality is made challenging by the structurally adaptive nature of Rh to surrounding environments. Specifically, in harsh rich feed and high temperature conditions, Rh agglomerates into particles.[31] In lean conditions, Rh is known to disperse into single atoms across an oxide support because the support interactions with ligated atomically dispersed Rh species can be stronger than the bonds formed between Rh atoms.[29] Developing structure-function relationships for heterogeneous Rh catalysts is complicated when Rh is known to speciate between atomically dispersed species and metal clusters and the Rh structure depends on composition in exhaust streams containing CO, NO, H_2 and H_2O.[32,33]

The Rh weight loadings in industrial TWCs are commonly lower than ~0.3%, where a mix of Rh nanoparticles, small clusters, and atomically dispersed species co-exist while the exhaust composition fluctuates.[14] While the reduction of NO by CO is well studied for Rh nanoparticles and extended Rh surfaces, the role of atomically dispersed species Rh in this chemistry, particularly under relevant conditions with H_2O in the feed, has not been addressed.[16,25,34–39] Understanding the mechanistic pathways in TWCs on oxide supported atomically dispersed Rh species is important for building up a complete description of NO reduction chemistry under relevant automotive conditions.[40–43] Next, the current

understanding of NO reduction by CO on extended Rh surfaces and Rh nanoparticles is provided as a backdrop to future studies aimed at elucidating the potentially distinct reactivity of atomically dispersed Rh species.

1.2 NO Reduction by CO on Extended Rh Surfaces and Particles

Previous experimental studies have primarily focused on NO reduction by CO over extended Rh surfaces and supported Rh nanoparticle catalysts, with minimal analyses of the influence of hydrogen sources (H_2O or H_2) or atomically dispersed Rh species on reactivity and selectivity.[16,36–38] These studies focused on well characterized single crystal Rh surfaces and oxide supported Rh nanoparticles with detailed investigations of NO and CO adsorption, interaction, dissociation, and desorption.[15,30,44] Smaller Rh particles on oxide supports have shown noticeably lower reaction rates and higher apparent activation barriers than extended Rh surfaces or large Rh particles, which highlights the structure sensitivity of NO reduction by CO over Rh catalysts. Differences between the reactivity of Rh nanoparticle catalysts as compared to extended Rh surfaces likely stems from differences in the distributions of active Rh geometric structures and the resulting influence on apparent activation barriers or reaction mechanisms. However, it has remained challenging to identify the source of discrepancies in the reactivity various Rh structures due to the array of potential intermediates, bonding configurations, and adsorbate-adsorbate interactions formed with just NO and CO in the feed. Both adsorbates can bond to Rh in different stoichiometries and at different sites, making the correlation of adsorbed species and reaction mechanisms challenging to disentangle. There are also factors that must be considered such as Rh restructuring and support contributions, although previous comparisons carried out using a series of supported Rh catalysts claim that variations in support composition minimally influence reaction kinetics.[36,40,45–47] The presence of oxygen,

water, and hydrocarbons in real feeds presents further complications due to their potential occupation of surface sites on the metal and support, as well as participation in NO reduction.

The elementary mechanism of NO reduction by CO over Rh catalysts has been proposed to follow one of two possibilities: either the Eley-Rideal (E-R) mechanism, where adsorbed species react with gas phase species, or the Langmuir-Hinshelwood (L-H) mechanism, where all species adsorb before reacting. Initially the E-R mechanism, with stable isocyanate (NCO) formation through gas phase CO reacting with adsorbed N, was generally accepted to be the reaction pathway. However, detailed kinetic studies have since supported a L-H mechanism over extended Rh surfaces and nanoparticles and have suggested that NCO is formed as a bystander that is not critical to the reaction.[25,48,49]

The proposed L-H mechanism assumes negligible N_2O production above NO light-off temperature, and an increase in NO dissociation with more vacant Rh sites forming during the reaction as products desorb. Primarily, N_2 is believed form through the recombination nitrogen atoms and is considered the rate-limiting step due to its low rate constant at temperatures below 125 °C.[50,51] Aside from this, N_2 can also form through the interaction of NO and N atoms through a L-H mechanism, depending on the partial pressures of NO. N_2 rapidly desorbs from Rh under typical catalytic operating temperatures.[22,52] But at lower temperatures, below 300 °C, the E-R mechanism is considered because of the higher selectivity towards N_2O, compared to higher temperatures where N_2O production is negligible. Even within these two classes of mechanism, many of the detailed steps are still debated.

In this section, we provide a detailed review of NO reduction on extended Rh surfaces and Rh single crystals and what initial insights were used to propose a mechanism in

these conditions. This includes why NO dissociation is generally proposed as an essential or the rate determining step via a Langmuir-Hinshelwood mechanism and how NO saturation over the surface leads to selectivity towards N_2O over N_2 below 300 ºC.[53–56] We then provide detail into NO reduction by CO on oxide supported Rh particles in realistic atmospheric pressures and operation temperatures. We learn that the reactive behavior of supported Rh particles show contradictions to extended Rh surfaces. Specifically, Rh single crystals exhibited substantially lower apparent activation energies, higher specific rates and lower N_2O selectivity than supported Rh/Al_2O_3 catalysts containing small ~1 nm Rh particles.[48] We also learn that a the major factor influencing the kinetics of the NO-CO reaction is metal particle size, such that the rate of NO dissociation decreases as Rh dispersion increases.[47,57–59]

The mechanistic origin of this difference in behavior is currently unknown although we proposed some suggestions. The presence of more than one active site may be able to explain why supported Rh particles exhibit lower reaction rates and higher selectivity towards N_2O at low temperature, below 300º C. It could also be that differences in saturation adsorbate coverage as a function of particle size plays a critical role in these differences. This review highlights the necessity for understanding the reactive properties of all Rh structures, as real catalytic convertors contain a mix of larger Rh particles, small Rh clusters, and atomically dispersed Rh species.

1.2.1 NO Reduction by CO Over Extended Rh Surfaces

The influence of Rh single crystal facets on NO reduction reactivity and selectivity has been studied in detail.[15,54,55,60,61] For example, Peden et al. investigated the selectivity toward N_2 and N_2O at relatively high pressures over Rh [110] and Rh [111] surfaces. It was suggested that the selectivity towards N_2 is greater than N_2O on the Rh [110] due to site

availability. Reactions over Rh [111] have a higher selectivity towards N_2O due to steric crowding of strongly adsorbed NO which inhibits NO dissociation.[56] This aligns with the idea that at low temperatures, below 300 ºC, less N_2 desorbs, and N_2O formation increases due to high NO surface coverage. Therefore, it can be concluded that N_2O formation is sensitive towards Rh surface structure. Additionally, the Rh [110] surface exhibits a lower apparent activation energy for NO dissociation compared to Rh [111] over a wide range of temperatures. However, in dry conditions NO consumption rates are similar over any Rh single crystal surface structure when reacting with CO.

The predominant adsorbate coverage also plays a critical role in dictating catalytic reactivity. Once NO absorbs onto a metallic Rh surface with neighboring open sites, the ability of metallic Rh to accomplish NO dissociation more readily is unique and many researchers claim that this is a key attribute to why Rh is highly active for NO reduction compared to other noble metals.[62,63] Therefore, NO dissociation is generally the proposed as an essential or the rate determining step in NO reduction by CO in the L-H mechanism. The elementary process of NO dissociation over well-characterized Rh extended polycrystalline and single-crystal surfaces has been established through application of various surface chemistry techniques that require ultrahigh vacuum.[34,45,64–66] DFT calculations have also suggested that on extended Rh [100] and [111] surfaces, the rate limiting step is NO dissociation and that NO is able to dissociate in the presence of CO with a relatively low energy barrier on the surface of Rh nanoparticles.[34,35]

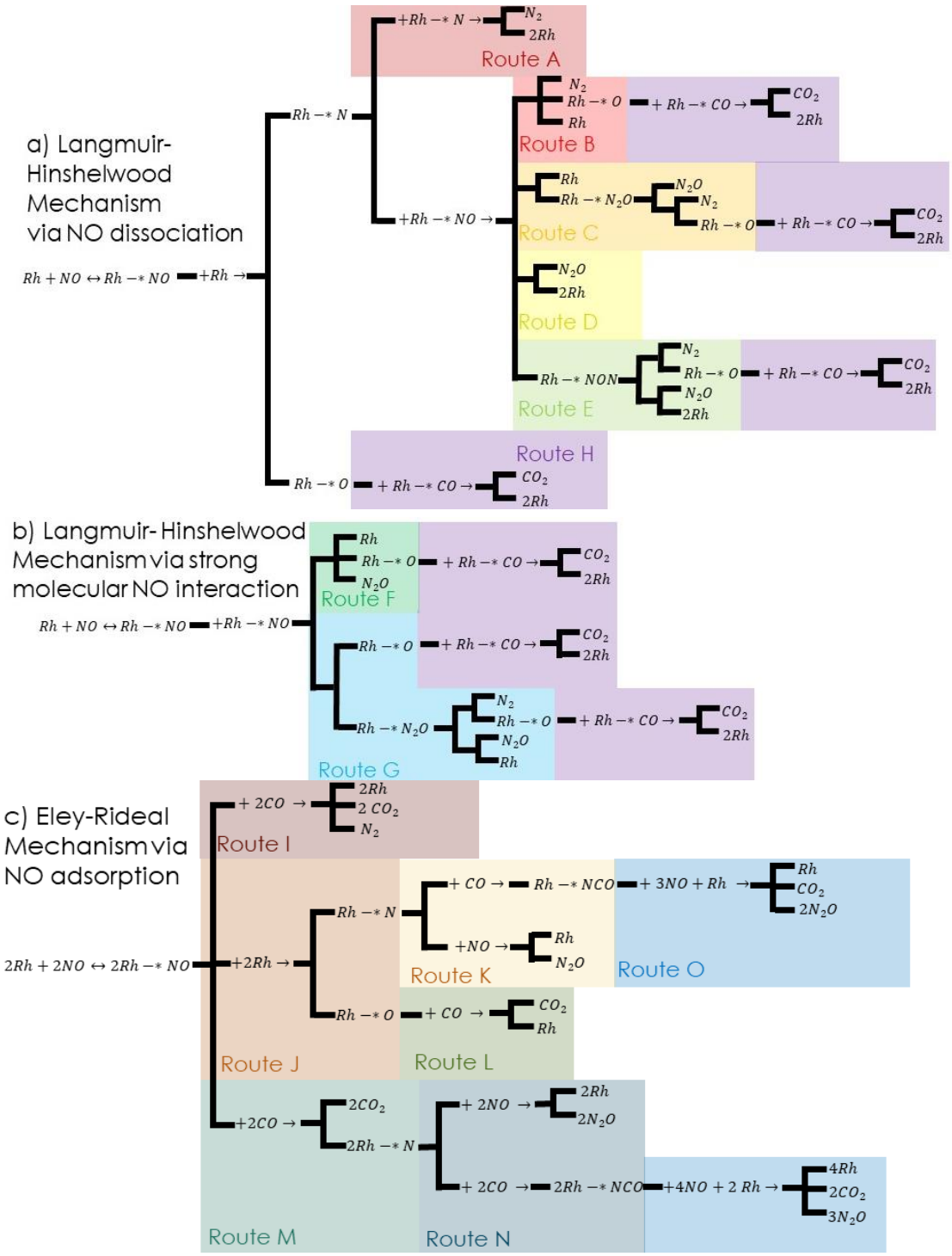

Figure 1.2: Proposed NO reduction pathways with CO over Rh a) Langmuir Hinshelwood mechanistic pathways proposed, starting with NO dissociation after adsorption b) Langmuir Hinshelwood mechanistic pathways proposed, starting with strong NO molecule adsorption after adsorption c) Eley-Rideal mechanistic pathways mechanistic proposed where gas phase reactants interact with adsorbed NO species.

Aside from NO interaction over the Rh surface, CO is also necessary for NO reduction to proceed over Rh. Until now, all discussions have assumed CO molecularly adsorbs to Rh and reacts with surface bound O to form CO_2. Yates and Williams investigated the dissociation of chemisorbed CO using auger spectroscopic and isotopic exchange measurements, at a surface temperature below 525 °C and found that that the maximum probability of dissociation of CO molecules in collision with Rh [111] was negligible when compared to the desorption of molecular CO.[67] Therefore, most mechanisms rule out simple dissociation of CO on Rh surface without the presence of other molecules. Additionally, Baird and Wynblatt suggested that CO chemisorbed and desorbed molecularly at all coverages over Rh [110] as shown by Temperature Programmed Desorption (TPD) and Ultraviolet Photoelectron Spectroscopy (UPS).[68] In comparison, NO could chemisorb and desorb molecularly at high NO coverage from Rh [110] but NO dissociation was observed above ~250 °C at low coverages. During TPDs of NO from [110] extended Rh surfaces molecular NO was observed via mass spectrometry to desorb, but at elevated temperatures and low coverages, N_2 rather than NO was detected.[45,69]

Thus, atomic oxygen from NO, rather than from CO, likely plays an intermediate role in CO_2 formation (figure 1.2a, route H). This finding was in line with Campbell and White's conclusion that monatomic N reacted to form N_2, but ignored the idea that atomic N reacted with adsorbed molecular NO because the NO was more likely to dissociate on the surface while atomic O reacted with CO to form CO_2 (figure 1.2a, route H). The NO dissociation reaction studies were again verified through TPD studies by Bowker, M. et al.[69] Their measurements showed that the N_2 desorption from Rh [110] occurred only after NO dissociation in the presence of oxygen atoms or after the removal of oxygen by CO oxidation (figure 1.2a, route H). The rate of CO_2 production was determined to be much lower than the

NO dissociation reaction, except at extreme temperatures. This was because NO competes with CO for surface sites and dissociates to provide oxygen atoms at higher rates on this surface, highlighting the importance of different crystal facets of the chemistry.[54,70–72]

Kinetics of NO reduction by CO over Rh [111] was studied at 1-2 atm pressure, and found to be in agreement with Campbell and White's UHV results that showed that N_2O formation was insignificant.[23,48,57] This model assumed N_2 desorption as the rate-limiting step, and involved a modified L-H mechanism where CO/NO adsorbed, adsorbed NO dissociated, nitrogen recombined to form gas phase N_2 and then CO was oxidized (figure 1.2a, route A).

However, kinetic studies of Rh [100] revealed that the order of CO in the reaction varied from +1 to -1 when CO partial pressure increased from 1 to 250 Pa at constant NO partial pressure. Hendershot and Hansen determined via electron diffraction and thermal desorption spectroscopy studies of Rh [100] that adsorbed CO and NO species self-inhibited their reaction rate as their partial pressure increased.[54,71,73] Simultaneously, the kinetic order for NO varied from +3/2 to -1 when the NO partial pressure increased from 1 to 1800 Pa at a constant CO partial pressure. Thus, they agreed on a L-H reaction mechanism with the traditional adsorption steps followed by N_2O formation between 2 adsorbed NO molecules and then N_2O decomposition into N_2 (figure 1.2b, route G).

Kinetics of the NO/CO reaction over Rh were further sensitive to changes in adsorbate coverage caused by the Rh surface morphology. Oh et al. studied the kinetics of the NO-CO reaction over single-crystal Rh [111] and Rh [100] in comparison to supported Rh/Al_2O_3 catalysts. They revealed differences in kinetic behavior at equal CO/NO partial pressure in these different cases. The Rh single crystal exhibited substantially lower apparent activation energies and higher specific rates than those over the supported Rh/Al_2O_3 catalyst.[47] This is

reiterated by a mathematical model of the reaction, which accounted for the individual elementary reaction steps consistent over bulk Rh [111] metal but inconsistent for supported Rh catalysts.[23] NO dissociation and CO desorption occurred quickly over a Rh [111] surface, thus the surface became predominately covered with nitrogen atoms, and nitrogen desorption was the rate-determining step. Nitrogen atoms can be removed from the surface by the reaction of nitrogen atoms by nitrogen atom recombination (figure 1.2a, route A) or with adsorbed NO (figure 1.2a, route C). At low temperatures below 300 °C, the reaction of adsorbed nitrogen atoms with adsorbed NO contributed to nitrogen atom removal. Modeled reactions indicated that at higher temperature, above 300 °C, nitrogen atom recombination determined the NO-CO reaction rate on extended Rh surfaces.

Zhdanov and Kasemo also extrapolated the rate equations from UHV TPD measurements on Rh [111] to scale to atmospheric pressures.[52] Their results indicated that nitrogen desorption is the rate-limiting step and N_2O formation is not significant when utilizing a reaction scheme similar to the one proposed by Oh et al.[23,57,74,75] However, the calculated apparent activation energy for equal NO/CO partial pressures did not match experimentally measured values on oxide supported Rh nanoparticles. They suggested that the activation energies in the model likely changed due to coverage dependence. Neglecting NO dissociation at high coverages in the model was better validated by the experimental data so they theorized that there is more than one type of adsorption site that causes NO dissociation.

1.2.2 NO Reduction by CO on Oxide Supported Rh

Rh surfaces exhibit substantially lower apparent activation energies and higher specific rates than those over the supported Rh/Al_2O_3 catalyst.[48] Generally, NO outcompetes CO to adsorb onto surfaces of Rh nanoparticles, consistent with extended Rh

surfaces.[25,45,47,76,77] However, Elementary steps such as NO dissociation and N_2 desorption may proceed at different rates on supported catalysts compared to extended Rh surfaces potentially due to coverage or surface structure effects.

Granger et al. studied the kinetics of NO/CO interaction and N_2O decomposition over supported Rh catalysts using TPD measurements and proposed a mechanism with multiple possible routes where NO and CO adsorbed, NO could dissociate, CO then formed CO_2, and then N_2 could form by either reacting adsorbed NO with one dissociated N atom or from two dissociated N atoms (figure 1.2a, routes A, B, and H).[16,78–83] The route of N_2O formation was also an alternative possibility (figure 1.2a, routes C or D). They suggested that the dissociation of adsorbed NO was the rate-determining step. They found that the barrier for N_2O decomposition was lower for supported Rh/Al_2O_3 compared to Rh surfaces. As with previous studies, N_2O selectivity rapidly decreased as temperature increased due to site availability becoming more prevalent as species desorbed.[84]

The subsequent order of dissociation, desorption, and reaction with gas phase molecules has been hypothesized through different mechanisms. Experimental data has shown that N_2O formation occurs only after NO dissociation, while oxygen does not inhibit the NO reduction rate. Over oxide supported Rh catalysts, Arai and Tominaga proposed an explanation for NCO and N_2O formation where NO and CO competed to bond with atomic N left behind from CO oxidation by NO (figure 1.2c, M and N). These pathways were predicted due to interaction between molecularly bonded structures following reactant adsorption and re-exposure.[76] Primary experimental evidence for these bonding geometries were found by in-situ FTIR of the NO-CO reaction over Rh catalysts, which have been interpreted in different ways depending on the size of the Rh particles, Rh dispersion, and oxide support effects. Thus, different molecular bonding geometries contribute to different reaction

pathways. These assignments have been verified by various techniques including tunneling spectroscopy measurements by Kroeker et al.[85] These and other molecular bonding geometries have been seen via in-situ FTIR and will be further discussed in a later section (including Rh_2CO, Rh-CO, $Rh(CO)_2$, and Rh-NO).[77,86]

In addition, FTIR measurements indicated the presence of an NCO complex that is sensitive to the feed composition and reaction conditions. The formation of NCO occurred when the reacting gas mixtures are at high temperatures, above 300 °C, or with excess NO.[25,29,60,77] This agreed with Dictor's speculation that at high temperatures, above 300 °C, the formation of N_2O and the formation of CO_2 follows an E-R mechanism, where oxidized Rh is reduced by CO (figure 1.2c, route J, K, and L). It is also worth considering Arai's version of the E-R mechanism under excess NO, where gas phase CO was directly oxidized by adsorbed NO, leaving atomic N, and then the formation of NCO or N_2O occurred (1.3c, route M and N). This leads to the speculation that there was more than one the reaction pathway for CO_2 formation due to the NCO intermediate. A reaction mechanism for an alternative N_2O formation route, where gaseous NO reacted with Rh-NCO after decomposition while CO_2 forms had been proposed after observing CO was necessary for N_2O formation because N_2O had not been observed in the absence of CO in the feed stream (1.3c, route O).[87]. A higher selectivity towards N_2O compared to N_2, at initial light off, made them conclude that the N_2O formation step was required in the rate expression. However, in this proposed mechanism, the rate-limiting step was the recombination of nitrogen atoms as shown by slowed reactivity when the surface was highly saturated.

NO reduction by CO in TWCs have shown noticeably different reactivity depending on Rh dispersion and conditions (reaction pressure, temperature, and environment). Rh metal's ability to dissociate NO molecules decreases with an increase in dispersion or a

decrease in Rh particle size. Previous kinetic studies of NO reduction on oxide supported catalysts, where the Rh particles were < 10 angstroms, claim that dominant reaction pathways shift from a low-temperature N_2/N_2O formation path (figure 1.2a routes B, C, or D, or figure 1.2b routes F, or G) to a high-temperature N_2 formation path (figure 1.2a route A, or figure 1.2c route I).[47] Previous analysis of NO reduction over oxide supported Rh has shown this discontinuity in reaction rates at the lower temperature regime and the high-temperature regime.[25,47] While factors such as the support beneath Rh nanoparticles or the Rh crystal surface had little influence on the overall reactivity, the major factor influencing the kinetics of the NO-CO reaction Rh catalysts was metal particle size.[47,57] The presence of more than one active site may be able to explain the difference in reactivity below 300 °C. For comparison, in the same low temperature range, there is a 45-fold increase in the specific rate of the NO-CO reaction over large Rh particles and they have exhibited a single apparent activation energy similar to Rh extended crystal surfaces.[23,57] The selectivity towards N_2O has been seen to significantly increase in TWCs at below 300 °C and at higher NO partial pressures. Nitrogen atom recombination, possibly prevented by catalyst dispersion or saturation at low temperature, could be the rate determining step in these conditions.[25] In order to minimize N_2O formation, Rh catalysts need to be preheated to allow availability of active Rh sites for NO dissociation. Thus, understanding the mechanism of NO reduction over atomically dispersed Rh could be relevant to preventing higher N_2O emissions.

Based on this review of NO reduction, we have gained mechanistic insights into NO reduction by CO over Rh but it is evident that there is also missing information. For example, it is clear that NO outcompetes CO on Rh sites on Rh particles and single crystals. Further, at low enough temperatures and high enough pressures, the Rh surface is saturated by NO and NO dissociation is critical in the reduction process. Under these conditions both N_2 and N_2O

are observed products, and their selectivity is temperature, NO coverage, and Rh surface structure dependent. Details regarding whether N_2O is a required intermediate in the N_2 formation pathway are unclear. At increased temperatures or lower pressures where NO coverage is decreased, and a significant vacant site concentration exists the selectivity is exclusively to N_2. There is still discussion of whether this is due to inherent kinetics of the competing pathways, or if N_2O readsorption and decomposition into N_2 and O causes the decreased N_2O selectivity under these conditions. Finally, there is still significant missing insights regarding the origin of decreased rates and increased apparent barriers for NO reduction over small Rh particles as compared to large Rh particles and extended surfaces. Based on the consistent observation of strong effects of NO coverage on reactivity and reaction mechanisms, it may be that NO coverages that approach or surpass monolayer coverage (ML) on small Rh crystallites as compared to ~0.7 ML saturation NO coverages on larger Rh surfaces is key to this remaining question.

Interestingly, Dent et al. were one of the first to investigate NO and CO interaction over oxide Rh nanoparticles at moderate temperatures (below 200 °C) to demonstrate that the Rh particles can fragment into atomically dispersed Rh species, bonding either via Rh -NO+ or $Rh(CO)_2$, and therefore dispersion increased when exposed to the reactants.[88] As reaction temperature increased, agglomeration occurred and the selective reaction towards N_2 became more efficient. In contrast to the idea that Rh atoms may sinter to produce reactivity, Chuang et al. was the first to propose that on highly atomically dispersed Rh/Al_2O_3 catalyst samples, the $Rh^+(CO)_2$ species was inactive towards gaseous NO but participated in the oxidation of CO.[89] They suggested that neutral Rh^0 had to be available for NO to adsorb and dissociate, and do not favorably replace CO on $Rh(CO)_2$ that are cationic in nature.

This leads into the detailed discussion of how cationic Rh^+ or Rh atoms that are atomically dispersed on oxide supports could be reactive for NO reduction and exhibit unique activity compared to Rh extended surfaces and Rh nanoparticles. First, we must distinguish atomically dispersed Rh from nanoparticle Rh. In order to identify the differences and unique characteristics of these structures, we turn to detailed analysis using FTIR.

1.3 Probe Molecule FTIR

1.3.1 Introduction to FTIR and DRIFTS

Fourier Transform Infrared (FTIR) spectroscopy has significant applications in the field of catalysis because it can characterize the vibrational frequencies of adsorbed species on surfaces, which can help to clarify the chemical nature of adsorption sites, reaction intermediates, and reaction products.[90] FTIR measures the frequency dependent absorption of IR photons through the excitation of vibrational modes of molecules.

To guide the discussion on IR photon absorption by a diatomic molecule is considered. At the diatomic molecule's ground state the bond distance oscillates around the equilibrium bond distance (vibrates) at the n=0 energy level (figure 1.4).[91] The equilibrium bond distance between the two atoms is a function of the forces between the atoms. The molecule can absorb electromagnetic radiation when the photon frequency is resonant with the vibrational frequency of the molecule. Photon absorption induces transitions within the molecule from the ground state to a excited vibrational state ($n > 0$). The absorbed light generally falls into the mid-infrared spectral range, from 400 to 4,000 cm^{-1} wavenumbers, due to the energy of the vibrational transition that is characteristic of most bonds in organic molecule. The frequency of the molecular vibration (ν) multiplied by Planck's constant (h) is proportional to the energy difference between the vibrational states. The potential energy

landscape of a diatomic bond is an anharmonic oscillator, which can be modeled by the Morse potential function. At short bond lengths the atoms repel each other due to Pauli repulsion and at long bond distances the energy asymptotes toward bond dissociation. Due to the asymmetry of the potential well, the quantized vibrational energy levels are not energetically equidistant. However, the stretching frequency of a bond can be approximated by Hooke's law, where a diatomic molecule vibrates as a one-dimensional harmonic oscillator with masses of each respective atoms (m_1 and m_2). The harmonic oscillator is usually a reasonable estimate of vibration frequencies and bond distances at low quantized energy levels, as shown in figure 1.3. Infrared light can only be absorbed by a molecule if the dipole moment of certain atomic bonds is significant during the vibration. The more significant the vibration in the dipole moment, the stronger intensity of the corresponding IR band (i.e. extinction coefficient) will be.

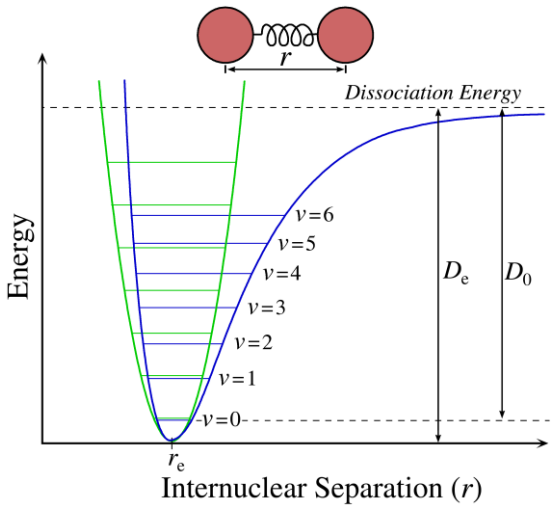

Figure 1.3: Quantum harmonic oscillator (green) vs. Morse potential (blue). Bond distance (r) during vibration at the quantized energy level (v) changes with extension and compression. The Morse potential describes bond dissociation(De), and the energy level spacing is unequal compared to the quantum harmonic oscillator.[91]

The most common spectrometer used in mid-infrared spectroscopy is the Fourier transform Infrared (FTIR).[92] In the FTIR, collimated beams of IR light are transmitted

through a beam splitter to send some light towards a fixed mirror and some light towards a moving mirror that oscillates at a specific frequency up to a distance of x (figure 1.4). The light beams are reflected from these mirrors to travel back to the beam splitter, where they recombine into a single light beam. When the light waves interact, the amplitude of the waves interfere, as the beams are out of phase with each other due to the difference in their relative pathlengths traveled before recombining, yielding a maximum or minimum intensity. The interference patterns produced by each wavelength from the polychromatic IR light source are summed to get the resulting interferogram. By changing the position of the moving mirror, a particular frequency of light will modulate in intensity with time. When this process is performed using a polychromatic light source it results in the modulation of different frequencies of light at different rates, which allows for the raw interferogram to be deconvoluted into a wavelength dependent spectrum by taking a Fourier transform. The advantage of FTIR is the ability for fast data collection over a broad range of light frequencies, as opposed to using a monochromatic beam over a series of different frequencies.

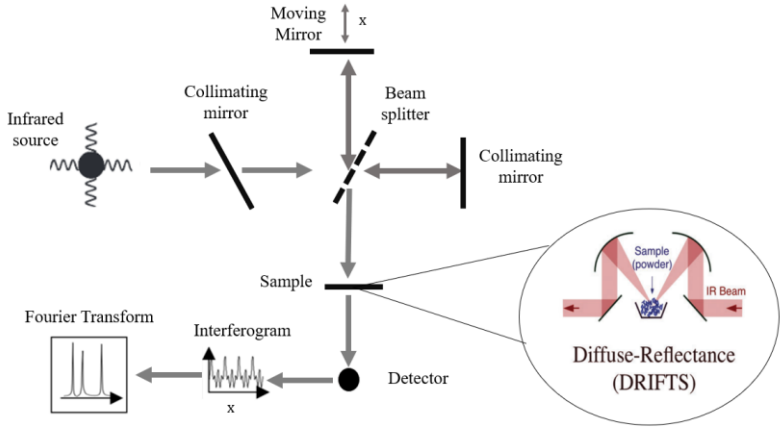

Figure 1.4: Process of the FTIR. Polychromatic infrared light passes through the interferometer, to the sample, and then to the detector where data is produced as an interferogram and then Fourier Transformed. The specific sample analysis is known as Diffuse-Reflectance Infrared Fourier Transform Spectroscopy (DRIFTS).

Diffuse-Reflectance Infrared Fourier Transform Spectroscopy (DRIFTS) is a technique used to characterize IR spectra of species bound to solid materials, such as heterogeneous catalysts. DRIFTS is used on powdered samples, where the IR light directed to a sample is diffusely scattered in all directions upon interaction with the powder and is collected by use of an ellipsoid or paraboloid mirror. This technique can be executed using in-situ cells that provide pathways for the beam to enter the reactor and scattered light to be collected after interacting with the catalyst. These in-situ measurements provide valuable insight to specific surface ligands, which is essential in understanding the function of catalytic materials.[93,94] In some cases, adsorbate species can be quantified, allowing the effective differentiation and counting of adsorption sites.[32,95] In the following the applications of IR for the characterization of catalytic Rh sites and hydroxyl groups on oxide supports, specifically CeO_2 and Al_2O_3, are discussed.

1.3.2 CO Probe Molecule FTIR

CO is commonly used as a probe molecule in FTIR analyses of supported metal catalysts because: (1) CO often chemisorbs on reduced metal surfaces or clusters, and on positively charged, atomically dispersed metal ions on supports; (2) the size of CO is comparable to the size on one adsorption site so it is not hindered by steric interactions; (3) in most cases, CO binds strongly enough be characterized in the adsorbed state at room temperature; (4) the stretching frequency of CO is responsive to changes in metal charge, dipole-dipole coupling with nearby CO, and the coordination number of the specific site.[90,96] Therefore, CO probe molecule FTIR is useful for identifying the oxidation state, stability, and coordination of metal clusters and atomically dispersed ions on oxide supports. [90,97–99]

CO bonds to metal surfaces similarly as a weak Lewis base would by donating electrons.[100] The internal CO stretching frequencies are generally shifted to lower

wavenumbers (red shifted) relative to free CO (~ 2143 cm^{-1}) following adsorption on metal sites, due to metal π bond to CO anti-π bond electron back donation, which weakens the CO bond resulting in a longer bond length.[100] The opposite is true for CO adsorption at metal acid sites, ie Al^{3+}, because the electron density from the CO molecule transfers to the metal site because there is a lack of electrons in the bonding orbitals of the metal atom.

a)

b)

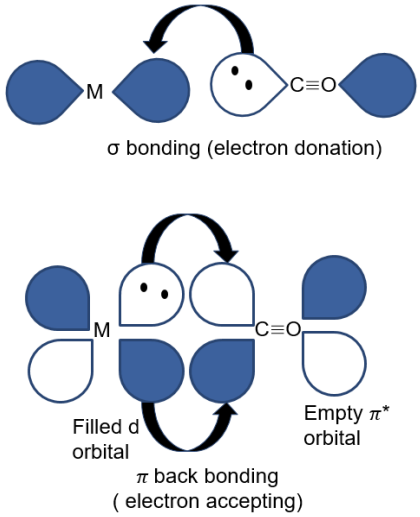

Figure 1.5: a) Visual example of σ bond forming by the overlap of orbitals with electrons transferring from CO σ orbital to metal σ orbital b) Visual example of π bond where electrons from metal π orbitals back donate to carbon π orbitals.[101]

The contributions from electrostatic bonding, **σ** bonding, and π bonding directly influence CO bond length, vibrational frequency, and corresponding FTIR peak intensity. In simple models, electrostatic bonding describes CO frequency shifts, which are proportional to the dipole moment and electric field strength, described as the Stark Effect.[102,103] Simultaneously, an increased frequency shift (blue shift) may be the result of a CO to metal cation **σ**-bond, which strengthens the bond and shortens the bond length similarly to an electrostatic bond (figure 1.5a). Electrostatic effects can be distinguished from **σ** bonding by the magnitude of the frequency shift, where the shift is significantly larger for electrostatic

effects compared to a **σ** bond shift.[102] Also, in the case of some precious metals, electrostatic bonds are much weaker than **σ** bonds, so they may only be observed via FTIR at cryogenic temperature. On the other hand, π-bonding via electron back donation creates a negative frequency shift (red shift) and a longer C-O bond that is weakened, corresponding to a stronger C-metal bond (figure 1.5b). The balance between the opposite shifts created by the different types of bonds depends on the amount and direction of the transferred electron density. Generally, increasing positive charge of the metal cation results in a blue shift of the FTIR band position because electrostatic and **σ** donation increases while contributions from π-bonding decrease. The opposite is true with decreasing metal ion oxidation state, which results in a red shift of the FTIR band position from π back donation with decreasing contributions from electrostatic effects and **σ** bonding.[104]

The intensity of IR absorption by monolayers of CO can also vary with changing CO coverage due to dipole-dipole coupling and coordination of the metal atoms binding to CO. The coordination number of a metal atom that CO is bound to has a large effect on the CO vibrational band intensity, and thus the extinction coefficient. In general, as the coordination number of the metal atom decreases, it has more electron density to donate to CO, forming a stronger CO-metal π bond. This has a significant effect on increasing the extinction coefficient of the CO stretch at this site because the CO-metal π bond increases the electron density in 2π* orbitals of CO, in which the electrons are much more mobile than in the **σ** bond, thereby increasing in the dynamic dipole moment of the CO molecule.[102] Compared to other probe molecules, the CO vibrational mode is enhanced two orders in magnitude by π back-donation, such as the case for linear bond CO to Rh.[105]

1.3.3 Rh Structure Dependent CO Bonding

FTIR studies have played an essential role in unveiling how CO bonds to supported and unsupported Rh, the electronic and oxidation state of Rh, and the structure of Rh species in supported catalysts[36,60,82,99]. CO adsorbed to Rh exhibits distinct stretching frequencies and coverage dependent characteristics for different Rh structures on oxide supports. For example, CO bonds to supported Rh on heterogeneous catalyst in 2:1, 1:1 or 1:2 CO:Rh stoichiometric ratios depending on Rh structure and local bonding environment. CO adsorption on single Rh atoms on oxide supports is known to result in the formation of a gem dicarbonyl species, $Rh(CO)_2$. The 2 COs create 2 vibrational modes, specifically a symmetric and asymmetric vibration assigned to ~2090 cm^{-1} and 2020 cm^{-1}, respectively. Stretches at ~2070 cm^{-1} and ~1850 cm^{-1} have been assigned to CO adsorbed in linear (1:1) and bridge bound (1:2) geometries respectively, at Rh metal cluster surfaces. [95,106–108] The exact energy of the CO vibration is highly dependent on the support, the oxidation state of the Rh, and the location of the Rh. For more complete characterization of Rh on oxides, probe molecule FTIR data is often supplemented with high-angle annular dark-field imaging scanning transmission electron microscope (HAADF-STEM), which provides nano-scale imaging of the supported Rh structure, or X-ray absorption spectroscopy (XAS), which provides information about the coordination environment around Rh.[109,110] There has been much work previously done to assign these bonding geometries to CO on Rh to develop a greater understanding of the potential of Rh as a catalytic material.

Extinction coefficients, ε_i, previously used for the symmetric gem-dicarbonyl, linear, and bridge configurations were calculated to be 74, 26, and 85 cm/mol, respectively.[106] These values and the intensities of the FTIR peaks, I_i, can be used in the equation 1.3.2.1 to calculate the relative quantitative fractions of the type of site that exists on the surface,

assuming complete coverage of all the sites. This has been shown to very useful when correlating and quantifying reactivity of a catalyst due to the specific quantity of types of sites.[40]

$$X_{iso} = \frac{I_{iso} / \left(\varepsilon_{iso} \times \left(\frac{CO}{Rh} \right)_{iso} \right)}{\sum_{i=1}^{3} \left[I_i / \left(\varepsilon_i \times \left(\frac{CO}{Rh} \right)_i \right) \right]} \quad (1.3.2.1)$$

In order to understand CO probe molecule FTIR on supported Rh materials, it is useful to first understand how CO behaves on well-defined surfaces of Rh. Surface science, using well-defined single crystal surfaces under highly controlled UHV conditions, can serve to benchmark CO stretch frequencies observed on supported Rh samples. Reflection absorption infrared spectroscopy (RAIRS) was utilized in a number of studies, which is sensitive even to low coverages of CO on Rh crystal surfaces due to image dipoles at the metal surface[111–113]. Jong and Niemantsverdriet assessed the population of CO in different adsorption sites on Rh [100] as a function of coverage using RAIRS[113]. On Rh crystals, CO occupies mainly linear adsorption sites (Rh-CO) at low coverages and then bridge bound adsorption sites (Rh_2-CO) at higher coverages. The frequency peak position and the area of the adsorption band also depend on coverage. As the CO coverage on Rh changes the frequency of the observed linear peak can be explained by dipole-dipole interactions, which is due to the electrostatic repulsion between neighboring CO adsorbates resulting in an increased CO stretch frequency and absorption intensity. Dubois and Somorjai performed additional experiments in which CO vibrational modes at 2070 and 1870 cm^{-1} were observed at CO saturation coverage on a Rh [111] single crystal and in addition used high resolution electron energy loss spectroscopy (HREELS) to further understand CO chemisorption on the Rh [111] single crystal surface to reach similar conclusions as on the Rh [100] surface.[114]

RAIRS in collaboration with DFT has verified linear adsorption sites at atop positions can be assigned to ~2040-2070 cm^{-1} and bridge adsorption sites at hollow positions can be assigned to ~1850-1940 cm^{-1} on a Rh [111] crystal and agree that the frequency and intensity shifts upward as a result of higher coverage and increased dipole-dipole coupling.[115,116] Additionally, as coverage of CO increases, the bond strength of the additional CO to the Rh is weaker as compared to the initially bound CO species[112,115]. The increase in wavenumber due to coverage effects agrees with what is observed for interacting CO molecules on most bulk metals due to dipole-dipole coupling, direct intermolecular repulsion, and indirect effects through the metal. Similar to Rh crystals, using CO probe molecule FTIR to study Rh surfaces formed when Rh particles or clusters are deposited on oxides has shown that CO binds to supported Rh nanoparticle surfaces in a bridge bound orientation (1 CO to 2 Rh) and a linear bound orientation (1 CO to 1 Rh) at vibrational modes of 1800-1950 and 2045-2070 cm^{-1}, respectively.[7–9] The bridge bound CO appears at lower vibrational frequencies than the linear bound CO because it has a lower effective bond order, resulting from one $\boldsymbol{\sigma}$ and one π molecular orbital. Strong interactions between Rh single atoms and CO results from Rh-C $\boldsymbol{\sigma}$-bonding and π orbital back-donation from the metal into C-O antibonding orbitals that creates significant differences in charge density between the metal and the adsorbate.

Yang and Garland systematically compared the IR spectra of dispersed Rh atoms and Rh nanoparticles to demonstrate the spectral properties of $Rh(CO)_2$. This was done by characterizing lower weight loadings (< 2%) of unsintered Rh on Al_2O_3 reduced at 150 °C, to samples with higher Rh weight loadings (8 and 16%) and to lower Rh weight loading samples that were sintered by reducing the sample at 400 °C. Notably, low Rh weight loadings (2%) displayed vibrational bands at 2095 and 2027 cm^{-1} that did not vary in frequency with increasing coverage, indicating minimal interaction of nearby C-O dipoles.

The IR bands disappeared simultaneously during CO desorption, indicating that the bands are coupled to the same species. It was hypothesized that these vibrational bands represented a single cationic metal atom of Rh in a highly dispersed state on the surface of the oxide due to the stably coupled appearance at lower metal concentrations. Yao and Rothschild made similar conclusions about the doublet assignment when finding that low weight loadings of Rh on Al_2O_3 that exhibit solely the doublet have a concentration of 2.5 Rh micromoles/m^2 , which equates to an average distance of 8 Å between neighboring Rh atoms that is necessary for $Rh(CO)_2$ formation.[118]

In Garland and Yang's experiments, vibrational bands appeared at 1800-1950 and 2045-2070 cm^{-1} in increasing intensity and frequency as the Rh weight loading increased. The linear and bridged bound CO stretches shifted to higher frequencies with increasing coverage due to interaction of a site with other adjacent sites. On the 2 % sintered sample, when CO was added stepwise, a 2045 cm^{-1} peak appeared at lower CO coverages, but 2095 and 2027 cm^{-1} appeared and convoluted this peak as the coverage of CO increased. The 2045 cm^{-1} peak for the 2% sintered sample was also found to appear first on the 8% and 16% sample when CO was added stepwise, analogous to what in seen with Rh crystals. This is in line with Arai and Tominaga's findings from performing CO desorption and stepwise addition because the bands associated with the linear and bridge bound species appeared at lower coverages than the $Rh(CO)_2$ species, indicating that CO prefers to occupy these sites, and thus forms a stronger bond to linear and bridge sites on Rh nanoparticles.[76]

Primet performed experiments on Rh materials and concluded that the oxidation state of Rh in the $Rh(CO)_2$ species is +1 on both Al_2O_3 and zeolite supports by using FTIR with complimentary XPS data, which provided the Rh chemical state by measuring characteristic binding energies of core level electrons in Rh.[119] Rice and Worley continued this

interpretation of the spectrum of CO adsorbed on Rh by assigning oxidation states to certain CO stretch frequencies, with higher frequencies corresponding to higher oxidation states.[120] For samples that produce the 2090 and 2020 cm^{-1} bands after reduction and CO exposure, a moderate reduction or O_2 pulsing prior to CO adsorption caused a CO stretching frequency of 2116- 2120 cm^{-1} to appear. Thus, this peak is assigned to CO adsorption on Rh in the +2 oxidation state.

The oxidation state of Rh species that forms bridge and linearly bound CO species also displays a red shift from higher frequencies to lower frequencies as the oxidation state of Rh decreases from +1 to 0 and the Rh atoms gain electron density. For example, it has been noted that high weight loadings (10% Rh) CO adsorption on reduced samples produces higher wave number (~1900 cm^{-1} vs. ~1850 cm^{-1}) features, while pre-oxidation results in disappearance of the ~1850 cm^{-1} and a shift in the ~ 2070 cm^{-1} band to higher frequency numbers, implying an increase in oxidation state of the Rh.

Table 1.1 summarizes the effects of oxidation state and coordination on the band position as a result of the type of bonding and electron density transfer happening in the C-Rh orbitals. Similarly, if the support is electron rich at the surface, it can shift band positions to higher wavenumbers because there is more electron density transfer. While using CO as a probe molecule can be very informative in analyzing Rh structure, bonding type, oxidation state, and electronic properties, CO has been shown to fragment Rh clusters into single atoms, because the binding energy between CO and dispersed Rh species is greater than the binding energy between Rh and the support, thus creating a driving force for particle fragmentation.[32]

Table 1.1: Summary of effects on band position according to oxidation state and coordination of Rh.		
Rh species	Effect on band position	Explanation
Increase in cationic nature (Increase in Rh Oxidation state) (Rh^{+3}>Rh^{+2}>Rh^{+1}>Rh^{0})	Increase in band position	Electrostatic and **σ** donation increases while contributions from π-bonding decrease, which strengthens the C-O bond and shortens the bond length.
Increase in neutral nature (decrease in Rh Reduction state) (Rh^{0}>Rh^{+1}>Rh^{+2}>Rh^{+3})	Decrease in band position	π-bonding electron back donation increases while contributions from electrostatic effects and **σ** bonding decrease, which strengthens the C-Rh bond and creates a longer C-O bond.
Under-coordinated (less Rh-Rh bonds such as edge and corner sites)	Decrease in band position	Higher electron density transfer to the C-Rh bond orbitals, which strengthens the C-Rh bond and creates a longer C-O bond.
Well-coordinated (multiple Rh-Rh bonds)	Increase in band position	Less electron density transfer to the C-Rh bond orbitals due to competition with additional Rh-Rh bonds, which strengthens the C-O bond and creates a shorter C-O bond.

Fragmentation of Rh clusters into dispersed species on oxide surfaces due to CO adsorption has been proposed to first involve the weakening of Rh-Rh bonds by the adsorption of CO on Rh_0 surface sites.[121] Then after the bond weakening, mobile [Rh_0-CO] * species can migrate across the oxide surface to isolated OH groups to react and displace hydrogen to form $Rh(CO)_2$. Smith et al. proposed the formation of cationic $Rh(CO)_2$ occurred via Rh cluster dispersion on a hydroxylated Al_2O_3 surface, such that multiple surface hydroxyls to attach to Rh and form the $Rh(CO)_2$ square planer structure, similar to the mechanism of Fe dispersion where surface hydroxyls perform a nucleophilic attack to bond to positively charged electrophilic metal atoms due to the electron rich surface.[122]

Thus, specific properties of the support in terms of acidity and hydroxyl content play an important role when analyzing the structure of Rh on oxide supported catalysts along with the knowledge of the $Rh(CO)_2$, linear and bridge Rh-CO bonded geometries. Also, recognizing hydroxyl groups present at the surface can affect how these peaks shift as a result of coverage, coordination, and electronic structure. The further understanding surface

hydroxyl chemistry on oxide supports is needed to better analyze the local structure of Rh, especially the $Rh(CO)_2$ species.

1.3.4 NO Probe Molecule FTIR

Using NO as a probe molecule in FTIR for oxide supported Rh structures has many commonalities with using CO as a probe molecule that make it a useful technique, specifically for NO reduction. However, there are key differences in the electronic structure of NO that create complications during characterization. Both CO and NO bond to ionic metal centers. Just as the CO stretching frequency generally does, increasing the positive charge of the metal cation results in a blue shift of the bonded NO stretching frequency in the positive direction. NO interacts with metal centers (both positively charged or neutral) to form surface nitrosyls, resulting in a wide range of stretching frequencies depending on the resulting bonding configurations and geometries[123]

However, unlike CO, the adsorbate–adsorbent bonding energy on non-transition metals is weaker than the adsorbate– adsorbate interaction because NO is a radical with an extra electron that enables adsorbate bonding and dimerization to form N_2O_2 species. The surface species observed on non-transition metal oxides are predominantly dimers formed by NO-NO interaction, and thus results in complicated spectroscopy signatures. When NO interacts with positively charged transition metal centers the presence of its extra electron allows NO to create strong bonds by sharing it (figure 1.6).[124] Also, the empty π^* orbital gives NO the ability to act as electron acceptor if there is an excess of electron density. The bonding of NO can be characterized by a larger back donation of electrons, associated with a larger oscillator strength. In comparison to CO, the NO probe molecule amplifies d–π overlap effects.[123] Resulting in a weaker intensity of NO in FTIR and a larger extinction coefficients.[125,126]

Due to its radical character, NO is more reactive than CO, and on metal surfaces easily undergoes dissociation or reaction with adsorbed oxygen. The formation of these species is the result of direct electron donation or electron abstraction. Therefore, the bonding structure of NO can be heavily influenced by the amount of electron density available. For example, if a support is electron deficient, then NO is more likely to donate an electron during probe molecule bonding and result in a neutral or positively charged NO^+ species. Unlike CO^+, NO^+ species are observed as stable species on oxide surfaces at room temperature. This makes NO a useful probe in comparison to CO when trying to identify the charge state of adsorbent sites. Therefore, NO is a widely used for the characterization of undercoordinated cationic sites and the measurement of the acidity of nearby surface hydroxyls.[127]

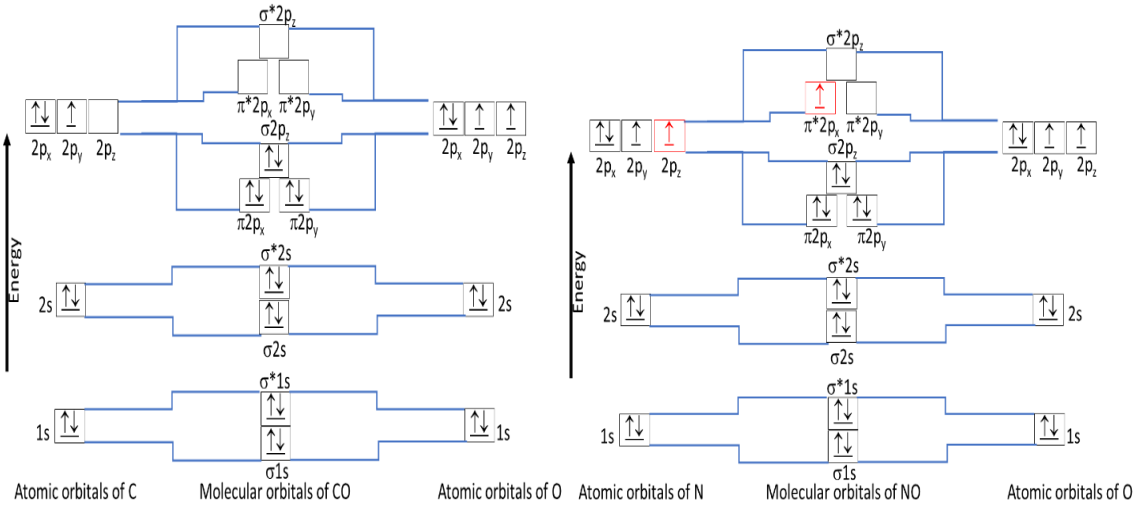

Figure 1.6: Comparison of CO molecular bonding orbital (left) and NO molecular bonding orbital (right), highlighting extra electron in red on the in π* orbital that can cause NO to act as a radical or dimerize.

Notably, the formation of NO^+ is not the result of the direct interaction with an electron acceptor site (strong Lewis acid site) but due to interaction of NO with nearby oxygen absorbed to the coordinated metal (see equation 1.3.4.1).[127] In some cases, such as

highly ionic surfaces, dimers of the ionic species, $(N_2O_2)^{2-}$, are observable by IR on oxide surfaces. Again, $(N_2O_2)^{2-}$ species are not the direct product of electron abstraction from the surface but the reaction with undercoordinated O^-. It was even reported that NO interaction red shifted the OH vibrational frequency on zeolite materials and at higher NO coverages, the OH–NO complexes converted into $OH(N_2O_2)$ species. When NO is coadsorbed with O_2 on zeolite material, it interacts with the acidic hydroxyls, localized at cationic zeolite exchange sites, to form NO^+ ions (stretching mode ~2133 cm).[128] The NO stretching frequency shift can also be used to estimate the basicity of the oxygen to which the NO^+ cation is bonded.

(1.3.4.1) $$2\,NO + \tfrac{1}{2}\,O_2 + 2\,O_{lattice} - H^+ \rightarrow H_2O + 2\,O_{lattice} - NO^+$$

In some cases where dimerized $(N_2O_2)^{2-}$ subsequently forms NO_2 or NO_3, a nitrosyl species can replace surface OH groups by disproportionation (equation 1.3.4.2 or 1.3.4.3).[127,129,130]

(1.3.4.2) $$3\,NO_2 + 2\,M - OH \rightarrow 2\,M - NO_3 + NO + H_2O,$$

(1.3.4.3) $$2\,NO_2 + 2\,M - OH \rightarrow M - NO_3 + M - NO_2 + H_2O.$$

Thus, probing oxide supported Rh catalysts with NO can be extremely useful and relevant, but one must carefully consider all the complexities. Arai and Tominaga studied NO/CO adsorption and bond strength over Rh/Al_2O_3 and found that NO primarily adsorbed in two forms; linearly and in a bent angle structure, see figure 1.7.[76] The adsorbed NO species is neutral, or net negatively charged, but can gain positive charge due to the electron withdrawing effect of oxygen atoms near Rh. Through an x-ray study of these compounds, both the Rh-N and N-O bonds of the linear structure were stronger than the bonds of the bent structure. This was attributed to the cationic nature of the linear NO and the anionic nature of the bent NO.[36] In addition, Anderson claimed that Rh^+ mononitrosyls, characterized by a

band at 1910 cm^{-1}, could be converted into dinitrosyl's species with characteristic bands at 1826 and 1734 cm^{-2} at high temperatures with NO_2.[131–133] Clear examples of a Rh dinitrosyls at room temperature have been observed on Rh on zeolites, such as Rh/Y and Rh/ZSM5, with characteristic bands at 1855 and 1780 cm^{-1}.[97,133–135] Notably, the specific oxide support influences the NO stretching frequency on Rh, how NO bonds to Rh, and the dimerization of NO over Rh. For example, Rh is commonly found in a neutral Rh^0 state on silica supports so $Rh^+(NO)_2$ species are not observed at room temperature via FTIR on pure silica.[136–138]

Anderson continued to study NO interaction over Rh/Al_2O_3 by comparing NO_2 decomposition over the catalyst to assign frequencies to NO-Rh via NO_2 decomposition and to NO_2-Rh/Al_2O_3 via NO dimerization .[131,132,139] This agreed with early assignments by Pozdnyakov who studied NO and NO_2 interactions over plain Al_2O_3 (table 1.2) and has also been shown to happen over TiO_2 and ZrO_2 by Hadjiivanov, and Knözinger.[130,139,140] In comparison, when Arai and Tominaga introduced oxygen to the NO adsorbed Rh/Al_2O_3 sample, the Rh-NO bond strength decreased rapidly as the NO reacted to form a bidentate nitro-structure. Subsequently in reducing conditions, the frequency of this structure decreases and the nitrosyl decomposes.[76] Seeing that the NO reacted differently due to being exposed to oxidizing or reducing conditions, Chuang et al. suggested the formation of different products from NO reduction by CO was due to NO interacting with Rh at variable charge states.[29,89] He reported that Rh^0 -NO^- were responsible for NO dissociation, producing N_2 while Rh^+ sites formed $Rh^+(CO)_2$ while in excess CO reduced Rh^+ to Rh^0 to form CO_2, creating more active sites for NO dissociation. Chafik et al. observed similar behavior on $Rh/W/TiO_2$.[36] Such studies refuels the concept of looking at how the reactivity of atomically dispersed Rh structures during NO reduction is important in TWCs and also highlights the importance of support interaction, specifically via hydroxyl groups with Rh and NO.

Table 1.2: Nitrosyl band assignments on a Rh/Al_2O_3 catalyst by Anderson et al.[131,132]			
Site	cm^{-1}	System	Notes
NO/Rh+	1986	$NO_2/Rh/Al_2O_3$	After adsorption and decomposition of NO_2
NO/Rh+	1944-1934	$NO_2/Rh/Al_2O_3$	After adsorption and decomposition of NO_2 20 °C
NO/Rh+	1910	$NO_2/Rh/Al_2O_3$	Formed from $Rh(NO)_2$, After adsorption and decomposition of NO_2 at 200 °C
2NO/Rh+	1826/1734	$NO/Rh/Al_2O_3$	$Rh(NO)_2$, 200 °C
NO/Rh+	1645	$NO/Rh/Al_2O_3$	200 °C when heating in NO
NO_2 / Al_2O_3	1620, 1593, 1560	NO_2 / Al_2O_3	20°C
	1311, 1289		bidentate nitro-structure
NO_2 $/Rh/Al_2O_3$	1592,1567	$NO_2/Rh/Al_2O_3$	
	1306, 1209		bidentate nitro-structure
NO_2 $/Rh/Al_2O_3$	1540	$NO_2/Rh/Al_2O_3$	Rh or Al
	1309, 1231		Rh or Al, bidentate nitro-structure
$NO_2/$ Rh/Al_2O_3	1564, 1520	$NO/Rh/Al_2O_3$	Rh or Al, 200 °C
	1233, 1317		Rh or Al, 200 °C, bidentate nitro-structure
NO/Al^{3+}	1985	NO/Al_2O_3	Previous assignment by Pozdnyakov
$NO_2/$ Al_2O_3	1620, 1600	$NO_2/$ Al_2O_3	Previous assignment by Pozdnyakov bridging bidentate nitro-structure, 20 °C,
$NO_2/$ Al_2O_3	1330, 1230	$NO_2/$ Al_2O_3	Previous assignment by Pozdnyakov, bridging bidentate nitro-structure, 20 °C
	1245		Previous assignment by Pozdnyakov, bridging bidentate nitro-structure, 20 °C

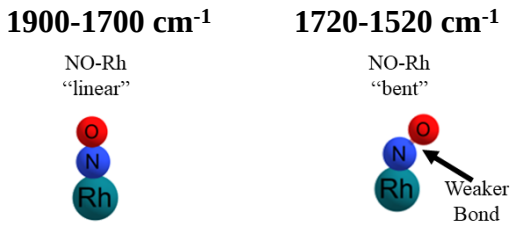

Figure 1.7: Most common NO to Rh bonding configurations; Linear NO to Rh in FTIR range 1900-1700, normally neutral or positively charged due to antibonding electron transfer to metal d-orbital; Bent NO to Rh in the FTIR range 1720-1520, normally neutral or anionic due electron transfer from metal d-orbital to NO.[76]

1.4 Oxide Support Surface Chemistry

1.4.1 Hydroxyl Surface Chemistry

Information gathered from probe molecule FTIR to identify specific kinds of Rh structures assists in understanding how these structures may be influenced by support properties. The support properties of surface acidity and hydroxyl content of metal oxide supports can greatly influence the placement of Rh during synthesis, the position of Rh atoms in reactive conditions, and the catalyst reactivity. [93,141–143] These properties are interrelated and aid in comprehending how the catalyst is created and how it functions.[144] Surface hydroxyls can influence the local position of Rh, the charge, and the stability by either acting as an in-between bonding ligand to the support, allowing Rh atoms to displace the hydroxyl to bond to the surface or being in physical proximity to the Rh site.

Hydroxyl formation may also be related to material synthesis where interaction of the metal oxide support with hydrogen containing reagents such as water, strong acids, or strong bases can modify hydroxyls to become OH^- and H^+ ligands. [141,145] In the case of water, two different types of hydroxyls will be formed with OH^- and H^+ ligands (see figure 1.8). In the case of strong electrostatic adsorption synthesis, anionic or cationic precursor ions are attracted to the receptor sites of cationic or anionic surface hydroxyls respectively (or in the

case of cationic precursors, anionic surface oxygens). The position of the Rh atom is altered after subsequent pretreatments. Hydroxyls may be produced when the oxidation state of a metal cation in the oxide is modified. For example, following the oxidation of a metal oxide support, additional hydroxyl groups can attach to the surface in a moist atmosphere to compensate for increased surface charge. Additionally, precursor ligands and some hydroxyls created from synthesis are removed and the oxidation state of the Rh metal is increased as the material is highly saturated with oxygen. Then following reduction, some oxygens are removed to form water that is purged out of the system and some surface oxygens can become hydroxyl groups by bonding to excess hydrogen to compensate for decreased surface charge.[127] The final state and position of Rh directly affects catalyst activity and selectivity because of the Rh stability, charge, and local environment. If the state of the Rh is more stable, it can provide more consistent catalyst reactivity rather than creating fluctuations due changes in position. The charge of the Rh may create a stronger or weaker bond with the reactant. Finally, the local environment may have reactive support effects such as interactions with oxygens, metal cationic sites, or with hydroxyls formed after reduction. The hydroxyls may even block certain metal or oxygen sites that could create different chemistry if the surface were hydroxyl free.

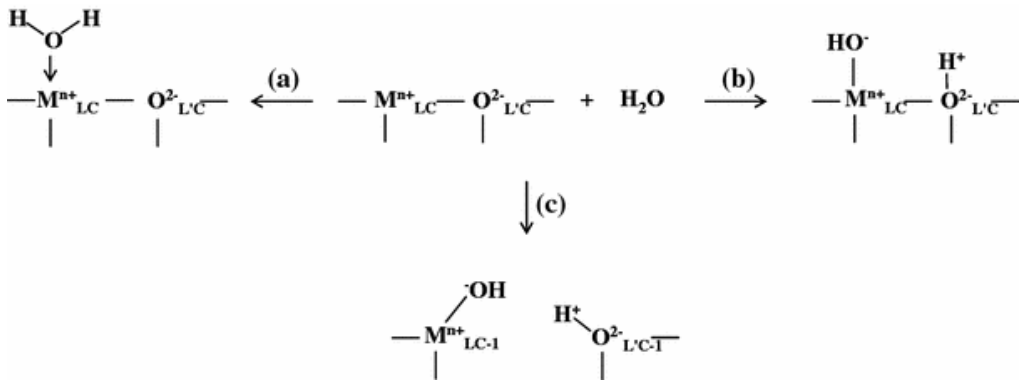

Figure 1.8: Interaction of water with the surface of an oxide: a) adsorption of molecular water, b) dissociation on metal- oxygen, M^{n+}–O_2^- pairs, c) hydrolysis of M^{n+}–O_2^- bond to change the local coordination (LC)[146]

There are four types of surface hydroxyl groups that can be identified by their coordination to local metal atoms where type I, II, III correspond to one hydroxyl group bonded to 1, 2, and 3 metal atoms, respectively and germinal, where two hydroxyl groups bond to one metal atom.[127,147] Hydroxyl groups at the surface of metal oxides compensate for charge deficiency, so the type of hydroxyl group created on the surface depends on the local charge density of the metal atoms that they are bound.[127] Hydroxyls can exist stoichiometrically due to an even distribution of charge density, or due to defects in the bulk structure[146].

The change in charge state of the metal due to the formation of hydroxyls has been shown to transform Lewis acid sites (unsaturated metal cations) into Brønsted acid sites (hydroxyl groups). [148,149] The Lewis basic sites are oxygen anions, and Brønsted acid sites involve oxygen from hydroxyl groups. [150] The acidity or basicity of surface OH groups depends on the electronic properties of corresponding metal cationic and the type of hydroxyl coordination to the metal cation[143]. Hydroxyls that are bound ionically with the cationic metal are more basic in nature and those that are bound covalently will be more acidic[127]. Type II is generally more acidic compared to type I, if the bonds are covalent, because the strongly bound oxygen to the surface results in a weak O–H bond. Type III hydroxyls cannot

accept protons because electrons from the oxygen atom are engaged in bonding to the three metal atoms, thus this coordination cannot have basic properties but may potentially acidic or neutral[127]. In cases where the cationic acidic hydroxyl is very loosely bound to the support, precious metals such as Rh can easily replace such a site in the synthesis of catalysts or potentially during fragmentation of small metal clusters. Certain hydroxyls can act at oxidizers. For example, CO adsorption on atomically dispersed Rh can lead to $Rh(CO)_2$ formation subsequent to Rh oxidation by hydroxyls, demonstrated earlier by the decrease in the hydroxyl region in FTIR, see equation 1.4.1.1 below. [127]

$$Rh^0 + OH^- + 2\,CO \rightarrow O^{2-} - Rh^+(CO)_2 + \tfrac{1}{2}H_2 \quad (1.4.1.1)$$

The proton in an OH group can be exchanged with another positive charge including metal cations, NH^{4+}, or NO^+. The more acidic the OH group, the easier the exchange. Because the bridging hydroxyls in zeolites are among the most acidic surface OH groups, where ion exchange is widely used to deposit precious metals such as Rh. The nature of the hydroxyl groups is support and surface dependent, therefore the following will provide specific detail on the supports of interest, γ-Al_2O_3, CeO_2, and TiO_2.

1.4.1.1 γ-Al_2O_3

Experimental and theoretical studies have shown γ-Al_2O_3 is a rhombohedral shape with the predominant exposed facet, making up ~75% of the surface, being the [110] cut of the tetragonal crystal structure.[151–153] The next most exposed surfaces are the [100] surface (~15% exposure) and the [111] surface (~10% exposure). The types of hydroxyls that exist are dependent on the specific surface but there are general properties of γ-Al_2O_3 that influence the hydroxyl content and acidity of the support.[154,155] The strong Lewis acidity of low coordination Al^{3+} cations create a highly hydroxylated surface when treated with water

because the strong Lewis acid sites adsorbs water very strongly prior to decomposition.[148,155] The hydroxyl groups on Lewis acid sites remain stable unless there is a molecule or atom that is capable of displacing it, such a strong base like pyridine, or if the oxide is exposed to vacuum conditions at elevated temperature. At the same time, there are basic oxygen sites at the surface that are capable of donating electrons and attaching onto H^+ ions, dissociated from water, to create acidic hydroxyl groups, Brønsted acid sites.[156]

According to Digne et al and Xinsheng, using a combination of experimental and theoretical knowledge, specific FTIR hydroxyl bands assigned to specific hydroxyl groups on the surface of γ-Al_2O_3 can be detected as follows.[151–153,157,158]

1. ~ 3650-3590 cm^{-1} corresponds to type III hydroxyl groups where H^+ is bound to an existing basic oxygen, which is coordinated to three 6-fold coordinated Al atoms on the [100].
2. ~3710- 3690 cm^{-1} corresponds to type II with 2 different cases: an existing basic oxygen is bonded to an H^+ ion and two 6 fold coordinated Al atoms on the [111] surface after hydration and another case where an OH^- ion bonds to two 5 fold coordinated Al atoms on the [110].
3. ~3735–3725 cm^{-1} corresponds to type I where an OH^- ion bonds to one 5 fold coordinated Al atom on the [110].
4. ~3745–3740 cm^{-1} corresponds to type III where an existing basic oxygen is bonded to an H^+ ion and three 6 fold coordinated Al atoms on the [111].
5. ~3780–3760 cm^{-1} corresponds to type I where an OH^- ion bonds to one 6 fold coordinated Al atom on the [100].
6. ~ 3800- 3785 cm^{-1} corresponds to type I where an OH^- ion bonds to one 4 fold coordinated Al atom on the [110].

These assignments have been debated but generally accepted when analyzing the structure of hydroxylated γ-Al_2O_3 surfaces. Some sites may be Brønsted acid sites but not all, based on the charge balance. Measuring the Brønsted acidity of the different hydroxyls can be challenging because the bands overlap and appear convoluted especially in the case bands at ~3710- 3690 cm^{-1}. Xinsheng was able assign weak, medium, and strong Lewis acidity to 5, 4, and 3 coordinated Al^{3+} ions, respectively, on the surface of γ-Al_2O_3 using pyridine adsorption to measure hydroxyl displacement by the strong base.[157] The weak Lewis acid sites are next to type II groups (~3710- 3690 cm^{-1}), the medium strong Lewis acid sites are next to type III (~ 3650-3590 cm^{-1}), and strong Lewis acid sites are next to type I (~3735–3725 cm^{-1}).[157] The existence of type I hydroxyls' location next to the strongest Lewis acid sites explains why they are considered the most reactive hydroxyl site because base molecules can adsorb onto the Lewis acid site and concurrently react with the hydroxyl.[158].

1.4.1.2 CeO_2

Ceria is considered an easily reducible oxide where H_2 reduces the metal cations from a Ce^{+4} to a Ce^{+3} state and the resulting converted H^+ reacts with lattice oxygen to form hydroxyl groups. Reduction and oxidation pretreatments strongly affect the existence of surface hydroxyl groups on CeO_2. The predominant [111] and [001] surfaces similarly have many basic surface oxygens when in an unreduced state.[159] Water strongly binds and decomposes at oxygen vacancy sites even at low temperatures on partially reduced surfaces. Surface hydroxyls on ceria can also be produced as a result of H_2 dissociation.[160]

Lavalley was able to assign specific FTIR hydroxyl bands to specific hydroxyl types on the surface of CeO_2 as follows[161]:

1. ~ 3720-3690 cm^{-1} corresponds to type I.

2. ~3660–3650 cm^{-1} corresponds to type II-A where an H^+ ion is bonded to a basic oxygen in a highly oxygen saturated environment where the hydroxyl bonds to 2 Ce^{4+} ions
3. ~3640–3620 cm^{-1} corresponds to type II-B where an H^+ ion is bonded to a basic oxygen in an unsaturated oxygen environment where there are many vacancy defects and where the oxygens bond to 2 Ce^{3+} ions
4. ~3600–3585 cm^{-1} corresponds to type III at the surface of particle.
5. ~3550- 3450 cm^{-1} corresponds to type III with in the pores of a porous material.

A gradual shift can be noted during reduction of CeO_2 from the predominant ~3660–3650 cm^{-1} bands to ~3640–3620 cm^{-1} bands. Only small intensity of type I and type III bands are usually observed.

1.4.1.3 TiO_2

TiO_2 comes in 2 distinct phases with different crystal structures and exposed facets: anatase and rutile. Hydroxyl groups are specific to the specific facet of the specific phase.[162] At ambient pressures and temperatures, the rutile phase is the thermodynamically stable phase of TiO_2 but anatase is most commonly found in natural and synthetic samples.[163] Anatase particles initially have 77% [101] /[011] and 33% [001] surfaces but in certain environments, pressures, and temperatures, the particle can morph to also have [100] and [110] surfaces (figure 1.9).[164] Rutile particles predominantly have 60% [110], 20% [101]/[011]/[001] and 20% [100] surfaces (figure 1.9).[165] Anatase restructures into Rutile in air when held at elevated temperatures above 650 °C.[166]

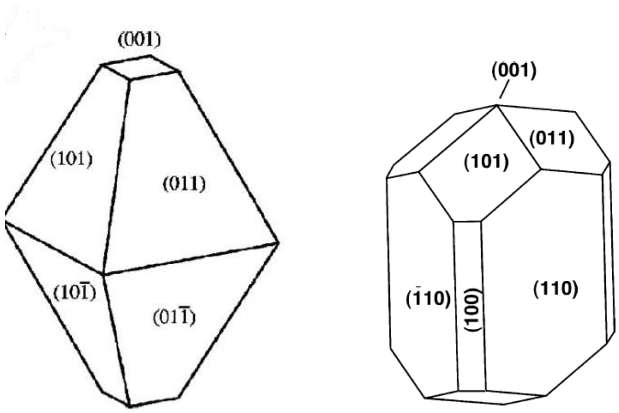

Figure 1.9: Most common phases of TiO_2 and exposed crystal facets; On the left, the less stable anatase phase with [101], [011], and [001] surfaces; On the right, the most stable Rutile phase with [110], [100], and [101]/[011]/[001] surfaces.[164]

Anatase OH groups and morphology were initially assigned by Tsyganenko and Filimonov experimentally and collaborated by many FTIR/DFT studies.[147,167–174] As follows, OH frequencies on anatase can be detected in IR such that:

1. ~3742-3730 cm^{-1} corresponds to type I hydroxyls where a H^+ ion + is bound to an existing basic oxygen, which is coordinated to a 5-fold coordinated Ti^{4+} atom on the [001]. Stable and located at crystal edge sites.

2. ~3720-3715 cm^{-1} corresponds to type I hydroxyls where a H^+ ion + is bound to an existing basic oxygen which was coordinated to a 5 fold and a 6 fold coordinated Ti^{4+} atom on the [101]

3. ~3699–3696 cm^{-1} corresponds to type II hydroxyls where a H^+ ion bonds to an existing oxygen bonded to a 5-fold and 6-fold coordinated Ti^{4+} atom on the [100]

4. ~3675 cm^{-1} corresponds to type II hydroxyls where OH- bonds to two 4-fold coordinated Ti^{4+} on [110]

5. ~3680-3620 cm^{-1} corresponds to weakly adsorbed type II hydroxyls where H_2O bonds to two 5-fold Ti^{4+} on [101]

Many hydroxyl sites on the anatase surface are composed of H^+ bonded to stongly bound surface oxygen. This agrees with findings that oxygen vacancies are formed in the bulk of the anatase material, rather than on the surface.[171,175,176] When rutile [110] is hydroxylated, OH^- ions lie directly above the surface Ti^{+4} cations. The rutile [110] crystal face adsorbs water dissociatively leading to the presence of equal quantities of two types of OH, similar to CeO_2. One of these types is associated with a surface five-fold coordinated Ti^{4+} after dissociated H^+ bonds to a nearby oxygen to create a type I hydroxyle (3650 cm^{-1} stretching frequency) and the other is a type II OH^- bound directly to two adjacent surface four-fold coordinated Ti^{4+} ions (3410 cm^{-1} stretching frequency).[165,172,177–181] These are normally formed due to H_2 reducing conditions or the direct decomposition of H_2O.

1.4.2 Water-Gas Shift Chemistry

The ability for oxides such as CeO_2 and TiO_2 to decompose H_2O can be amplified by active Rh metal. Atomically dispersed Rh can directly react with exposed oxide surfaces and oxide adsorbed species, thus making it an interesting candidate for interacting with CO to provide pathways for the water-gas shift reaction (WGS), resulting in H_2 and CO_2 gas. While the objective to make stable atomically dispersed Rh catalyst is appealing to utilize for real world applications that require a non-hydrocarbon hydrogen source, it is likely that this reaction is already present in TWC chemistry.

The WGS reaction was first discovered by Italian physicist Felice Fontana in 1780.[182] However, the reaction was first patented by the British scientists Mond and Langer in 1888 for the first working fuel cell application with a Fe catalyst for the conversion of coal-derived Mond gas (the product of the reaction of air and steam passed through coal/coke, which became the basis for the future coal gasification processes).[182–184] In 1913, the WGS found industrial application in the production of synthesis gas (CO_2 and H_2) as a part of the Haber-

Bosch process for NH_3 used as fertilizers, arguably the most important catalytic process in the world that revolutionized the economics of farming production and allowed for mass food supply.[184–186]

The specific catalyst used in the Haber-Bosch process for H_2 production via water-gas shift is a Cu-ZnO-Al_2O_3 material and operates at the low, and economical temperature of 150-250 °C. However, there is also significant interest in developing noble metal catalysts for water-gas shift to operate at even lower temperatures. Pt, Rh, Ru, Au, or Pd deposited on CeO_2, ZrO_2, TiO_2, Fe_2O_3, or mixed oxides have been seen to be active at 250-400 °C for WGS.

Grenoble et al. studied the kinetics of WGS to propose a reaction rate expression that correlated with several oxide supported precious metal catalysts (including Rh/Al_2O_3, Rh/SiO_2, Pt/Al_2O_3, Pt/SiO_2, or Pt/Al_2O_3+CeO_2).[187] He suggested that the initial H-O bond in H_2O was broken via CO insertion and resulted in formic acid (HCOOH) formation as an intermediate. He highlighted that support interaction/selection was important because precious metal proximity to strong Lewis acid sites was required for molecular H_2O to adsorb via the oxygen (see figures 1.8a). This type of support interaction was preferred over H_2O decomposing on metal-oxygen, M_{n+}–O_{2-} pairs (see figure 1.8b). Based on these mechanistic steps, industrial data was used to derive a valid equilibrium constant and empirical model for the reaction.[188] While Phatak et al. proposed that the previously studied Goodridge/ Qazi WGS model could be applied with a first order dependence on H_2O for precious metal catalysts, and Thinon et al. proposed a model with Carboxylic acid (COOH) as an intermediate over precious metal catalysts, both of these model examples were only demonstrated for Pt catalysts, and not applied to Rh catalysts.[189,190]

Alternatively, Wheeler et al. proposed a Langmuir Hinshelwood reaction model (where both adsorbates initially adsorb and then interact) that did not require precious metal proximity to support Lewis acid sites but instead applied to noble metal catalysts that were easily reducible or supported on highly reducible CeO_2 (including Ru, Ru/CeO_2, Rh, Rh/CeO_2, Ni, Ni/CeO_2, Pd, Pd/CeO_2, Pt, or Pt/CeO_2).[191] Because Ce can easily convert between a +3 and +4 charge state, it could act as an adsorption and decomposition site for H_2O interchangeably with precious metal sites in proximity. However, in this model by Wheeler, the precious metal site is required for CO absorption and oxidation into CO_2.

In contrast, Shido et al. specifically looked at Rh doped CeO_2 in a combination of FTIR and kinetic studies and found that CO reacts with OH groups from dissociated H_2O over Ce ions to form a bidentate formate, which then decomposes into H_2. The presence of Rh decreased the reaction barrier compared to performing the reaction over plain CeO_2.[192] More recent studies suggest similar theoretical pathways for WGS for other atomically dispersed precious metal sites on reducible oxide supports.[193–195] WGS has also been observed over atomically dispersed Rh on other supports such as zeolites experimentally via hydroxyl interaction, similar to what was discussed by Grenoble. Utilizing FTIR, Fang, Gates, et. al recently suggested WGS occurred over Rh on zeolite Y hydroxyls through a mechanism in which Rh sites disperse into single atom sites and then re-agglomerate into Rh clusters.[31] This type of Rh mechanism involving reconstruction is a possibility for NO reduction in industrial TWC, especially at low temperatures in the presence of H_2O when NH_3 is a product.

1.5 Summary of Chapters

Shown in Chapter 2, we initially sought to develop a general approach for synthesizing atomically dispersed Rh catalyst on various oxide supports. Synthesizing

atomically dispersed Rh catalysts is challenging because the metal species often thermodynamically prefer to form Rh clusters. Characterizing the structure of oxide supported Rh species can also be challenging because Rh is known to be mobile on oxide supports, leading to sintering or redispersion. Here, we used principles of strong electrostatic adsorption (SEA) to establish pH dependence, precursor speciation, and support influence on the synthesis of atomically dispersed Rh catalysts on commercially relevant oxide supports (CeO_2 and γ-Al_2O_3). We used cryogenic CO probe molecule infrared spectroscopy to distinguish atomically dispersed Rh from small clusters Rh, which prevents CO-induced mobility. The structural analysis of Rh species is substantiated by aberration corrected scanning transmission electron microscopy. The general approach to synthesizing and characterizing atomically dispersed Rh catalysts presented here provides a straightforward approach for the development of structure-function relationships for important catalytic processes.

In Chapter 3, we considered the case of atomically dispersed Rh on rutile TiO_2 to investigate the optimal structure during O_2 calcination, H_2 reduction, CO adsorption, and reverse water gas shift (RWGS) reaction conditions. We used cryogenic CO probe molecule FTIR in collaboration with STEM imaging, XPS and DFT calculations to distinguish local Rh bonding structure and demonstrated that Rh atoms adapt their local coordination and reactivity in response to variation in redox environmental conditions. In agreement with DFT calculations, the most stable coordination of atomically dispersed Rh atoms on rutile TiO_2 in an oxidative environment is coordinately saturated and does not bind CO. However, after exposure to reducing conditions and CO saturation, the $Rh(CO)_2$ structure is prevalent because oxygen vacancies nearby Rh are formed. In RWGS conditions, atomically dispersed Rh coordinates to 1 CO and 1 H. These findings show that atomically dispersed Rh species

should not be considered static during pre-treatment, characterization with probe molecules, or under reaction conditions, and may change from inactive to active in certain conditions, hence explaining some conflicting accounts in the literature.

In Chapter 4, we expand on findings shown in Chapter 3. We provide evidence that atomically dispersed Rh exists in varying local coordination environments on oxide surfaces, depending on the reductive environment (H_2 vs CO reduction). When reduced by CO and $Rh(CO)_2$ is formed, and during TPD both COs desorb simultaneously. However, when H_2 is used below 200 °C as a reductant, the COs in $Rh(CO)_2$ desorb sequentially. This was explained through correlation with DFT calculations where OH species generated from H_2 reduction coordinate to Rh-CO species after the first CO desorption, thus stabilizing the monocarbonyl. Without the local OH, both COs adsorb simultaneously. This assignment is confirmed based on DFT calculations of the binding energy of each CO to the Rh atom with and without hydroxyls.

Ultimately, in Chapter 5 we show that the reactivity of atomically dispersed Rh, compared to Rh clusters, is distinct by performing temperature programmed reactions (extracting light off curves) with a feed of NO, CO and H_2O. The present work demonstrates that even for a simple feed containing only NO, CO, and H_2O, dramatic differences in rate and selectivity as a function of the Rh active site structure. Specifically, atomically dispersed Rh species selectively produce NH_3 at low temperature in the reduction of NO by CO when H_2O is present, while Rh clusters exclusively produce N_2 and N_2O. These conclusions indicate that reformulating the TWC in catalytic converters to prevent the formation of atomically dispersed Rh could reduce NH_3 emissions from gasoline burning automobiles. This study also clearly identifies the important role of minimizing the distribution of active site types in catalytic materials to facilitate structure-function relationship elucidation.

Finally, in Chapter 6 we summarize how these studies come together to demonstrate that Rh structure plays a large role in the reactivity of Rh for NO reduction in TWCs in relevant conditions. Specifically, atomically dispersed Rh display unique qualities for NO reduction reactivity and there are detailed structural attributes that contribute to the reactivity. In conclusion, we show NO reduction reactivity in catalytic converters is dependent on the Rh structure. In future studies, we also provide evident that oxide support has direct connection to atomically dispersed Rh reactivity. In other future work we also aim to develop a realistic model of atomically dispersed Rh species on Al_2O_3 under reaction conditions of NO reduction by CO and the effects of surface hydroxylation on their characteristics. To best predict accurate reaction mechanistic pathways, we will determine the model structure by comparing observed binding properties of CO and NO on atomically dispersed Rh/γ-Al_2O_3 comparable to experimental observation to we provide model coordinated with variety of OH coverages and facets of γ-Al_2O_3. Through cryogenic FTIR and DFT calculations on our narrowed down selection of sites, we will show that Rh species does not strongly bond NO because the highly reactive nature of the Rh site converts NO into N_2O from the $Rh(NO)_2$ form. Further, it is expected that Rh structure and coordination to the support may be quite dynamic under the complex feed conditions of the TWC, a consideration that will be critical for future mechanistic analyses. Early kinetic studies show that exposure to high NO or high CO will restructure the atomically dispersed Rh species. The reconstruction of Rh ranging from atomically dispersed Rh to Rh clusters and how this affects reactivity will be continued to be looked at in future work. Further understanding into the NO reduction mechanism at active Rh single atom structures and clusters would enable a more sustainable TWC design and act as an example for future catalyst structures.

1.6 References

(1) Dey, S.; Mehta, N. S. Automobile Pollution Control Using Catalysis. *Resour. Environ. Sustain.* **2020**, *2* (100006).

(2) Sharma, S. K.; Goyal, P.; Maheshwari, S.; Chandra, A. A Technical Review of Automobile Catalytic Converter: Current Status and Perspectives. *Strateg. Technol. Complex Environ. Issues-A Sustain. Approach* **2015**, *1*, 171–179.

(3) Cholakov, G. S. Control of Exhaust Emissions from Internal Combustion Engine Vehicles. *Pollut Control Technol* **2010**, *3*, 1–8.

(4) Shelef, M.; McCabe, R. W. Twenty-Five Years after Introduction of Automotive Catalysts: What Next? *Catal. Today* **2000**, *62* (1), 35–50.

(5) Khurana, S.; Rayat, K. K.; Tadepalli, S.; Mishra, S. Review Paper on Catalytic Converter for Automotive Exhaust Emission. **2012**.

(6) Collins, N. R.; Twigg, M. V. Three-Way Catalyst Emissions Control Technologies for Spark-Ignition Engines — Recent Trends and Future Developments. *Top. Catal.* **2007**, *42.1-4*, 323–332.

(7) Bhandarkar, S. Vehicular Pollution, Their Effect on Human Health and Mitigation Measures. *Veh. Eng* **2013**, *1* (2), 33–40.

(8) Ruzaik, F. Air Pollution Caused Devastating Impacts on Children ' s Health in Urban Area of Sri Lanka. **2020**, *10* (12), 409–421.

(9) Liu, Y.; Ge, Y.; Tan, J.; Wang, H.; Ding, Y. Research on Ammonia Emissions Characteristics from Light-Duty Gasoline Vehicles. *J. Environ. Sci.* **2021**, *106*, 182–193.

(10) Gandhi, H. S.; Graham, G. W.; McCabe, R. W. Automotive Exhaust Catalysis. *J.*

Catal. **2003**, *216* (1–2), 433–442.

(11) Kašpar, J.; Fornasiero, P.; Hickey, N. Automotive Catalytic Converters : Current Status and Some Perspectives. **2003**, *77*, 419–449.

(12) Moore, E. M. The Forces That Shape Transportation Control Measures under the Clean Air Act: A Case Study of Cambridge, Massachusetts, Massachusetts Institute of Technology, 1994.

(13) Getsoian, A. B.; Theis, J. R.; Lambert, C. K. Sensitivity of Three-Way Catalyst Light-Off Temperature to Air-Fuel Ratio. *Emiss. Control Sci. Technol.* **2018**, *4* (3), 136–142.

(14) Getsoian, A. (Bean); Theis, J. R.; Paxton, W. A.; Lance, M. J.; Lambert, C. K. Remarkable Improvement in Low Temperature Performance of Model Three-Way Catalysts through Solution Atomic Layer Deposition. *Nat. Catal.* **2019**, *2* (7), 614–622.

(15) Shelef, M.; Graham, G. W. Why Rhodium in Automotive Three-Way Catalysts? *Catal. Rev.* **1994**, *36* (3), 433–457.

(16) Granger, P.; Dhainaut, F.; Pietrzik, S.; Malfoy, P.; Mamede, A. S.; Leclercq, L.; Leclercq, G. An Overview: Comparative Kinetic Behaviour of Pt, Rh and Pd in the NO+CO and NO+H2 Reactions. *Top. Catal.* **2006**, *39* (1–2), 65–76.

(17) Fangmeierfl, A.; Angelika Hadwiger-Fangmeier, L. V. der E.; Jäger, H.-J. Effects of Atmospheric Ammonia on Vegetation—a Review. *Environ. Pollut.* **1994**, *86* (1), 43–82.

(18) Clark, C. A.; Reddy, C. P.; Xu, H.; Heck, K. N.; Luo, G.; Senftle, T. P.; Wong, M. S. Mechanistic Insights into PH-Controlled Nitrite Reduction to Ammonia and Hydrazine over Rhodium. *ACS Catal.* **2019**, *10*, 494–509.

(19) Behera, S. N.; Sharma, M. Science of the Total Environment Investigating the Potential Role of Ammonia in Ion Chemistry of Fine Particulate Matter Formation for an Urban Environment. *Sci. Total Environ.* **2010**, *408* (17), 3569–3575.

(20) Gong, L.; Lewicki, R.; Griffin, R. J.; Tittel, F. K.; Lonsdale, C. R.; Stevens, R. G.; Pierce, J. R.; Malloy, Q. G. J.; Travis, S. A.; Bobmanuel, L. M.; et al. Role of Atmospheric Ammonia in Particulate Matter Formation in Houston during Summertime. *Atmos. Environ.* **2013**, *77*, 893–900.

(21) Bergstro, A.; Jansson, M. Atmospheric Nitrogen Deposition Has Caused Nitrogen Enrichment and Eutrophication of Lakes in the Northern Hemisphere. *Glob. Chang. Biol.* **2006**, *12* (4), 635–643.

(22) Zhdanov, V. P.; Kasemo, B. Mechanism and Kinetics of the NO□ CO Reaction on Rh. *Surf. Sci. Rep.* **1997**, *29* (2), 31–90.

(23) Oh, S. H.; Fisher, G. B.; Carpenter, J. E.; Goodman, D. W. Comparative Kinetic Studies of CO-O2 and CO-NO Reactions over Single Crystal and Supported Rhodium Catalysts. *J. Catal* **1986**, *100* (2), 360–376.

(24) Oh, S. H.; Triplett, T. Reaction Pathways and Mechanism for Ammonia Formation and Removal over Palladium-Based Three-Way Catalysts : Multiple Roles of CO. *Catal. Today* **2014**, *231*, 22–32.

(25) Hecker, W. C.; Bell, A. T. Reduction of NO by CO over Silica-Supported Rhodium: Infrared and Kinetic Studies. *J. Catal.* **1983**, *84* (1), 200–215.

(26) Araya, P.; Gracia, F.; Cortés, J.; Wolf, E. E. FTIR Study of the Reduction Reaction of NO by CO over Rh/SiO2 Catalysts with Different Crystallite Size. *Appl. Catal. B Environ.* **2002**, *38* (2), 77–90.

(27) Hendriksen, D. E.; Meyer, C. D.; Eisenberg, R. Nature of the Active Catalyst in the Rhodium Complex Catalyzed Reduction of Nitric Oxide by Carbon Monoxide. *Inorg. Chem.* **1977**, *16* (4), 970–972.

(28) Dictor, R. An Infrared Study of the Behavior of CO , NO , and CO + NO over Rh / A1203 Catalysts. **2000**, *99* (1988), 89–99.

(29) Chuang, S. S. C.; Tan, C. Mechanistic Studies of the NO – CO Reaction on Rh / Al 2 O 3 under Net-Oxidizing Conditions. **1998**, *104*, 95–104.

(30) Srinivasan, A.; Depcik, C. Review of Chemical Reactions in the NO Reduction by CO on Rhodium/Alumina Catalysts. *Catal. Rev. - Sci. Eng.* **2010**, *52* (4), 462–493.

(31) Fang, C.-Y.; Zhang, S.; Hu, Y.; Vasiliu, M.; Perez-Aguilar, J. E.; Conley, E. T.; Dixon, D. A.; Chen, C.-Y.; Gates, B. C. Reversible Metal Aggregation and Redispersion Driven by the Catalytic Water Gas Shift Half-Reactions: Interconversion of Single-Site Rhodium Complexes and Tetrarhodium Clusters in Zeolite HY. *ACS Catal.* **2019**, *9* (4), 3311–3321.

(32) Goldsmith, B. R.; Sanderson, E. D.; Ouyang, R.; Li, W. X. CO- and NO-Induced Disintegration and Redispersion of Three-Way Catalysts Rhodium, Palladium, and Platinum: An Ab Initio Thermodynamics Study. *J. Phys. Chem. C* **2014**, *118* (18), 9588–9597.

(33) Guzman, J.; Gates, B. C. Supported Molecular Catalysts : Metal Complexes and Clusters on Oxides and Zeolites. *Dalt. Trans.* **2003**, *17*, 3303–3318.

(34) Tan, L.; Huang, L.; Liu, Y.; Wang, Q. Detailed Mechanism of the NO + CO Reaction on Rh(1 0 0) and Rh(1 1 1): A First-Principles Study. *Appl. Surf. Sci.* **2018**, *444*, 276–286.

(35) Deushi, F.; Ishikawa, A.; Nakai, H. Density Functional Theory Analysis of

Elementary Reactions in NOxReduction on Rh Surfaces and Rh Clusters. *J. Phys. Chem. C* **2017**, *121* (28), 15272–15281.

(36) Chafik, T.; Kondarides, D. I.; Verykios, X. E. Catalytic Reduction of NO by CO over Rhodium Catalysts: 1. Adsorption and Displacement Characteristics Investigated by In Situ FTIR and Transient-MS Techniques. *J. Catal.* **2000**, *190* (2), 446–459.

(37) McCabe, R. W.; Wong, C. Steady-State Kinetics of the CON2O Reaction over an Alumina-Supported Rhodium Catalyst. *J. Catal.* **1990**, *121* (2), 422–431.

(38) Almusaiteer, K. A.; Chuang, S. S. C. Infrared Characterization of Rh Surface States and Their Adsorbates during the NO-CO Reaction. *J. Phys. Chem. B* **2000**, *104* (10), 2265–2272.

(39) Vityuk, A. D.; Ma, S.; Alexeev, O. S.; Amiridis, M. D. NO Reduction with CO over HY Zeolite-Supported Rhodium Dicarbonyl Complexes: Giving Insight into the Structure Sensitivity. *React. Chem. Eng.* **2019**, *4* (2), 418–426.

(40) Matsubu, J. C.; Yang, V. N.; Christopher, P. Isolated Metal Active Site Concentration and Stability Control Catalytic CO2 Reduction Selectivity. *J. Am. Chem. Soc.* **2015**, *137* (8), 3076–3084.

(41) Qi, J.; Christopher, P. Atomically Dispersed Rh Active Sites on Oxide Supports with Controlled Acidity for Gas-Phase Halide-Free Methanol Carbonylation to Acetic Acid. *Ind. Eng. Chem. Res.* **2019**, *58* (28), 12632–12641.

(42) Shan, J.; Li, M.; Allard, L. F.; Lee, S.; Flytzani-Stephanopoulos, M. Mild Oxidation of Methane to Methanol or Acetic Acid on Supported Isolated Rhodium Catalysts. *Nature* **2017**, *551* (7682), 605–608.

(43) Serna, P.; Gates, B. C. Zeolite-Supported Rhodium Complexes and Clusters: Switching Catalytic Selectivity by Controlling Structures of Essentially Molecular Species. *J. Am. Chem. Soc.* **2011**, *133* (13), 4714–4717.

(44) Taylor, K. C. Nitric Oxide Catalysis in Automotive Exhaust Systems Nitric Oxide Catalysis in Automotive Exhaust Systems. *Catal. Rev. Eng.* **1993**, *35* (4), 457–481.

(45) Altman, E. I.; Gorte, R. J. A Temperature-Programmed Desorption Study of NO on Rh Particles Supported on α-Al2O3 {0001}. *J. Catal.* **1988**, *113* (1), 185–192.

(46) Matsubu, J. C.; Zhang, S.; DeRita, L.; Marinkovic, N. S.; Chen, J. G.; Graham, G. W.; Pan, X.; Christopher, P. Adsorbate-Mediated Strong Metal-Support Interactions in Oxide-Supported Rh Catalysts. *Nat. Chem.* **2017**, *9* (2), 120–127.

(47) Oh, S. H.; Eickel, C. C. Influence of Metal Particle Size and Support on the Catalytic Properties of Supported Rhodium: CO+ O2 and CO+ NO Reactions. *J. Catal.* **1991**, *128* (2), 526–536.

(48) Campbell, C. T.; White, J. M. Chemisorption and Reactions of Nitric Oxide on Rhodium. *Appl. Surf. Sci.* **1978**, *1* (3), 347–359.

(49) Chin, A. A.; Bell, A. T. Kinetics of Nitric Oxide Decomposition on Silica-Supported Rhodium. *J. Phys. Chem.* **1983**, *87* (19), 3700–3706.

(50) Na-Ranong, D.; Yuangsawad, R.; Kitchaiya, P.; Aida, T. Application of Periodic Operation to Kinetic Study of NO–CO Reaction over Rh/Al2O3. *Chem. Eng. J.* **2009**, *146* (2), 275–286.

(51) Zaera, F.; Gopinath, C. S. Evidence for an N2O Intermediate in the Catalytic Reduction of NO to N2 on Rhodium Surfaces. *Chem. Phys. Lett.* **2000**, *332* (3–4), 209–214.

(52) Zhdanov, V. P.; Kasemo, B. Steady-State Kinetics of the N O - C O Reaction on Rh (111): Extrapolation from 10 -1 ~ to 1 Bar. **1996**, *40*, 197–202.

(53) Permana, H.; Ng, K. Y. S.; Peden, C. H. F.; Schmieg, S. J.; Lambert, D. K.; Belton, D. N. Adsorbed Species and Reaction Rates for NO–CO over Rh (111). *J. Catal.* **1996**, *164* (1), 194–206.

(54) Herman, G. S.; Peden, C. H. F.; Schmieg, S. J.; Belton, D. N. A Comparison of the NO–CO Reaction over Rh (100), Rh (110) and Rh (111). *Catal. Letters* **1999**, *62* (2–4), 131–138.

(55) Belton, D. N.; DiMaggio, C. L.; Schmieg, S. J.; Ng, K. Y. S. Reaction of Coadsorbed Nitric Oxide and Nitrogen Atoms on Rh (111). *J. Catal.* **1995**, *157* (2), 559–568.

(56) Peden, C. H. F.; Belton, D. N.; Schmieg, S. J. Structure Sensitive Selectivity of the NO-CO Reaction over Rh (110) and Rh (111). *J. Catal.* **1995**, *155* (2), 204–218.

(57) Peden, C. H. F.; Goodman, D. W.; Blair, D. S.; Berlowitz, P. J.; Fisher, G. B.; Oh, S. H. Kinetics of Carbon Monoxide Oxidation by Oxygen or Nitric Oxide on Rhodium (111) and Rhodium (100) Single Crystals. *J. Phys. Chem.* **1988**, *92* (6), 1563–1567.

(58) Beck, D. D.; Carr, C. J. Effects of High-Temperature Aging on the Dispersion of Rh/Al2O3. *J. Catal.* **1993**, *144* (1), 296–310.

(59) Kašpar, J.; De Leitenburg, C.; Fornasiero, P.; Trovarelli, A.; Graziani, M. NO Reduction by CO over RhAl2O3. Effects of Rhodium Dispersion on the Catalytic Properties. *J. Catal.* **1994**, *146* (1), 136–143.

(60) Hyde, E. A.; Robert, R.; Rochester, C. H. Infrared Study of the Interactions between NO and CO on Rh / Al2O3 Catalysts. *J. Chem. Soc. Faraday Trans. 1 Phys. Chem. Condens. Phases* **1984**, *80* (3), 531–541.

(61) Gopinath, C. S.; Zaera, F. NO+ CO+ O2 Reaction Kinetics on Rh (111): A Molecular

Beam Study. *J. Catal.* **2001**, *200* (2), 270–287.

(62) Winter, E. R. S. The Catalytic Decomposition of Nitric Oxide by Metallic Oxides. *J. Catal.* **1971**, *22* (2), 158–170.

(63) Amirnazmi, A.; Benson, J. E.; Boudart, M. Oxygen Inhibition in the Decomposition of NO on Metal Oxides and Platinum. *J. Catal.* **1973**, *30* (1), 55–65.

(64) Oh, S. Comparative Kinetic Studies of CO-O2 and CO-NO Reactions over Single Crystal and Supported Rhodium Catalysts. *J. Catal.* **1986**, *100* (2), 360–376.

(65) Burch, R.; Breen, J. P.; Meunier, F. C. A Review of the Selective Reduction of NOxwith Hydrocarbons under Lean-Burn Conditions with Non-Zeolitic Oxide and Platinum Group Metal Catalysts. *Appl. Catal. B Environ.* **2002**, *39* (4), 283–303.

(66) Baraldi, A.; Dhanak, V. R.; Comelli, G.; Kiskinova, M.; Rosei, R. NO Dissociation and NO+ CO Reaction on Rh (110): Influence of the Surface Structure and Composition on the Reaction Rates. *Appl. Surf. Sci.* **1993**, *68* (3), 395–405.

(67) Yates Jr, J. T.; Williams, E. D.; Weinberg, W. H. Does Chemisorbed Carbon Monoxide Dissociate on Rhodium? *Surf. Sci.* **1980**, *91* (2–3), 562–570.

(68) Baird, R. J.; Ku, R. C.; Wynblatt, P. The Chemisorption of CO and NO on Rh (110). *Surf. Sci.* **1980**, *97* (2–3), 346–362.

(69) Bowker, M.; Guo, Q.; Joyner, R. W. The CO/NO Reaction on Rh (110). *Catal. Today* **1991**, *10* (3), 409–412.

(70) Liao, D.; Glassford, K. M.; Ramprasad, R.; Adams, J. B. DFT–LDA Study of NO Adsorption on Rh(110) Surface. *Surf. Sci.* **1998**, *415* (1), 11–19.

(71) Kondratenko, E. V; Kraehnert, R.; Radnik, J.; Baerns, M.; Pe, J. Distinct Activity and Time-on-Stream Behavior of Pure Pt and Rh Metals and Pt – Rh Alloys in the High-Temperature N 2 O Decomposition. **2006**, *298*, 73–79.

(72) Hirano, H.; Yamada, T.; Tanaka, K. I.; Siera, J.; Nieuwenhuys, B. E. The Reduction of Nitric Oxide by Hydrogen Over Pt, Rh and Pt-Rh Single Crystal Surfaces. In *New Frontiers in Catalysis - Proceedings of the 10th International Congress on Catalysis, Budapest, 19-24 July 1992*; GUCZI, L., SOLYMOSI, F., TÉTÉNYI, P. B. T.-S. in S. S. and C., Eds.; Elsevier, 1993; Vol. 75, pp 345–357.

(73) Hendershot, R. E.; Hansen, R. S. Reduction of Nitric Oxide with Carbon Monoxide on the Rh (100) Single-Crystal Surface. *J. Catal.* **1986**, *98* (1), 150–165.

(74) Root, T. W.; Schmidt, L. D.; Fisher, G. B. Adsorption and Reaction of Nitric Oxide and Oxygen on Rh (111). *Surf. Sci.* **1983**, *134* (1), 30–45.

(75) Schwartz, S. B.; Fisher, G. B.; Schmidt, L. D. Nitric Oxide+ Carbon Monoxide on Rhodium (111): Steady-State Rates and Adsorbate Coverages. *J. Phys. Chem.* **1988**, *92* (2), 389–395.

(76) Tominga, H.; H. Arai. An Infrared Study of Nitric on Rhodium-Alumina Oxide Adsorbed Catalyst. **1976**, *142*, 131–142.

(77) Solymosi, F.; Sarkany, J. An Infrared Study of the Surface Interaction between NO and CO on Rh/Al2O3 Catalyst. *Appl. Surf. Sci.* **1979**, *3* (1), 68–82.

(78) Granger, P.; Dujardin, C.; Paul, J.-F.; Leclercq, G. An Overview of Kinetic and Spectroscopic Investigations on Three-Way Catalysts: Mechanistic Aspects of the CO+ NO and CO+ N2O Reactions. *J. Mol. Catal. A Chem.* **2005**, *228* (1–2), 241–253.

(79) Granger, P.; Praliaud, H.; Billy, J.; Leclercq, L.; Leclercq, G. Infrared Investigation of the Transformation of NO over Supported Pt- and Rh-Based Three-Way Catalysts. **2002**, No. 8010, 92–96.

(80) Granger, P.; Delannoy, L.; Leclercq, L.; Leclercq, G. On the Effect of Deactivation on the Kinetics of CO Oxidation by NO over Pt–Rh Catalysts. *J. Catal.* **1998**, *177* (1), 147–151.

(81) Granger, P.; Lecomte, J. J.; Leclercq, L.; Leclercq, G. An Attempt at Modelling the Activity of Pt-Rh / Al 2 O 3 Three-Way Catalysts in the CO + NO Reaction. **2001**, *208*, 369–379.

(82) Granger, P.; Delannoy, L.; Lecomte, J. J.; Dathy, C.; Praliaud, H.; Leclercq, L.; Leclercq, G. Kinetics of the CO + NO Reaction over Bimetallic Platinum-Rhodium on Alumina: Effect of Ceria Incorporation into Noble Metals. *J. Catal.* **2002**, *207* (2), 202–212.

(83) Granger, P.; Lecomte, J. J.; Leclercq, L.; Leclercq, G. An Attempt at Modelling the Activity of Pt-Rh/Al2O3 Three-Way Catalysts in the CO+NO Reaction. *Appl. Catal. A Gen.* **2001**, *208* (1), 369–379.

(84) Centi, G.; Olio, L. D.; Perathoner, S. Oscillating Behavior in N 2 O Decomposition over Rh Supported on Zirconia-Based Catalysts. **2000**, *139*, 130–139.

(85) Kroeker, R. M.; Kaska, W. C.; Hansma, P. K. How Carbon Monoxide Bonds to Alumina-Supported Rhodium Particles: Tunneling Spectroscopy Measurements with Isotopes. *J. Catal.* **1979**, *57* (1), 72–79.

(86) Solymosi, F.; Pasztor, M. An Infrared Study of the Influence of Carbon Monoxide Chemisorption on the Topology of Supported Rhodium. *J. Phys. Chem.* **1985**, *89* (22), 4789–4793.

(87) Kiss, J.; Solymosi, F. The Effect of Adsorbed Oxygen on the Stability of NCO on Rh (

111) Studied by Reflection Absorption Infrared Spectroscopy. **1998**, *282*, 277–282.

(88) Dent, A. J.; Evans, J.; Fiddy, S. G.; Jyoti, B.; Newton, M. A.; Tromp, M. Rhodium Dispersion during NO/CO Conversions. *Angew. Chemie* **2007**, *119* (28), 5452–5454.

(89) Chuang, S. S. C.; Tan, C. Combined Infrared and Mass Spectrometric Study of Reactions of Adsorbed NO and CO on 0 . 5 Wt % Rh/ SiO2 Catalyst. *Catal. Today* **1997**, *35*, 369–377.

(90) Ryczkowski, J. IR Spectroscopy in Catalysis. *Catal. Today* **2001**, *68*, 263–381.

(91) Kendall, D. N. Infrared Radiation: Description and Simple Theory of Absorption by Molecules. Applied Infrared Spectroscopy (Kendall DN, Ed.). Reinhold Publishing Corporation: New York 1966.

(92) Hollas, J. M. *Modern Spectroscopy*; John Wiley & Sons, 2004.

(93) Bourikas, K.; Kordulis, C.; Lycourghiotis, A. The Role of the Liquid-Solid Interface in the Preparation of Supported Catalysts. *Catal. Rev. - Sci. Eng.* **2006**, *48* (4), 363–444.

(94) Janusz, W.; Sworska, A.; Szczypa, J. The Structure of the Electrical Double Layer at the Titanium Dioxide/Ethanol Solutions Interface. *Colloids Surfaces A Physicochem. Eng. Asp.* **1999**, *152* (3), 223–233.

(95) Yates, J. T.; Duncan, T. M.; Worley, S. D.; Vaughan, R. W. Infrared Spectra of Chemisorbed CO on Rh. *J. Chem. Phys.* **1979**, *70* (3), 1219.

(96) Asokan, C.; Derita, L.; Christopher, P. Using Probe Molecule FTIR Spectroscopy to Identify and Characterize Pt - Group Metal Based Single Atom Catalysts. *Chinese J. Catal.* **2017**, *38* (9), 1473–1480.

(97) Chakarova, K.; Mihaylov, M.; Hadjiivanov, K. FTIR Spectroscopic Study of CO Adsorption on Pt – H – ZSM-5. *Microporous Mesoporous Mater.* **2005**, *81* (1–3), 305–312.

(98) Stakheev, A. Y.; Shpiro, E. S.; Tkachenko, O. P.; Jaeger, N. I.; Schulz-Ekloff, G. Evidence for Monatomic Platinum Species in H-ZSM-5 from FTIR Spectroscopy of Chemisorbed CO. *J. Catal.* **1997**, *169* (1), 382–388.

(99) Lamberti, C.; Zecchina, A.; Groppo, E.; Bordiga, S. In-Situ Characterization of Heterogeneous Catalysts Themed Issue. *Chem. Soc. Rev.* **2010**, No. 12.

(100) Frenking, G.; Loschen, C.; Krapp, A.; Fau, S.; Strauss, S. H. Electronic Structure of CO—An Exercise in Modern Chemical Bonding Theory. *J. Comput. Chem.* **2009**, *30* (10), 1545–1614.

(101) Blyholder, G. Molecular Orbital View of Chemisorbed Carbon Monoxide. *J. Phys. Chem* **1800**, No. 1, 2772–2777.

(102) Hadjiivanov, K. I.; Vayssilov, G. N. Characterization of Oxide Surfaces and Zeolites by Carbon Monoxide as an IR Probe Molecule; Advances in Catalysis; Academic Press, 2002; Vol. 47, pp 307–511.

(103) Gruver, V.; Fripiat, J. J. Lewis Acid Sites and Surface Aluminum in Aluminas and Mordenites: An Infrared Study of CO Chemisorption. *J. Phys. Chem.* **1994**, *98* (34), 8549–8554.

(104) Pacchioni, G.; Bagus, P. S. Metal-Phosphine Bonding Revisited. σ-Basicity, π-Acidity, and the Role of Phosphorus d Orbitals in Zerovalent Metal-Phosphine Complexes. *Inorg. Chem.* **1992**, *31* (21), 4391–4398.

(105) Cv, B.; Brown, B. T. L. Intensities of CO Stretching Modes in the Infrared Spectra of Adsorbed CO and Metal Carbonyls1. **1967**, *6* (5).

(106) Duncan, T. M.; Vaughan, R. W. A 13C NMR Study of the Adsorbed States of CO on Rh Dispersed on Al2O3. *J. Chem. Phys.* **1980**, *73* (2), 975–985.

(107) Garland, C. W.; Yang, A. Infrared Studies of Carbon Monoxide Chemisorbed on Rhodium. *J. Phys. Chem.* **1957**, *61* (11), 1504–1512.

(108) Goellner, J. F.; Gates, B. C.; Vayssilov, G. N.; Rösch, N. Structure and Bonding of a Site-Isolated Transition Metal Complex: Rhodium Dicarbonyl in Highly Dealuminated Zeolite Y. *J. Am. Chem. Soc.* **2000**, *122* (33), 8056–8066.

(109) Qiao, B.; Wang, A.; Yang, X.; Allard, L. F.; Jiang, Z.; Cui, Y.; Liu, J.; Li, J.; Zhang, T. Single-Atom Catalysis of CO Oxidation Using Pt1/FeOx. *Nat. Chem.* **2011**, *3* (8), 634–641.

(110) Peterson, E. J.; DeLaRiva, A. T.; Lin, S.; Johnson, R. S.; Guo, H.; Miller, J. T.; Hun Kwak, J.; Peden, C. H. F.; Kiefer, B.; Allard, L. F.; et al. Low-Temperature Carbon Monoxide Oxidation Catalysed by Regenerable Atomically Dispersed Palladium on Alumina. *Nat. Commun.* **2014**, *5*, 4885.

(111) Gurney, B. A.; Richter, L. J.; Villarrubia, J. S.; Ho, W. The Populations of Bridge and Top Site CO on Rh (100) vs Coverage , Temperature , and during Reaction with O. **1998**, *6710* (June).

(112) Koch, H. P.; Singnurkar, P.; Schennach, R. A RAIRS , TPD , and DFT Study of Carbon Monoxide Adsorption on Stepped Rh (553). **2008**, No. 553, 806–812.

(113) Phys, J. C. The Adsorption of CO on Rh (100): Reflection Absorption Infrared Spectroscopy , Low Energy Electron Diffraction , and Thermal Desorption Spectroscopy. **2015**, *144703* (100).

(114) Dubois, L. H.; Somorjai, G. A. The Chemisorption of CO and CO2on Rh(111) Studied by High Resolution Electron Energy Loss Spectroscopy. *Surf. Sci.* **1980**, *91* (2–3), 514–532.

(115) Phys, J. C. CO Adsorption and CO and O Coadsorption on Rh (111) Studied by Reflection Absorption Infrared Spectroscopy and Density Functional Theory. **2006**, *144703* (111).

(116) Linke, R.; Curulla, D.; Hopstaken, M. J. P.; Niemantsverdriet, J. W. CO/Rh (111): Vibrational Frequency Shifts and Lateral Interactions in Adsorbate Layers. *J. Chem. Phys.* **2001**, *115* (17), 8209–8216.

(117) Yates, J. T.; Kolasinski, K. Infrared Spectroscopic Investigation of the Rhodium Gem-Dicarbonyl Surface Species. *J. Chem. Phys.* **1983**, *79* (2), 1026.

(118) Yao, H. C.; Rothschild, W. G. Infrared Spectra of Chemisorbed CO on Rh / γ – Al2O3 : Site Distributions and Molecular Mobility Infrared Spectra of Chemisorbed CO on Rh / ' Y-AI203 : Site Distributions and Molecular Mobility. **1983**, *4774* (1978).

(119) Primet, M. Infrared Study of CO Chemisorption on Zeolite and Alumina Supported Rhodium. *J. Chem. Soc. Faraday Trans. 1* **1978**, *74*, 2570.

(120) Rice, C. A.; Worley, S. D.; Curtis, C. W.; Guin, J. A.; Tarrer, A. R. The Oxidation State of Dispersed Rh on Al2O3. *J. Chem. Phys.* **1981**, *74* (11), 6487–6497.

(121) Panayotov, P. B.; Yates, J. T. Rhodium-Carbon Monoxide Surface Chemistry: The Involvement of Surface Hydroxyl Groups on A12O3and SiO2Supports. *J. Am. Chem. Soc.* **1988**, *110* (7), 2074–2081.

(122) Hugues, F.; Basset, J. M.; Vi, U. D. P. Catalytic Synthesis of Low Molecular Weight Olefins from CO and H, with Fe(CO),, Fe,(CO),,, and [HFe3(CO),,] - Supported on Inorganic Oxides. **1980**, *3* (154).

(123) Lamberti, C.; Zecchina, A.; Groppo, E.; Bordiga, S. Probing the Surfaces of Heterogeneous Catalysts by in Situ IR Spectroscopy. *Chem. Soc. Rev.* **2010**, *39* (12), 4951.

(124) De La Cruz, C.; Sheppard, N. A Structure-Based Analysis of the Vibrational Spectra of Nitrosyl Ligands in Transition-Metal Coordination Complexes and Clusters. *Spectrochim. Acta Part A Mol. Biomol. Spectrosc.* **2011**, *78* (1), 7–28.

(125) Thiel, P. A.; Williams, E. D.; Yates, J. T.; Weinberg, W. H. The Chemisorption of CO on Rh(111). *Surf. Sci.* **1979**, *84* (1), 54–64.

(126) Tamura, M.; Shimizu, K.; Satsuma, A. Applied Catalysis A : General Comprehensive IR Study on Acid / Base Properties of Metal Oxides. *"Applied Catal. A, Gen.* **2012**, *433*, 135–145.

(127) Hadjiivanov, K. Identification and Characterization of Surface Hydroxyl Groups by Infrared Spectroscopy. In *Advances in Catalysis*; Academic Press, 2014; Vol. 57, pp 99–318.

(128) Hadjiivanov, K.; Saussey, J.; Freysz, J. L.; Lavalley, J. C. FT-IR Study of NO+ O 2 Co-Adsorption on H-ZSM-5: Re-Assignment of the 2133 Cm-1 Band to NO+ Species. *Catal. Letters* **1998**, *52* (1), 103–108.

(129) Börensen, C.; Kirchner, U.; Scheer, V.; Vogt, R.; Zellner, R. Mechanism and Kinetics of the Reactions of NO2 or HNO3 with Alumina as a Mineral Dust Model Compound. *J. Phys. Chem. A* **2000**, *104* (21), 5036–5045.

(130) Hadjiivanov, K.; Avreyska, V.; Klissurski, D.; Marinova, T. Surface Species Formed after NO Adsorption and NO+ O2 Coadsorption on ZrO2 and Sulfated ZrO2: An FTIR Spectroscopic Study. *Langmuir* **2002**, *18* (5), 1619–1625.

(131) Anderson, J. A.; Rochester, C. H. Infrared Study of NO 2–CO Reactions over Supported Rhodium and Platinum Catalysts. *J. Chem. Soc. Faraday Trans.* **1991**, *87* (9), 1485–1489.

(132) Anderson, J. A.; Millar, G. J.; Rochester, C. H. Infrared Study of the Adsorption of NO, NO 2 and CO on Rh/Al 2 O 3 Catalysts. *J. Chem. Soc. Faraday Trans.* **1990**, *86* (3), 571–576.

(133) Ward, T. R.; Hoffmann, R.; Shelef, M. Coupling Nitrosyls as the First Step in the Reduction of NO on Metal Surfaces : The Special Role of Rhodium. **1993**, No. group 10, 22–26.

(134) Miessner, H.; Burkhardt, I.; Gutschick, D.; Zecchina, A.; Morterra, C.; Spoto, G. Surface Chemistry of Rh Carbonyls and Nitrosyls on Dealuminated Y-Zeolite at Low Temperature. *J. Chem. Soc. Faraday Trans.* **1990**, *86* (12), 2321–2327.

(135) Iizuka, T.; Lunsford, J. H. The Reduction of Nitric Oxide by Carbon Monoxide over Rhodium—Y Zeolites. *J. Mol. Catal.* **1980**, *8* (4), 391–400.

(136) Tomishige, K.; Asakura, K.; Iwasawa, Y. Observation of Molecular Reaction Intermediate and Reaction Mechanism for NO Dissociation and NO-H2 Reaction on Rh-Sn/SiO2 Catalysts. *J. Catal.* **1995**, *157* (2), 472–481.

(137) Srinivas, G.; Chuang, S. S. C.; Debnath, S. An in Situ Infrared Study of the Reactivity of Adsorbed NO and CO on Rh Catalysts. *J. Catal.* **1994**, *148* (2), 748–758.

(138) Van Slooten, R. F.; Nieuwenhuys, B. E. An Infrared Study of the Interaction of CO and NO with a Silica Supported Pt-Rh Alloy Catalyst. *J. Catal.* **1990**, *122* (2), 429–437.

(139) Hadjiivanov, K.; Knözinger, H. Species Formed after NO Adsorption and NO+ O 2

Co-Adsorption on TiO 2: An FTIR Spectroscopic Study. *Phys. Chem. Chem. Phys.* **2000**, *2* (12), 2803–2806.

(140) Pozdnyakov, D. V; Filimonov, V. N. Infrared Study of Molecular Complexes Arising from Adsorption of NO and NO2 on the Surface of Oxides. *Adv. Mol. Relax. Process.* **1973**, *5* (1), 55–63.

(141) Rudziński, W.; Piasecki, W.; Janusz, W.; Panas, G.; Charmas, R. A Thermodynamic Analysis of Ion Adsorption in the Metal Oxide/Electrolyte Systems in Which PZC and CIP Do Not Coincide. *Adsorption* **2001**, *7* (4), 327–338.

(142) Park, J.; Regalbuto, J. R. A Simple, Accurate Determination of Oxide PZC and the Strong Buffering Effect of Oxide Surfaces at Incipient Wetness. *Journal of colloid and interface science*. 1995, pp 239–252.

(143) Kosmulski, M. Surface Charging and Points of Zero Charge. 1998.

(144) Brown, M. A.; Fujimori, Y.; Ringleb, F.; Shao, X.; Stavale, F.; Nilius, N.; Sterrer, M.; Freund, H. J. Oxidation of Au by Surface OH: Nucleation and Electronic Structure of Gold on Hydroxylated MgO(001). *J. Am. Chem. Soc.* **2011**, *133* (27), 10668–10676.

(145) Osman, A. I.; Abu-Dahrieh, J. K.; Rooney, D. W.; Halawy, S. A.; Mohamed, M. A.; Abdelkader, A. Effect of Precursor on the Performance of Alumina for the Dehydration of Methanol to Dimethyl Ether. *Appl. Catal. B Environ.* **2012**, *127*, 307–315.

(146) Chizallet, C.; Digne, M.; Arrouvel, C.; Raybaud, P.; Delbecq, F.; Costentin, G.; Che, M.; Sautet, P.; Toulhoat, H. Insights into the Geometry, Stability and Vibrational Properties of OH Groups on γ-Al2O3, TiO2 -Anatase and MgO from DFT Calculations. Topics in Catalysis. *Top. Catal.* **2009**, 1005–1016.

(147) Tsyganenko, A. A.; Filimonov, V. N. Infrared Spectra of Surface Hydroxyl Groups and Crystalline Structure of Oxides. *Spectrosc. Lett.* **1972**, *5* (12), 477–487.

(148) Trueba, M.; Trasatti, S. P. γ-Alumina as a Support for Catalysts: A Review of Fundamental Aspects. *Eur. J. Inorg. Chem.* **2005**, *2005* (17), 3393–3403.

(149) Zaki, M. I.; Knözinger, H. Carbon Monoxide - A Low Temperature Infrared Probe for the Characterization of Hydroxyl Group Properties on Metal Oxide Surfaces. *Mater. Chem. Phys.* **1987**, *17* (1–2), 201–215.

(150) Tamura, M.; Shimizu, K. I.; Satsuma, A. Comprehensive IR Study on Acid/Base Properties of Metal Oxides. *Appl. Catal. A Gen.* **2012**, *433–434*, 135–145.

(151) Digne, M.; Sautet, P.; Raybaud, P.; Euzen, P.; Toulhoat, H. Use of DFT to Achieve a Rational Understanding of Acid-Basic Properties of ??-Alumina Surfaces. *J. Catal.* **2004**, *226* (1), 54–68.

(152) Digne, M.; Sautet, P.; Raybaud, P.; Euzen, P.; Toulhoat, H. Hydroxyl Groups on γ-Alumina Surfaces: A DFT Study. *J. Catal.* **2002**, *211* (1), 1–5.

(153) Digne, M.; Raybaud, P.; Sautet, P.; Guillaume, D.; Toulhoat, H. Atomic Scale Insights on Chlorinated Gamma-Alumina Surfaces. *J. Am. Chem. Soc.* **2008**, *130* (6), 11030–11039.

(154) Li, J.; Zhang, R.; Wang, B. Influence of the Hydroxylation of γ-Al2O3surfaces on the Stability and Growth of Cu for Cu/γ-Al2O3catalyst: A DFT Study. *Appl. Surf. Sci.* **2013**, *270*, 728–736.

(155) Morterra, C.; Department, G. M. A Case Study : Surface Chemistry and Surface Structure of Catalytic Aluminas , as Studied by Vibrational Spectroscopy of Adsorbed Species. *Catal. Today* **1996**, *27*, 497–532.

(156) Busca, G. The Surface of Transitional Aluminas: A Critical Review. *Catal. Today* **2014**, *226*, 2–13.

(157) Liu, X. FTIR Spectroscopic Studies of Silication of γ-Alumina with FCC Catalysts via Steaming. *J. Phys. Chem. B* **1999**, *103* (14), 2647–2652.

(158) Liu, X. DRIFTS Study of Surface of γ-Alumina and Its Dehydroxylation. *J. Phys. Chem. C* **2008**, *112* (13), 5066–5073.

(159) Fernández-Torre, D.; Kośmider, K.; Carrasco, J.; Ganduglia-Pirovano, M. V.; Pérez, R. Insight into the Adsorption of Water on the Clean CeO2(111) Surface with van Der Waals and Hybrid Density Functionals. *J. Phys. Chem. C* **2012**, *116* (25), 13584–13593.

(160) Zhang, C.; Yu, Y.; Grass, M. E.; Dejoie, C.; Ding, W.; Gaskell, K.; Jabeen, N.; Hong, Y. P.; Shavorskiy, A.; Bluhm, H.; et al. Mechanistic Studies of Water Electrolysis and Hydrogen Electro-Oxidation on High Temperature Ceria-Based Solid Oxide Electrochemical Cells. *J. Am. Chem. Soc.* **2013**, *135* (31), 11572–11579.

(161) Badri, A.; Binet, C.; Lavalley, J. An FTIR Study of Surface Ceria Hydroxy Groups during a Redox Process with H2 Published. *Faraday* **1996**, *92* (c), 4669–4673.

(162) Diebold, U. The Surface Science of Titanium Dioxide. **2003**, *48* (x).

(163) Barnard, A. S.; Curtiss, L. A. Prediction of TiO2 Nanoparticle Phase and Shape Transitions Controlled by Surface Chemistry. *Nano Lett.* **2005**, *5* (7), 1261–1266.

(164) Bourikas, K.; Kordulis, C.; Lycourghiotis, A. The Role of the Liquid-solid Interface in the Preparation of Supported Catalysts. *Catal. Rev.* **2006**, *48* (4), 363–444.

(165) Jones, P.; Hockey, J. Infra-Red Studies of Rutile Surfaces. *Trans. Faraday Soc.* **1971**, *67*, 2679-2685.

(166) Porter, J. F.; Li, Y. G.; Chan, C. K. Effect of Calcination on the Microstructural Characteristics and Photoreactivity of Degussa P-25 TiO2. *J. Mater. Sci.* **1999**, *34* (7), 1523–1531.

(167) Tsyganenko, A. A.; Filimonov, V. N. Infrared Spectra of Surface Hydroxyl Groups and Crystalline Structure of Oxides. *J. Mol. Struct.* **1973**, *19*, 579–589.

(168) Arrouvel, C.; Digne, M.; Breysse, M.; Toulhoat, H.; Raybaud, P. Effects of Morphology on Surface Hydroxyl Concentration: A DFT Comparison of Anatase-TiO2 and γ-Alumina Catalytic Supports. *J. Catal.* **2004**, *222* (1), 152–166.

(169) Asokan, C.; Thang, H. V.; Pacchioni, G.; Christopher, P. Reductant Composition Influences the Coordination of Atomically Dispersed Rh on Anatase TiO2. *Catal. Sci. Technol.* **2020**, *10* (6), 1597–1601.

(170) Patrick, C. E.; Giustino, F. GW Quasiparticle Bandgaps of Anatase TiO2 Starting from DFT + U. *J. Phys. Condens. Matter* **2012**, *24*, 202201.

(171) He, Y.; Dulub, O.; Cheng, H.; Selloni, A.; Diebold, U. Evidence for the Predominance of Subsurface Defects on Reduced Anatase TiO 2 (101). *Phys. Rev. Lett.* **2009**, *102* (10), 106105.

(172) Setvin, M.; Franchini, C.; Hao, X.; Schmid, M.; Janotti, A.; Kaltak, M.; Van De Walle, C. G.; Kresse, G.; Diebold, U. Direct View at Excess Electrons in TiO2 Rutile and Anatase. *Phys. Rev. Lett.* **2014**, *113* (8), 1–5.

(173) Hadjiivanov, K. I.; Klissurski, D. G. Surface Chemistry of Titania (Anatase) and Titania-Supported Catalysts. *Chem. Soc. Rev.* **1996**, *25* (1), 61–69.

(174) Guo, D.; Wang, G.-C. Partial Oxidation of Methane on Anatase and Rutile Defective TiO2 Supported Rh4 Cluster: A Density Functional Theory Study. *J. Phys. Chem. C* **2017**, *121* (47), 26308–26320.

(175) Cheng, H.; Selloni, A. Surface and Subsurface Oxygen Vacancies in Anatase TiO2 and Differences with Rutile. *Phys. Rev. B* **2009**, *79* (9), 2–5.

(176) Nolan, M.; Parker, S. C.; Watson, G. W. The Electronic Structure of Oxygen Vacancy Defects at the Low Index Surfaces of Ceria. *Surf. Sci.* **2005**, *595* (1–3), 223–232.

(177) Bezrodna, T.; Puchkovska, G.; Shymanovska, V.; Baran, J.; Ratajczak, H. IR-Analysis of H-Bonded H2O on the Pure TiO2 Surface. *J. Mol. Struct.* **2004**, *700* (1–3), 175–181.

(178) Panagiotou, G. D.; Petsi, T.; Bourikas, K.; Garoufalis, C. S.; Tsevis, A.; Spanos, N.; Kordulis, C.; Lycourghiotis, A. Mapping the Surface (Hydr)Oxo-Groups of Titanium Oxide and Its Interface with an Aqueous Solution: The State of the Art and a New Approach. *Adv. Colloid Interface Sci.* **2008**, *142* (1–2), 20–42.

(179) Panayotov, D. A.; Burrows, S.; Mihaylov, M.; Hadjiivanov, K.; Tissue, B. M.; Morris, J. R. Effect of Methanol on the Lewis Acidity of Rutile TiO2 Nanoparticles Probed through Vibrational Spectroscopy of Coadsorbed CO. *Langmuir* **2010**, *26* (11), 8106–8112.

(180) Hadjiivanov, K. FTIR Study of CO and NH3 Co-Adsorption on TiO2 (Rutile). *Appl. Surf. Sci.* **1998**, *135* (1–4), 331–338.

(181) Primet, M.; Pichat, P.; Mathieu, M. Infrared Study of the Surface of Titanium Dioxides . Hydroxyl Groups. **1970**, *562* (7), 319–323.

(182) Burns, D. T.; Piccardi, G.; Sabbatini, L. Some People and Places Important in the History of Analytical Chemistry in Italy. *Microchim. Acta* **2008**, *160* (1–2), 57–87.

(183) Ladebeck, J. R.; Wagner, J. P. Handbook of Fuel Cells–Fundamentals, Technology and Applications. Ed. W. Vielstich, HA Gasteiger, A. Lamm 2003.

(184) Topham, S. A. The History of the Catalytic Synthesis of Ammonia. In *Catalysis*; Springer, 1985; pp 1–50.

(185) Schlögl, R. Catalytic Synthesis of Ammonia—A "Never-Ending Story"? *Angew. Chemie Int. Ed.* **2003**, *42* (18), 2004–2008.

(186) Tamaru, K. The History of the Development of Ammonia Synthesis. In *Catalytic ammonia synthesis*; Springer, 1991; pp 1–18.

(187) Grenoble, D. C.; Estadt, M. M.; Ollis, D. F. The Chemistry and Catalysis of the Water Gas Shift Reaction: 1. The Kinetics over Supported Metal Catalysts. *J. Catal.* **1981**, *67* (1), 90–102.

(188) Smith, B.; Muruganandam, L.; Murthy Shekhar, S. A Review of the Water Gas Shift Reaction Kinetics. *Int. J. Chem. React. Eng.* **2010**, *8* (1).

(189) Atitar, F. M.; Belhadj, H.; Dillert, R.; Bahnemann, D. W. The Relevance of ATR-FTIR Spectroscopy in Semiconductor Photocatalysis. *Emerg. Pollut. Environ. - Curr. Furth. Implic.* **2015**.

(190) Thinon, O.; Rachedi, K.; Diehl, F.; Avenier, P.; Schuurman, Y. Kinetics and Mechanism of the Water–Gas Shift Reaction over Platinum Supported Catalysts. *Top. Catal.* **2009**, *52* (13), 1940–1945.

(191) Wheeler, C.; Jhalani, A.; Klein, E. J.; Tummala, S.; Schmidt, L. D. The Water–Gas-Shift Reaction at Short Contact Times. *J. Catal.* **2004**, *223* (1), 191–199.

(192) Shido, T.; Iwasawa, Y. Reactant-Promoted Reaction Mechanism for Water-Gas Shift Reaction on Rh-Doped CeO2. *J. Catal.* **1993**, *141* (1), 71–81.

(193) Liang, J.; Lin, J.; Liu, J.; Wang, X.; Zhang, T.; Li, J. Dual Metal Active Sites in an Ir 1 / FeO x Single-Atom Catalyst : A Redox Mechanism for the Water-Gas Shift Reaction Research Articles. **2020**.

(194) Ammal, S. C.; Heyden, A. Water-Gas Shift Activity of Atomically Dispersed Cationic Platinum versus Metallic Platinum Clusters on Titania Supports. **2017**, *2* (110).

(195) Xing, M.; Guo, L. Theoretical Study of the Single Noble Metal Stabilized on Metal Oxide Clusters Catalyze the Water-Gas Shift Reaction. **2018**, No. June, 1–10.

(196) Nehasil, V.; Stará, I.; Matolín, V. Study of CO Desorption and Dissociation on Rh Surfaces. *Surf. Sci.* **1995**, *331–333* (PART A), 105–109.

(197) Tang, Y.; Asokan, C.; Xu, M.; Graham, G. W.; Pan, X.; Christopher, P.; Li, J.; Sautet, P. Rh Single Atoms on TiO2 Dynamically Respond to Reaction Conditions by Adapting Their Site. *Nat. Commun.* **2019**, *10* (1), 4488.

(198) Asokan, C.; Yang, Y.; Dang, A.; Getsoian, A. "Bean"; Christopher, P. Low-Temperature Ammonia Production during NO Reduction by CO Is Due to Atomically Dispersed Rhodium Active Sites. *ACS Catal.* **2020**, *10* (9), 5217–5222.

(199) Worley, S. D.; Rice, C. A.; Mattson, G. A. The Effect of Rhodium Precursor on Rhl Al2O3 Catalysts. **1982**, *76* (1), 20–25.

(200) McCabe, R. W.; Usmen, R. K.; Ober, K.; Gandhi, H. S. The Effect of Alumina Phase-Structure on the Dispersion of Rhodium/Alumina Catalysts. *Journal of Catalysis*. 1995, pp 385–393.

(201) Miessner, H.; Gutschick, D.; Ewald, H.; Miller, H. The Influence of Support on the Geminal Dicarbonyl Species RhI (CO) 2 on Supported Rhodium Catalysts: An IR Spectroscopic Study. **2000**, *36* (1986), 369–373.

(202) Dictor, R.; Roberts, S. Influence of Ceria on Alumina-Supported Rhodium: Observations of Rhodium Morphology Made Using FTIR Spectroscopy. *J. Phys. Chem.* **1989**, *93* (15), 5846–5850.

(203) Campbell, C. T.; Mao, Z. Chemical Potential of Metal Atoms in Supported Nanoparticles: Dependence upon Particle Size and Support. *ACS Catal.* **2017**, *7* (12), 8460–8466.

(204) Lou, Y.; Liu, J. CO Oxidation on Metal Oxide Supported Single Pt Atoms: The Role of the Support. *Ind. Eng. Chem. Res.* **2017**, *56* (24), 6916–6925.

(205) Beyer, H.; Emmerich, J.; Chatziapostolou, K.; Köhler, K. Decomposition of Nitrous Oxide by Rhodium Catalysts: Effect of Rhodium Particle Size and Metal Oxide Support. *Appl. Catal. A Gen.* **2011**, *391* (1), 411–416.

(206) Yates, J. T.; Duncan, T. M.; Worley, S. D.; Vaughan, R. W. Infrared Spectra of Chemisorbed CO on Rh. *J. Chem. Phys.* **1979**, *70* (3), 1219.

(207) Solymosi, F.; Pásztor, M. Infrared Study of the Effect Of. *J. Phys. Chem.* **1986**, *90*, 5312–5317.

(208) Roscioni, O. M.; Dyke, J. M.; Evans, J. Structural Characterization of Supported Rh I (CO) 2 /γ-Al 2 O 3 Catalysts by Periodic DFT Calculations. *J. Phys. Chem. C* **2013**, *117* (38), 130911121850001.

(209) Cavanagh, R. R., Yates Jr., J. T. Site Distribution Studies of Rh Supported on Al2O3—An Infrared Study of Chemisorbed CO. *J. Chem. Phys.* **1981**, *74* (7), 4150.

(210) Serna, P.; Gates, B. C. Zeolite-Supported Rhodium Complexes and Clusters: Switching Catalytic Selectivity by Controlling Structures of Essentially Molecular Species. *J. Am. Chem. Soc.* **2011**, *133* (13), 4714–4717.

(211) Hoffman, A. S.; Fang, C.; Gates, B. C. Homogeneity of Surface Sites in Supported Single- Site Metal Catalysts : Assessment with Band Widths of Metal Carbonyl Infrared Spectra. **2016**.

(212) Redhead, P. A. Thermal Desorption of Gases. *Vacuum* **1962**, *12* (4), 203–211.

(213) Nehasil, V.; Star, I.; Matolln, V. Study of CO Desorption and Dissociation on Rh Surfaces. **1995**, *333*, 105–109.

(214) Hadjiivanov, K. I. Identification of Neutral and Charged N x O y Surface. **2007**, *4940*.

(215) Miessner, H.; Burkhardt, I.; Gutschick, D. Coadsorption and Interaction of Nitric Oxide and Carbon Monoxide on Rh Supported on Highly Dealuminated Y Zeolite. Formation of Mixed Rh Carbonyl–Nitrosyls on the Surface. *J. Chem. Soc. Faraday Trans.* **1990**, *86* (12), 2329–2335.

(216) Tyson, W. R.; Miller, W. A. Surface Free Energies of Solid Metals: Estimation from Liquid Surface Tension Measurements. *Surf. Sci.* **1977**, *62* (1), 267–276.

(217) Matsushima, T.; Imamura, K.; Horino, H.; Hiratsuka, A.; Ma, Y.-S.; Rzeznicka, I. I.; Nakagoe, O. Inclined N2 Desorption in N2O Decomposition on Rh (1 1 0). *Appl. Surf. Sci.* **2005**, *244* (1–4), 141–144.

Chapter 2:

Synthesis of Atomically Dispersed Rh Catalysts on Oxide Supports via Strong Electrostatic Adsorption and Characterization by Cryogenic Infrared Spectroscopy.

Adapted from article (To be submitted):
Asokan, C., Xu, M., Dai, S., Pan, X., & Christopher P. “Synthesis of Atomically Dispersed Rh Catalysts on Oxide Supports via Strong Electrostatic Adsorption and Characterization by Cryogenic Infrared Spectroscopy.” (In preparation)

2.1 Introduction

Atomically dispersed metal catalysts provide the optimal utilization of expensive precious metals (such as Pt, Pd, and Rh) and the potential for distinct reactivity compared to metal clusters. These active sites are likely present in many industrial catalysts, particularly where low metal weight loadings are commonly used, such as the three-way catalyst (TWC) in catalytic converters.[1] TWC contain mixtures of precious metals, such as Pd and Rh, to convert species present in the exhaust of gasoline burning engines, such as NO_x and carbon byproducts, into non-toxic gases.[2–4] TWC commonly contain less than 0.3% Rh, which exists as a mixture of large particles, small clusters, and atomically dispersed species.[5] While much work has been dedicated to studying the reactivity of Rh nanoparticles and extended surfaces for NO_x reduction reactions, there exists minimal insights into the role of atomically dispersed Rh species in automotive catalysis.[6–14]

Interrogating the reactivity of atomically dispersed Rh active sites is challenging due to difficulties in the synthesis of catalysts containing exclusively this active site, the stability of these active sites under reaction environments, and convincing characterization of the distribution of active sites in a catalyst sample.[15] Recently, stable catalysts consisting of atomically dispersed Pt on TiO_2 and CeO_2 were synthesized by applying principles of strong electrostatic adsorption (SEA), using low Pt weight loadings, and employing small diameter (~ 5 nm) oxide nanoparticles as supports.[16–20] This approach enabled the synthesis of atomically dispersed metal catalysts with a high degree of uniformity in the active site environment and stability against sintering even in reducing environments.

While SEA has been demonstrated as an effective approach for synthesizing highly dispersed Pt catalysts, much less works exists using SEA for the synthesis of highly dispersed

Rh catalysts.[21–28] An important distinction between SEA based synthesis of Pt and Rh catalysts is the speciation of common precursors under pH controlled aqueous environments. For the case of Pt, widely available and commonly used precursors such as H_2PtCl_6 and $Pt(NH_4)_4(NO_3)_2$ form distinct and stable ions in pH controlled aqueous solutions, making it relatively straightforward to predict the interaction between metal precursors and charged support surfaces. Alternatively, common Rh precursors, such as $RhCl_3$ and $Rh(NO_3)_3$, speciate to form a manifold of ions in solution as a function of pH.[29,30] The variation of Rh ions present in solution during synthesis make it challenging to design synthetic conditions that maximize metal dispersion on the support, as designed electrostatic interactions in solution between the metal precursor and support surface are key to successful SEA syntheses.[21,22,24,26,31–34]

There are also challenges associated with characterizing the distribution of Rh structures in a synthesized catalyst. For example, quantitative imaging of Rh structure distribution down to the limit of single atoms by transmission electron microscopy is challenging for supports made of heavy cations (e.g. CeO_2), because of the lack of Z-contrast between Rh and Ce.[35–37] Furthermore, x-ray absorption spectroscopy provides only a measure of the average coordination environment of Rh species, rather than information about the distribution of Rh structures. CO probe molecule Fourier-transform infrared spectroscopy (FTIR) is a powerful technique for characterizing the distribution of Rh species in a catalyst sample.[38–46] This stems from the distinct bonding geometry of CO to Rh clusters and atomically dispersed Rh species and the known site-specific extinction coefficients for the resulting CO stretches.[47–50] While using CO as a probe molecule can be informative, CO can fragment Rh clusters into atomically dispersed species. Fragmentation occurs because the binding energy between CO and dispersed Rh species

is greater than the cohesive energy of Rh metal, thus creating a driving force for particle fragmentation.[51–54]

In this work, we analyze the synthesis of atomically dispersed Rh species on Al_2O_3 and CeO_2 supports (the most common supports in TWC) from a $RhCl_3$ precursor through SEA. The electrostatic adsorption of Rh precursors onto the oxide supports was experimentally and theoretically analyzed by considering the pH dependence speciation of $RhCl_3$ in solution and the interactions of these species with the oxide surfaces. Cryogenic probe molecule CO FTIR was used to characterize the distribution of Rh structures in synthetized catalysts and low temperature analysis was shown to be critical to minimize CO-induced fragmentation of Rh clusters that is prevalent at room temperature. The FTIR based analysis was supported with high-angle annular dark-field scanning transmission electron microscopy (HAADF-STEM), to substantiate the conclusions.[19,20,46,55] We identify simple synthetic protocols and characterization approaches for the production of atomically dispersed Rh species on CeO_2 and Al_2O_3. We expect that model catalysts synthesized through this approach will help rationalize the performance of industrial Rh catalysts and provide design rules for enhanced catalyst performance.

2.2 Experimental Methods

2.2.1 Materials

Rhodium (III) chloride hydrate (RhCl3·xH2O) purchased from Sigma-Aldrich (#206261) was used as precursor for catalyst synthesis. High surface area CeO_2 (70 m^2/g) and γ-Al_2O_3 (127 m^2/g) nanoparticles (5-10 nm diameter) were purchased from US Research Nanomaterials (US Nano Stock #US3037 and #US3007, respectively). Reagent

grade ammonium hydroxide, NH_4OH, (28-30% concentration obtained from Sigma-Aldrich, #221228) was used to produce basic pH solutions. Diluted hydrochloric acid, HCl, (certified ACS Plus 36.5 to 38.0% from Fisher Chemical) was used to produce acidic pH solutions. High-performance liquid chromatography (HPLC) grade water from J.T Baker (#4218) was used for all dilutions.

2.2.2 Support Point of Net Zero Charge (PNZC) Measurement

The point of net zero charge (PZNC) was experimentally determined by titration of the oxide supports with protons from solution. A series of eight 30 mL aqueous solutions with acidic or basic pH values (~1, 2, 3, 4, 5, 8, 9,10, and 11) were prepared through addition of HCl or NH_4OH. Dry oxide powder (20 mg) was added to each solution and thoroughly mixed for 1 hour. The pHs of the equilibrated solutions were measured and the PZNC was determined by averaging final pH values at the plateau at which the support reaches a neutral charge due to proton exchange (Figure 2.1).

2.2.3 Analysis of Rh Precursor Speciation

To measure the speciation of $RhCl_3$ in solution, UV-Vis spectroscopy (via Thermo Scientific Evolution 300 spectrophotometer) and electrospray ionization-mass spectrometry, ESI-MS, (via Waters LCT Premier ESI TOF with high resolution orthogonal Time-of-Flight MS, 12000 FWHM resolution and 100-2000m/z range, and multi-mode ionization source for fast switching between positive and negative polarities) were used. $RhCl_3 \cdot xH_2O$ was diluted in water to make a 60 mL stock solution containing 50 ppm of Rh. The stock solution was split into 6 separate solutions. One solution was kept aside without adjustment, which stabilized at a pH of ~3. The remaining solutions

were adjusted with NH_4OH to target pH values 5, 8, 9, 10, and 11 within +/- 0.5 and analyzed by ESI and UV-Vis.

2.2.4 Rhodium Uptake

The uptake of Rh onto the oxide supports was determined by mixing pH adjusted oxide and precursor solutions, followed by filtration to retrieve the oxide support and analysis of the residual Rh concentration in solution by inductively coupled plasma optical emission spectroscopy, ICP-OES (Thermo iCAP 6300). The ICP-OES measurements were calibrated using 0, 100, 20, 300, 400, and 500 ppm stock Rh solutions made from diluting a commercial Rh standard (Millipore #04736) for ICP measurements with 2% HCl acid. A series of solutions containing 50 mg of oxide support with final pH values of 3, 5, 8, 9, 10, and 11 and corresponding pH adjusted solutions containing 200 ppm $RhCl_3 \cdot xH_2O$ were prepared using NH_4OH or HCl. The liquid ratio of precursor to support solution was 1:5, which resulted in 2 wt.% Rh on the oxide support. Support solutions were mixed with their corresponding precursor solutions with the same pH for 1 hour. The solute was filtered out under vacuum with Lab Safety Supply Filter Paper (# 14A842, Pore 0.45 µm, 4.7 cm diameter) and the filtrate was kept for analysis. The percent uptake of the Rh precursor by the oxide support was calculated by subtracting the final Rh concentration from the initial concentration measured by ICP-OES. Each experiment was repeated three times and the reported values are the average and standard deviation of the triplicate experiments.

2.2.5 Catalyst Synthesis

100 mg of CeO_2 (or γ-Al_2O_3) support and the desired amount of $RhCl_3$ precursor based on the targeted wt% were diluted in water separately to create separate solutions at a volumetric ratio of 4:1 (support liquid solution: precursor liquid solution) to combine for a total of 100 ml. NH_4OH or HCl was added to the support and precursor solutions to target pH values corresponding to those used in the Rh uptake analyses. The precursor solution was injected at a rate of 4 ml/min into the support solution while constantly stirring. Then, the solution was heated to 70 ˚C while being mixed in evaporation dish until the water was evaporated and the sample was dried completely. The sample was kept overnight in a 100 ˚C oven and then ex-situ calcined in air for 4 hours at 350 ˚C.

2.2.6 Cryogenic IR Characterization

Catalysts were loaded into a Harrick low temperature reaction chamber mounted inside a ThermoScientific Praying Mantis diffuse reflectance adapter. A Nicolet iS10 FTIR spectrometer with a Mercury Cadmium Telluride (MCT) detector cooled by liquid nitrogen was used to collect IR spectra. All gases passed across an isopropyl alcohol liquid nitrogen cold trap held at -40 ˚C and a glass trap filled with Drierite desiccant to remove trace moisture. Catalysts were pretreated in situ by oxidation for 30 minutes at 350˚ C in 10% O_2, followed by reduction for 1 hour at 200 ˚C in 10% H_2. Calcination removed residual moisture from storing catalysts in the lab and the reduction treatment enabled CO adsorption. Following pretreatment, catalysts were cooled to cryogenic temperatures (-120 ˚C) in Ar under vacuum and then exposed to 10% CO in Ar for 10 minutes, followed by purging in Ar for 10 minutes. Spectra were recorded with 32 scans and 0.482 cm^{-1} data spacing. To track potential Rh structure changes as temperature was

increased to room temperature, spectra were continuously collected while 10% CO in Ar was flown in vacuum. In all measurements, spectra were obtained by averaging 32 sequentially collected scans at a resolution of 4 cm^{-1} in absorbance mode.

2.2.7 STEM

Samples were oxidized ex-situ at 350 ˚C for 30 min in pure O_2 and then reduced at 200˚C for 60 min in 10% H_2 in He. HAADF-STEM images were taken on a JEOL Grand ARM 300CF TEM/STEM with double spherical aberration correctors operated at 300 kV with a probe current of 23 pA and pixel time of 4 μs. Samples for STEM measurements were prepared by dropping 60 μL of catalyst dispersed in methanol on a lacey carbon-coated copper grid.

2.3 Results

2.3.1 Surface Charge and Rh Speciation pH Dependency

We were motivated to study SEA as a mechanism for the synthesis of atomically dispersed metal catalysts due to the scalability and industrial viability of the method.[21,32,33] The fundamental concept relies on the electrostatic adsorption of ligated metal ions from solution onto specific surface sites on the support.[23,24,26] At low metal loadings, the synthesis approach produces isolated metal ion precursors well distributed on the support. Thus, if the electrostatic interactions between the metal precursor and support surfaces are well-designed and the pre-treatment steps are chosen to minimize metal mobility, a facile and cheap synthetic method for atomically dispersed metal catalysts can be realized.

Hydroxyls on oxide surfaces play a central role in the SEA synthesis approach, as their local environments and proton exchange with solution dictate the local oxide surface charge. Hydroxyls at the surface of metal oxides compensate for charge deficiency in the oxide.[56] Hydroxyl species can exhibit a uniform distribution of charge density across an oxide surface, or more often hydroxyls exhibit varying charge densities across the support due to defects in the oxide structure.[57] The intrinsic nature of surface hydroxyls on an oxide surface and relative abilities to protonate or de-protonate dictate the pH conditions where energetically favorable electrostatic interactions exist with metal ion precursors in solution.[54,58]

When an oxide surface is in contact with a solution containing ions, charged species will adsorb or desorb from the surface to equilibrate with the surroundings. Under certain conditions, equilibration of an oxide surface with an aqueous environment will result in a neutral oxide surface charge. The pH of the solution where the oxide surface becomes neutral is known as the point of zero net charge (PZNC).[23,59] The PZNC can result from a homogeneously neutral surface, or a surface where there is an even but heterogeneous distribution of positive and negative charge. The electrostatic adsorption of Rh ions onto an oxide surface requires the existence of a pH where the metal ion charge in solution is opposite to that of the net charge of the support surface. This results in a negative Gibbs Free Energy associated with the electrostatic interaction between the metal ion and the oxide surface and thus electrostatic adsorption. CeO_2 and γ-Al_2O_3, the most prevalent supports in TWC and the focus of this study, exhibit distinct hydroxyl characteristics and therefore should require different optimal solution pHs for the SEA based synthesis of atomically dispersed Rh catalysts.

We start by considering the pH dependent charge of the oxide support surfaces. The PZNCs for small CeO_2 and γ-Al_2O_3 nanoparticles were estimated by measuring the uptake and removal of protons from the oxide surfaces, (Figure 2.1). The PZNC values for CeO_2 and γ-Al_2O_3 were measured as 3.3 and 7.2, respectively, which are consistent with previous literature reports.[23] Because γ-Al_2O_3 has a PZNC at near neutral pH, cationic or anionic Rh precursors should electrostatically adsorb by working at basic or acidic pHs, respectively. Alternatively, CeO_2 has a large pH range (above the PZNC) where favorable interactions with cationic Rh precursors exist, but only a minimal pH window where adsorption of anionic Rh precursors would be favorable.[60] Thus, CeO_2 should be able to electrostatically adsorb Rh cations when the solution pH is greater than 3.3. γ-Al_2O_3 should adsorb Rh cations when the solution pH is greater than 7.2 or absorb Rh anions when the solution pH is lower than 7.2. However, the uptake of metal ions onto oxide surfaces typically occurs well above or below the PZNC once the strength of the electrostatic attraction is sufficiently large.

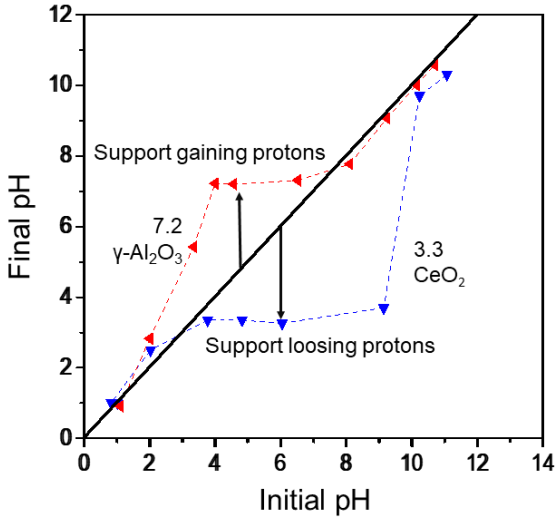

Figure 2.1: Evaluation of γ-Al_2O_3 and CeO_2 PZNC by measuring initial pH of solution and final pH after solution is mixed with support thoroughly for 1 hour.

A key component and complication to the SEA based synthesis of supported Rh catalysts is the speciation of Rh ions from common Rh precursors as a function of the pH and composition of the aqueous environment. For example, it has been shown that diluting $RhCl_3 \cdot xH_2O$ in liquid produces a range of Rh ions with varying Cl, OH and H_2O coordination, as well as overall charge, which each exhibit distinct UV-Vis absorbance spectra.[61–64] UV-vis analysis of a dilute (125 ppm Rh with a resulting pH of 3) solution of $RhCl_3 \cdot xH_2O$ in water results in a spectrum with primary, but broad, bands at ~411 and 518 nm, figure 2.2a. Both experimental and theoretical analyses have previously assigned these features to $RhCl_6^{3-}$.[65–67] The $RhCl_6^{3-}$ complex favorably forms in an acidic solution when excess Cl is present.[61,66,68] In this experiment no additional Cl was added to the solution, which suggests that $RhCl_6^{3-}$ species either form due to excess Cl concentration in the stock solution, from Cl in the water, or from disproportionation of $RhCl_3$ into a combination of species with higher and lower Cl coordination as compared to the starting precursor. The speciation of $RhCl_3$ is known to be kinetically viable under these conditions and results in a distribution of the charged metal–aqua complexes.[62,66,68]

The broadness of the bands observed here in comparison to previous measurements on isolated species, suggests that the initial precursor solution contains a range of anionic Rh species with varying Cl, H_2O, and OH coordination.[69] As pH of the solution was increased with NH_3OH, the absorbance features associated with Rh-Cl aquo complexes shift to lower wavelengths (higher energy), become less resolved and the overall absorbance of the solution increases. This is consistent with the exchange of Cl ligands for H_2O, OH, or NH_3 and likely results in decreasing charge or switching to positive charge of the Rh ions in solution.[67,68,70]. These results are consistent with previous examples where the $RhCl_3 \cdot xH_2O$ precursor

undergoes hydrolysis when diluted with watered and then, when mixing with desired reagents, has results in the formation new ionic complexes in solution.[66–68,70–72] Given the broadness of the bands at low pH and the resulting featureless spectra at higher pH, the results suggest that $RhCl_3$ initially speciates into a range of anionic complexes, including $RhCl_6^{3-}$, which then undergo ligand exchange to begin producing predominantly cationic species above a pH of about 7.

To support conclusions from the UV-Vis measurements, ESI-MS measurements were executed. ESI-MS allows analysis of the type of ion complexes present and can be performed in negative and positive ion detection modes depending on the ions being anionic or cationic.[73] While an absolute ionic concentration cannot be determined quantitatively by ESI-MS, the relative concentrations of positive or negative ionic species can be tracked in a normalized manner as function of pH by examining mass to charge (m/z) peak areas as a function of prepared pH (see figures 2.3 and 2.4). At an initial pH of 3 when $RhCl_3 \cdot xH_2O$ was diluted in water (125 ppm Rh), a predominant anionic species was observed in the ESI mass spectrum with m/z values in the range of 243.0–246.9 in negative mode. This feature could be assigned to $RhCl_4^-$, as has previously been done in literature, or to $[RhCl_2(H_2O)_2(OH)_2]^-$ (see figure 2.3).[74] The ESI-MS identification of a chlorinated Rh species with anionic charge is consistent with expectations and with the UV-Vis results. The known $RhCl_6^{3-}$ complex should in principle be present in the solution analyzed by ESI-MS, as seen in UV-vis, but the fast kinetics of its aquation make it undetectable.[74] The positive mode ESI-MS analysis of the pH=3 solution did not indicate any known m/z values associated with Rh complexes.

As the solution pH was increased through the addition of NH_3OH, the relative area of the peaks at 243.0–246.9 decrease and we observe the formation of additional species in the negative detection mode at 260.1-266 and 278.9-288.9 that can be attributed to $RhCl_3(H_2O)_2OH^-$ and $RhCl_4(H_2O)_2^-$ respectively. Above a pH of 8, there remains no detectable anionic species by analysis of the ESI-MS in negative mode. The results are generally consistent with the UV-Vis measurements where a loss of absorbance features associated with anionic chlorinated Rh species was observed at a pH of 9. By positive mode ESI-MS analysis, distinct cationic Rh species was observed to be present above a pH of 5 (Figure 2.4). This is consistent with the UV-Vis measurements, which showed a transition in the spectra above a pH of 5. The primary positive m/z peak values 112.6-114.9 could be assigned to $RhCl(H_2O)_4(NH_3)^{+2}$, $RhCl(H_2O)_3(NH3)_2^{+2}$, or $RhCl(H_2O)_2(NH3)_3^{+2}$, all which seem reasonable as ligand exchange products at increasing NH_3 concentrations. The growth in relative intensity of this feature as a function of pH, Figure 2.2b, is consistent with the loss of the primary anionic species observed from negative mode ESI-MS. It is particularly interesting to note that there is a range from pH of 5 to 9, where the co-existence of cationic and anionic Rh species is observed.

Based on the UV-Vis and ESI-MS, it is clear that the parent $RhCl_3$ speciates initially in the aqueous solution and then undergoes ligand exchange as NH_4OH is added to increase the solution pH. From both analyses, evidence was provided that there likely exists a range of Rh species in solution at each pH and further than both cationic and anionic Rh species likely exist in solution at intermediate pHs. A more detailed look at the expected or existing mixture of complexes would require detailed thermodynamic modelling including Cl, OH, H_2O, and NH_3 ions accompanied by X-ray absorption spectroscopy, which is outside the scope of these

studies. To effectively model the uptake of Rh ions onto the supports we simplified the picture to assume that the range of cationic species can be described by a $Rh(Cl)_x(H_2O)_y(NH_3)_z^{2+}$ complex, while the anionic species can be described by a $Rh(Cl)_x(H_2O)_y(OH)_z^{2-}$ complex, and that their relative concentrations vary as seen in the ESI-MS data in Figure 2.4b.

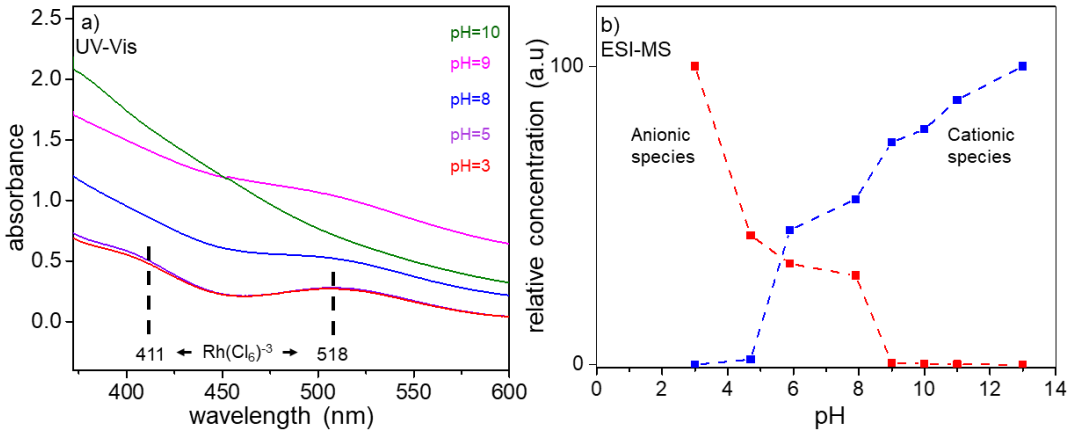

Figure 2.2: a) Measurements by UV-Vis of $RhCl_3\ xH_2O$ diluted in water and adjusted to target pH with NH_4OH. Initial $Rh(Cl_6)^{-3}$ anionic species is identified at at ~411 nm and~518 nm. Shift in intensity towards lower wavelengths as pH increases denotes ligand exchange. b) Trends showing relative appearance of dominant anionic and cationic species present in pH adjusted $RhCl_3 \cdot xH_2O$ solutions measured by normalized ESI-MS peak area.

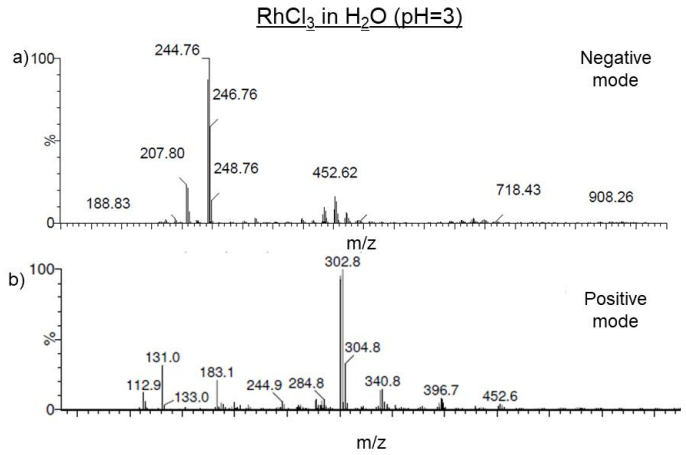

Figure 2.3: ESI-MS measurement $RhCl_3$ diluted in H_2O (125 ppm Rh, pH=3) a) negative mode b) positive mode

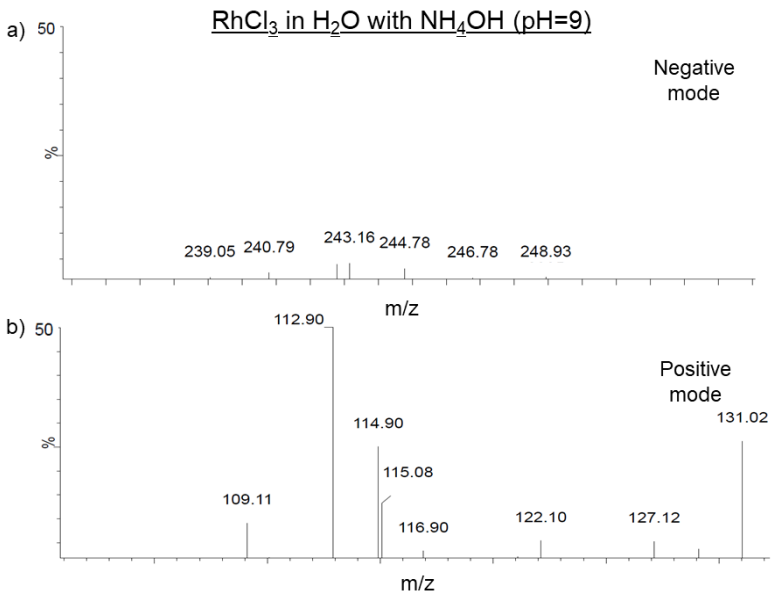

Figure 2.4: ESI-MS measurement $RhCl_3$ diluted in H_2O with NH_3OH (125 ppm Rh, pH=9) a) negative mode b) positive mode

2.3.2 Uptake Analysis

The uptake of Rh species from solution onto the oxide supports was modelled using the revised physical adsorption (RPA) model.[22,59] The uptake of Rh ions was assumed to follow Langmuir isotherm adsorption (equation 2.1) in which the equilibrium constant (equation 2.2) was calculated using the coulombic Gibbs free energy (equation 2.3) of adsorption of Rh ions onto each oxide support. The Gibbs free energy takes into the account the species' ionic charge identified by ESI-MS, Faraday's constant, and the electric double layer potential. The electric double layer potential was found by a Laplace solution of the Gouy and Chapman equation (equations 2.4-2.6), which is dependent on the Debye-Huckel double layer length (equation 2.7) and ionic charge strength of the solution (equation 2.8). The ionic charge strength is calculated at each specific pH by summing all positive and negative ionic concentrations, including $[H^+]$ and $[OH^-]$, present in the liquid solution. Support specific PNZCs were used to calculate the equilibrium of

the surface charge density, although the surface charge of the oxide is assumed to be homogeneous across the support. After assigning support specific parameters, solving for the surface potential as a function of the surface charge density (equations 2.9 -2.12) dictates the surface attraction to oppositely charged ions from solution. Parameters used in the modelling are listed in Table 2.1.

Table 2.1: RPA model parameters

	CeO_2	γ-Al_2O_3
PZC	3.3	7.2
Surface Loading (m^2/L)	466	1000
Rh concentration (mol/L)	0.002	0.002
Hydroxyl site density (OH/nm)	3.4	11
Ion charge	-1 or +2	- 1 or +2

Figure 2.5 shows the uptake of Rh ions (-1 anions below PZNC, +2 cations above PZNC) modeled for CeO_2 and γ-Al_2O_3 (blue and red solid lines, respectively). As predicted from its PZNC, CeO_2 adsorbed cationic Rh over a large range above a pH of 8, while anions absorb over a very narrow range. Anions are predicted to readily adsorb onto γ-Al_2O_3 below its PZNC and cations above its PZNC, but because the anion charge is less negative, the overall adsorption is slightly lower.

Figure 2.5 also shows experimental ICP-OES measurements of the uptake of Rh onto (a) CeO_2 and (b) γ-Al_2O_3 as a function of solution pH. The experimentally measured Rh uptake onto the oxide supports, presented in a % of Rh ions in solution adsorbed to the oxide, exhibits similarities and differences compared to the RPA model predictions. On CeO_2, the maximum uptake occurred at pH = 9, while on Al_2O_3 the maximum uptake

was observed at pH = 10. At these pHs, cationic Rh species are the dominant ions in solution, and the RPA model predicts that cations should adsorb on the negatively charged oxide surfaces.[25] The Rh uptake at acidic pHs (<7) was higher on γ-Al_2O_3 compared to CeO_2, which is consistent with the higher PZNC of γ-Al_2O_3, which creates a stronger driving force for the uptake of anionic Rh species onto the positively charged oxide surface.

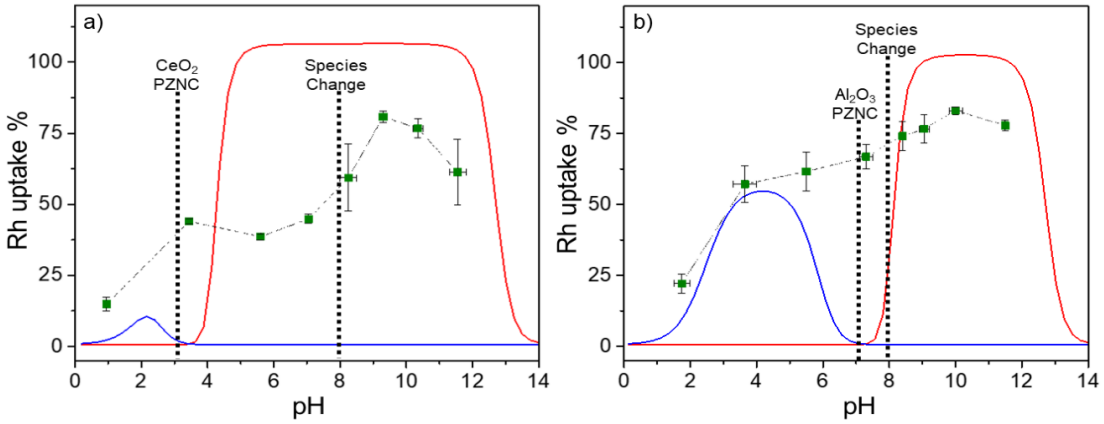

Figure 2.5: RPA modeled uptake of Rh -1 anions (blue line) and +2 cations (red line) for a range of 0-14 pH overlapped with experimentally determined % uptake of using ICP analysis of pH adjusted $RhCl_3xH_2O$ (green dots with error bars) on a) CeO_2 support b) γ-Al_2O_3

Qualitatively, the experimentally measured Rh uptake curves follow the general shape of the predictions from the RPA model. However, the primary range of pHs where the model and experiment disagreed was between the PZNC of each oxide and the pH where Rh species transformed from predominantly anionic to cationic (noted as "species change" in figure 2.3). It is hypothesized that the manifold of Rh species existing at each pH (likely simultaneous existence of anionic and cationic species around pH of 8) and the non-homogeneity of surface charge on the oxide, both of which were not accounted for in

the RPA model, caused poor agreement between the experimental and model at pHs near the PZNCs and point of species charge change.

2.3.3 Cryogenic IR and STEM Analysis of Synthesized Materials

Having understood the adsorption behavior of Rh ions onto the oxide supports, we used CO probe molecule IR to characterize the structures of Rh formed on the oxide supports as a function of synthesis pH. We hypothesized that conditions that yielded optimum SEA based Rh uptake would be optimal for forming dispersed Rh species. To target the formation of atomically dispersed Rh species, catalysts were synthesized at a low weight loading of 0.25% Rh in dilute synthesis volumes, calcined at 350 °C and were mildly reduced (200 °C in 10% H_2), which together allows for spatial separation of deposited Rh precursors and minimal induced mobility of Rh species.[21,24,26,75]

CO probe molecule FTIR analysis was used to assess Rh structure because it provides unique spectral signatures of bound CO, which correspond to specific structures of Rh deposited on oxide supports.[40] CO binds to supported Rh species on oxide supports in 2:1, 1:1 or 1:2 CO:Rh stoichiometries, depending on the type of binding site and Rh structure.[50,76] CO adsorbed to atomically dispersed Rh anchored on oxide supports is known to form Rh gem-dicarbonyl species, $Rh(CO)_2$. The 2 COs can be identified based on 2 vibrational CO stretching modes, specifically a symmetric and asymmetric vibration at ~2090 cm^{-1} and 2020 cm^{-1}, respectively.[76] CO adsorption on extended Rh surfaces, single crystals or particles on oxide supports, results in the formation of bridge bound species (1 CO to 2 Rh) and linearly bound species (1 CO to 1 Rh), which can be identified by characteristic stretches at 1800-1950 cm^{-1} and 2045-2070 cm^{-1}, respectively.[77–86]

Probe molecule CO FTIR spectra collected following exposure of the materials to CO at room temperature showed signatures of only $Rh(CO)_2$ species, suggesting that Rh is atomically dispersed in catalysts synthesized under all explored pHs, figure 2.6. However, CO probe molecule FTIR spectra collected following exposure of the materials to CO at cryogenic temperatures (< -120 °C) demonstrated the co-existence of atomically dispersed $Rh(CO)_2$ species and CO adsorption on Rh clusters, and a dependence of Rh structure on synthesis pH, figure 2.7. The difference in spectra collected at cryogenic temperatures and room temperature stems from the well-known ability of CO to induce oxidative fragmentation of Rh clusters to form atomically dispersed Rh species.[51,87,88] Performing the measurements at cryogenic temperatures allows the Rh clusters to remain kinetically trapped against fragmentation and effective analysis of the Rh structures in the as-synthesized state.

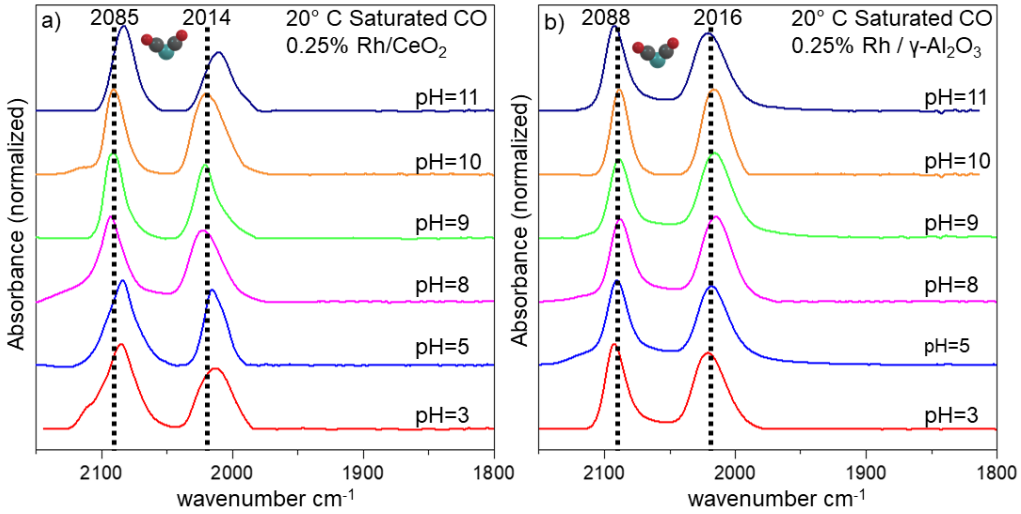

Figure 2.6: IR spectra of CO adsorbed at saturation coverage of catalysts prepared after in- situ pretreatment in pure O_2 for 30 min at 350 °C and 10% H_2/Ar for 1 h at 200 °C taken at 20 °C a) 0.25 wt % Rh/CeO_2 b) 0.25 wt% Rh/ γ-Al_2O_3.

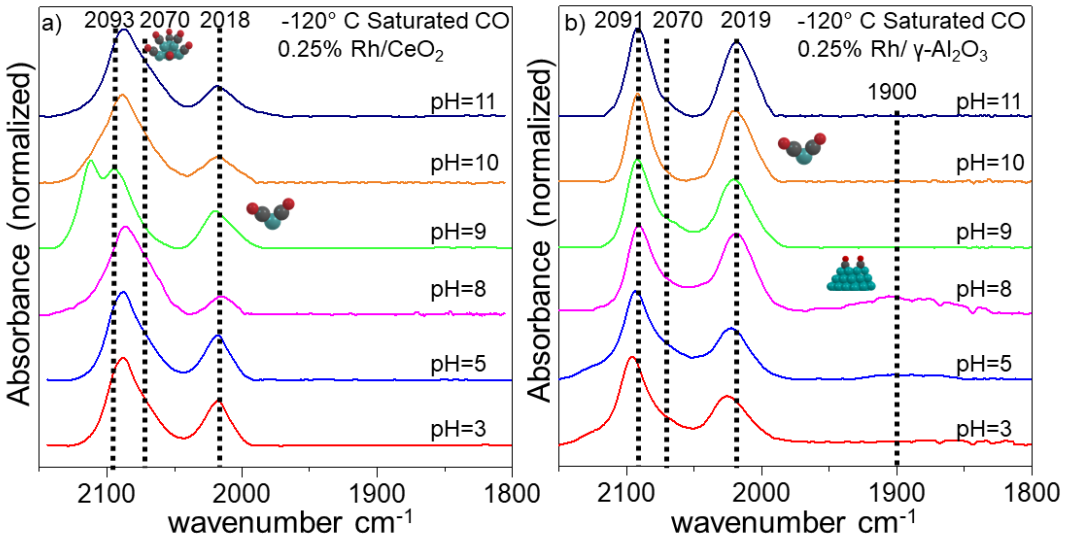

Figure 2.7: IR spectra of CO adsorbed at saturation coverage of catalysts prepared after in- situ pretreatment in pure O_2 for 30 min at 350 °C and 10% H_2/Ar for 1 h at 200 °C taken at -120 °C a) 0.25 wt % Rh/CeO_2 b) 0.25 wt% Rh/ γ-Al_2O_3.

In the cryogenic CO FTIR measurements all Rh/CeO_2 samples showed predominant features at ~2090 cm^{-1} and 2018 cm^{-1} associated with atomically dispersed $Rh(CO)_2$ species. The weaker relative intensity of the asymmetric stretch is assigned to electronic asymmetry in the local environment of $Rh(CO)_2$ species, likely caused by a neighboring oxygen vacancy or reduced Ce metal center.[54] A shoulder at 2070 cm^{-1} on the symmetric $Rh(CO)_2$ vibrational stretch (~2090 cm^{-1}) was observed for all synthesized CeO_2 materials except for at pH=9 (Figure 2.7a). In addition, a shoulder appears at ~2120 cm^{-1} specifically for the pH = 9 synthesis, which has been identified in literature as ionic Rh^{+2} bonded to one CO and an extra O, in addition to the 2 support Os.[89,90] This experiment was repeated on multiple samples with consistent results providing confidence in the observed trends.

Cryogenic CO FTIR measurements for Rh/ γ-Al_2O_3 were similar to Rh/CeO_2 with a few differences, Figure 2.7b. At all synthesis pHs, stretches were predominantly

observed at 2091 cm^{-1} and 2018 cm^{-1}, associated with $Rh(CO)_2$. Clear signatures of CO bound to Rh clusters or particles were observed at pH < 10 based on measurable absorbance at ~2070 cm^{-1} and < 1900 cm^{-1}, associated with linearly and bridge bound CO species. For the synthesis pH of 10 and 11 on γ-Al_2O_3, the $Rh(CO)_2$ spectra still showed a slight deviation from the identical intensity of the two CO stretches that is expected for a square planar complex. This again suggests a local asymmetry in the environment surrounding $Rh(CO)_2$, likely vicinal OH species on the support.[91]

To relate the SEA uptake measurements and model predictions in Figure 2.5 to the resulting distribution of Rh structures, the fractions of atomically dispersed Rh (X_{iso}) and nanoparticle Rh (X_{nano}) adsorption sites were calculated based on analysis of the cryogenic CO FTIR spectra. X_{iso} and X_{nano} were calculated by deconvoluting the spectra with set peak positions and full width at half maxima (FWHM), shown in Table 2.2, and using equation 2.13 with established relative extinction coefficients and adsorption stoichiometries for each vibrational mode.[50,92] Table 2.3 shows the result of this analysis, where it is observed that Rh/γ-Al_2O_3 samples synthesized at pH = 10-11 resulted in the highest fraction of atomically dispersed species, while Rh/CeO_2 samples synthesized at pH = 9 resulted in the highest fraction of atomically dispersed species. Interestingly, the samples with the highest fraction of atomically dispersed Rh species corresponded to synthesis pHs that resulted in the highest Rh uptake in SEA measurements (Figure 2.5). This provides strong evidence that optimal conditions for SEA based catalyst synthesis (ie maximum metal uptake) are also optimal for the production of atomically dispersed metal species.

Table 2.2: FTIR Spectral fitting parameters for I_{iso} values

	peak	Single CO on Rh_{iso}	Symmetric $Rh(CO)_2$	Linear CO on Rh_{nano}	Asymmetric $Rh(CO)_2$
CeO_2	cm^{-1}	2113	2092.44	2078	2017.81
	FWHM	15	23.23	-*	19.47
γ-Al_2O_3	cm^{-1}	-	2091.12	2070.6	2018.4
	FWHM	-	19.38	-*	22.43

*multiple overlapping linear bands exist with variable FWHM

Table 2.3: Fraction of atomically dispersed Rh sites (X_{iso}) vs fraction of nanoparticle Rh sites (X_{nano}) on 0.25% Rh CeO_2 and γ-Al_2O_3 at variable pH

	CeO_2 0.25 Rh wt. %		**γ-Al_2O_3 0.25 Rh wt.%**	
pH:	**X_{iso} (%)**	**X_{nano} (%)**	**X_{iso} (%)**	**X_{nano} (%)**
3	23	77	26	74
5	22	78	14	86
8	36	64	16	84
9	100	0	40	60
10	43	56	100	0
11	25	75	100	0

STEM imaging was used to support the assigned distributions of Rh structures from CO probe molecule FTIR measurements. STEM is a common tool to prove the existence of atomically dispersed species on oxide supports.[39] However, a limited number of localized STEM images do not develop a complete quantitative description of the fraction of atomically dispersed species throughout a sample. Thus, coupling STEM with FTIR provides a more insightful confirmation of the distribution of Rh species throughout a given sample. STEM images were collected from samples which showed

the highest fraction of atomically dispersed Rh in FTIR measurements, Rh on γ-Al_2O_3 made at pH=10 (figure 2.8a) and Rh on CeO_2 made at pH=9 (figure 2.9), after they had been calcined ex-situ and reduced through identical protocols used prior to FTIR characterization.

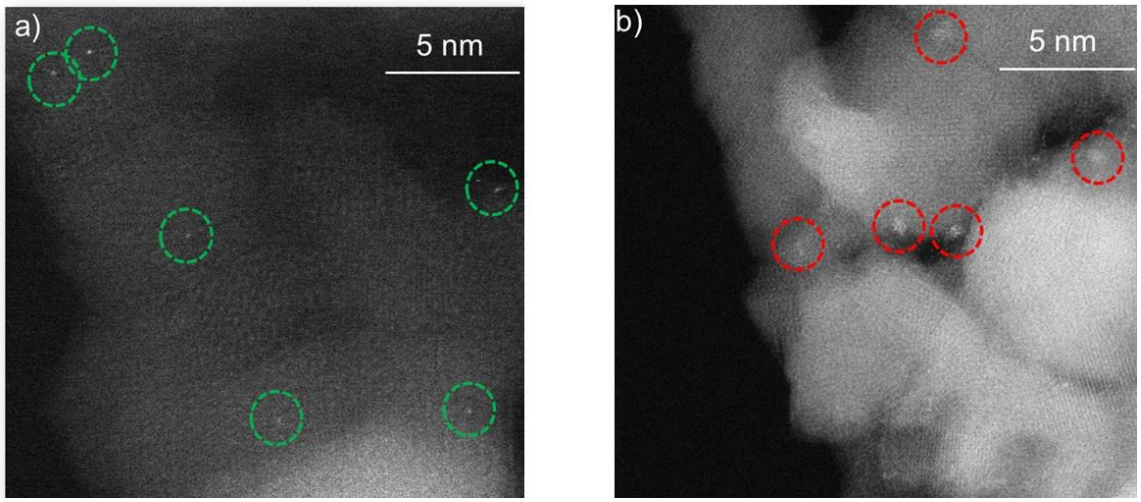

Figure 2.8: Representative STEM images of samples after pretreatment in pure O_2 for 30 min at 350 °C and 10% H_2/Ar for 1 h at 200 °C a) 0.25 wt % Rh/ γ-Al_2O_3 adjusted in synthesis solution at pH=10. Green circles indicate atomically dispersed Rh. b) 0.25 wt % Rh/ γ-Al_2O_3 with synthesis solution at pH=8. Red circles indicate Rh clusters.

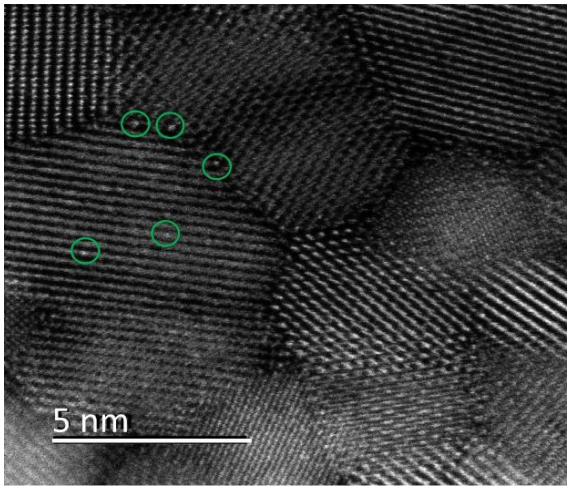

Figure 2.9: Representative STEM images of 0.25 wt % Rh/CeO_2 adjusted at pH=9 after in-situ pretreatment in pure O_2 for 30 min at 350 °C and 10% H_2/Ar for 1 h at 200 °C.

In figure 2.8a, STEM images identified exclusively atomically dispersed Rh species on the 0.25% γ-Al_2O_3 sample made at pH=10. Rh is clearly identified in these images as bright diffraction spots, created by the higher atomic number of Rh (Z=45) as compared to Al (Z=13) and the dependence of intensity in HAADF-STEM imaging on $Z^{1.7\text{-}2.0}$.[30,93–96] This is in excellent agreement with the analysis of IR spectra of the same sample, figure 2.6. It is more challenging to identify atomically dispersed Rh species on CeO_2 through HAADF-STEM imaging because the intensity of Ce atoms, Z=58, is greater than that of Rh. This was overcome by angling the sample away from the exact zone axis where Ce ions line up into columns to create contrast for surface bound Rh atoms.[97] Using this method, STEM images identifying exclusively atomically dispersed Rh species on CeO_2 (figure 2.9) were acquired, which is again in agreement with the analysis by cryogenic CO probe molecule FTIR, figure 2.6a. To contrast the samples where only atomically dispersed species were identified, STEM images were also taken of 0.25% Rh on γ-Al_2O_3 sample made at pH= 8 (figure 2.6b), where a mix of Rh clusters and atomically dispersed species could be identified using cryogenic FTIR. In this sample, more than 50% of the Rh species identified were in the form of small clusters. The STEM results corroborated the conclusion from cryogenic CO IR analysis and reaffirm the assertion that room temperature CO FTIR observations do not accurately portray the distribution of Rh structures prior to probe molecule exposure.

While the primary focus here was to identify the role of SEA synthesis in the production of atomically dispersed Rh catalysts at low Rh loadings, it is worth considering how performing synthesis at optimum pH and increasing Rh loadings influences the distribution of Rh structures. Catalysts were synthesized at support-dependent optimal pHs (pH=9 for CeO_2 and pH=10 for γ-Al_2O_3) and varying Rh

loadings, followed by characterization using cryogenic CO FTIR. While evidence of CO adsorption on Rh clusters becomes apparent at 0.5% Rh on CeO_2, evidence of CO adsorption on Rh clusters was not prevalent until 1.0% Rh on γ-Al_2O_3 (figure 2.8, table 2.4). Given the surface area of γ-Al_2O_3 being ~2x larger than CeO_2 used in these studies, the results suggest that the two supports have a similar capacity for supporting atomically dispersed Rh species. We note however, that the mobility of Rh species is likely different on the two supports and thus higher temperature reductive treatments may produce very different structural distributions at the same Rh loading per surface area due to support dependent Rh mobility.

While the primary focus here was to identify the role of SEA synthesis in the production of atomically dispersed Rh catalysts at low Rh loadings, it is worth considering how performing synthesis at optimum pH and increasing Rh loadings influences the distribution of Rh structures. Catalysts were synthesized at support-dependent optimal pHs (pH=9 for CeO_2 and pH=10 for γ-Al_2O_3) and varying Rh loadings, followed by characterization using cryogenic CO FTIR. While evidence of CO adsorption on Rh clusters becomes apparent at 0.5% Rh on CeO_2, evidence of CO adsorption on Rh clusters was not prevalent until 1.0% Rh on γ-Al_2O_3 (figure 2.10). Given the surface area of γ-Al_2O_3 being ~2x larger than CeO_2 used in these studies, the results suggest that the two supports have a similar capacity for supporting atomically dispersed Rh species. We note however, that the mobility of Rh species is likely different on the two supports and thus higher temperature reductive treatments may produce very different structural distributions at the same Rh loading per surface area due to support dependent Rh mobility.

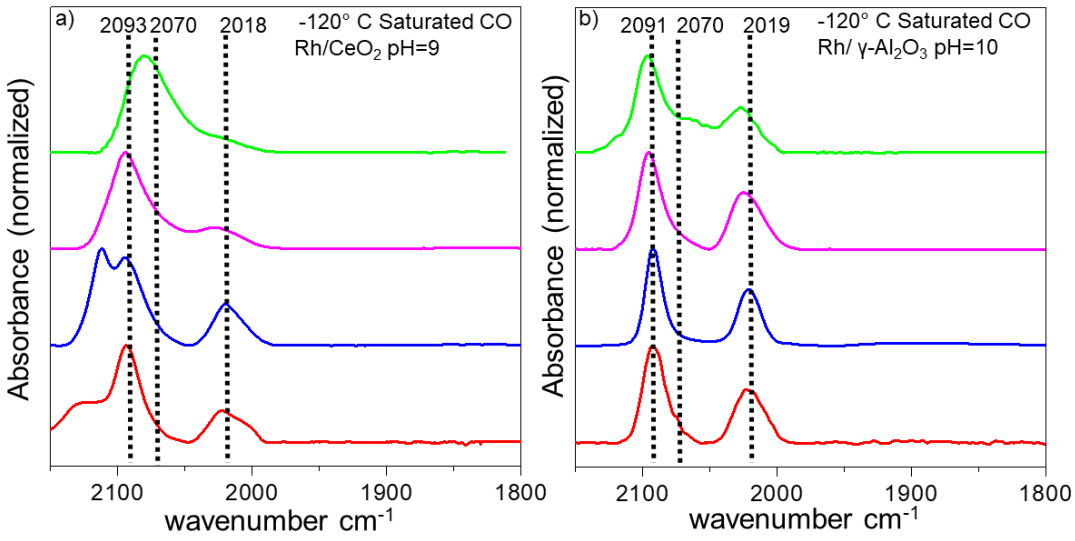

Figure 2.10: Cryogenic CO probe FTIR measurement at -120 °C and saturation coverage, after pretreatment in pure O_2 for 30 min at 350 °C and 10% H_2/Ar for 1 h at 200 °C, of Rh on a) CeO_2 at 0.1, 0.25, 0.5, and 1 wt. %, synthesized at pH=9 b) γ-Al_2O_3 at 0.1, 0.25, 0.5, and 1 wt. %, synthesized at pH=10.

Table 2.4: Fraction of atomically dispersed Rh sites (X_{iso}) vs fraction of nanoparticle Rh sites (X_{nano}) on CeO_2 and **γ**-Al_2O_3 at optimum pH and variable weight loading

	CeO_2		**γ-Al_2O_3**	
	pH=9		**pH=10**	
wt. %	**X_{iso} (%)**	**X_{nano} (%)**	**X_{iso} (%)**	**X_{nano} (%)**
0.1	100	0	100	0
0.25	100	0	100	0
0.5	46	54	100	0
1	22	78	29	71

2.4 Discussion

The objective of this work was to synthesize and identify stable atomically dispersed Rh catalysts on relevant types of oxide supports. We demonstrated that the evident trends, relating the uptake of ionic Rh complexes onto oxide supports, CeO_2 and Al_2O_3, as a function of synthesis solution pH, is connected to optimizing dispersion of the precious metal at low weight loadings into atomically dispersed sites on high surface area oxide supports. The relationship between optimized pH uptake to fraction of Rh_{iso} was demonstrated as consistent with principles from the SEA synthesis technique. The concept of the SEA approach is that the simplest and most effective way to synthesize highly dispersed metal catalysts is to achieve a high dispersion of the metal precursors in solution during wet impregnation. Once impregnated, pretreatment, calcination and reduction, are done in mild conditions to maintain high metal dispersion.[21,25,26,98] In agreement with SEA principles, utilizing pH controlled solutions promoted repulsive interactions between Rh ions in solution and attractive interactions between the ions and the high surface area oxide.[21,25] By modifying the support surface through pH adjustment by the addition of NH_4OH, the oxide surface formed adsorption sites that Coulombically attracted metal ions, as shown in figure 2.11.[75] The surface potential ultimately dictates the surface attraction to oppositely charged ions and spatially disperses the ions away from sites of the same charge. However, the lack of hydroxyl charge uniformity on the oxide support surface also contributes to uptake seen at the PZNC, as depicted in figure 2.11 by the various examples of different types of hydroxyl groups and charged sites that can exist on the surface of oxide supports. Catalyst with unoptimized dispersion fell in the pH range in between the support PZC and the point where Rh ionic complexes transition or speciate from anionic to cationic.[63,69,99,100] This likely suggests that in this range both anionic and cationic Rh species adsorb to positively and

negatively charged surface sites and this may cause Rh adsorption in closer proximity such that Rh cluster formation occurs.[50]

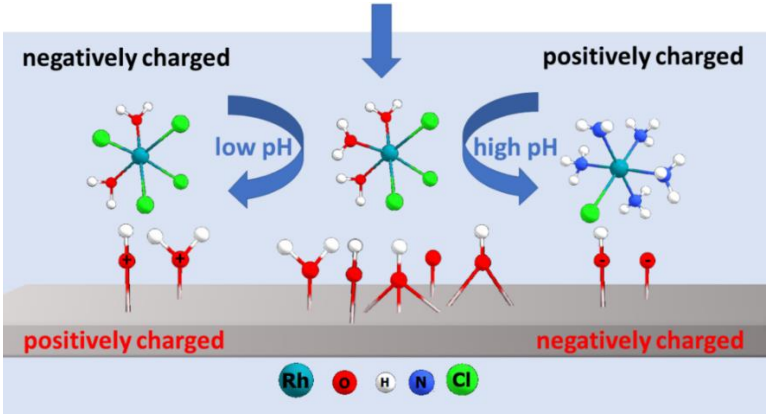

Figure 2.11: Hydrolyzed oxide surface and $RhCl_3$ precursor in water. At pH below PZNC, the oxide surface becomes positively charged while the precursor stays as an anion. At a pH above PZNC, the oxide surface becomes negatively charged while at a certain equilibrium pH, the precursor speciates into a cation.

Further work to perfect the procedure to synthesize atomically dispersed Rh catalysts potentially at an industrial scale could include detailed fluid dynamic studies to better model the electric double layer where precursor interacts with the oxide surface containing a mix of negatively and positively charged sites. Variables important to this analysis of fluid dynamic interactions include mixing speed, ion contact time, and contact space. Additionally, a titration of electrostatically charged sites available that produce atomically dispersed catalysts would lead to a scalable procedure on each variable support.

The percentage of atomically dispersed sites can be quantified by calculating the site fraction, equation 2.13, using Rh extinction coefficients and accounting for adsorption stoichiometry (ratio of Rh to CO). The relative quantity of atomically dispersed species was estimated by deconvoluting spectra taken at cryogenic temperature and integrating the peak areas associated with CO on various adsorption sites.[50,77,101,102] To properly analyze the spectral data to calculate the fraction of nanoparticles and

atomically dispersed sites, both the cryogenic and the room temperature FTIR must be observed to identify accurate frequencies for the asymmetric and symmetric vibrational stretches as well as corresponding FWHM values. When deconvoluting these cryogenic FTIR spectra, we assign $Rh(CO)_2$ stretching frequencies and FWHM values known by deconvoluting a sample that only contains atomically dispersed Rh species, as confirmed by FTIR and corroborated by STEM images.

For example in figure 2.12a, the spectra of 0.25% Rh on CeO_2 made at a pH of 9 taken at room temperate (dotted line) overlaps with the spectra taken at -120 °C (solid blue line) in the region at ~2070 cm^{-1}, indicating a lack of linearly bound CO on Rh clusters. In the specific case of deconvoluting atomically dispersed Rh on CeO_2 made at a pH of 9 in figure 2.12b, an additional peak must be included in the deconvolution, at 2112 cm^{-1}, identified in literature as a single CO attached to an atomically dispersed Rh site with an extra O bond.[77,81,103] The extra O bond to Rh was not detected at room temperature spectra because it is reduced by gas phase CO to form CO_2. This can also be used as an additional indication that atomically dispersed Rh was present at low weight loadings. Detecting this frequency at cryogenic temperature can provide additional details of the original atomically dispersed Rh structure before absorbent interactions and thus suggests cryogenic FTIR is necessary to accurately characterize low Rh weight loading catalyst before CO exposure.

Even when including this peak in deconvolution, an atomically dispersed catalyst can be identified using CO probe molecule FTIR by overlapping the spectra taken at -120 °C with spectra taken at 20 °C to closely look at the region between the symmetric and asymmetric peaks. The example provided in figure 2.12a of the sample containing atomically dispersed Rh on CeO_2 contrasts with figure 2.12c where the linear stretch

associated with Rh clusters was identified. Figure 2.12c presents an example of how a spectra taken at room temperate (dotted line) of a higher wt% loading sample of 0.5% Rh on CeO_2 may appear to have completely dispersed Rh sites while the spectra taken at -120 °C (solid red line) indicates evidence of a shoulder at ~2070 cm^{-1} associated with linearly bound CO on Rh clusters. When fixing the $Rh(CO)_2$ stretch positions to deconvolute 0.5% Rh on CeO_2 in figure 2.12d, an extra stretch is revealed at ~2070 cm^{-1}.

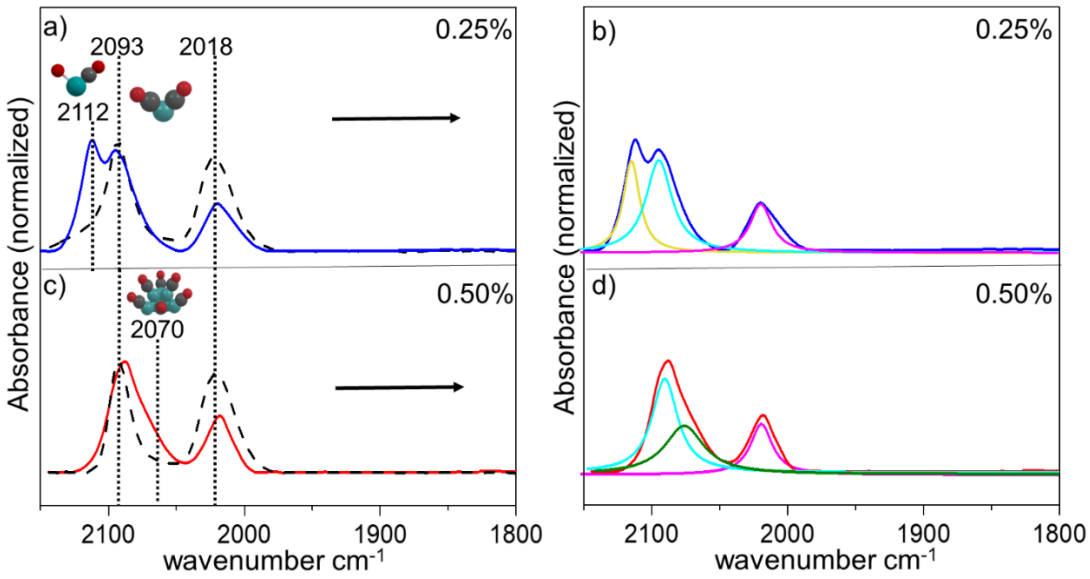

Figure 2.12: IR spectra of CO adsorbed at saturation coverage of Rh/CeO_2 catalysts prepared in pH=9 solution and after in situ pretreatment in pure O_2 for 30 min at 350 °C and 10% H_2/Ar for 1 h at 200 °C a) 0.25 wt% Rh/CeO_2 taken at 20 °C (dotted lines) and -120 °C (solid blue line) b) Deconvolution of 0. 25 wt % Rh/ CeO_2 at -120 °C (solid blue line) with oxygenated atomic Rh bonded to one CO with frequency at 2112 cm^{-1} (yellow) and $Rh(CO)_2$ symmetric frequency at 2093 cm^{-1} (cyan), and asymmetric frequency at 2018 cm^{-1} (magenta). c) 0.5 wt% Rh/CeO_2 at -120 °C (solid red line) and 20 °C (dotted lines) d) Deconvolution of 0. 5 wt % Rh/ CeO_2 at -120 °C (solid red line) with $Rh(CO)_2$ symmetric frequency at 2093 cm^{-1} (cyan), asymmetric frequency at 2018 cm^{-1} (magenta), and linear CO frequency at 2070 cm^{-1}

Based on this detailed deconvolution of cryogenic spectra to calculate site fractions, Rh nanoparticles are the major species (50-93% of sites) in pH adjusted samples where there is an indication of linear or bridge bound CO, see table 2.2, 2.3, and 2.4. Therefore, samples with no indication of a linear or bridge bound CO contains a

majority of atomically dispersed sites, as was the case for Rh on CeO_2 when synthesized in a pH =9 solution and Rh on γ-Al_2O_3 when synthesized in a pH =10-11 solution. This calculation is also useful for observing how the fraction of nanoparticle sites can grow drastically with increased wt% as seen in figure 2.10. In the case of CeO_2, the fraction of nanoparticle Rh sites increases from 0 to ~50% when Rh wt% is increased from 0.25% to 0.5% and in the case of γ-Al_2O_3 this fraction increases from 0% to ~70% when Rh wt% is increased to 1%, table 2.4.

Another notable difference in the room temperature CO probe molecule FTIR measurement of Rh samples compared to the cryogenic measurement was that asymmetric peak grows in height, and thus changes the height ratio of the asymmetric to symmetric peak. Figure 2.13 provides spectra systematically taken while CO flows in vacuum condition as temperature rises from - 120 ºC to 20 ºC and the ratio asymmetric to symmetric peak height grows. Historically, this ratio has been connected to the angle between the two CO molecules bonded to Rh.[39,77,104,105] This would provide evidence that the $Rh(CO)_2$ is reconstructing bonding geometries due to interaction with the CO probe molecule and could correspond to an increased bond distance between the Rh atom and the support as if the gaseous CO is pulling the Rh atom away from the support. However, recent studies that compare $Rh(CO)_2$ asymmetric to symmetric peak ratios of atomically dispersed Rh on Anatase phase to Rutile phase TiO_2 have found the apparent difference in ratios is attributed to electronic effects of surface oxygen vacancies in Rutile. Thus, saying that the asymmetric to symmetric peak ratio changes due to bond angle is a simplification that requires further research for a complete explanation. Details such as this show the complexity in analysis that cryogenic CO probe molecule FTIR brings to single atom catalyst identification. Thus reiterating the point that cryogenic

analysis is important because CO exposure at room temperature can cause either Rh cluster fragmentation, or reconstruction of the $Rh(CO)_2$ species.

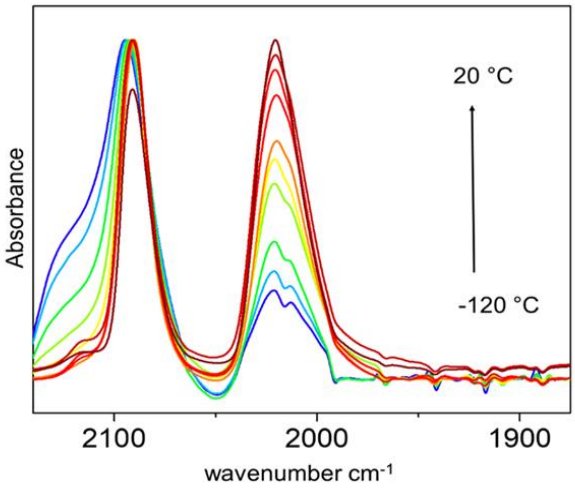

Figure 2.13: IR spectra of CO saturated 0.1% Rh/CeO_2, after in- situ pretreatment in pure O_2 for 30 min at 350 °C and 10% H_2/Ar for 1 h, taken incrementally while cryogenic temperature increases to room temperature (-120 °C to 20 °C) under vacuum as 10% CO in Ar flows over the catalyst.

2.5 Conclusion

By examining the effect that pH has on the supports and precursors, we draw conclusions on the optimal conditions for ionic Rh to disperse on specific oxide supports according to principles of SEA where an oppositely charged cationic Rh is attracted to the negatively charged surface adjusted with base. For complete Rh dispersion, conditions where pH=9 is the optimum for CeO_2 and pH=10-11 is the optimum for γ-Al_2O_3. This informs the synthesis of atomically dispersed Rh on these relevant supports as evidenced by cryogenic FTIR and complimentary STEM images. With this established protocol for creating atomically dispersed materials, we can move forward to look at how this structure influences reactivity as compared to extended surfaces on Rh nanoparticles. Work towards understanding the nature of atomically dispersed Rh as an active site can give way to alternative reactivities on new types of catalysts.

2.6 Appendix

2.6.1 RPA Model

RPA Model equations and variables: The RPA model is based on a basic Langmuir isotherm model where the equilibrium constant is calculated by solely using the coulombic Gibbs free energy of the adsorption of the precious metal to the oxide support. The Gibbs free energy takes into the account the surface potential from Laplace's equation assuming a simple electric double layer in which all species adsorb in one plane. Using Gouy –Chapman Diffuse layer charge-potential relationship, the surface potential is a function of the precious metal complex radius, surface loading, variable ionic strength, and the point of zero charge. The double layer length is dependent on the ionic strength. The ionic strength changes with the concentration of positive and negative ions due to pH. The point of zero charge is used to calculate the equilibrium of the surface charge density.

$$\text{Rh uptake\%} = \frac{\Gamma}{\Gamma_{\max}} = \frac{KC}{1+KC} \quad (2.1)$$

(2.2) where:

$$\Delta G_{\text{coul}} = zF\Psi_x \quad (2.3)$$

$$K = \exp\left(\frac{-\Delta G_{a\ ds}}{RT}\right) = \exp\left(\frac{-\Delta G_{coul}}{RT}\right)$$

$$\Psi_X = \left[\frac{2RT}{ZF}\right]\ln\left(\frac{(Y+1)+(Y-1)\mathrm{e}^{-\kappa x}}{(Y+1)-(Y-1)\mathrm{e}^{-\kappa x}}\right) \quad (2.4)$$

(2.5, 2.6, 2.7)

$$Y = \exp\left(\frac{ZF\Psi_0}{2RT}\right) \quad ,$$

where:

$$\kappa = 3.31 \times 10^9\sqrt{I}, \qquad x = (r_{ion} + 2r_w)$$

$$\text{where: } I = \frac{1}{2}\sum_i z_i^2 C_i \quad (2.8)$$

(2.9) $$\sigma_o = (8 \times 10^{-5} \varepsilon \varepsilon_o RIT)^{1/2} \sinh(e\Psi_0 / 2kT)$$

(2.10) $$\sigma_o = eN_s \frac{([H^+]/K_1)exp^{-e\Psi_0/2kT} - (K_2/[H^+])exp^{e\Psi_0/2kT}}{([H^+]/K_1)exp^{-e\Psi_0/2kT} + (K_2/[H^+])exp^{e\Psi_0/2kT}}$$

(2.11, 2.12) where $K_1 = 10^{(-PZNC+0.5\Delta pK)}$, $K_2 = 10^{(-PZNC-0.5\Delta pK)}$

where:

Γ = metal uptake, µmol/m^2

Γ_{max}= maximum possible metal uptake, µmol/m^2

C = ion concentration

T = temperature, 293° K

R = ideal gas constant, J / mol

ΔG_{ads} = adsorbed Gibbs free energy

ΔG_{coul} = Coulombic Gibbs free energy

z = ionic charge

F = Faraday's constant 96485, coulombs/mol

Ψ_X = double layer potential

Z= compressibility factor,1

Ψ_0 = surface potential

I = ionic strength

r_w = radius of water ion

r_{ion} = radius of Rh ion

σ_o= Surface charge density

e = charge of electron, 4.35 × 10^{-19} coulombs

ε_0 = dielectric constant of metal

ε = dielectric constant of water

N_s= OH concentration (mol/nm)

k= Boltzmann constant

PZNC= point of net zero charge

$[H^+]$ = solution proton concentration

ΔpK = acidity constant

2.6.2 Quantifying Site Fraction

The relative fraction of atomically dispersed Rh species, X_{iso}, was estimated using equation 2.13, using the specific CO:Rh stoichiometries in each adsorption mode, and the extinction coefficients of CO species associated with $Rh(CO)_2$ (X_{iso}), Rh-CO (CO linearly bound to Rh nanoparticles), and Rh_2CO (CO bridge bound to Rh nanoparticles). The extinction coefficients, ε_i, used for the symmetric $Rh(CO)_2$, Rh-CO, and Rh_2CO, were 74, 26, and 85 ($x10^6$ m/mol), respectively. The CO:Rh ratios for the symmetric gem-dicarbonyl, linear, and bridge configurations were 2, 1, and 0.5, respectively. The fraction of exposed sites existing as atomically dispersed species was then quantified by integrating the relative intensity, *I*, of the respective CO stretch. The symmetric peak is measured to quantify the I_{iso} value because the asymmetric peak is influenced by geometric and electronic structure of $Rh(CO)_2$.

$$X_{\mathrm{iso}} = \frac{I_{\mathrm{iso}} / \left(\varepsilon_{\mathrm{iso}} \times \left(\frac{\mathrm{CO}}{\mathrm{Rh}} \right)_{\mathrm{iso}} \right)}{\sum_{i=1}^{3} \left[I_i / \left(\varepsilon_i \times \left(\frac{\mathrm{CO}}{\mathrm{Rh}} \right)_i \right) \right]} \quad (2.13)$$

2.7 References

(1) Armor, J. N. A History of Industrial Catalysis. *Catal. Today* **2011**, *163* (1), 3–9.

(2) Collins, N. R.; Twigg, M. V. Three-Way Catalyst Emissions Control Technologies for Spark-Ignition Engines — Recent Trends and Future Developments. *Top. Catal.* **2007**, *42.1-4*, 323–332.

(3) Shelef, M.; Graham, G. W. Why Rhodium in Automotive Three-Way Catalysts? *Catal. Rev.* **1994**, *36* (3), 433–457.

(4) Shelef, M.; McCabe, R. W. Twenty-Five Years after Introduction of Automotive Catalysts: What Next? *Catal. Today* **2000**, *62* (1), 35–50.

(5) Asokan, C.; Yang, Y.; Dang, A.; Getsoian, A. “Bean”; Christopher, P. Low-Temperature Ammonia Production during NO Reduction by CO Is Due to Atomically Dispersed Rhodium Active Sites. *ACS Catal.* **2020**, *10* (9), 5217–5222.

(6) Lou, Y.; Liu, J. CO Oxidation on Metal Oxide Supported Single Pt Atoms: The Role of the Support. *Ind. Eng. Chem. Res.* **2017**, *56* (24), 6916–6925.

(7) Haruta, M. Size- and Support-Dependency in the Catalysis of Gold. *Catal. Today* **1997**, *36* (1), 153–166.

(8) Andersson, M. P.; Abild-Pedersen, F.; Remediakis, I. N.; Bligaard, T.; Jones, G.; Engbæk, J.; Lytken, O.; Horch, S.; Nielsen, J. H.; Sehested, J.; et al. Structure Sensitivity of the Methanation Reaction: H2-Induced CO Dissociation on Nickel Surfaces. *J. Catal.* **2008**, *255* (1), 6–19.

(9) Nørskov, J. K.; Bligaard, T.; Hvolbæk, B.; Abild-Pedersen, F.; Chorkendorff, I.; Christensen, C. H. The Nature of the Active Site in Heterogeneous Metal Catalysis. *Chem. Soc. Rev.* **2008**, *37* (10), 2163–2171.

(10) Hammer, B. Special Sites at Noble and Late Transition Metal Catalysts. *Top. Catal.* **2006**, *37* (1), 3–16.

(11) Haruta, M. When Gold Is Not Noble: Catalysis by Nanoparticles. *Chem. Rec.* **2003**, *3* (2), 75–87.

(12) Liu, J. Catalysis by Supported Single Metal Atoms. *ACS Catal.* **2016**, *7* (1), 34–59.

(13) Yang, X.; Wang, A.; Qiao, B.; Li, J. U. N. Single-Atom Catalysts : A New Frontier in Heterogeneous Catalysis. *Acc. Chem. Res.* **2013**, *46* (8), 1740–1748.

(14) Qi, J.; Christopher, P. Atomically Dispersed Rh Active Sites on Oxide Supports with Controlled Acidity for Gas-Phase Halide-Free Methanol Carbonylation to Acetic Acid. *Ind. Eng. Chem. Res.* **2019**, *58* (28), 12632–12641.

(15) Ji, S.; Chen, Y.; Wang, X.; Zhang, Z.; Wang, D.; Li, Y. Chemical Synthesis of Single Atomic Site Catalysts. *Chem. Rev.* **2020**.

(16) Karelovic, A.; Ruiz, P. Mechanistic Study of Low Temperature CO_2 Methanation over Rh/TiO_2 Catalysts. *J. Catal.* **2013**, *301*, 141–153.

(17) Panagiotopoulou, P.; Kondarides, D. I.; Verykios, X. E. Selective Methanation of CO over Supported Noble Metal Catalysts: Effects of the Nature of the Metallic Phase on Catalytic Performance. *Appl. Catal. A Gen.* **2008**, *344* (1–2), 45–54.

(18) DeRita, L.; Dai, S.; Lopez-Zepeda, K.; Pham, N.; Graham, G. W.; Pan, X.; Christopher, P. Catalyst Architecture for Stable Single Atom Dispersion Enables Site-Specific Spectroscopic and Reactivity Measurements of CO Adsorbed to Pt Atoms, Oxidized Pt Clusters, and Metallic Pt Clusters on TiO2. *J. Am. Chem. Soc.* **2017**, *139* (40), 14150–14165.

(19) DeRita, L.; Resasco, J.; Dai, S.; Boubnov, A.; Thang, H. V.; Hoffman, A. S.; Ro, I.; Graham, G. W.; Bare, S. R.; Pacchioni, G.; et al. Structural Evolution of Atomically Dispersed Pt Catalysts Dictates Reactivity. *Nat. Mater.* **2019**, *18* (7), 746–751.

(20) Resasco, J.; DeRita, L.; Dai, S.; Chada, J. P.; Xu, M.; Yan, X.; Finzel, J.; Hanukovich, S.; Hoffman, A. S.; Graham, G. W. Uniformity Is Key in Defining Structure–Function Relationships for Atomically Dispersed Metal Catalysts: The Case of Pt/CeO2. *J. Am. Chem. Soc.* **2019**, *142* (1), 169–184.

(21) Jiao, L.; Regalbuto, J. R. The Synthesis of Highly Dispersed Noble and Base Metals on Silica via Strong Electrostatic Adsorption: II. Mesoporous Silica SBA-15. *J. Catal.* **2008**, *260* (2), 342–350.

(22) Schreier, M.; Regalbuto, J. R. A Fundamental Study of Pt Tetraammine Impregnation of Silica: 1. The Electrostatic Nature of Platinum Adsorption. *J. Catal.* **2004**, *225* (1), 190–202.

(23) Park, J.; Regalbuto, J. R. A Simple, Accurate Determination of Oxide PZC and the Strong Buffering Effect of Oxide Surfaces at Incipient Wetness. *Journal of colloid and interface science*. 1995, pp 239–252.

(24) Miller, J. T.; Schreier, M.; Kropf, J. A.; Regalbuto, J. R. A Fundamental Study of Platinum Tetraammine Impregnation of Silica: 2. The Effect of Method of Preparation, Loading, and Calcination Temperature on (Reduced) Particle Size. *J. Catal.* **2004**, *225* (1), 203–212.

(25) Regalbuto, J. R. A Scientific Method to Prepare Supported Metal Catalysts. In *Surface and nanomolecular catalysis*; CRC Press, 2006; pp 175-208.

(26) Regalbuto, J. R. A Simple, Rational Method to Prepare Nanodispersed Metal Catalysts Supported on Silica. In *Silica and Silicates in Modern Catalysis*; Transworld Research Network, 2010; Vol. 42, pp 345–374.

(27) Uheida, A.; Iglesias, M.; Fontàs, C.; Hidalgo, M.; Salvadó, V.; Zhang, Y.; Muhammed, M. Sorption of Palladium(II), Rhodium(III), and Platinum(IV) on Fe3O4 Nanoparticles. *J. Colloid Interface Sci.* **2006**, *301* (2), 402–408.

(28) Martens, J. H. A.; Prins, R. Influence of PH on the Preparation of Monometallic Rhodium and Platinum, and Bimetallic RhodiumPlatinum Catalysts Supported on γ-Alumina. *Appl. Catal.* **1989**, *46* (1), 31–44.

(29) Palmer, D. A.; Harris, G. M. Kinetics, Mechanism, and Stereochemistry of the Aquation and Chloride Anation Reactions of Fac- and Mer-Trichlorotriaquorhodium(III) Complexes in Acidic Aqueous Solution. A Complete Reaction Scheme for Complex Ions of the General Formula [RhCln(OH2)6-n] 3. *Inorg. Chem.* **1975**, *14* (6), 1316–1321.

(30) Ro, I.; Xu, M.; Graham, G. W.; Pan, X.; Christopher, P. Synthesis of Heteroatom Rh–ReO x Atomically Dispersed Species on Al2O3 and Their Tunable Catalytic

Reactivity in Ethylene Hydroformylation. *ACS Catal.* **2019**, *9* (12), 10899–10912.

(31) Keels, J. M.; Chen, X.; Karakalos, S.; Liang, C.; Monnier, J. R.; Regalbuto, J. R. Aqueous-Phase Hydrogenation of Succinic Acid Using Bimetallic Ir − Re/C Catalysts Prepared by Strong Electrostatic Adsorption. *ACS Catal.* **2018**, *8* (7), 6486–6494.

(32) Hao, X.; Barnes, S.; Regalbuto, J. R. Fundamental Study of Pt Impregnation of Carbon: Adsorption Equilibrium and Particle Synthesis. *J. Catal.* **2011**, *279* (1), 48–65.

(33) Feltes, T. E.; Espinosa-Alonso, L.; Smit, E. De; D'Souza, L.; Meyer, R. J.; Weckhuysen, B. M.; Regalbuto, J. R. Selective Adsorption of Manganese onto Cobalt for Optimized Mn/Co/TiO2 Fischer-Tropsch Catalysts. *J. Catal.* **2010**, *270* (1), 95–102.

(34) Zhu, X.; Cho, H.; Pasupong, M.; Regalbuto, J. R. 6.Charge-Enhanced Dry Impregnation A Simple Way to Improve the Preparation of Supported Metal Catalysts.Pdf. **2013**, 1–6.

(35) Onn, T. M.; Zhang, S.; Arroyo-Ramirez, L.; Xia, Y.; Wang, C.; Pan, X.; Graham, G. W.; Gorte, R. J. High-Surface-Area Ceria Prepared by ALD on Al2O3 Support. *Appl. Catal. B Environ.* **2017**, *201*, 430–437.

(36) Resasco, J.; Dai, S.; Graham, G.; Pan, X.; Christopher, P. Combining In-Situ Transmission Electron Microscopy and Infrared Spectroscopy for Understanding Dynamic and Atomic-Scale Features of Supported Metal Catalysts. *J. Phys. Chem. C* **2018**, *122* (44), 25143–25157.

(37) Badwal, S. P. S.; Fini, D.; Ciacchi, F. T.; Munnings, C.; Kimpton, J. A.; Drennan, J. Structural and Microstructural Stability of Ceria – Gadolinia Electrolyte Exposed to Reducing Environments of High Temperature Fuel Cells. *J. Mater. Chem. A* **2013**, *1* (36), 10768.

(38) Ryczkowski, J. IR Spectroscopy in Catalysis. *Catal. Today* **2001**, *68*, 263–381.

(39) Asokan, C.; Derita, L.; Christopher, P. Using Probe Molecule FTIR Spectroscopy to Identify and Characterize Pt - Group Metal Based Single Atom Catalysts. *Chinese J. Catal.* **2017**, *38* (9), 1473–1480.

(40) Lamberti, C.; Zecchina, A.; Groppo, E.; Bordiga, S. Probing the Surfaces of Heterogeneous Catalysts by in Situ IR Spectroscopy. *Chem. Soc. Rev.* **2010**, *39* (12), 4951.

(41) Chakarova, K.; Mihaylov, M.; Hadjiivanov, K. FTIR Spectroscopic Study of CO Adsorption on Pt – H – ZSM-5. *Microporous Mesoporous Mater.* **2005**, *81* (1–3), 305–312.

(42) Stakheev, A. Y.; Shpiro, E. S.; Tkachenko, O. P.; Jaeger, N. I.; Schulz-Ekloff, G. Evidence for Monatomic Platinum Species in H-ZSM-5 from FTIR Spectroscopy of

Chemisorbed CO. *J. Catal.* **1997**, *169* (1), 382–388.

(43) Khivantsev, K.; Vityuk, A.; Aleksandrov, H. A.; Vayssilov, G. N. Synthesis , Modelling , and Catalytic Properties of HY Zeolite- Supported Rhodium Dinitrosyl Complexes. *ACS Catal.* **2017**, *7* (9), 5965–5982.

(44) Hoffman, A. S.; Fang, C. Y.; Gates, B. C. Homogeneity of Surface Sites in Supported Single-Site Metal Catalysts: Assessment with Band Widths of Metal Carbonyl Infrared Spectra. *J. Phys. Chem. Lett.* **2016**, *7* (19), 3854–3860.

(45) Zhang, B.; Asakura, H.; Yan, N. Atomically Dispersed Rhodium on Self-Assembled Phosphotungstic Acid : Structural Features and Catalytic CO Oxidation Properties. *Ind. Eng. Chem. Res.* **2017**, *56* (13), 3578–3587.

(46) Peterson, E. J.; DeLaRiva, A. T.; Lin, S.; Johnson, R. S.; Guo, H.; Miller, J. T.; Hun Kwak, J.; Peden, C. H. F.; Kiefer, B.; Allard, L. F.; et al. Low-Temperature Carbon Monoxide Oxidation Catalysed by Regenerable Atomically Dispersed Palladium on Alumina. *Nat. Commun.* **2014**, *5*, 4885.

(47) Guzman, J.; Gates, B. C. Supported Molecular Catalysts : Metal Complexes and Clusters on Oxides and Zeolites. *Dalt. Trans.* **2003**, *17*, 3303–3318.

(48) Hyde, E. A.; Robert, R.; Rochester, C. H. Infrared Study of the Interactions between NO and CO on Rh / Al2O3 Catalysts. *J. Chem. Soc. Faraday Trans. 1 Phys. Chem. Condens. Phases* **1984**, *80* (3), 531–541.

(49) Granger, P.; Delannoy, L.; Lecomte, J. J.; Dathy, C.; Praliaud, H.; Leclercq, L.; Leclercq, G. Kinetics of the CO + NO Reaction over Bimetallic Platinum-Rhodium on Alumina: Effect of Ceria Incorporation into Noble Metals. *J. Catal.* **2002**, *207* (2), 202–212.

(50) Matsubu, J. C.; Yang, V. N.; Christopher, P. Isolated Metal Active Site Concentration and Stability Control Catalytic CO2 Reduction Selectivity. *J. Am. Chem. Soc.* **2015**, *137* (8), 3076–3084.

(51) Goldsmith, B. R.; Sanderson, E. D.; Ouyang, R.; Li, W. X. CO- and NO-Induced Disintegration and Redispersion of Three-Way Catalysts Rhodium, Palladium, and Platinum: An Ab Initio Thermodynamics Study. *J. Phys. Chem. C* **2014**, *118* (18), 9588–9597.

(52) Uzun, A.; Gates, B. C. Real-time Characterization of Formation and Breakup of Iridium Clusters in Highly Dealuminated Zeolite Y. *Angew. Chemie* **2008**, *47* (48), 9245–9248.

(53) Uzun, A.; Gates, B. C. Dynamic Structural Changes in a Molecular Zeolite-Supported Iridium Catalyst for Ethene Hydrogenation. *J. Am. Chem. Soc.* **2009**, *131* (43), 15887–15894.

(54) Tang, Y.; Asokan, C.; Xu, M.; Graham, G. W.; Pan, X.; Christopher, P.; Li, J.; Sautet,

P. Rh Single Atoms on TiO2 Dynamically Respond to Reaction Conditions by Adapting Their Site. *Nat. Commun.* **2019**, *10* (1), 4488.

(55) Qiao, B.; Wang, A.; Yang, X.; Allard, L. F.; Jiang, Z.; Cui, Y.; Liu, J.; Li, J.; Zhang, T. Single-Atom Catalysis of CO Oxidation Using Pt1/FeOx. *Nat. Chem.* **2011**, *3* (8), 634–641.

(56) Hadjiivanov, K. Identification and Characterization of Surface Hydroxyl Groups by Infrared Spectroscopy. In *Advances in Catalysis*; Academic Press, 2014; Vol. 57, pp 99–318.

(57) Chizallet, C.; Digne, M.; Arrouvel, C.; Raybaud, P.; Delbecq, F.; Costentin, G.; Che, M.; Sautet, P.; Toulhoat, H. Insights into the Geometry, Stability and Vibrational Properties of OH Groups on γ-Al2O3, TiO2 -Anatase and MgO from DFT Calculations. Topics in Catalysis. *Top. Catal.* **2009**, 1005–1016.

(58) Asokan, C.; Thang, H. V.; Pacchioni, G.; Christopher, P. Reductant Composition Influences the Coordination of Atomically Dispersed Rh on Anatase TiO2. *Catal. Sci. Technol.* **2020**, *10* (6), 1597–1601.

(59) Hao, X.; Quach, L.; Korah, J.; Spieker, W. a.; Regalbuto, J. R. The Control of Platinum Impregnation by PZC Alteration of Oxides and Carbon. *J. Mol. Catal. A Chem.* **2004**, *219* (1), 97–107.

(60) Trueba, M.; Trasatti, S. P. γ-Alumina as a Support for Catalysts: A Review of Fundamental Aspects. *Eur. J. Inorg. Chem.* **2005**, *2005* (17), 3393–3403.

(61) Gerber, W. J.; Koch, K. R.; Rohwer, H. E.; Hosten, E. C.; Geswindt, T. E. Talanta Including Stereoisomers , by Means of Ion-Pair HPLC – ICP-MS. **2010**, *82*, 348–358.

(62) Colombo, C.; Oates, C. J.; Monhemius, A. J.; Plant, J. A. Complexation of Platinum, Palladium and Rhodium with Inorganic Ligands in the Environment. *Geochemistry Explor. Environ. Anal.* **2008**, *8* (1), 91–101.

(63) Benguerel, E.; Demopoulos, G. P.; Harris, G. B. Speciation and Separation of Rhodium (III) from Chloride Solutions : A Critical Review. **1996**, *40* (94), 135–152.

(64) Wolsey, B. W. C.; Reynolds, C. A. Complexes in the Rhodium (III) -Chloride System in Acid Solution. **1963**, *2* (3), 1–2.

(65) Endo, K.; Saikawa, M.; Sugimoto, M.; Hada, M.; Nakatsuji, H. Theoretical Study of the Transition Energies of the Visible Absorption Spectra of [RhCl6] 3− and [RhCl5 (H2O)] 2− Complexes in Aqueous Solution. *Bull. Chem. Soc. Jpn.* **1995**, *68*, 1601–1605.

(66) Vasilchenko, D. B.; Berdyugin, S. N.; Korenev, S. V; Kennedy, S. O.; Gerber, W. J. Spectroscopic and DFT Study of Rh III Chloro Complex Transformation in Alkaline Solutions. **2017**.

(67) Samuels, A. C.; Boele, C. A.; Bennett, K. T.; Clark, S. B.; Wall, N. A.; Clark, A. E.

Integrated Computational and Experimental Protocol for Understanding Rh (III) Speciation in Hydrochloric and Nitric Acid Solutions. **2014**, No. Iii.

(68) Le, M. N.; Lee, M. S.; Senanayake, G. A Short Review of the Separation of Iridium and Rhodium from Hydrochloric Acid Solutions by Solvent Extraction. *J. Solution Chem.* **2018**, *47* (8), 1373–1394.

(69) Colombo, C.; Oates, C. J.; Monhemius, A. J.; Plant, J. A. Complexation of Platinum , Palladium and Rhodium with Inorganic Ligands in the Environment. **2015**, *1998* (1999).

(70) Nadolinny, V.; Belyaev, A.; Komarovskikh, A.; Yushina, I.; Tkachev, S. The Photochemical Generation of Superoxide Rh (III) Complexes. **2018**, *2*, 15231–15236.

(71) Mahlamvana, F.; Kriek, R. J. Applied Catalysis B : Environmental Dioxide Suspension : The Role of Structurally Different Sacrificial Reducing Agents. *"Applied Catal. B, Environ.* **2015**, *162*, 445–453.

(72) Mcskimming, A.; Colbran, S. B. Hydride Ion-Carrier Ability in Rh (I) Complexes of a Nicotinamide- Functionalised N-Heterocyclic Carbene Ligand Hydride Ion-Carrier Ability in Rh (I) Complexes of a Nicotinamide-Functionalised N -Heterocyclic Carbene Ligand †. **2010**, No. April 2017.

(73) Ho, C. S.; Lam, C. W. K.; Chan, M. H. M.; Cheung, R. C. K.; Law, L. K.; Lit, L. C. W.; Ng, K. F.; Suen, M. W. M.; Tai, H. L. Electrospray Ionisation Mass Spectrometry: Principles and Clinical Applications. *Clin. Biochem. Rev.* **2003**, *24* (1), 3.

(74) Sánchez, J. M.; Hidalgo, M.; Havel, J.; Salvadó, V. The Speciation of Rhodium (III) in Hydrochloric Acid Media by Capillary Zone Electrophoresis. *Talanta* **2002**, *56*, 1061–1071.

(75) DeRita, L.; Dai, S.; Lopez-Zepeda, K.; Pham, N.; Graham, G. W.; Pan, X.; Christopher, P. Catalyst Architecture for Stable Single Atom Dispersion Enables Site-Specific Spectroscopic and Reactivity Measurements of CO Adsorbed to Pt Atoms, Oxidized Pt Clusters, and Metallic Pt Clusters on TiO2. *J. Am. Chem. Soc.* **2017**, *139* (40), 14150–14165.

(76) Garland, C. W.; Yang, A. Infrared Studies of Carbon Monoxide Chemisorbed on Rhodium. *J. Phys. Chem.* **1957**, *61* (11), 1504–1512.

(77) Yates, J. T.; Duncan, T. M.; Worley, S. D.; Vaughan, R. W. Infrared Spectra of Chemisorbed CO on Rh. *J. Chem. Phys.* **1979**, *70* (3), 1219.

(78) Duncan, T. M.; Vaughan, R. W. A 13C NMR Study of the Adsorbed States of CO on Rh Dispersed on Al2O3. *J. Chem. Phys.* **1980**, *73* (2), 975–985.

(79) Rice, C. A.; Worley, S. D.; Curtis, C. W.; Guin, J. A.; Tarrer, A. R. The Oxidation State of Dispersed Rh on AI2O3. *J. Chem. Phys.* **1981**, *74* (11), 6487–6497.

(80) Cavanagh, R. R. Site Distribution Studies of Rh Supported on Al2O3—An Infrared Study of Chemisorbed CO. *J. Chem. Phys.* **1981**, *74* (7), 4150.

(81) Yates, J. T.; Kolasinski, K. Infrared Spectroscopic Investigation of the Rhodium Gem-Dicarbonyl Surface Species. *J. Chem. Phys.* **1983**, *79* (2), 1026.

(82) Solymosi, F.; Pasztor, M. An Infrared Study of the Influence of Carbon Monoxide Chemisorption on the Topology of Supported Rhodium. *J. Phys. Chem.* **1985**, *89* (22), 4789–4793.

(83) Trautmann, S.; Baerns, M. Infrared Spectroscopic Studies of CO Adsorption on Rhodium Supported by SiO2, Al2O3, and TiO2. *J. Catal.* **1994**, *150* (2), 335–344.

(84) Goellner, J. F.; Gates, B. C.; Vayssilov, G. N.; Rösch, N. Structure and Bonding of a Site-Isolated Transition Metal Complex: Rhodium Dicarbonyl in Highly Dealuminated Zeolite Y. *J. Am. Chem. Soc.* **2000**, *122* (33), 8056–8066.

(85) Serna, P.; Gates, B. C. Zeolite-Supported Rhodium Complexes and Clusters: Switching Catalytic Selectivity by Controlling Structures of Essentially Molecular Species. *J. Am. Chem. Soc.* **2011**, *133* (13), 4714–4717.

(86) Mcclure, S. M.; Lundwall, M. J.; Goodman, D. W. Planar Oxide Supported Rhodium Nanoparticles as Model Catalysts. *Proc. Natl. Acad. Sci.* **2011**, *108* (3), 931–936.

(87) Yates, J. T.; Duncan, T. M.; Worley, S. D.; Vaughan, R. W. Infrared Spectra of Chemisorbed CO on Rh. *J. Chem. Phys.* **1979**, *70* (3), 1219.

(88) Novak, E.; Sprinceana, D.; Solymosi, F. A : CO-Induced Structural Changes of Supported Rh Promoted by NO. *Appl. Cataylysis A.* **1997**, *149*, 89–101.

(89) Finocchio, E.; Busca, G.; Forzatti, P.; Groppi, G.; Beretta, A. State of Supported Rhodium Nanoparticles for Methane Catalytic Partial Oxidation (CPO); FT-IR Studies. *Langmuir* **2007**, *23* (20), 10419–10428.

(90) Kistler, J. D.; Chotigkrai, N.; Xu, P.; Enderle, B.; Praserthdam, P.; Chen, C.; Browning, N. D.; Gates, B. C. A Single-Site Platinum CO Oxidation Catalyst in Zeolite KLTL : Microscopic and Spectroscopic Determination of the Locations of the Platinum Atoms. *Angew. Chemie* **2014**, *53* (34), 8904–8907.

(91) Asokan, C.; Thang, H. V.; Pacchioni, G.; Christopher, P. Reductant Composition Influences the Coordination of Atomically Dispersed Rh on Anatase TiO 2. *Catal. Sci. Technol.* **2020**, *Published*.

(92) Resasco, J.; Yang, F.; Mou, T.; Wang, B.; Christopher, P.; Resasco, D. E. Relationship between Atomic Scale Structure and Reactivity of Pt Catalysts: Hydrodeoxygenation of m-Cresol over Isolated Pt Cations and Clusters. *ACS Catal.* **2019**, *10* (1), 595–603.

(93) Ezekoye, O. K.; Drews, A. R.; Jen, H.-W.; Kudla, R. J.; McCabe, R. W.; Sharma, M.; Howe, J. Y.; Allard, L. F.; Graham, G. W.; Pan, X. Q. Characterization of Alumina-Supported Pt and Pt–Pd NO Oxidation Catalysts with Advanced Electron Microscopy.

J. Catal. **2011**, *280* (1), 125–136.

(94) Pennycook, S. J. Z-Contrast STEM for Materials Science. *Ultramicroscopy* **1989**, *30* (1–2), 58–69.

(95) Pennycook, S. J. Z-Contrast Transmission Electron Microscopy: Direct Atomic Imaging of Materials. *Annu. Rev. Mater. Sci.* **1992**, *22* (1), 171–195.

(96) Pennycook, S. J.; Nellist, P. D. Z-Contrast Scanning Transmission Electron Microscopy. In *Impact of electron and scanning probe microscopy on materials research*; Springer, 1999; pp 161–207.

(97) Tieu, P.; Yan, X.; Xu, M.; Christopher, P.; Pan, X. Directly Probing the Local Coordination, Charge State, and Stability of Single Atom Catalysts by Advanced Electron Microscopy: A Review. *Small* **2021**, 2006482.

(98) Regalbuto, J. R.; Navada, A.; Shadid, S.; Bricker, M. L.; Chen, Q. An Experimental Verification of the Physical Nature of Pt Adsorption onto Alumina. *J. Catal.* **1999**, *184* (2), 335–348.

(99) Svecova, L.; Papaïconomou, N.; Billard, I. Rh (III) Aqueous Speciation with Chloride as a Driver for Its Extraction by Phosphonium Based Ionic Liquids. **2019**, No. Iii.

(100) Volchek, V. V; Sheven, D. G.; Berdyugin, S. N.; Shuvaeva, O. V; Vasilchenko, D. B.; Korenev, S. V. Rh(III) Hydroxocomplexes Speciation Using HPLC- ESI-MS. **2020**, 2631–2637.

(101) Cavanagh, R. R., Yates Jr., J. T. Site Distribution Studies of Rh Supported on Al2O3—An Infrared Study of Chemisorbed CO. *J. Chem. Phys.* **1981**, *74* (7), 4150.

(102) Duncan, T. M.; Yates Jr, J. T.; Vaughan, R. W. A 13C NMR Study of the Adsorbed States of CO on Rh Dispersed on Al2O3. *J. Chem. Phys.* **1980**, *73* (2), 975–985.

(103) Panayotov, P. B.; Yates, J. T. Rhodium-Carbon Monoxide Surface Chemistry: The Involvement of Surface Hydroxyl Groups on A12O3and SiO2Supports. *J. Am. Chem. Soc.* **1988**, *110* (7), 2074–2081.

(104) Babucci, M.; Hoffman, A. S.; Debefve, L. M.; Kurtoglu, S. F.; Bare, S. R.; Gates, B. C.; Uzun, A. Unraveling the Individual Influences of Supports and Ionic Liquid Coatings on the Catalytic Properties of Supported Iridium Complexes and Iridium Clusters. *J. Catal.* **2020**, *387*, 186–195.

(105) Miessner, H.; Burkhardt, I.; Gutschick, D.; Zecchina, A.; Morterra, C.; Spoto, G. The Formation of a Well Defined Rhodium Dicarbonyl in Highly Dealuminated Rhodium-Exchanged Zeolite Y by Interaction with CO. *J. Chern. Soc* **1989**, *85* (8), 2113–2126.

Chapter 3:

Reductant Composition Influences the Coordination of Atomically Dispersed Rh on Anatase TiO_2

Adapted from *Catalysis Science & Technology* article:
Asokan, C., Thang, H. V., Pacchioni, G., & Christopher, P. "Reductant Composition Influences the Coordination of Atomically Dispersed Rh on Anatase TiO_2," *Catalysis Science & Technology*, 10(6), 1597-1601 (2020).

3.1 Introduction

Catalysts consisting of atomically dispersed metals on oxide supports could promote the sustainable usage of rare earth metals and enable alternative reaction pathways with distinct catalytic performance. Oxide support surfaces present heterogeneous local coordination environments for atomically dispersed metals, making site-reactivity assignment challenging. Here, we identify how reductant composition (H_2 or CO) influences the local coordination of atomically dispersed Rh on anatase TiO_2. Temperature programmed desorption (TPD) of CO via in-situ Fourier Transformed Infrared (FTIR) spectroscopy was combined with density functional theory (DFT) calculations to identify the influence of H_2 reduction generated hydroxyl species on the desorption of CO from atomically dispersed Rh. When atomically dispersed $Rh(CO)_2$ species are proximal to hydroxyls the 2 COs desorb sequentially during a TPD, whereas $Rh(CO)_2$ species spatially separated from hydroxyls exhibit simultaneous CO desorption. This work highlights the combined use of CO FTIR-TPD and DFT to distinguish atomically dispersed metal atoms with different local coordination environments on oxide supports.

3.2 Experimental Methods

3.2.1 Catalyst Synthesis

Atomically dispersed Rh on anatase TiO_2 was synthesized by utilizing strong electrostatic adsorption (SEA) principles a Rh weight loading of 0.1 wt%. High surface area anatase TiO_2 support (US Nano # US3838, 5 nm diameter, 99.9% purity) and the Rh precursor (Sigma Aldrich # 206261, Rh(III) chloride hydrate) were diluted in water separately with total liquid volumes of the two solutions at a 4:1 ratio, which gives a support surface loading of 2900 m^2/L based on a measured TiO_2 surface area of 290 m^2/g. NH_4OH was added to the separate

support and precursor solutions to target a pH of 9. The precursor solution was injected at a rate of 4 ml/min into the support solution while constantly stirring at a high rate of 350 rpm. Then, the solution was heated to 70 °C until water evaporated, and the sample was dried completely. The sample was kept overnight in a 100 °C oven and then ex-situ calcined in 10% O_2 /He for 4 hours at 350 °C.

3.2.2 Probe CO FTIR

The catalyst was loaded in a Harrick Low Temperature Reaction chamber mounted inside a ThermoScientific Praying Mantis diffuse reflectance adapter set in a Nicolet iS10 FTIR spectrometer with a Mercury Cadmium Telluride (MCT) detector and mass flow controllers (Teledyne Hastings) were used to control the gas flow rates across the reactor bed. Catalysts were in-situ pretreated for 30 minutes at 350 °C in pure O_2 and then subsequently in 10% H_2/Ar at 100 °C or in 10% CO/Ar at 300 °C for 1 hr. CO probe molecule IR was executed by decreasing the temperature following pretreatment in Ar to room temperature, exposing the sample to 10% CO in Ar for 10 minutes, purging in Ar for 10 minutes, and then collecting spectra with 12 scans and 0.482 cm−1 data spacing. Temperature programmed desorption (TPD) measurements were executed by heating in Ar at a rate of 20 °C /min until complete desorption of CO was observed and taking spectra every 20 °C during desorption. The rate of loss of CO band intensity (corresponding to CO desorption) were calculated using the change in peak areas of deconvoluted (integrated and fit using Origin®) over 40 °C. Probe molecule CO and TPD experiments were also done for samples in-situ pretreated for 30 minutes at 350 C° in pure O2 and then subsequently in 10% H2/Ar at 200 °C and 300 °C for 1 hr.

3.2.3 TPD and Redhead Analysis

OriginPro was used to deconvolute overlapping peaks using Lorentzian functions and defining 2 parameters, the peak position and FWHM. In the case where Rh/TiO_2 was reduced at 100 °C in H_2, the deconvolution of the band at 2031 was kept at constant frequency and FWHM. To calculate the rate of change of the bands assigned to Rh(CO) monocarbonyls, 2012 and 1999 cm^{-1} , the area of asymmetric stretch of the $Rh(CO)_2$ species, 2031 cm^{-1} was subtracted from the total normalized integrated area of the 3 peaks. The rate of loss of CO stretch band intensity was calculated by using central finite difference method (equation 3.1) over 40 °C intervals and was assigned to the desorption of CO from Rh.

(3.1)
$$\left(\frac{d(\frac{A}{A_o})}{dT}\right)_x = \frac{\frac{A_{x+1}}{A_o} - \frac{A_{x-1}}{A_o}}{T_{x+1} - T_{x-1}}$$

Where:
A= Peak area at temperature T
A_o= Maximum peak area
T= Temperature
x= Point of measurement (at specific T)
$\left(\frac{d(\frac{A}{A_o})}{dT}\right)_x$ = Change in area over change in temperature

T_{x+1}= Temperature at x+1

T_{x+1}= Temperature at x-1

A_{x+1}= Area of peak at temperature T_{x+1}

A_{x-1}= Area of peak at temperature T_{x-1}

To estimate CO binding energy to Rh from experimental data, Redhead analysis[1] was used according to equation 3.2.

Where:

(3.2) $$\frac{E}{RT_p} = ln\left(\frac{\nu T_p}{\beta}\right) - 3.46$$

β = Rate of Temperature, 20 °K/min

E= Energy, kJ/mol

Tp= Temperature at peak desorption rate, K

R= 8.3124 kJ/ K kmol

ν = rate constant, $10^{13.6}$ /sec

3.3 Results and Discussion

Identifying "the" active site on oxide supported metal heterogeneous catalysts is challenging because metal clusters present a range of sites with various local coordination environments including metal terraces, steps and metal-support interfaces[2]. Elucidation of active site structures is further complicated by reconstruction, or coverage effects.[2,3] It has been proposed that single late-transition metals atoms (or ions) on oxide supports, sometimes called atomically dispersed metal or single atom catalysts, enable precise structure-function relationships. However, understanding the catalytic properties of atomically dispersed metals is convoluted by the inherent heterogeneity of the support, where the metal can adsorb at cation vacancies, anion vacancies, on stoichiometric surfaces, on oxidized surfaces and near hydroxyls with distinct characteristics.[4,5] Further, the preferred adsorption geometry may vary as a function of metal loading or environmental conditions.[6–8] Thus, developing structure function relationships for this class of catalysts requires knowledge of the atomic

scale coordination of the metal to the oxide support, the uniformity of this environment, and the response to environmental conditions.

Pre-treatment of atomically dispersed metal catalysts produced via impregnation of metal salts typically starts with high temperature oxidation to remove ligands remaining from synthesis. For reducible oxide supports, this results in atomically dispersed metals localizing at cation vacancies at the oxide surface.[9–11] Catalysts are often then reduced to decrease the oxygen coordination number to the atomically dispersed metal and enable interaction with reactants or adsorbing molecules. If the reducing agent is CO, oxygen is removed as CO_2, after which CO can bond to the atomically dispersed metal site.[12–14] CO is known to impart mobility to atomically dispersed metal species, allowing species to adopt different coordination sites on the support.[15,16] Alternatively, when materials are reduced in hydrogen, oxygen is removed via the formation of water and new hydroxyl groups form, which can modify atomically dispersed metal site characteristics.[17–19]

Here we elucidate how the local environment of atomically dispersed Rh species on anatase TiO_2 is influenced by varying reductive pretreatments. We demonstrate the distinct local environments for Rh species resulted from reduction treatments under CO and H_2. We attributed this to varying proximal hydroxyl characteristics, which modifies CO adsorption and desorption processes on Rh. Our finding highlights how subtle changes in local environment can modify the properties of atomically dispersed metals. These studies also highlight how characterizing atomically dispersed metal catalysts by temperature programmed desorption (TPD) of CO using probe molecule Fourier Transformed Infrared (FTIR) spectroscopy, combined with density functional theory (DFT) calculations, is a powerful approach to elucidate metal coordination environments.

To synthesize atomically dispersed Rh on TiO_2, we applied principles of strong electrostatic adsorption (SEA) to high surface area (290 m^2/g) 5 nm diameter anatase TiO_2 nanoparticles with low Rh weight loadings (0.1%).[7] The catalyst was ex-situ and in-situ pre-treated at 350 °C in O_2, which rendered Rh species unable to adsorb CO following room temperature exposure, see Figure 3.1, suggesting Rh species resided in cation (Ti) vacancies in the lattice.[10] The influence of reductive treatments on Rh local coordination was investigated using CO probe molecule FTIR and TPD following pretreatment of the sample in H_2 at 100-300 °C or in CO at 300 °C.

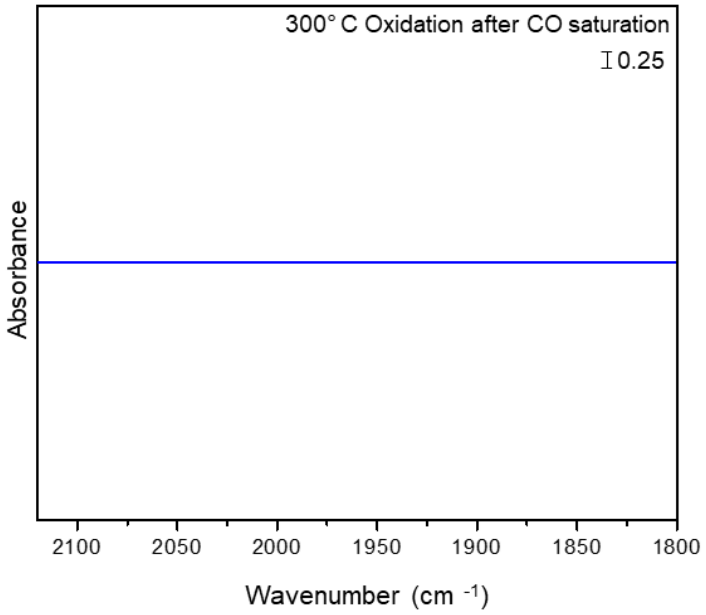

Figure 3.1: FTIR spectrum of Rh/TiO_2 following in-situ oxidation at 350 °C in O_2, exposure to CO at room temperature, and flushing in Ar. This shows that there is no measurable CO adsorption following oxidation pre-treatment.

When the material was pretreated in CO at 300 °C or in H_2 at 100 °C, and then exposed to 10% CO in Argon at room temperature, bands at ~2092-2094 and ~2029-2031 cm^{-1} were observed in FTIR measurements (see Figure 3.2 and Table 3.1). These bands are assigned to the symmetric and asymmetric stretches of CO ligands in oxide supported Rh

gem-dicarbonyl species, $Rh(CO)_2$, which is unique to atomically dispersed Rh.[20] Extensive DFT+U calculations of Rh in various coordination environments on anatase TiO_2 (Figure 3.8-11A, Table 3.2 and Table 3.3) support this assignment: a model of $Rh(CO)_2$ consisting of a Rh atom adsorbed on anatase [101] and interacting with two lattice O_{2c} atoms (Figure 3.12A) result in computed (scaled) frequencies at 2097 and 2026 cm^{-1} for the complex formed on the terrace sites, and of 2095 and 2031 cm^{-1} for $Rh(CO)_2$ formed at anatase [145] step sites (Table 3.3). The lack of CO bands in the experimental FTIR spectra at frequencies characteristic of linear (~2080-2040 cm^{-1}) and bridge (~1950-1850 cm^{-1}) bound CO on Rh clusters confirms that Rh primarily existed as atomically dispersed species following CO exposure.[21] The similar intensity of the symmetric and asymmetric stretches suggest that pre-treatment or CO exposure at room temperature forced Rh to move from a cation replaced coordination to a supported coordination environment that is capable of coordinating 2 CO ligands.[10]

The CO stretching frequencies and full width at half maxima (FWHM) of the $Rh(CO)_2$ bands were similar for both pretreatments (~10-15 cm^{-1}), see Table 3.1. The observed CO stretch FWHM, which characterizes the homogeneity of the local coordination environment of $Rh(CO)_2$ species, are smaller than typically observed for $Ir(CO)_2$ and $Rh(CO)_2$ species on oxide supports (>15 cm^{-1}), but broader than observed for zeolite supports (< 10 cm^{-1}).[8,22,23] The narrowness of the CO stretches in comparison to previous observations on oxide supports and the similarities between the two pretreatments suggest that the $Rh(CO)_2$ species sit in a relatively homogeneous local coordination environment on the support and that this local environment is similar following CO and H_2 reductive treatments.

While the $Rh(CO)_2$ IR spectra for the CO and H_2 pre-treated sample appear indistinguishable at near room temperature, significant differences were observed during

TPD experiments. For the CO pretreated sample, the maximum rate of CO desorption occurred at 240 °C, with the simultaneous loss of the symmetric and asymmetric stretching features, see Figure 3.2a and 3.3. The simultaneous loss of both bands without the formation of any others suggests both CO molecules have similar binding energy to Rh. This is consistent with the DFT calculations: the two CO molecules have binding energies of 2.03 eV and 2.05 eV for the terrace $Rh(CO)_2$ complex, and of 1.96 eV and 2.0 eV for the step $Rh(CO)_2$ complex, Table 3.2 (the computed values are about 0.5 eV larger than the measured E_{ads} from TPD spectra, Table 3.4). Further, the relatively narrow temperature window of desorption, in comparison to CO desorption from metal clusters, supports the uniformity in local coordination environment of the Rh species, an aspect which is corroborated by the similar properties computed at DFT level for $Rh(CO)_2$ species formed on terrace or step sites.[4,6]

When the sample was pre-treated in H_2 at 100 °C, additional CO stretching features at 2012 and 1999 cm^{-1} formed at ~120 °C during the TPD. This observation indicates that the $Rh(CO)_2$ coordination environments are distinct following CO and H_2 pretreatments. Importantly, this would not have been concluded by only looking at the static IR spectra at room temperature, which is a common approach used in literature.[23–28]

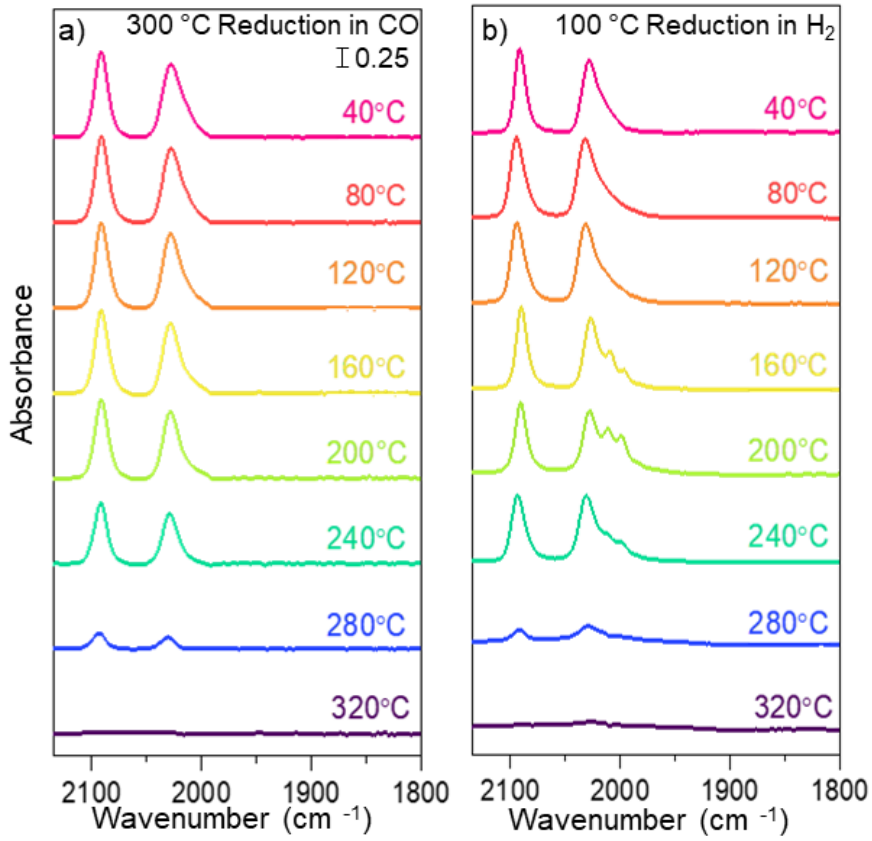

Figure 3.2: FTIR spectra following CO saturation and during a TPD of CO from $Rh(CO)_2$ supported on anatase TiO_2 following varied pretreatment conditions: a) reduction in CO at 300 °C, b) reduction in H_2 at 100 °C.

To understand the origin of the features at 2012 and 1999 cm^{-1}, spectra collected during the CO TPD following 100 °C pre-treatment in H_2 were deconvoluted into 4 distinct bands, (see Figure 3a and Table 3.1). The rate of change of peak areas, and thus change in surface adsorbate concentration, was analyzed as a function of temperature, see Figure 4b. This analysis identifies that the maximum rate of formation of the bands at 2012 and 1999 cm^{-1} occurs simultaneously with a maximum in the rate of loss of $Rh(CO)_2$ species at 160 °C. See the SI for discussion on peak deconvolution and integration during the TPD. This provides evidence that for some $Rh(CO)_2$ species on the sample reduced at 100 °C in H_2, an

intermediate species is formed during CO desorption, rather than both CO molecules desorbing simultaneously.

Table 3.1 Experimentally observed CO stretching frequencies ω (cm^{-1}), corresponding full width at half max, and adsorption energy E_{ads} (eV) calculated using Redhead Analysis.[1,29,30]

*** First desorption event associated with loss of intensity in $Rh(CO)_2$**

**** Second desorption event associated with loss of intensity in $Rh(CO)_2$**

***** Desorption event associated with loss of intensity of species formed during TPD**

	ω_1 (cm^{-1})	ω_2 (cm^{-1})	$FWHM_1$	$FWHM_2$	~E_{ads} (eV)
300 °C CO reduced					
$Rh(CO)_2$	2092	2029	11.5	15.2	1.5
100 °C H_2 reduced					
***$Rh(CO)_2$**	2094	2031	13.2	13.8	1.3
****$Rh(CO)_2$**	2094	2031	13.2	13.8	1.5
*****Rh(CO)**	2012, 1999		12.9, 8.00		1.7

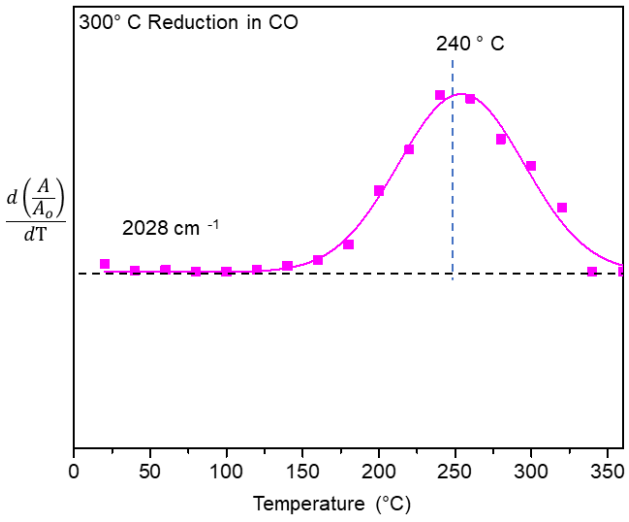

Figure 3.3: The rate of change of the asymmetric stretch band (2028 cm^{-1}) intensity as a function of temperature during CO TPD following 300 °C reduction in CO. The temperature where the maximum rate of loss (CO desorption) is highlighted.

The remaining intensity of the $Rh(CO)_2$ bands showed a second maxima in the rate of loss at 240 °C, similar to what was observed for the $Rh(CO)_2$ species following 300 °C CO pre-treatment. This suggests that some fraction of the $Rh(CO)_2$ species formed following the two pre-treatments were equivalent local coordination, while an additional species was formed following H_2 reduction. The maximum rate of loss of the peaks at 2012 and 1999 cm^{-1} was observed at ~280° C, as shown in Figure 4b. Thus, the intermediate species formed during the TPD for the material reduced at 100 °C in H_2 exhibits a stronger CO binding energy as compared to the $Rh(CO)_2$ species that was common to both pre-treatments.[31,32]

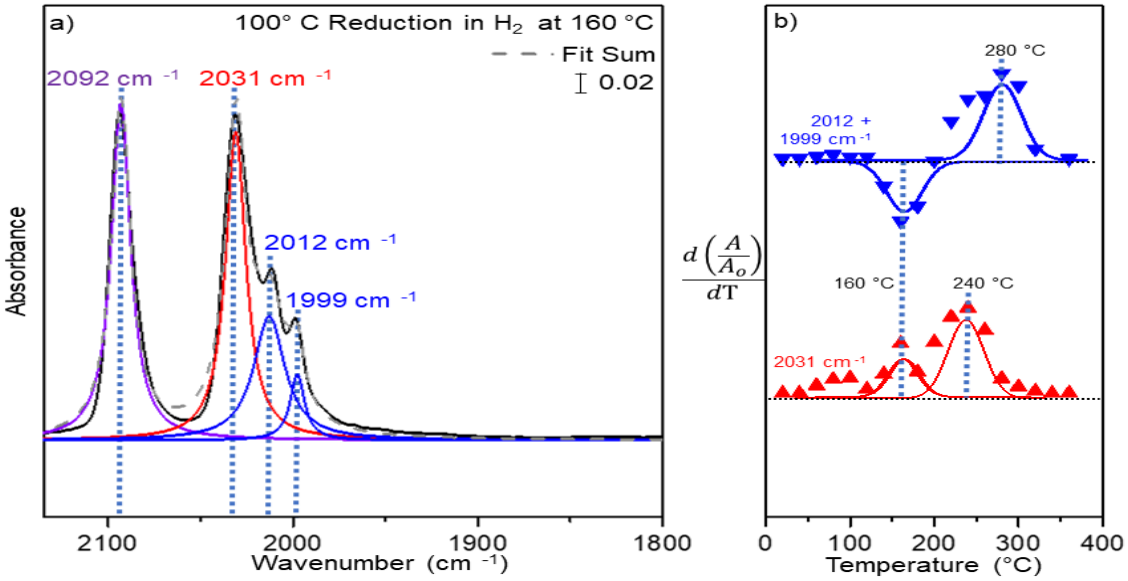

Figure 3.4: a) CO Probe module FTIR spectra of sample reduced in H_2 at 100 °C taken during the CO TPD at 160 °C, where spectral features at 2012 and 1999 cm^{-1} were clearly observed. Multiple overlapping peaks were deconvoluted from the original spectra in black with the band in purple identified as the $Rh(CO)_2$ symmetric stretch at 2092 cm^{-1}, $Rh(CO)_2$ asymmetric stretch at 2031 cm^{-1} in red, and formed bands at 2012 and 1999 cm^{-1} in blue. b) Comparison of temperature dependent rate of change in normalized CO band intensity (A/A_0) for the asymmetric stretch (2031 cm^{-1}, red) and newly formed features (2012 and 1999 cm^{-1}, blue). Maxima and minima in the rate of change, associated with the formation and loss of species, are highlighted with characteristic temperatures.

Based on known differences in using H_2 and CO reductions, and the unfavorable energy associated with oxygen vacancy formation on the anatase surface, hydroxyl

interactions with $Rh(CO)_2$ is the most favorable hypothesis to explain the difference between species formed in the two treatments. Increasing the H_2 reduction temperature led to an increase in the hydroxyl density and diversity on the TiO_2 surface, as observed from changes to the hydroxyl region of the FTIR spectra, 3000- 4000 cm^{-1} (figure 5a).[33–36] Furthermore, adsorbed water indicated by features at ~1260 and 1100 cm^{-1} were observed after hydrogen reduction, but not CO reduction, which demonstrates increased oxide surface complexity (figure 5b).[34,35,37] Increased hydroxyl coverage on the TiO_2 surface caused by increasing temperature reduction in H_2 increased the heterogeneity of the local coordination environment of $Rh(CO)_2$ species. The increased heterogeneity in the Rh local coordination environment following reduction at 200 °C in H_2, compared to 100 °C, is evidenced by broadening of the $Rh(CO)_2$ asymmetric band FWHM (24.0 cm^{-1}), as well as CO bands at 1999-2012 cm^{-1} associated with intermediate species formed during the TPD. When the same material was reduced in H_2 at 300 °C, Rh formed clusters, demonstrated by the emergence of a CO vibrational stretch between the symmetric and asymmetric peak, which is characteristic of linear bound CO on small clusters of Rh (~2050 cm^{-1}). However, a significant quantity of $Rh(CO)_2$ species were still observed, although with modified CO TPD characteristics likely due to changes in local coordination from support hydroxylation and water adsorption (Figure 3.6).

In order to identify the nature of the different Rh species, including the experimentally hypothesized $Rh(OH)(CO)_2$, an extensive series of models of Rh atomic species and their computed properties has been considered by DFT calculation. Two modeled configurations matched experimental observations; figure 7a where the Rh atom bounds to two lattice O_{2c} ions of the surface, $Rh(CO)_2$, and figure 7b that differs only by the presence of an additional surface OH group, $Rh(OH)(CO)_2$. Surprisingly, the two complexes exhibit very

similar CO vibrational features: on terrace sites 2097 and 2026 cm^{-1} for $Rh(CO)_2$, and 2090 and 2019 cm^{-1} for $Rh(OH)(CO)_2$; on step sites 2095 and 2031 cm^{-1} for $Rh(CO)_2$, and 2096-2029 cm^{-1} for $Rh(OH)(CO)_2$, Table 3.2. Clearly, a distinction of the two species based on the vibrational properties of the Rh $(CO)_2$ complex is not possible. However, while $Rh(CO)_2$ gives rise to a simultaneous desorption of the CO molecules (E_{ads} about 2 eV), for $Rh(OH)(CO)_2$ the two molecule have distinct adsorption energies, hence desorption temperatures, with a CO molecule bound by 1.62 eV and the other by 2.72 eV. While the absolute DFT values of E_{ads} are systematically overestimated compared to experiment, the trend is correct, Table 3.4. CO desorption leaves on the surface a Rh(OH)(CO) mono-carbonyl complex with a CO stretching frequency of 2016 cm^{-1} for both complexes formed on terraces or steps. This is in agreement with the IR features at 2012-1999 cm^{-1} observed experimentally, when no other species considered exhibits a stretching frequency in this region (see SI). CO binds to Rh(OH) with E_{ads} = 2.70 eV (terrace) or 2.90 eV (step), consistent with a higher CO desorption temperature for this species observed from experiments.

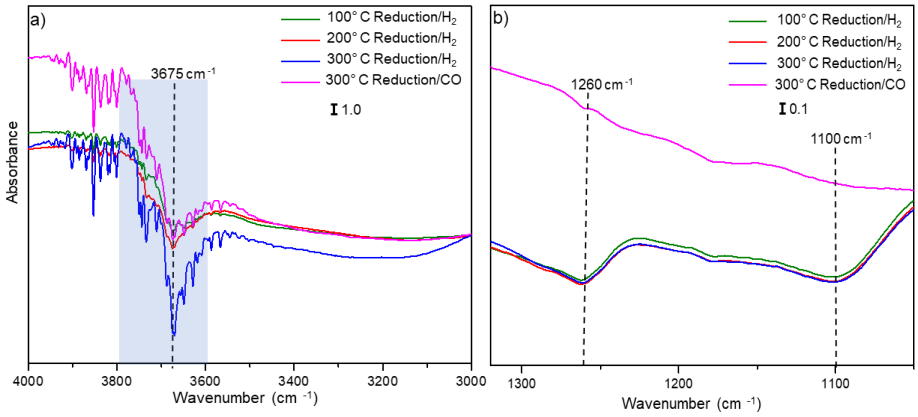

Figure 3.5: a) Background spectra taken at room temperature in Argon after specified reduction conditions. The highlighted region is associated with the hydroxyl species bound to TiO_2, with the intensity (negative) and peak width characterizing the density and heterogeneity, respectively. b) Background spectra taken at room temperature in Argon after specified reduction conditions. Bands at 1260 and 1100 cm^{-1} correspond to physisorbed water weakly bounded to hydroxyls at defect TiO_2 surface sites.

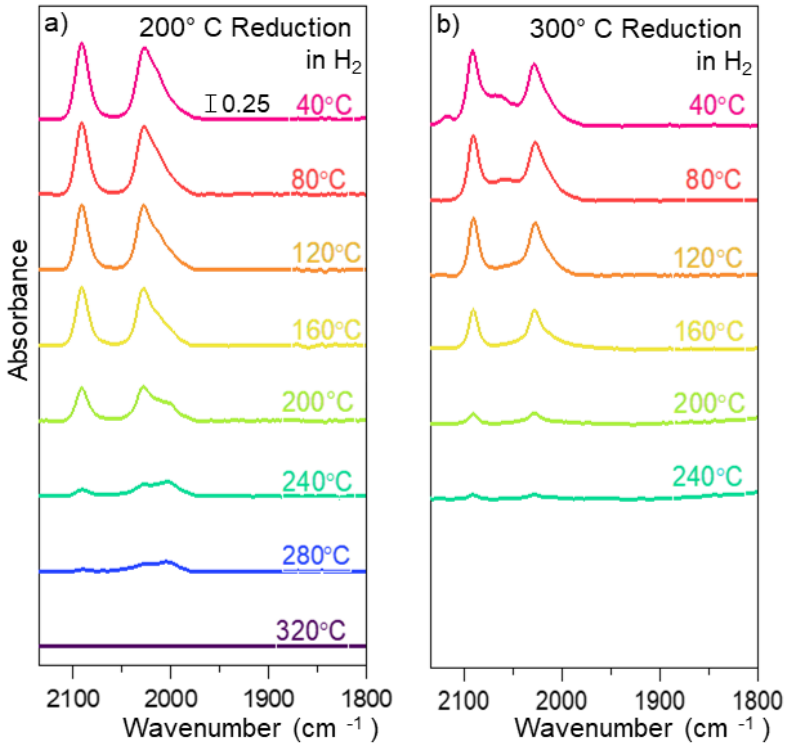

Figure 3.6: FTIR spectra after CO saturation and during TPD of CO from $Rh(CO)_2$ supported on anatase TiO_2 following varied pretreatment conditions : a) Reduced in H_2 at 200 °C. b) Reduced in H_2 at 300 °C.

In summary, it was identified that when atomically dispersed Rh on anatase TiO_2 was reduced at 100 °C in H_2 or in 300 °C in CO, adsorbed CO had similar characteristics in static IR measurements at room temperature. However, TPD measurements demonstrated clear differences in the CO desorption process, which suggests variations in $Rh(CO)_2$ local coordination. Based on a comparison with DFT calculations we propose for both pretreatments $Rh(CO)_2$ species with two bonds to two lattice O atoms form, while in the case of H_2 pre-treatment an additional species with a proximal hydroxyl forms, $Rh(OH)(CO)_2$. This demonstrates how subtle changes in the local coordination of atomically dispersed metals can have strong influences on their surface chemistry.

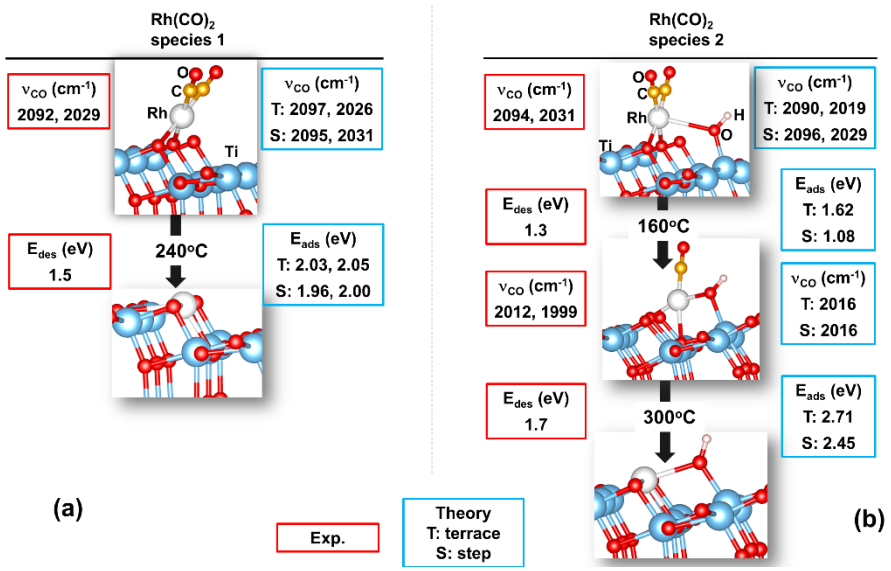

Figure 3.7: Structure of $Rh(CO)_2$ species identified based on FTIR and TPD spectra and DFT calculations and their evolution with temperature on (a) $(Rh)_{ads}$ and (b) $(RhOH)_{ads}$ specices. Red boxes (left): experimental results; blue boxes (right): DFT results.

3.4 Appendix

Via Thang, H. V., and Pacchioni, G. at the Dipartimento di Scienza dei Materiali, Università di Milano-Bicocca

3.4.1 DFT Methods

Spin-polarized calculations were carried out with the Perdew-Burke-Ernzerhof (PBE) generalized gradient approximation (GGA) exchange-correlation functional implemented in the Vienna Ab-initio Simulation Package (VASP).[38,39] The self-interaction error has been partly corrected by applying the DFT+U approach in which the Hubbard's U parameter is empirically set to 3 eV for 3d orbital of Ti ions.[40–42] The core electrons and nuclei interactions are described by projector augmented wave (PAW) method.[43,44] The valence electrons of Ti (3s, 3p, 3d, 4s), Rh (4p, 4d, 5s), O (2s, 2p), H (1s) and C (2s, 2p) are explicitly considered with plane wave basis set applying a cutoff energy of 400 eV. The calculations

were done at the *Gamma* point only and optimized structures were converged when the forces are less than |0.01| eV/Å. described in detail in a previous study.[45] The corresponding formula of TiO_2 [101] and TiO_2 [145] surface models are $Ti_{60}O_{120}$ and $Ti_{88}O_{176}$, respectively. The side view and top view of TiO_2 [101] surface are shown in the Figure 3.8A where two distinguished Ti sites: 5-fold-coordinated, Ti_{5c} and 6-fold-coordinated, Ti_{6c} and two inequivalent O site, 2-fold-coordinated, O_{2c} and 3-fold-coordinated, O_{3c} are presented. A vacuum by more than 15 Å is created between the slabs to minimize interaction of two neighboring slabs.

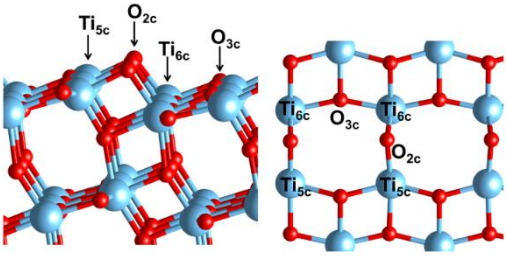

Figure 3.8A: Side view (left) and top view (right) of TiO_2 [101] surface. The different Ti and O sites are indicated. Ti and O atoms are blue and red spheres, respectively.

The CO adsorption energies, in eV, were obtained by the difference between isolated species and the adsorption complexes. Stable adsorbed species correspond to positive values. The stretching frequencies of CO were calculated within the harmonic approximation, where CO and its first nearest atoms were considered in the calculation. Van der Waals interactions were not included, but it has been shown that for small molecules, such as CO or H_2, the dispersion contribution is minor and does not affect adsorption energies and geometries.[46]

We adopted the models of (3 x 1) and (2 x 1) supercell slabs including five-atomic layers for the anatase TiO_2 [101] and the stepped TiO_2 [145] surfaces, respectively. The bond length and corresponding stretching frequency of gas-phase CO at the PBE level are 1.144 Å and 2125 cm^{-1}, respectively. We applied a scaling factor $\alpha = 2143/2125 = 1.0085$ for all calculated frequencies to take into account the difference with respect to the experimental

CO frequency of 2143 cm^{-1}. The effective charge of Rh atoms was analyzed by applying the Bader method.[47–50] The reaction pathways were searched by using the climbing-image nudged elastic band (CI-NEB) method.[51] Six images were created between reactants and products to find the minimum energy pathway.

3.4.2 Single Rh Atom on TiO_2 [101] and Stepped [145] Surfaces

We adopted six models to describe the nature of a Rh single atom anchored on the TiO_2 surface, Figure 3.8A, including four adsorption species: $(Rh)_{ads}$, $(RhO)_{ads}$, $(RhOH)_{ads}$, $(RhO_2)_{ads}$, and two substitutional positions: a Rh atom substitutional to a lattice Ti, $(Rh)_{subTi}$ and to a lattice O, $(Rh)_{subO}$. In principle two sites, Ti_{5c} and Ti_{6c}, can be replaced by Rh; however, Rh at a Ti_{6c} site is unstable, thus only Rh substitutional to Ti_{5c} site, $(Rh)_{subTi5c}$ was considered.16 For Rh replacing a lattice O site, we considered only Rh substitutional to O_{2c}, $(Rh)_{subO2c}$. In fact, also Rh at O_{3c} sites is unstable.[51]

The preferred adsorption site on the TiO_2 [101] surface for $(Rh)_{ads}$ is in the center of an hollow site formed by two O_{2c} and two O_{3c} sites, with Rh-O_{2c} bond length of 2.057 and with Rh-O_{3c} bond length of 2.215 Å, Figure 3.9A. At a stepped site of the TiO_2 [145] surface $(Rh)_{ads}$ is bound to two O_{2c} sites with Rh-O_{2c} distances of 2.129 Å to O_{2c} on the top terrace and of 2.185 Å to O_{2c} at the bottom terrace, Figure 3.10Aa.

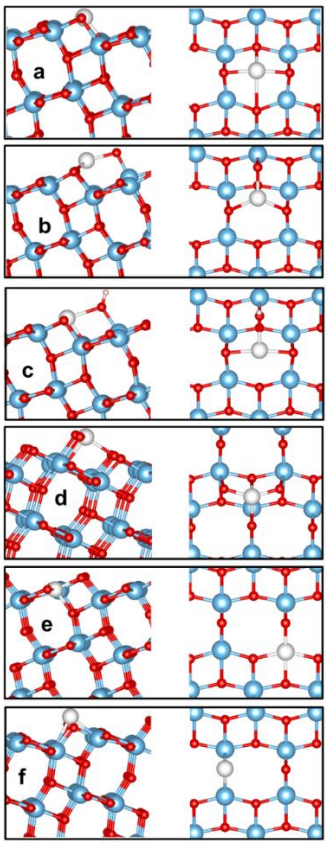

Figure 3.9A: Side view (left) and top view (right) of isolated Rh atom on terrace sites of the TiO_2 [101] surface shown for a) $(Rh)_{ads}$, b) $(RhO)_{ads}$, c) $(RhOH)_{ads}$, d) $(RhO_2)_{ads}$, e) $(Rh)_{subTi5c}$ and f) $(Rh)_{subO2c}$. Ti, O, H and Rh atoms are blue, red, light-pink and white spheres, respectively.

$(RhO)_{ads}$ units are formed by bonding with an extra O (formally deriving from a surface OH group). Here the Rh atom is bound to two O_{2c} atoms with an identical distance of 2.112 Å on [101] surface (Figure 3.9Ab) and of 1.972 and 2.102 Å on stepped [145] surface (Figure 3.10Ab).

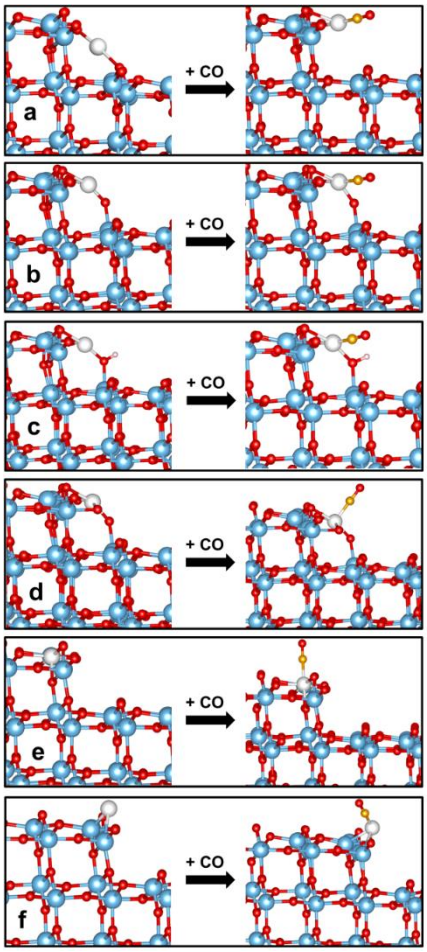

Figure 3.10A: Rh atoms at step site (left) and the corresponding single CO adsorption complex at step site of TiO_2 [145] surface shown for a) $(Rh)_{ads}$, b) $(RhO)_{ads}$, c) $(RhOH)_{ads}$, d) $(RhO_2)_{ads}$, e) $(Rh)_{subTi5c}$, and f) $(Rh)_{subO2c}$ Ti, O, C, H and Rh atoms are blue, red, gold, light-pink and white spheres, respectively.

The presence of OH groups has been observed experimentally. Thus, we also considered $(RhOH)_{ads}$ species on both terrace and step sites of TiO_2. The optimized structures of $(RhOH)_{ads}$ on terrace and step sites of TiO_2 are shown in Figure 3.9Ac and Figure 3.10Ac, respectively. The Rh-O and O-H distances are 2.30 Å and 0.97 Å (terrace) and 2.00 Å and 0.97 Å (step). The Rh-O bond length of $(RhOH)_{ads}$ species is larger than that on $(RhO)_{ads}$ species on terrace (2.00 Å) and on step site (1.86 Å). This indicates a weaker bonding of Rh with extra the O in $(RhOH)_{ads}$ species compared to that in $(RhO)_{ads}$ species.

$(RhO_2)_{ads}$ units are formally deriving from the interaction with two surface OH groups. Here the Rh atom forms four bonds: two with the two extra O atoms anchored on Ti_{5c} sites, with a distance of 1.831 Å, and the other two with surface O_{2c} and O_{3c} sites with a bond length of 2.129 Å and 2.132 Å, respectively, Figure 3.10Ad. Similarly, the $(RhO_2)_{ads}$ unit is anchored at step sites of the [145] surface: two bonds with two extra O atoms with distances of 1.998 and 2.088 Å, and two bonds with two O_{2c} sites with a bond length of 1.827 Å, Figure 3.10Ad.

For $(Rh)_{subTi5c}$ species, the substitution of Rh atom at Ti_{5c} does not result in changes in the geometrical parameters of the TiO_2 [101] surface (Figure 3.9A2e) and TiO_2 [145] surface (Figure 3.10Ae). On the other hand, $(Rh)_{subO2c}$ species are moving up from the original O_{2c} site with elongation of Rh-Ti bonds to 2.453 Å (original O-Ti bond length of 1.889 Å, Figure 3.9Af (TiO_2 [101] surface) and Figure 3.10Af (TiO_2 [145] surface).

The formal oxidation state of Rh, defined by the number of bonds between the Rh atom and the excess O atoms on the surface, is 0, +I, 0, +II for $(Rh)_{ads}$, $(RhO)_{ads}$, $(RhOH)_{ads}$, $(RhO_2)_{ads}$, respectively. For $(Rh)_{subTi5c}$ and $(Rh)_{subO2c}$ species, we assumed the same formal charge of Rh of the lattice Ti and O sites, i.e. +IV and –II, respectively.

3.4.3 Adsorption of a Single CO Molecule

The adsorption properties of single CO on supported Rh single atom and on bare TiO_2 are reported in Table 3.2, Figure 3.10A and Figure 3.11A. On terrace and step site of bare TiO_2 anatase surface CO is weakly absorbed on Ti_{5c} cation sites with an adsorption energy of 0.34 and 0.41 eV, respectively. The corresponding stretching frequencies are 2187 and 2193 cm^{-1} which are blueshifted with respect to free CO by +44 and +50 for terrace and step site, respectively, Table 3.2. When CO is placed on Rh single atom species, we observed a strong

adsorption energy and a large redshift of the CO stretching frequency with respect to gas-phase CO.

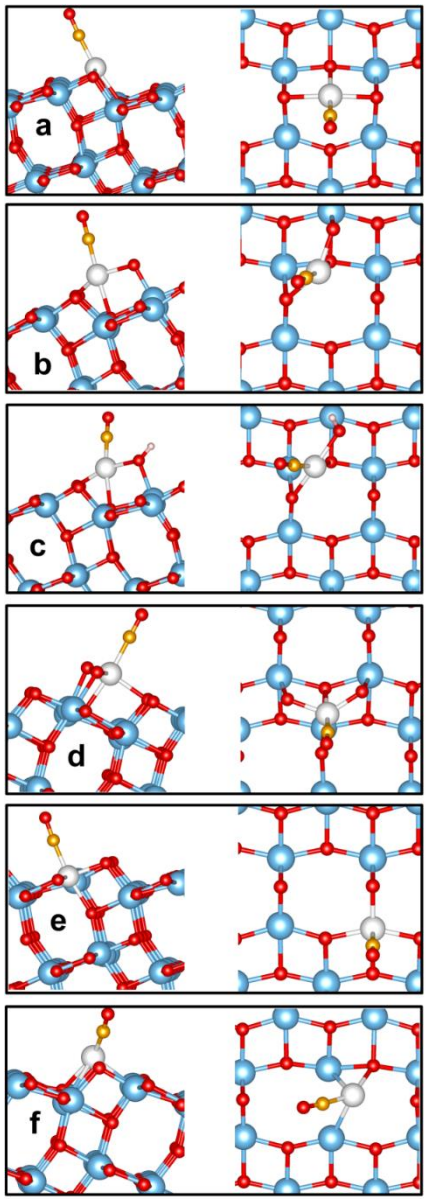

Figure 3.11A: Side view (left) and top view (right) of single CO adsorption on a) $(Rh)_{ads}$, b) $(RhO)_{ads}$, c) $(RhOH)_{ads}$, d) $(RhO_2)_{ads}$, e) $(Rh)_{subTi5c}$ and f) $(Rh)_{subO2c}$ on anatase TiO_2 [101] surface. Ti, O, C, H and Rh atoms are blue, red, gold, light-pink and white spheres, respectively.

Table 3.2. Adsorption energy, E_{ads} (eV), C-O bond length, R_{CO} (Å), C-Rh distance, R_{CRh} (Å), Bader charge of Rh, Q(Rh) (|e|), harmonic CO stretching frequency scaled by 2143/2125 factor, ν (cm^{-1}), and frequency shift, $\Delta\nu$ (cm^{-1}), with respect to gas-phase CO, for CO adsorption on various single atom Rh/TiO_2 structures.

System		CO site	E_{ads} (eV)	R_{CO} (Å)	R_{CRh} (Å)	Q(Rh) (|e|)	ν (cm^{-1})	$\Delta\nu$ (cm^{-1})
$(TiO_2)_{60}$[a]	Terrace	Ti^{IV}	0.34	1.138	2.467		2187	+44
$(TiO_2)_{88}$[a]	Step	Ti^{IV}	0.41	1.138	2.454		2193	+50
$(Rh)_{ads}(TiO_2)_{60}$	Terrace	Rh^0	2.05	1.166	1.813	0.64	2017	-126
$(Rh)_{ads}(TiO_2)_{88}$	Step	Rh^0	2.00	1.168	1.822	0.30	2001	-142
$(RhO)_{ads}(TiO_2)_{60}$	Terrace	Rh^I	2.24	1.160	1.828	0.97	2059	-84
$(RhO)_{ads}(TiO_2)_{88}$	Step	Rh^I	2.45	1.159	1.841	0.92	2053	-90
$(RhOH)_{ads}(TiO_2)_{60}$	Terrace	Rh^0	2.70	1.166	1.807	0.70	2016	-127
$(RhOH)_{ads}(TiO_2)_{88}$	Step	Rh^0	2.90	1.166	1.813	0.64	2016	-127
$(RhO_2)_{ads}(TiO_2)_{60}$	Terrace	Rh^{II}	1.91	1.151	1.876	1.32	2099	-44
$(RhO_2)_{ads}(TiO_2)_{88}$	Step	Rh^{II}	1.08	1.156	1.796	1.34	2091	-52
$Rh_{subTi5c}(Ti_{59}O_{120})$	Terrace	Rh^{IV}	1.58	1.149	1.863	1.45	2120	-23
$Rh_{subTi5c}(Ti_{87}O_{176})$	Step	Rh^{IV}	1.65	1.148	1.875	1.45	2117	-26
$Rh_{subO2c}(Ti_{60}O_{119})$	Terrace	Rh^{-II}	2.70	1.170	1.808	-0.02	1997	-146
$Rh_{subO2c}(Ti_{88}O_{175})$	Step	Rh^{-II}	2.56	1.170	1.811	-0.11	1993	-150

On $(Rh)_{ads}$ species, similar characteristics are found for CO adsorbed on Rh located on terrace and on step sites of the TiO_2 surface. Particularly, adsorption energies and stretching frequencies of CO are 2.05 eV, 2017 cm^{-1} for terrace sites and 2.00 eV, 2001 cm^{-1} for step sites, Table 3.2. The strong adsorption of CO on $(Rh)_{ads}$ species is mainly due to the strong back donation of electrons from the 4d states of Rh to $2\pi*$ state of CO. As a consequence, the CO bond length is elongated from 1.144 Å of free CO to 1.166 Å and 1.168 Å for $CO/(Rh)_{ads}$ on terrace and step sites, respectively.

Considering CO on $(RhO)_{ads}$ species, the adsorption energies are slightly stronger than on $(Rh)_{ads}$ species: 2.24 eV vs. 2.05 eV for terrace sites and 2.45 eV vs. 2.00 eV for step sites, while the CO frequency redshifts are smaller, in absolute values, than those on $(Rh)_{ads}$ species, -84 cm^{-1} vs. -126 cm^{-1} for terrace sites and -90 cm^{-1} vs. -142 cm^{-1} for step sites,

Table 3.2. This is consistent with the lower charge transfer from $(RhO)_{ads}$ species to the $2\pi*$ orbitals of CO compared to $(Rh)_{ads}$ which is confirmed by the Bader charge of Rh: +0.97 |e| vs. +0.64 |e| on terrace sites and +0.92 |e| vs. +0.30 |e| on step sites, Table 3.2.

We first analyzed the frequency of OH of anatase without CO adsorption. The results are in good agreement with experiment (3730-3789 cm^{-1} vs. 3734 cm^{-1}). Then, we considered the characteristics of $CO/(RhOH)_{ads}$ species, Table 3.2. Here CO is strongly bound, 2.70 eV (terrace) and 2.90 eV (step), and has a stretching frequency of 2016 cm^{-1} at both terrace and step sites, with a negative shift of 127 cm^{-1} with respect to free CO. This is quite different from the previous case of $(RhO)_{ads}$ due to a formally higher oxidation state of the Rh atom, consistent with a less positive Bader charge, Table 3.2.

Things are different when we consider CO adsorbed on $(RhO_2)_{ads}$ species on terrace and step sites. While a strong adsorption energy is still observed for CO bound to $(RhO_2)_{ads}$ on terrace, 1.91 eV, the bonding is about 1 eV weaker (1.08 eV) on $(RhO_2)_{ads}$ on step sites. This is due to the difference in adsorption of the RhO_2 unit on terrace and step sites, reflecting the bond-order conservation principle: the binding energy of the RhO_2 unit on step site (1.9 eV) is about 1 eV stronger than that on terrace sites (1.0 eV). However, the Bader charge and redshifts of CO frequency are virtually the same, +1.32 |e| and -44 cm^{-1} for $CO/(RhO_2)_{ads}$ on terrace sites and +1.33 |e| and -52 cm^{-1} for $CO/(RhO_2)_{ads}$ on step sites, Table 3.2.

On $(Rh)_{subTi5c}$ CO is strongly bound with an adsorption energy of 1.58 eV (terrace) and 1.65 eV (step). Due to the lower charge transfer from Rh to CO only a moderate redshift of CO frequency is found (-23 cm^{-1} for $CO/(Rh)_{subTi5c}$ on terrace, and -26 cm^{-1} for $CO/(Rh)_{subTi5c}$ on step sites, Table 3.2).

On the last configuration considered, $(Rh)_{subO2c}$, CO is very strongly bound with an adsorption energy of 2.70 eV and 2.56 eV for terrace and step sites, respectively. This is

consistent with the largest charge donation from Rh to CO (Bader charge of Rh of -0.02 and -0.11 |e| for terrace and step sites, respectively). As a result, the CO bond length is elongated to 1.170 Å, resulting in the largest redshift of CO stretching frequencies of -146/-150 cm^{-1}, Table 3.2.

3.4.4 Adsorption of Two CO Molecules

The adsorption of a second CO (geminal CO complex) was considered for all Rh single atom configurations. In most cases, strong adsorption energies are still observed, except for the case of $(Rh)_{subTi5c}$ where the second CO spontaneously interacts with a lattice oxygen atom forming a CO_2 species. The properties of geminal CO molecules on $(RhO_x)_{ads}$ species are presented in Table 3.3.

On $(Rh)_{ads}$ the second CO is bound as strongly as the first CO molecule with an energy of 2.03 eV on terrace and 1.96 eV on step sites, Figure 3.12A. The two CO molecules on $(Rh)_{ads}$ result in symmetric and antisymmetric stretching frequencies of 2097 and 2026 cm^{-1} (terrace) and 2095 cm^{-1} and 2031 cm^{-1} (step). These values are in very good agreement with IR spectra of geminal CO molecule on isolated Rh species.

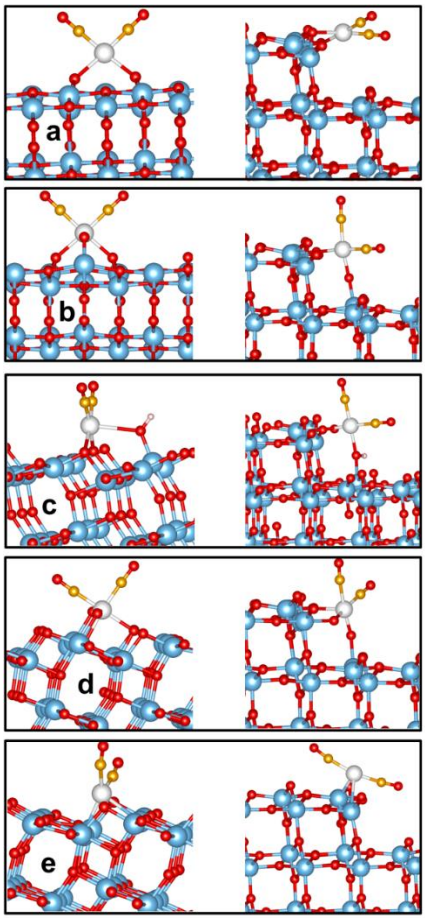

Figure 3.12A: Geminal CO molecules on isolated Rh atoms on terrace (left) and step sites (right): a) $(Rh)_{ads}$, b) $(RhO)_{ads}$, c) $(RhOH)_{ads}$, d) $(RhO_2)_{ads}$, and e) $(Rh)_{subO2c}$. Ti, O, C, H and Rh atoms are blue, red, gold, light-pink and white spheres, respectively.

When we consider the second CO on the $(RhO)_{ads}$ species, Figure 3.12A, smaller adsorption energies (about 1eV) were found compared to the first CO molecule, 1.25 eV vs. 2.24 eV (terrace) and 1.08 eV vs. 2.45 eV (step). This is consistent with the smaller charge transfer from Rh to the second CO compared to the first CO molecule, in line with the Bader charge on Rh (+1.02 vs. +0.70 on terrace and +0.97 vs. +0.68 on step). The symmetric and antisymmetric frequencies of geminal CO molecules on terrace sites (2117, 2059 cm^{-1}) are similar to those on step sites (2108, 2057 cm^{-1}), Table 3.3. Also $(RhO)_{ads}$ species have CO

stretching frequencies close to the experimental one, although not as good as the one obtained for $(Rh)_{ads}$.

Table 3.3. Adsorption energy, E_{ads} (eV), C-O bond length, R_{CO} (Å), C-Rh distance, R_{CRh} (Å), Bader charge of Rh, Q(Rh) (|e|), harmonic CO stretching frequency scaled by 2143/2125 factor, ν (cm^{-1}), and frequency shift, $\Delta\nu$ (cm^{-1}), with respect to gas-phase CO for geminal CO molecules adsorption on various single atom Rh/TiO_2 structures.

System		CO site	E_{ads} (eV)	R_{CO} (Å)	R_{CRh} (Å)	Q(Rh) (|e|)	ν (cm^{-1})	$\Delta\nu$ (cm^{-1})
$(Rh)_{ads}(TiO_2)_{60}$	Terrace	Rh^0	2.05 2.03	1.160 1.160	1.818 1.828	0.70	2097 2026	-46 -117
$(Rh)_{ads}(TiO_2)_{88}$	Step	Rh^0	2.00 1.96	1.159 1.159	1.836 1.837	0.68	2095 2031	-48 -112
$(RhO)_{ads}(TiO_2)_{60}$	Terrace	Rh^I	2.24 1.25	1.154 1.154	1.853 1.853	1.02	2117 2059	-26 -84
$(RhO)_{ads}(TiO_2)_{88}$	Step	Rh^I	2.45 1.08	1.154 1.153	1.899 1.863	0.97	2108 2057	-35 -86
$(RhOH)_{ads}(TiO_2)_{60}$	Terrace	Rh^0	2.71 1.62	1.161 1.161	1.824 1.824	0.77	2090 2019	-53 -124
$(RhOH)_{ads}(TiO_2)_{88}$	Step	Rh^0	2.90 1.66	1.159 1.160	1.836 1.831	0.70	2096 2029	-47 -114
$(RhO_2)_{ads}(TiO_2)_{60}$	Terrace	Rh^{II}	1.91 0.62	1.143 1.151	1.907 1.874	1.29	2159 2095	+16 -48
$(RhO_2)_{ads}(TiO_2)_{88}$	Step	Rh^{II}	1.08 -0.07	1.145 1.147	2.009 1.972	1.24	2129 2098	-14 -45
$Rh_{subO2c}(Ti_{60}O_{119})$	Terrace	Rh^{-II}	2.70 0.75	1.155 1.168	1.990 1.817	0.03	2055 1994	-88 -149
$Rh_{subO2c}(Ti_{88}O_{175})$	Step	Rh^{-II}	2.56 1.01	1.159 1.159	1.907 1.919	-0.17	2043 2001	-100 -142

We also considered the possible reactivity of the second CO adsorbed molecule with an extra O atom from the $(RhO)_{ads}$ complex. In this case, a CO_2 molecule forms, leaving behind the $CO/(Rh)_{ads}$ monocarbonyl complex. The process, Figure 3.13A, occurs with a relatively low energy barrier, 0.45 eV, and leads to a structure where an activated CO_2 molecule is bound to the $CO/(Rh)_{ads}$ complex; from this precursor, CO_2 can desorb with an enthalpy cost of 0.63 eV. Thus, the calculations indicate that the formation of CO_2 from the reactive adsorption of the second CO molecule is a feasible process on $(RhO)_{ads}$.

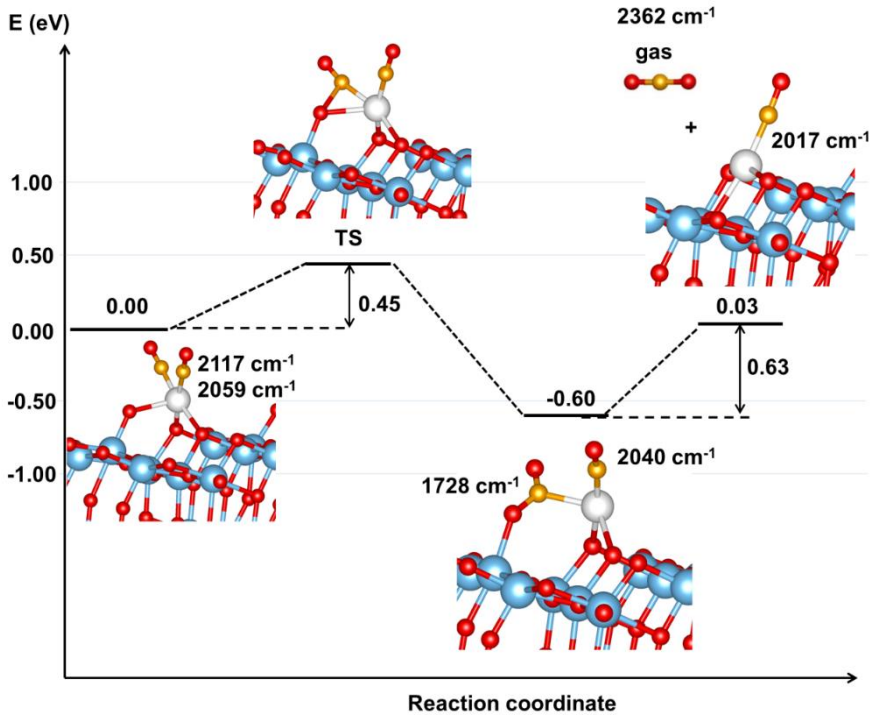

Figure 3.13A: Reaction profile for the combination of an adsorbed CO molecule with the extra O atom of the $(RhO)_{ads}$ complex with formation and desorption of a CO_2 molecule.

Now we consider the second CO on the $(RhOH)_{ads}$ species, Figure 3.12Ac. The second CO is still strongly bound, but considerably less than the first one, suggesting two different desorption temperatures. The symmetric and antisymmetric CO stretching frequencies (2090 and 2019 cm^{-1} for terrace sites and 2096 and 2029 $cm^{-1}$for step sites) are in close agreement with experimental observation (2094 and 2031 cm^{-1}) for geminal CO; this, together with the frequencies for single CO, Table 3.2, 2016 cm^{-1} vs. 2010 cm^{-1} makes $(RhOH)_{ads}$ a potential candidate for the observed features.

For geminal CO molecules on $(RhO_2)_{ads}$ species, Figure 3.12Ad, the second CO is weakly bound on terrace (0.62 eV), while it is unbound (-0.07 eV) on step sites. As a result, the symmetric and antisymmetric CO stretching frequencies are blue-shifted or slightly redshifted, +16, -48 cm^{-1} for terrace sites, and -14, -45 cm^{-1} for step sites, Table 3.3. These two bands are completely different from those observed experimentally (see below).

Therefore, one can rule out $(RhO_2)_{ads}$ species as a structure of single Rh atom on the TiO_2 surface.

Considering the second CO on $(Rh)_{subO2c}$ species, Figure 3.12Ae the adsorption energies are about 2 eV lower than the first CO molecule with binding energies of 0.75 eV and 1.01 eV for terrace and step sites, respectively, Table 3.3. However, the symmetric and antisymmetric CO stretching frequencies are largely redshifted, -88/-199 cm^{-1} and -100/-142 cm^{-1} for $(CO)_2/(Rh)_{subO2c}$ on terrace and step sites, respectively. These results are far from what seen experimentally, allowing us to dismiss $(Rh)_{subO2c}$ as potential candidate of a Rh single atom anchored on the TiO_2 surface.

3.4.5 Metallic Rh Cluster on TiO_2 [101]

To compare the nature of isolated Rh atoms and metallic Rh clusters on TiO_2 surface, we adopted a Rh_4 cluster as a model for metallic Rh aggregates on TiO_2 surface. Note that the size of this cluster is much smaller than that observed from experiments, about 1 nanometer.[23] However, this can show qualitatively the different CO adsorption properties on cluster and isolated Rh atoms. On TiO_2 surface, the most stable structure of tetrahedral Rh_4 is with three bottom Rh atoms bound to three O_{2c} atoms with distance of 2.04-2.10 Å and the remaining Rh on the top of the triangle with Rh-Rh bond lengths of 2.32 – 2.54 Å, Figure 3.14Aa. This is in good agreement with previous DFT+U calculations. The average Bader charge of each Rh atom is almost neutral (+0.13 |e|).[52]

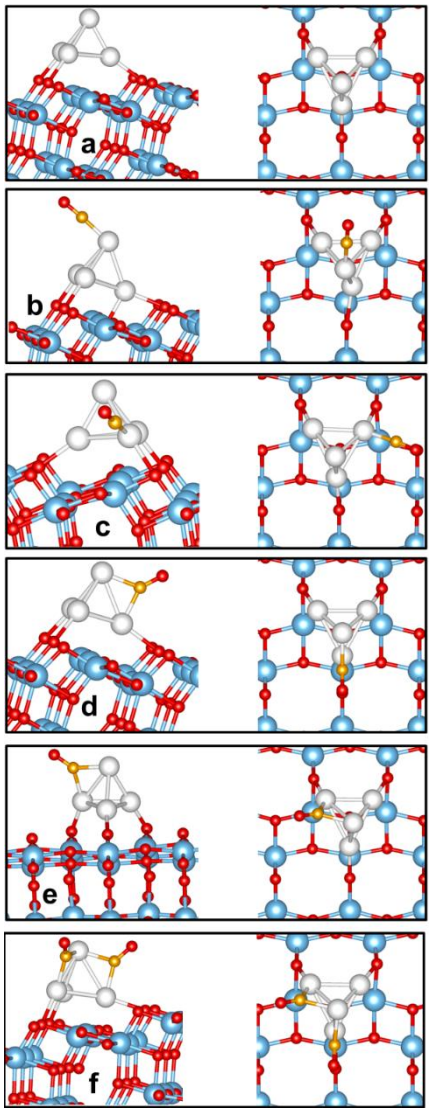

Figure 3.14A: Side view (left) and top view (right) of a) Rh_4/TiO_2, b) mono CO adsorbed on a top Rh atom of Rh_4/TiO_2 , c) mono CO adsorbed at interface Rh site between Rh_4 and TiO_2 [101] surface, d) and e) the mono CO adsorbed bridge sites of Rh_4/TiO_2, f) the two CO molecules adsorbed at two different bridge sites of Rh_4/TiO_2. Ti, O, C and Rh atoms are blue, red, gold and white spheres, respectively.

For CO adsorption complexes on Rh_4/TiO_2, we considered the single and geminal CO complexes as obtained on atomic Rh species, Table 3.4. The single CO was considered to adsorb on different Rh sites, on the topmost (Rh^0-top) or interface (Rh^0-int) sites with linear or bridge (two-fold coordinated sites) bonding mode, (Rh^0-Rh^0), Figure 3.14A. As can be seen from Table 3.4, the CO molecule prefers to bind at the bridge sites with an adsorption

energy of 2.89 eV, Figure 3.14Ad, stronger than the linear configuration either on the topmost Rh site (2.26 eV), Figure 3.14Ab, or at the interface Rh sites between Rh_4 and TiO_2 [101] surface (2.00 eV), Figure 3.14Ac. This is due to the fact that electron back donation from Rh_4 to CO at bridge site is higher than that at linear site. This is demonstrated by a large elongation the CO bond length to 1.195 Å compared to the linear structure (1.172 Å for CO on topmost Rh and 1.168 Å for CO at interface sites), Table 3.4. As a result, large redshifts are found for CO at bridge site (-326 cm^{-1}), while smaller redshifts are observed on linear structures (-159/-158 cm^{-1}).

Table 3.4 Adsorption energy, E_{ads} (eV), C-O bond length, R_{CO} (Å), C-Rh distance, R_{CRh} (Å), Bader charge of Rh bound to CO, Q(Rh) (|e|), harmonic CO stretching frequency scaled by 2143/2125 factor, ν (cm^{-1}), and frequency shift $\Delta\nu$ (cm^{-1}) with respect to gas-phase for CO adsorption on Rh_4/TiO_2 structures.

System	CO site	E_{ads} (eV)	R_{CO} (Å)	R_{CRh} (Å)	Q(Rh) (|e|)	ν (cm^{-1})	$\Delta\nu$ (cm^{-1})
$(CO)Rh_4(TiO_2)_{60}$	Rh^0-top	2.26	1.172	1.800	0.19	1984	-159
$(CO)Rh_4(TiO_2)_{60}$	Rh^0-int	2.00	1.168	1.843	0.25	1985	-158
$(CO)Rh_4(TiO_2)_{60}$	Rh^0-Rh^0	2.89	1.195	1.930, 1.937	0.15	1817	-326
$(CO)_2Rh_4(TiO_2)_{60}$	Rh^0-Rh^0	2.89 2.33	1.197 1.196	1.958, 1.927 1.916, 1.969	0.23	1835 1795	-308 -348

Given that the most stable structure of CO is at the bridge site of Rh_4/TiO_2, the second CO was only considered at another bridge site, Figure 3.14Af. A strong adsorption of the second CO was observed with an adsorption energy of 2.33 eV. The redshifts of symmetric and antisymmetric frequencies are still large, -308 and -348 cm^{-1}, respectively, Table 3.4. Clearly, CO adsorbed on supported metallic Rh cluster is much more strongly bound than on isolated Rh atoms (2.33 - 2.89 eV vs 1.25 - 2.42 eV); it also gives rise to much larger redshifts (more than 300 cm^{-1}) of CO frequencies.

3.5 References

(1) Redhead, P. A. Thermal Desorption of Gases. *Vacuum* **1962**, *12* (4), 203–211.

(2) Liu, L.; Corma, A. Metal Catalysts for Heterogeneous Catalysis: From Single Atoms to Nanoclusters and Nanoparticles. *Chem. Rev.* **2018**, *118* (10), 4981–5079.

(3) Matsubu, J. C.; Zhang, S.; DeRita, L.; Marinkovic, N. S.; Chen, J. G.; Graham, G. W.; Pan, X.; Christopher, P. Adsorbate-Mediated Strong Metal-Support Interactions in Oxide-Supported Rh Catalysts. *Nat. Chem.* **2017**, *9* (2), 120–127.

(4) Thang, H. V.; Pacchioni, G.; DeRita, L.; Christopher, P. Nature of Stable Single Atom Pt Catalysts Dispersed on Anatase TiO2. *J. Catal.* **2018**, *367*, 104–114.

(5) Chang, T.-Y.; Tanaka, Y.; Ishikawa, R.; Toyoura, K.; Matsunaga, K.; Ikuhara, Y.; Shibata, N. Direct Imaging of Pt Single Atoms Adsorbed on TiO2 (110) Surfaces. *Nano Lett.* **2013**, *14* (1), 134–138.

(6) DeRita, L.; Resasco, J.; Dai, S.; Boubnov, A.; Thang, H. V.; Hoffman, A. S.; Ro, I.; Graham, G. W.; Bare, S. R.; Pacchioni, G.; et al. Structural Evolution of Atomically Dispersed Pt Catalysts Dictates Reactivity. *Nat. Mater.* **2019**, *18* (7), 746–751.

(7) DeRita, L.; Dai, S.; Lopez-Zepeda, K.; Pham, N.; Graham, G. W.; Pan, X.; Christopher, P. Catalyst Architecture for Stable Single Atom Dispersion Enables Site-Specific Spectroscopic and Reactivity Measurements of CO Adsorbed to Pt Atoms, Oxidized Pt Clusters, and Metallic Pt Clusters on TiO2. *J. Am. Chem. Soc.* **2017**, *139* (40), 14150–14165.

(8) Hoffman, A. S.; Fang, C. Y.; Gates, B. C. Homogeneity of Surface Sites in Supported Single-Site Metal Catalysts: Assessment with Band Widths of Metal Carbonyl Infrared Spectra. *J. Phys. Chem. Lett.* **2016**, *7* (19), 3854–3860.

(9) Mayernick, A. D.; Janik, M. J. Methane Oxidation on Pd–Ceria: A DFT Study of the Mechanism over PdxCe1− XO2, Pd, and PdO. *J. Catal.* **2011**, *278* (1), 16–25.

(10) Tang, Y.; Asokan, C.; Xu, M.; Graham, G. W.; Pan, X.; Christopher, P.; Li, J.; Sautet,

P. Rh Single Atoms on TiO2 Dynamically Respond to Reaction Conditions by Adapting Their Site. *Nat. Commun.* **2019**, *10* (1), 4488.

(11) Qiao, B.; Wang, A.; Yang, X.; Allard, L. F.; Jiang, Z.; Cui, Y.; Liu, J.; Li, J.; Zhang, T. Single-Atom Catalysis of CO Oxidation Using Pt1/FeOx. *Nat. Chem.* **2011**, *3* (8), 634–641.

(12) Cavanagh, R. R., Yates Jr., J. T. Site Distribution Studies of Rh Supported on Al2O3—An Infrared Study of Chemisorbed CO. *J. Chem. Phys.* **1981**, *74* (7), 4150.

(13) Yates, J. T.; Duncan, T. M.; Worley, S. D.; Vaughan, R. W. Infrared Spectra of Chemisorbed CO on Rh. *J. Chem. Phys.* **1979**, *70* (3), 1219.

(14) Hadjiivanov, K. I.; Vayssilov, G. N. Characterization of Oxide Surfaces and Zeolites by Carbon Monoxide as an IR Probe Molecule; Advances in Catalysis; Academic Press, 2002; Vol. 47, pp 307–511.

(15) Goldsmith, B. R.; Sanderson, E. D.; Ouyang, R.; Li, W. X. CO- and NO-Induced Disintegration and Redispersion of Three-Way Catalysts Rhodium, Palladium, and Platinum: An Ab Initio Thermodynamics Study. *J. Phys. Chem. C* **2014**, *118* (18), 9588–9597.

(16) Parkinson, G. S.; Novotny, Z.; Argentero, G.; Schmid, M.; Pavelec, J.; Kosak, R.; Blaha, P.; Diebold, U. Carbon Monoxide-Induced Adatom Sintering in a Pd–Fe 3 O 4 Model Catalyst. *Nat. Mater.* **2013**, *12* (8), 724.

(17) Hadjiivanov, K. Identification and Characterization of Surface Hydroxyl Groups by Infrared Spectroscopy. In *Advances in Catalysis*; Academic Press, 2014; Vol. 57, pp 99–318.

(18) Panagiotou, G. D.; Petsi, T.; Bourikas, K.; Garoufalis, C. S.; Tsevis, A.; Spanos, N.; Kordulis, C.; Lycourghiotis, A. Mapping the Surface (Hydr)Oxo-Groups of Titanium Oxide and Its Interface with an Aqueous Solution: The State of the Art and a New Approach. *Adv. Colloid Interface Sci.* **2008**, *142* (1–2), 20–42.

(19) Panayotov, P. B.; Yates, J. T. Rhodium-Carbon Monoxide Surface Chemistry: The

Involvement of Surface Hydroxyl Groups on A12O3and SiO2Supports. *J. Am. Chem. Soc.* **1988**, *110* (7), 2074–2081.

(20) Garland, C. W.; Yang, A. Infrared Studies of Carbon Monoxide Chemisorbed on Rhodium. *J. Phys. Chem.* **1957**, *61* (11), 1504–1512.

(21) Smith, A.K.; Hugues, F.; Theolier, A.; Basset, J.M.; Ugo, R.; Zanderighi, G.M.; Bilhou, J.L.; and Graydon, W. F. . Surface-Supported Metal Cluster Carbonyls. Chemisorption Decomposition and Reactivity of Hexadecacarbonylhexarhodium Supported on Alumina, Silica-Alumina, and Magnesia. **1979**, *18* (11), 3104–3112.

(22) Serna, P.; Gates, B. C. Zeolite-Supported Rhodium Complexes and Clusters: Switching Catalytic Selectivity by Controlling Structures of Essentially Molecular Species. *J. Am. Chem. Soc.* **2011**, *133* (13), 4714–4717.

(23) Matsubu, J. C.; Yang, V. N.; Christopher, P. Isolated Metal Active Site Concentration and Stability Control Catalytic CO2 Reduction Selectivity. *J. Am. Chem. Soc.* **2015**, *137* (8), 3076–3084.

(24) Yates, J. T.; Kolasinski, K. Infrared Spectroscopic Investigation of the Rhodium Gem-Dicarbonyl Surface Species. *J. Chem. Phys.* **1983**, *79* (2), 1026.

(25) Ivanova, E.; Mihaylov, M.; Thibault-Starzyk, F.; Daturi, M.; Hadjiivanov, K. FTIR Spectroscopy Study of CO and NO Adsorption and Co-Adsorption on Pt/TiO2. *J. Mol. Catal. A Chem.* **2007**, *274* (1), 179–184.

(26) Zaera, F. New Advances in the Use of Infrared Absorption Spectroscopy for the Characterization of Heterogeneous Catalytic Reactions. *Chem. Soc. Rev.* **2014**, *43* (22), 7624–7663.

(27) Varga, E.; Pusztai, P.; Ovari, L.; Oszko, A.; Erdohelyi, A.; Papp, C.; Steinruck, H. P.; Konya, Z.; Kiss, J. Probing the Interaction of Rh, Co and Bimetallic Rh-Co Nanoparticles with the CeO2 Support: Catalytic Materials for Alternative Energy Generation. *Phys Chem Chem Phys* **2015**, *17* (40), 27154–27166.

(28) Trautmann, S.; Baerns, M. Infrared Spectroscopic Studies of CO Adsorption on

Rhodium Supported by SiO2, Al2O3, and TiO2. *J. Catal.* **1994**, *150* (2), 335–344.

(29) Nehasil, V.; Stará, I.; Matolín, V. Study of CO Desorption and Dissociation on Rh Surfaces. *Surf. Sci.* **1995**, *331–333* (PART A), 105–109.

(30) Thiel, P. A.; Williams, E. D.; Yates Jr, J. T.; Weinberg, W. H. The Chemisorption of Co on Rh (111). *Surf. Sci.* **1979**, *84* (1), 54–64.

(31) Cheng, H.; Selloni, A. Surface and Subsurface Oxygen Vacancies in Anatase TiO2 and Differences with Rutile. *Phys. Rev. B* **2009**, *79* (9), 2–5.

(32) He, Y.; Dulub, O.; Cheng, H.; Selloni, A.; Diebold, U. Evidence for the Predominance of Subsurface Defects on Reduced Anatase TiO 2 (101). *Phys. Rev. Lett.* **2009**, *102* (10), 106105.

(33) Hadjiivanov, K. I.; Klissurski, D. G. Surface Chemistry of Titania (Anatase) and Titania-Supported Catalysts. *Chem. Soc. Rev.* **1996**, *25* (1), 61–69.

(34) Bezrodna, T.; Puchkovska, G.; Shymanovska, V.; Baran, J.; Ratajczak, H. IR-Analysis of H-Bonded H2O on the Pure TiO2 Surface. *J. Mol. Struct.* **2004**, *700* (1–3), 175–181.

(35) Panayotov, D. A.; Yates, J. T. Depletion of Conduction Band Electrons in TiO2by Water Chemisorption - IR Spectroscopic Studies of the Independence of Ti-OH Frequencies on Electron Concentration. *Chem. Phys. Lett.* **2005**, *410* (1–3), 11–17.

(36) Li, G.; Li, L.; Boerio-Goates, J.; Woodfield, B. F. High Purity Anatase TiO2 Nanocrystals: Near Room-Temperature Synthesis, Grain Growth Kinetics, and Surface Hydration Chemistry. *J. Am. Chem. Soc.* **2005**, *127* (24), 8659–8666.

(37) Panayotov, D.; Yates, T. Rhodium-Carbon Monoxide Surface Chemistry : The Involvement of Surface Hydroxyl Groups on A1203 and Si02 Supports. **1988**, No. 14, 2074–2081.

(38) Perdew, J. P.; Burke, K.; Ernzerhof, M. Generalized Gradient Approximation Made Simple. *Phys. Rev. Lett.* **1996**, *77* (18), 3865.

(39) Kresse, G.; Furthmüller, J. Efficient Iterative Schemes for Ab Initio Total-Energy Calculations Using a Plane-Wave Basis Set. *Phys. Rev. B* **1996**, *54* (16), 11169.

(40) Anisimov, V. I.; Zaanen, J.; Andersen, O. K. Band Theory and Mott Insulators: Hubbard U Instead of Stoner I. *Phys. Rev. B* **1991**, *44* (3), 943.

(41) Dudarev, S. L.; Botton, G. A.; Savrasov, S. Y.; Humphreys, C. J.; Sutton, A. P. Electron-Energy-Loss Spectra and the Structural Stability of Nickel Oxide: An LSDA+ U Study. *Phys. Rev. B* **1998**, *57* (3), 1505.

(42) Chen, H.-Y. T.; Tosoni, S.; Pacchioni, G. A DFT Study of the Acid–Base Properties of Anatase TiO2 and Tetragonal ZrO2 by Adsorption of CO and CO2 Probe Molecules. *Surf. Sci.* **2016**, *652*, 163–171.

(43) Blöchl, P. E. Projector Augmented-Wave Method. *Phys. Rev. B* **1994**, *50* (24), 17953.

(44) Kresse, G.; Joubert, D. From Ultrasoft Pseudopotentials to the Projector Augmented-Wave Method. *Phys. Rev. b* **1999**, *59* (3), 1758.

(45) Chen, H.-Y. T.; Tosoni, S.; Pacchioni, G. Adsorption of Ruthenium Atoms and Clusters on Anatase TiO2 and Tetragonal ZrO2 (101) Surfaces: A Comparative DFT Study. *J. Phys. Chem. C* **2015**, *119* (20), 10856–10868.

(46) Janthon, P.; Vines, F.; Sirijaraensre, J.; Limtrakul, J.; Illas, F. Adding Pieces to the CO/Pt (111) Puzzle: The Role of Dispersion. *J. Phys. Chem. C* **2017**, *121* (7), 3970–3977.

(47) Tang, W.; Sanville, E.; Henkelman, G. A Grid-Based Bader Analysis Algorithm without Lattice Bias. *J. Phys. Condens. Matter* **2009**, *21* (8), 84204.

(48) Sanville, E.; Kenny, S. D.; Smith, R.; Henkelman, G. Improved Grid-based Algorithm for Bader Charge Allocation. *J. Comput. Chem.* **2007**, *28* (5), 899–908.

(49) Henkelman, G.; Arnaldsson, A.; Jónsson, H. A Fast and Robust Algorithm for Bader Decomposition of Charge Density. *Comput. Mater. Sci.* **2006**, *36* (3), 354–360.

(50) Yu, M.; Trinkle, D. R. Accurate and Efficient Algorithm for Bader Charge Integration.

J. Chem. Phys. **2011**, *134* (6), 64111.

(51) Henkelman, G.; Jónsson, H. Improved Tangent Estimate in the Nudged Elastic Band Method for Finding Minimum Energy Paths and Saddle Points. *J. Chem. Phys.* **2000**, *113* (22), 9978–9985.

(52) Guo, D.; Wang, G.-C. Partial Oxidation of Methane on Anatase and Rutile Defective TiO2 Supported Rh4 Cluster: A Density Functional Theory Study. *J. Phys. Chem. C* **2017**, *121* (47), 26308–26320.

Chapter 4:

Rh Single Atoms on TiO_2 Dynamically Respond to Reaction Conditions by Adapting their Site

Adapted from *Nature Communications* article:

Tang, Y., Asokan, C., Xu, M., Graham, G.W., Pan, X., Christopher, P., Li, J., & Sautet, P. "Rh Single Atoms on TiO_2 Dynamically Respond to Reaction Conditions by Adapting their Site," *Nature Communications*, 10(1), 4488 (2019).

4.1 Introduction

Single-atom catalysts are widely investigated heterogeneous catalysts, however, the identification of the local environment of single atoms under experimental conditions, as well as operando characterization of their structural changes during catalytic reactions are still challenging. Here, we consider Rh single atoms on TiO_2 to investigate the optimal structure of the single atoms during O_2 calcination, H_2 reduction, CO adsorption, and reverse water gas shift (RWGS) reaction conditions. The combination of theoretical and experimental studies clearly demonstrates that Rh single atoms adapt their local coordination and reactivity in response to variation in redox environmental conditions. These findings show that single-atom catalysts are not at all static but can switch from inactive to active structure under reaction conditions, hence explaining some conflicting accounts in the literature. The insight on the real nature of the active site is key for the design of high-performance catalysts.

Supported noble metal nanoparticles are widely investigated heterogeneous catalysts due to their high activity and selectivity for valuable products. However, the high prices and finite resources of these noble metals limit their applications in large-scale production. Heterogeneous single-atom catalysts (SAC), which consist of isolated atoms anchored onto supports, maximize the efficiency of noble metal utilization.[1-5] Moreover, developing catalysts that precisely place the single metal atoms homogeneously at a single site on the support can offer high selectivity towards a specific product. Thus, as a bridge between homogeneous and heterogeneous catalysis, SACs have become a new frontier in catalysis science and thus attracted significant attention recently.[6-15]

A single atom (SA) on a support possesses unique chemical and physical properties due to its particular local chemical environment, inducing an electronic structure that differs from that of conventional supported nanoparticle catalysts. However, the identification of this

local environment of SAs under experimental conditions, as well as operando characterization of structural changes of SAs during catalytic reactions is still challenging despite the development of in situ microscopy and spectroscopy techniques.[16] The local environment determines the electronic structure, charge distribution and oxidation state of the SAs, and hence also the stability, activity and selectivity of the catalyst. Two main types of structures have been described for SACs; either substituting a cation at the oxide surface or supported on-top of the support, and these two types of SAs generally exhibit different catalytic properties.[17] Fabris et al. reported that substitutional Au^{3+} ions at the ceria surface, and not supported Au^{+} adatoms, activate molecular CO and oxidize it to CO_2.[18] In the case of cobalt oxide (CoO) supported Rh single-atom catalysts, Rh substituted at the Co site was shown to be active and selective towards propene hydroformylation[19], while Rh substituted at the O site (Rh_1Co_3 bimetallic single-cluster sites) exhibit an excellent catalytic performance in the reduction of NO with CO at low temperature[20] and a potential application in ammonia synthesis via N_2 reduction.[21] Datye and co-workers highlighted that atomically dispersed Pt on ceria can achieve a high activity for low-temperature CO oxidation after a steam treatment at 750 °C, which affects the environment of the single Pt atom on the support.[22]

There are several factors that can potentially affect the local structure of SACs, including specific pretreatment, reactants, intermediate species, and temperature. Here, we consider a single Rh atom supported on the rutile TiO_2 [110] surface to investigate the stability of different Rh structures under typical experimental conditions with first principles atomistic thermodynamics, in order to show how single atoms dynamically respond to reaction conditions. Stabilization of SAC requires strong interaction between the metal atom and the oxide, and although several oxides have been shown to be adequate (Fe_3O_4, TiO_2, CeO_2, Co_3O_4), TiO_2 avoids additional theoretical challenges linked with magnetic properties or

relativistic effects. We experimentally characterize single Rh atoms on rutile after different reduction steps under hydrogen by CO probe molecule infrared (IR) spectroscopy and scanning transmission electron microscopy (STEM) imaging.[23,24] The combination clearly demonstrates that Rh SAs change their structure and adapt their catalytic site under reaction conditions towards a structure active for CO_2 reduction to CO under hydrogen by reverse water gas shift (RWGS).

4.2 Methods

4.2.1 Sample Preparation

Rh SACs were synthesized by utilizing strong electrostatic adsorption principles at the low Rh weight loading of 0.05 wt%. The rutile TiO_2 support (US Nano # US3520, 30 nm diameter, 99.9% purity) and precursor (Sigma-Aldrich # 206261, Rhodium(III) chloride hydrate) were diluted in water separately at ratio of 4:1 and according to a support surface loading of 260m^2/l based on a measured TiO_2 surface area of 26m^2/g. NH_4OH was added to the separate support and precursor solutions to target a pH of 8.25. The precursor solution was injected at a rate of 4 ml/min into the support solution while constantly stirring. Then, the solution was heated to 70 °C until water evaporated and sample was dried completely. The sample was kept overnight in a 100 °C in an oven and then ex situ calcined in 10% O_2 in He for 4 h at 350 °C. XPS was done to indicate that no Cl remained on catalyst to influence local Rh structure (Figure 4.1).

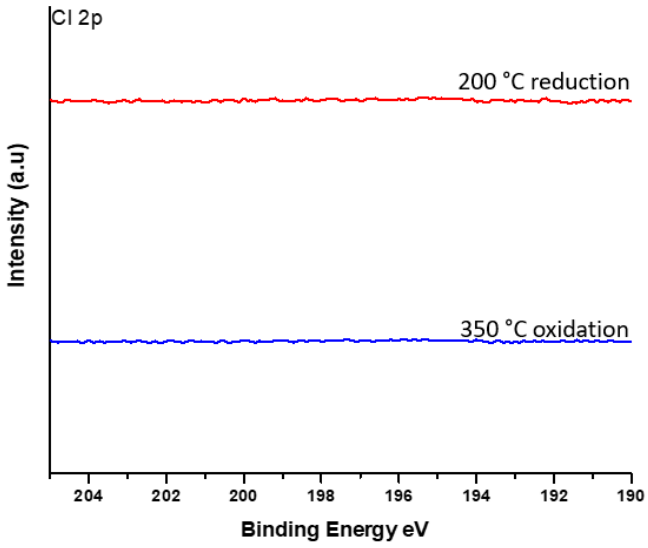

Figure 4.1: XPS spectra in Cl 2p region of Rh SAC on TiO_2 after oxidation in pure O_2 at 350 °C for 30 min and after reduction in 5% H_2 in Ar at 200 °C for 1 hour. After both samples were oxidized or reduced, they were vacuum sealed without exposure to air, transferred to a glovebox under inert gas to be mounted in the sample holder and then transferred directly into XPS for analysis.

4.2.2 FTIR Characterization

The catalyst was loaded in a Harrick low-temperature reaction chamber mounted inside a Thermo Scientific Praying Mantis diffuse reflectance adapter set in a Nicolet iS10 FTIR spectrometer with a Mercury Cadmium Telluride (MCT) detector and mass flow controllers (Teledyne Hastings) were used to control the gas flow rates across the reactor bed. Catalysts were pretreated in situ by either oxidation for 30 min at 350 °C in 10% O_2 in He, or subsequent reduction for 1 h at a specified temperature (100, 200, and 300 °C) in 10% H_2 in Ar. CO probe molecule IR was executed by decreasing the temperature following pretreatment in Ar below −120 °C in vacuum, then exposing to 10% CO in Ar for 10 min, followed by purging in Ar for 10min, and spectra collection. The temperature was then increased to room temperature and 10% CO in Ar was flown to the cell for 10 min and flushed with Ar prior to room temperature spectra collection.

4.2.3 STEM Characterization

The two samples were taken from the same batch of Rh SAC. Both samples were ex situ oxidized at 350 °C for 30 min in pure O_2 and then one was reduced at 100 °C and one at 300 °C for 60 min in 10% H_2 in He. Atomic resolution bright field (BF) and HAADF-STEM images were taken on JEOL Grand ARM 300CF TEM/STEM with double spherical aberration correctors operated at 300 kV with probe current of 23 pA and pixel time of 4 μs. BF image was taken with outer collection angle of 31 mrad and HAADF image was taken with 53–180 mrad
collection angle. Samples for STEM measurements were prepared by dropping 60 μl nanoparticles dispersion in methanol on a lacey carbon-coated copper grid.

4.2.4 XPS Characterization

The two samples were taken from the same batch of Rh SAC. Both samples were oxidized at 350 °C for 30 min in pure O_2 and then one was reduced at 200 °C for 60 min in 5% H_2 in Ar. After samples were oxidized or reduced, they were vacuum sealed without exposure to air, transferred to a glovebox under inert gas, and mounted on copper tape in a sample holder for XPS analysis. The sample holder was directly transferred from the glovebox to the chamber of the XPS to prevent air and moisture exposure. XPS characterization was carried out under vacuum using a Kratos AXIS ULTRA DLD XPS system equipped with an Al Kα monochromated X-ray source and a 165mm mean radius electron energy hemispherical analyzer. Binding energy calibrations were done with reference to the carbon 1s peak by adjusting spectra to 284.8 eV.

4.3 Results

4.3.1 Compared Stability of Various Sites

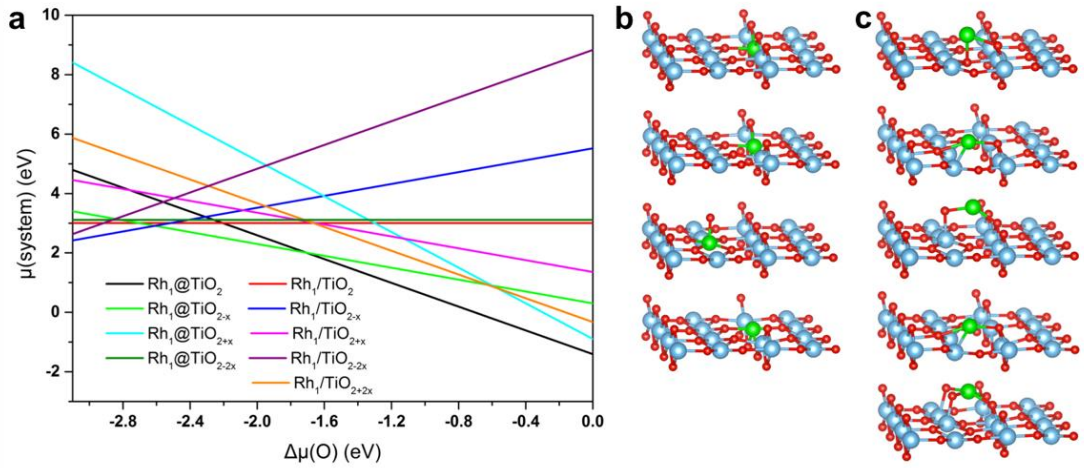

Figure 4.2: Stability and structure of substitutional(@) and supported(/) single atom Rh on the TiO_2 [110] surface including O vacancies or adatoms. a, Relative stability as a function of oxygen chemical potential Δμ(O). b,c, The optimal structures for substitutional (b) and supported (c) Rh SAs on the considered TiO_2 surfaces. The structures in b,c follows the placement and order in the legend of a. Color code: O-red; Ti-blue; Rh-green.result agrees with HAADF-STEM images for various oxide-supported SACs, which show the metal at the site of the oxide cation, suggesting that it tends to replace the metal cations in the oxides.[1,25]

The two main parameters controlling the structure of the Rh atom/TiO_2 [110] interface are the oxygen stoichiometry for the TiO_2 surface and the position of the Rh atom. We systematically studied the stoichiometric termination, two oxygen deficient ones (0.65 and 1.30 vacancies by nm^2) and one oxygen rich one (0.65 additional O by nm^2) and we explored a large range of positions for the Rh atom, in substitution of a Ti atom (denoted as Rh_1@support) or supported on the surface (denoted as Rh_1/support), and of relative positions between the Rh atom and the vacancies/additional O. This allowed us to generate multiple environments and electronic structures for the Rh atom. The stability of the various terminations can be compared using first-principles atomistic thermodynamic, using oxygen chemical potential (μ) as a descriptor (Ti chemical potential is then fixed from the bulk

energy of TiO_2). For each selected TiO_2 surface termination, and each type of Rh site (supported or substitutional), all Rh atom positions have been evaluated, but only the most stable one is considered in the surface stability diagram (Figure 4.2). Other positions and their relative energies can be seen in Figures 4A.1 and 4A.2.

Under oxygen-rich conditions (high chemical potential of oxygen, $-1.7 < \Delta\mu(O) < 0$), Rh substituted at the 6-fold Ti site in the stoichiometric TiO_2 ($Rh_1@TiO_2$) is the most favorable structure (Figure 4.2a). Terminations with additional O atoms, and Rh appearing as a supported oxide moiety ($Rh_1@TiO_{2+x}$, Rh_1/TiO_{2+2x}), are close in energy in the highest part of the interval, but never appear as most stable. Under oxygen-poor conditions, with a decreased $\mu(O)$, one oxygen vacancy is formed, and initially the Rh atom remains in the substitutional site ($Rh_1@TiO_{2-x}$), the vacancy corresponding to a surface O atom bridging Rh and Ti. If $\mu(O)$ is further decreased below -2.5 eV, the most stable configuration shifts from the substituted model ($Rh_1@TiO_{2-x}$) to the supported model (Rh_1/TiO_{2-x}). The most favorable structure for this adsorbed Rh atom is above an O-vacancy corresponding to a 3-fold subsurface oxygen, which is not the most stable vacancy position on the bare TiO_2 surface. Under typical conditions used during catalyst calcination (700 K in air, which is used to remove organic species deposited during catalyst synthesis), where $\Delta\mu(O)$ is calculated to be -0.78 eV, the substitutional structure is most favorable and the surface is stoichiometric. The local environment for $Rh_1@TiO_2$ is Rh_1O_6 with a calculated Rh charge of +1.84 |e| and a formal oxidation number of Rh(+4). A supported neutral Rh atom on stoichiometric TiO_2 (Rh_1/TiO_2) is ~3 eV less stable. Two additional O atoms can stabilize the supported Rh as a cation (RhO_2/TiO_2), but this structure remains ~1 eV less stable than the substitutional cation site. Changing the temperature and O_2 partial pressure does not affect the preferred structure for Rh (Figure 4.15A). Rh SAs always prefer to localize at the 6-fold Ti site under the

presence of O_2 gas even in cases of low O_2 partial pressure or rather high temperature. The result agrees with high-angle annular dark-field-STEM (HAADF-STEM) images for various oxide-supported SACs, which show the metal at the site of the oxide cation, suggesting that it tends to replace the metal cations in the oxides.[1, 25]

4.3.2 Stability in H_2 Reduction Conditions

Hydrogen can adsorb on the Rh atom or on the two-coordinated surface O atoms of TiO_2, and the optimal coverage at thermodynamic equilibrium depends on the H chemical potential μ(H) (Figure 4.16). Under a typical condition for H_2 reduction (0.1 atm H_2 at 500 K), where Δμ(H) is calculated to be -0.35 eV, a high coverage of H on the surface O atoms is reached with 7H in the selected unit cell (containing 8 two-coordinated O atoms) for Rh1@TiO_2 and Rh_1@TiO_{2-x}, and 6H for the other structures (Rh_1@TiO_{2-2x}, Rh1/TiO_2, Rh1/TiO_{2-x} and Rh1/TiO_{2-2x} respectively). The optimal hydrogenated structures are shown in Figure 4.17A. Rh at a substitutional site is coordinated to six O atoms, and hence unable to bind H. O vacancies, created preferentially near the Rh, lead to unsaturation and 1 (resp. 2) H binds to the substituted Rh in the presence of 1 (resp. 2) vacancies. In a rather similar way, the supported Rh atom binds 2 H atoms, if 1 or 2 O vacancies are present.

At the given μ(H) value, the relative stability for each model still depends on the chemical potential of oxygen, as shown in Figure 4.3a, in a similar way to Figure 4.21A. A major difference is that the high pressure of H_2 drives the system into an O poor condition. Under reduction conditions, H_2 will react with surface O atoms to form water and if we assume an H_2 conversion of 0.01% to H_2O, and still 0.1 atm H_2 at 500 K, Δμ(O) is then fixed at the low value of -3.23 eV. At this O chemical potential, the substitutional and supported Rh atom structures have almost the same free energy (Figure 4.3b) and hence both coexist at thermodynamic equilibrium. This supported Rh becomes stable versus the substitutional

cation upon the formation of two O vacancies around Rh, and in this situation, it is liganded to two H atoms. Therefore, Rh SAs on TiO_2 adapt their site from substitutional to supported when going from oxygen-rich preparation to H_2-reduction conditions. Mobility of TiO_2 surface at high temperature under H_2 allows the filling of the Ti vacancy formed after extraction of the Rh atom.[16]

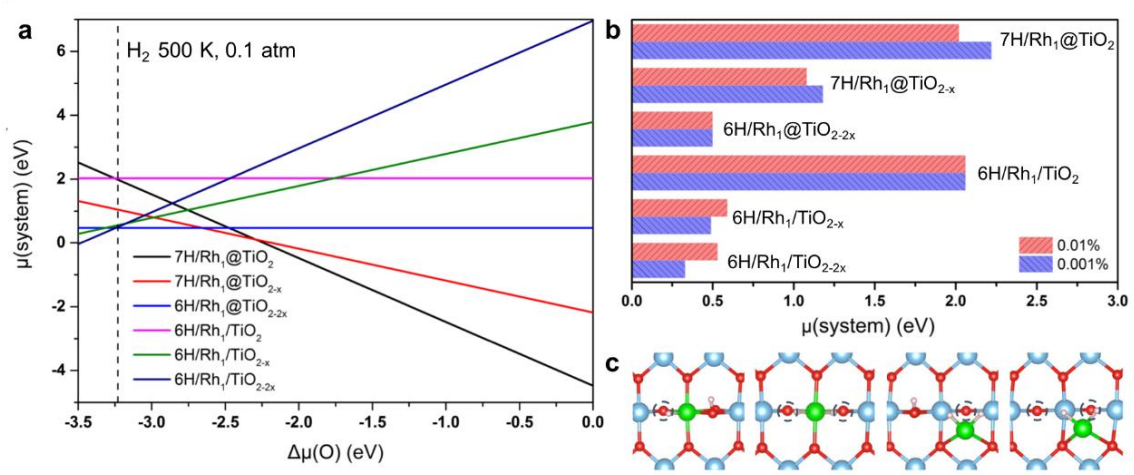

Figure 4.3: Stability of substitutional(@) and supported(/) single atom Rh on the TiO_2 [110] surface under a pressure of H_2. a, Relative stability as a function of Δμ(O) under a typical condition of H_2 reduction (H_2 pressure of 0.1 atm at 500 K, i.e. Δμ(H) = -0.35 eV). b, Free energy for different Rh atom configurations in specific condition corresponding to water formation equilibrium (Δμ(H) = -0.35 eV and Δμ(O) = -3.23 (-3.33) eV for 0.01% (0.001%) conversion). The dash line in a represents the condition (0.01% conversion) in b. c, The local environment of Rh SAs in $Rh_1@TiO_{2-x}$, $Rh_1@TiO_{2-2x}$, Rh_1/TiO_{2-x} and Rh_1/TiO_{2-2x} (from left to right). O vacancies are indicated by small dashed circles. Conversion fixes the pressure of H_2O. For instance, 0.01% conversion means a H_2O pressure of 10-5 atm. Then μ(O) is obtained by $\mu(H_2O) - \mu(H_2)$.

If Δμ(O) and Δμ(H) are independent, a 2D surface stability diagram can be constructed as a function of these two descriptors (Figure 4.4). High Δμ(O) stabilizes the substitutional sites, and low Δμ(O) the supported sites, but the frontier between the stability regions of the two sites (shown as a thick black line) is moved towards lower Δμ(O) when Δμ(H) (and hence the H coverage) is increased, especially in the temperature region corresponding to reduction conditions (400-600 K). This trend is explained by the strong adsorption energy of

H on Rh (-2.30 eV) in the presence of two O vacancies, which extends the stability of the green zone in Figure 4.4. Hence H_2 pressure stabilizes both the substitutional and the supported site, but the shift to very O poor conditions strongly favors the supported site, that becomes more stable.

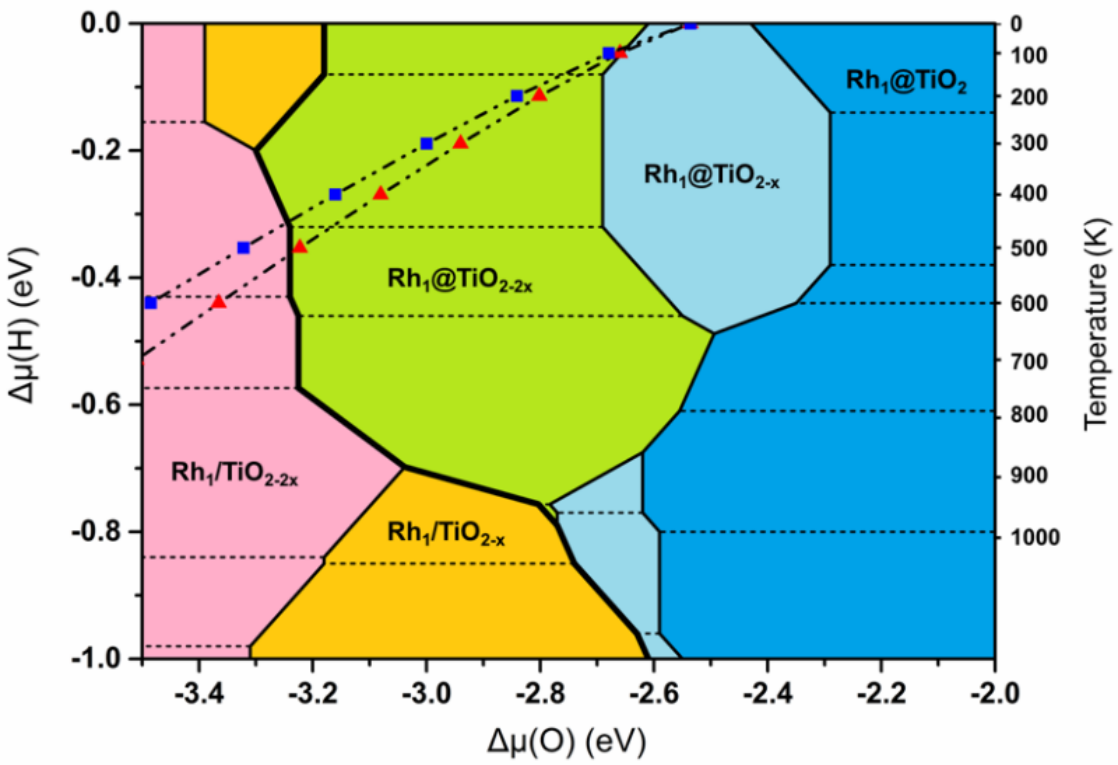

Figure 4.4: Surface stability diagram for single atom Rh on the TiO_2 [110] surface in the presence of H_2 as a function of H and O chemical potentials (noted Δμ(H) and Δμ(O)). Different colors indicate the various configurations for the Rh and the TiO_2 surface, where blue, light blue and green denote regions where Rh is preferentially substituting a 6-coordinated surface Ti with zero, one or two O vacancies ($Rh_1@TiO_2$, $Rh_1@TiO_{2-x}$, $Rh_1@TiO_{2-2x}$) and orange and pink zones where the supported Rh structure is favored (Rh_1/TiO_{2-x} and Rh_1/TiO_{2-2x}), respectively. The amount of H_2 adsorbed on the TiO_2 surface and the Rh atom depends on Δμ(H) and dash lines limit the zones corresponding to different H_2 coverage (see Figure 4.18A). The red (blue) triangle line shows the relation between Δμ(O) and Δμ(H) when water formation reaction is included with 0.01% (0.001%) conversion. Δμ(H) values for 0.1 atm H_2 and various temperatures are shown on the right vertical axis.

4.3.3 Stability Under CO Pressure

Upon submitting the system to a pressure of CO, its stability is governed by the O and CO chemical potentials. CO adsorbs on the supported single atom and all possible adsorption sites for single-atom Rh with one or two CO adsorbed have been tested (Figure 4.19A). The most stable structure for each Rh site, TiO_2 termination and CO coverage is chosen to establish the stability diagram. The complete 2D stability diagram, as a function of $\Delta\mu(O)$ and $\Delta\mu(CO)$, is shown in Figure 4.5a. Partial diagrams constrained to 1 CO or 2 CO adsorption for a fixed $\Delta\mu(CO)$ value can be seen in Figure 4.20A. Upon CO pressure, the zones corresponding to Rh being stable as a supported atom (purple in Figure 4.5a) are strongly extended. This is especially the case for a typical condition of CO adsorption used in volumetric chemisorption or probe molecule IR experiments (a 10% gas mixture of CO, and 90% He at atmospheric pressure and room temperature), in which $\Delta\mu(CO)$ is calculated to be -0.59 eV, a situation where the supported Rh is more stable than the substitutional one for the almost entire range of O chemical potential considered here (Figure 4.5a and 4A.9). CO adsorption hence completely changes the thermodynamic site preference for the Rh atom, irrespective of the presence of O vacancies. This is explained by the fact that CO adsorbs significantly more strongly on the supported Rh (-4.89 eV for $Rh1/TiO_2$), compared to the substitutional Rh (-2.74 eV for $Rh1@TiO_{2-2x}$). Charge density difference demonstrates that the strong interaction between Rh SAs and CO molecules results from not only Rh-C π -bonding but also back-donation from the metal towards the antibonding π^*CO orbital (Figure 4.5c, 4.5d).

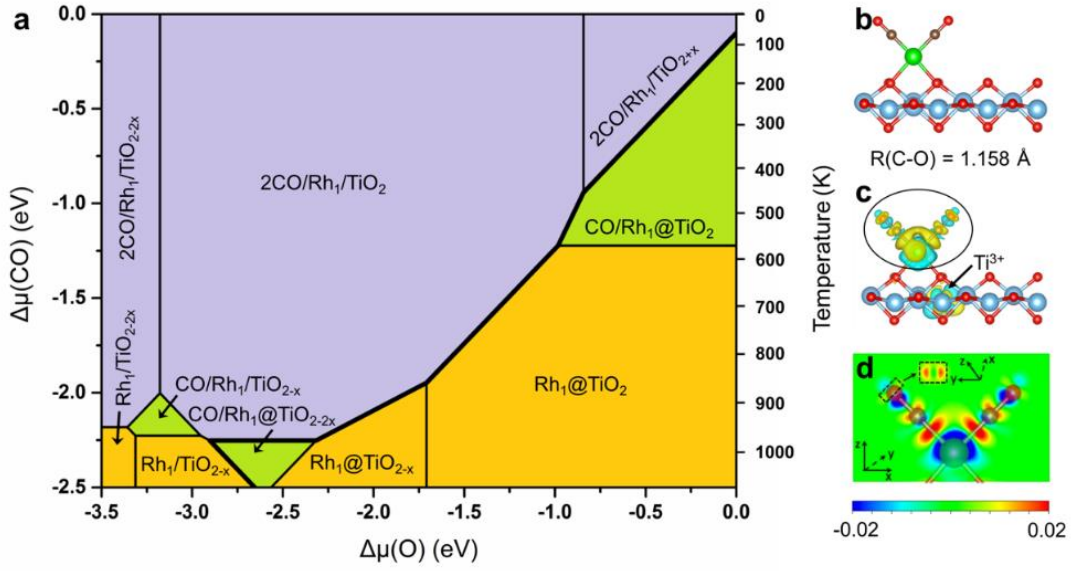

Figure 4.5: a) Surface stability diagram for single atom Rh on the TiO_2 [110] surface in the presence of CO as a function of CO and O chemical potentials. Colors indicate the different number of CO molecules adsorbed on Rh_1TiO_2, where orange, green and purple represent the 0CO, 1CO and 2CO, respectively. The temperature in right axis corresponds to the Δμ(CO) in left axis with 0.1 atom CO. b) The local environment of Rh1/TiO_2 in the presence of CO. c.d, The 3D (c) and 2D (d) representations of the charge density difference between $2CO/Rh_1/TiO_2$ and Rh_1/TiO_2, show the donation and back-donation electron transfers.

Hence thermodynamics under CO pressure tends to drive all Rh atoms to a supported site, if the temperature is high enough for kinetic aspects not to be limiting. Thus, the CO molecule plays a role in stabilizing the supported Rh SAs. Experimentally, CO is typically adsorbed on Rh after H_2 reduction, so the surface is partially reduced by H_2 with the formation of two oxygen vacancies and thus the most favorable structure under CO pressure should be $2CO/Rh_1/TiO_{2-2x}$.

To further illustrate the potential for Rh site modification of H_2 or CO adsorption, we can define the driving energy of the transformation as the difference of free energy between the most favorable supported site and the most favorable substituted site, a negative driving energy indicating that the site change towards the supported case is thermodynamically favorable. During CO adsorption, the driving energy is markedly negative, with a value of ~-

1.5 eV in the relevant region of chemical potential (see Figure 4.22Ab). This driving energy for site change is much stronger under a pressure of CO than under a pressure of H_2, where it becomes negative only at very low μ(O) and remains close to energy neutral. This result further proves that CO and H_2 molecules adapt the sites of SAs via different mechanisms and with different strength due to difference in their bonding mechanism.

4.3.4 Stability vs. Cluster Formation and FTIR Studies

Thermodynamic analyses hence show that Rh SACs on TiO_2 will adapt their sites in response to reaction conditions, such as under H_2 or CO pressure. Beyond its position on the oxide, the stability of the SA vs. clustering is another key aspect, especially when it is in supported situation and hence has potential mobility. Our calculations show that under a pressure of CO (2CO/Rh/TiO_2 structure), dimerization of the $Rh(CO)_2$ species is less stable by 1.14 eV (Figure 4.23A). Hence initial clustering of the SA is thermodynamically unfavorable. In addition, the Rh SA liganded to two CO is more stable than bulk Rh metal (Figure 4.23A), precluding the formation of large nanoparticles. Similarly, under H_2 reduction condition (6H/Rh/TiO_{2-x} structure), the dimerization of the RhH_2 surface species into a supported Rh_2H_4 unit is endothermic by 1.24 eV (Figure 4.23A). However, in that case, the H-liganded Rh SA is less stable than bulk Rh (Figure 4.3c). Since dimer formation is endothermic, the nucleation process is difficult, and the SA is metastable at reasonable temperature. There is hence a risk of particle formation only under H_2 at high temperature.

In order to validate our conclusions, we synthesized Rh SAs on rutile TiO_2 support, varied in situ pretreatments conditions, and used spectroscopy and microscopy to analyze the evolution of the Rh structure and TiO_2 support. CO probe molecule IR experiments were executed at −120 °C, which allows us to kinetically trap the structure, avoiding any changes induced by the adsorption of CO. CO adsorption on Rh SAs supported on TiO_2 has

previously been shown to yield a specific doublet of peaks at ~2097 and ~2028 cm^{-1}, associated with the symmetric and asymmetric stretches of the $Rh(CO)_2$ gem-dicarbonyl species.[26] Figure 4.6a shows the IR spectrum of CO adsorption at −120 °C on four differently in situ pretreated samples (oxidized at 350 °C, reduced at 100, 200, and 300 °C), to correlate with the predicted structures that would form in varying oxidation and reduction conditions. The pre-oxidized (350 °C in O_2 for 1 h) sample does not adsorb CO at −120 °C. This is fully consistent with aforementioned calculation results, since during O_2 pretreatment, O chemical potential is high (−0.61 eV) and Rh SAs are stabilized in a +4 oxidation state in the substitutional site of Ti ($Rh_1@TiO_2$), a situation where CO cannot adsorb on the Rh cation.

After reduction in H_2 at 100 °C, CO adsorbs on Rh at −120 °C with a predominant stretch at 2094 cm^{-1} and a very small accompanying stretch at 2026 cm^{-1}. The formation of a majority species with CO adsorbing to Rh atoms with a 1:1 stoichiometry agrees with calculations of the $Rh@TiO_{2-x}$ species, which show preference for the adsorption of single CO with a vibrational frequency of 2071 cm^{-1}. This is consistent with the pathway followed in Figure 4.4, where $Rh@TiO_{2-x}$ forms due to exposure of $Rh@TiO_2$ species (that do not adsorb CO) to mild reduction conditions. Further reduction in H_2 at 200 °C induces the growth of the stretch at 2031 cm^{-1} and a shift in the stretch at 2094 to 2097 cm^{-1}. This result is consistent with the calculations that predict the formation of the gem-dicarbonyl species $2CO/Rh_1/ TiO_{2-2x}$ (Figure 4.5b), and the calculated frequencies for CO are 2082 and 2023 cm^{-1}, in good agreement with the experimental values. However, when the reduction temperature is increased to 300 °C, one notes the appearance of a CO band at 2070 cm^{-1}, showing the agglomeration of Rh SAs in Rh clusters.

The primary conclusions of the CO probe molecule IR characterization were substantiated via ex situ atomic resolution STEM imaging of the Rh/TiO_2 sample following

reduction in H_2 at 100 and 300 °C, see Figure 4.6c, d and 4A.12. For the sample that had been reduced at 100 °C, single Rh atoms were primarily observed in all images. Alternatively, for the sample that had been reduced at 300 °C, a mixture of Rh clusters and SAs were observed. Both observations are in agreement with the interpretation of the CO IR characterization. It is interesting to note that while 300 °C reducing conditions in H_2 were observed to drive encapsulation of Rh particles by reduced TiO_2 overlayers (see Figure 4.7), the combination of CO IR and STEM imaging presented here suggests that single Rh atoms will not be encapsulated by TiO_2 under similar conditions.[27]

When CO adsorption is performed at 20 °C, all three reduced samples show similar $Rh(CO)_2$ spectral features, suggesting that CO adsorption, when the temperature is high enough to allow atom mobility, drives Rh atoms to similar supported $Rh(CO)_2$ geometries, even though they may be in different starting locations, Figure 4.6b. The small difference in the CO stretch frequencies likely derives from small differences in surface Ovacancy coverage on the TiO_2 support. From the sample pretreated at 300 °C, the feature at 2070 cm^{-1} disappears after CO adsorption at 20 °C, showing that supported Rh particles can be readily fragmented to Rh SAs in the presence of CO, see Figure 4.6b, in line with the calculated high stability of supported SAs in these conditions.[28] This scenario is reminiscent of the dynamic SA formation during nanogold catalysis.[29–31] As expected, the intensity of the symmetric stretch (~2090 cm^{-1}) at 20° C is stronger than that of the asymmetric stretch (2023 cm^{-1}) for the $Rh(CO)_2$ species due to the existence of nearby O vacancies in TiO_2, but the exact ratio of intensity depends on reduction conditions.

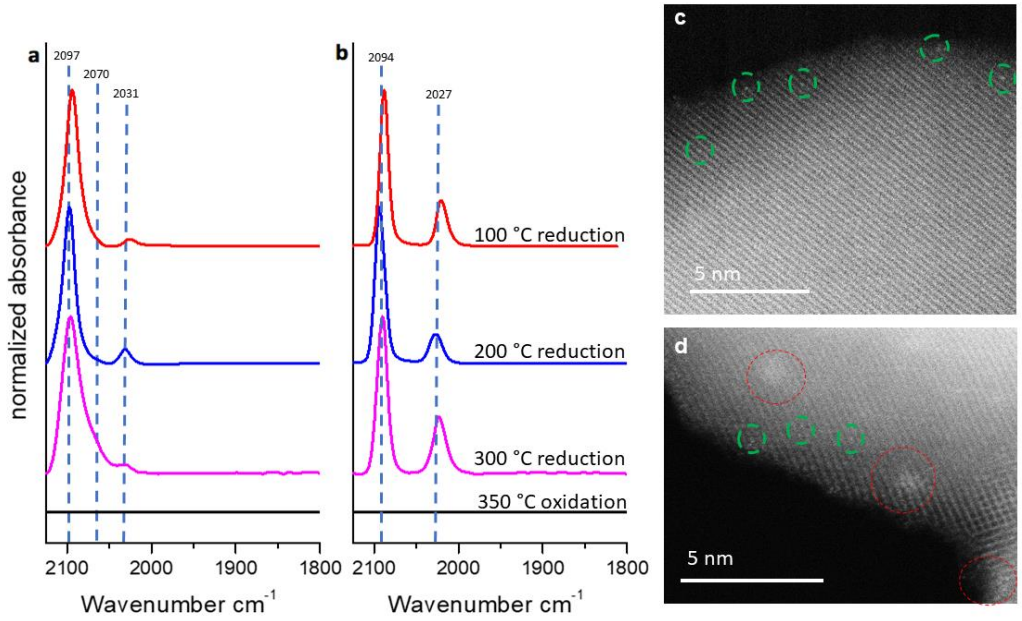

Figure 4.6: Experimental analysis of Rh SAC on TiO_2 following varying environmental treatments. IR spectra of CO adsorbed at full saturation coverage following varied pretreatment conditions (oxidized at 350 °C, reduced at 100 °C, 200 °C and 300 °C) measured at a. -120 °C and b. 20 °C. Corresponding representative high-angle annular dark-field (HAADF) STEM images of c. 100 °C H_2 reduction case in which single Rh atoms are observed and d. 300 °C H_2 reduction case in which small Rh clusters and Rh single atoms are observed. Green circles identify the single Rh atoms, while red circles identify Rh clusters.

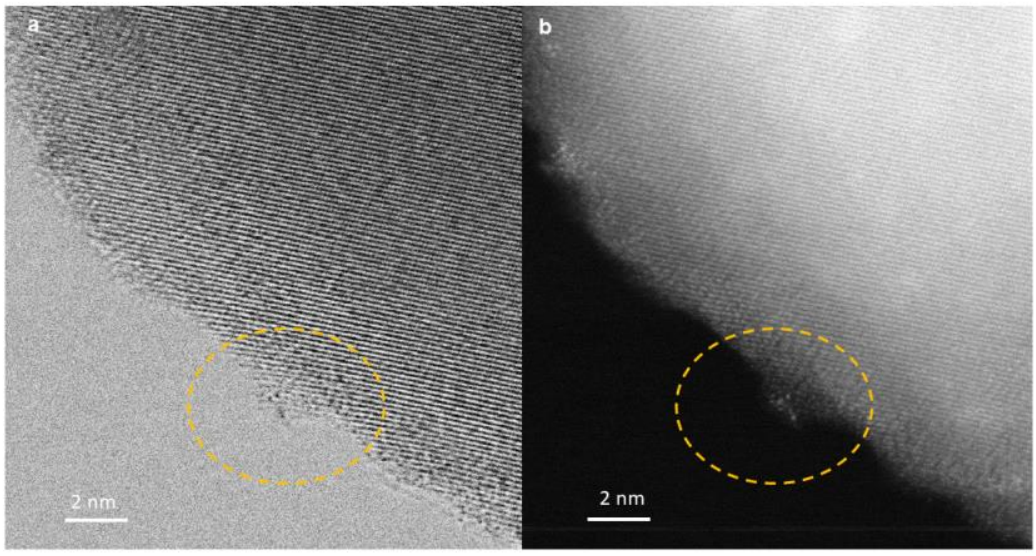

Figure 4.7: a. 300 °C H_2 reduced sample in which SMSI formation over small Rh clusters can be observed in the Bright Field (BF) image and b. corresponding HAADF image where small Rh cluster can be observed.

It should be noted that for the pre-oxidized Rh sample, exposure to 20 °C CO does not change the properties at all, Figure 4.6b, and in fact exposure to CO at 300 °C is required to induce O-vacancy formation that enables CO adsorption, Figure 4.8. That is because the stable and highly coordinated substitutional site cannot provide an adsorption site for CO, so that CO is unable to interact and to transform the site to the supported structure. Hydrogen hence has a special role in creating O vacancies around the substitutional Rh cation, reducing its coordination and opening a channel for CO adsorption, and subsequent migration of the CO stabilized Rh species. The creation of oxygen vacancies when CO acts alone as a reductant at 300 °C is further evident because CO_2 was observed to form, presumably through oxidation by TiO2 lattice oxygen, and these O vacancies in turn enabled the formation of $Rh(CO)_2$ species, Figure 4.6.

X-ray photoelectron (XPS) spectra showed a downshift of the XPS Ti 2p core level by 0.3 eV, from 459.0 to 458.7 eV, when comparing oxidation at 350 °C to reduction under hydrogen at 200 °C, indicating a reduction of some of the Ti in the sample, most likely at the surface of the oxide nanoparticle as indicated by the DFT calculations. Additionally, the O1s level in the reduced case is also downshifted by 0.4 eV, together with the appearance of a new feature at higher (+1.9 eV) binding energy, Figure 4.9 .[32,33] This peak is assigned to the formation of surface hydroxyls under hydrogen pressure. In addition, by using the integrated area of the Ti and O peaks and associated sensitivity factors, it was observed that the O:Ti ratio decreased by 5% after reduction.[34] The XPS and IR results are in agreement with the DFT calculations, and that reduction of the Rh/TiO_2 catalysts induces hydroxylation and oxygen vacancy formation, which in turn drive the switch in the preferred Rh local coordination, enabling interaction with adsorbates.

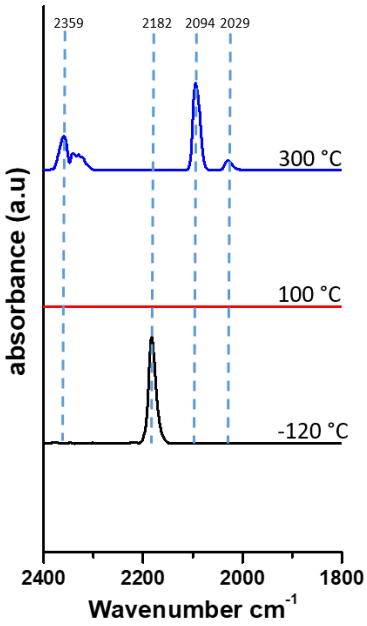

Figure 4.8: IR spectra of Rh SAC on TiO_2 that had been pre-oxidized at 350 °C and then exposed to CO at -120 °C where CO adsorbs onto Ti^{+4} (evident by 2182 cm^{-1} peak) , 100 °C where no CO is adsorbed, and 300 °C where CO acts as a reducing agent to create oxygen vacancies (evident by CO_2 2359 cm^{-1} peak) so that CO may adsorb onto Rh (evident by 2094 and 2029 cm^{-1} peaks).

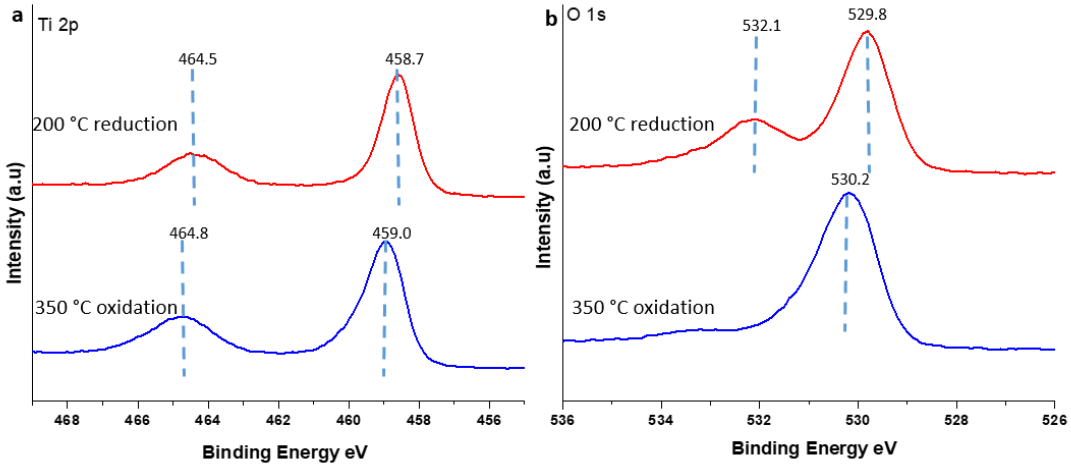

Figure 4.9: a) XPS spectra in Ti 2p region b) XPS spectra in O 1s region of Rh SAC on TiO_2 after oxidation in pure O_2 at 350 °C for 30 min and after reduction in 5% H_2 in argon at 200 °C for 1 hour. After both samples were oxidized or reduced, they were vacuum sealed without exposure to air, transferred to a glovebox under inert gas to be mounted in the sample holder and then transferred directly into XPS for analysis.

4.3.5 Catalytic Reactivity

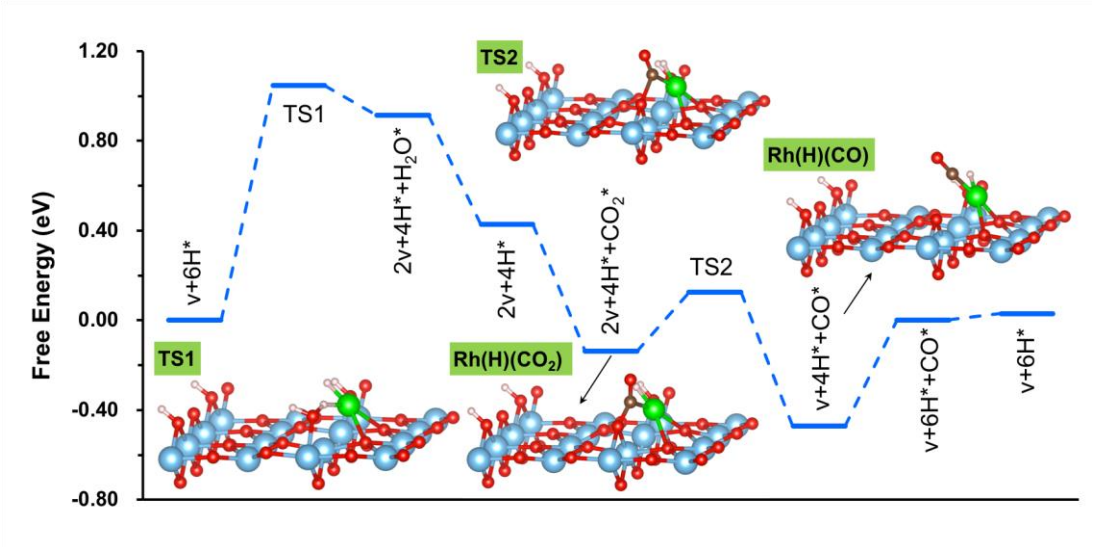

Figure 4.10: Free energy profile of RWGS reaction on the supported structure of the Rh atom $6H/Rh_1/TiO_{2-x}$ by the dissociation mechanism. The first steps correspond to water formation and additional O vacancy creation, followed by easy activation of CO_2 forming CO. Color code: O-red; Ti-blue; Rh-green. T = 500 K and pressure in experimental conditions at equilibrium are used to evaluate free energies (Appendix Table 4.1). The rate controlling intermediate is the supported Rh(H)(CO) unit.

In a nutshell, the combination of theory and experiment shows here that Rh atoms adapt their binding site to the presence of various reactants (O_2, H_2, and CO). It is hence important to explore whether this adaptive character has an impact on catalytic properties. We selected the RWGS reaction as an example for this purpose since when submitting a mixture of CO_2 and H_2 to a Rh on TiO_2 catalyst, it was shown that dispersed Rh SAs are active and selective for CO formation (from RWGS), while Rh nanoparticles lead to methanation.[35]

Under reaction condition (500 K, 10 CO_2:1 H_2), $6H/Rh_1@TiO_{2-2x}$ and $6H/Rh_1/TiO_{2-x}$ are the most favorable hydrogenated structures for substitutional and supported models, respectively (Appendix Table 4.1). Hence, both structures were considered as initial state for the RWGS pathways and considering two mechanisms: via CO_2 dissociation or COOH-

mediated. In the first case, the key step is the direct dissociation of CO_2 to CO, while for the second possibility, adsorbed CO_2 will react with surface OH species to form COOH that dissociates to OH and CO species.[36] For the supported Rh atom structure $6H/Rh_1/ TiO_{2-x}$, the CO_2 dissociation path is the most favorable and the first step consists in forming a second O vacancy, necessary to activate CO_2. One of the two H on Rh reacts with a neighboring OH species, forming one water and one oxygen vacancy, with a barrier of 1.05 eV (Figure 4.10 and Appendix Table 4.2). Water easily desorbs at reaction temperature, creating a vacancy site where CO2 can adsorb in an exergonic way, with an adsorption internal energy of −1.70 eV and a bent geometry, indicating a strong activation of CO_2 at this site. Then, the dissociation of CO_2 to CO occurs with a very low activation barrier (0.26 eV), the CO naturally coordinating to the Rh atom. The final steps (H_2 dissociative adsorption and CO desorption) occur easily, but the order is important since H_2 adsorption assists CO desorption. According to the energetic span model[37], the effective barrier of the reaction is 1.52 eV. In contrast, the reaction is much more difficult if one starts from Rh in substitution of Ti in $6H/Rh_1@TiO_{2-2x}$. The Rh atom is saturated by two H atoms and, in order to create an adsorption site for CO_2, one H must be transferred to a nearby O atom (Figure 4.25A Table 4.3). Reaction with a surface –OH species to form H_2O is not allowed here, since it is endothermic (+1.49 eV) with a barrier of 3.00 eV. Transfer to subsurface oxygen is still not favorable, with an endothermic energy of +1.46 eV and a barrier of 2.30 eV. Activation of the Rh center for RWGS is hence not possible, and the substitutional structure for the Rh atom is not catalytically active, because the strong adsorption energy of hydrogen on Rh prevents CO_2 adsorption. This indicates clearly that the active site for Rh SAC on TiO_2 in the case of the RWGS reaction is the supported site rather than the substitutional site. Further electronic structure analysis (Figure 4.25A) shows that Rh, liganded to two H atoms, is

slightly negatively charged (−0.06 |e|) in $6H/Rh_1/TiO_{2-x}$ and that its oxidation state is zero. In the unit cell, four protons and one vacancy provide six electrons. Five Ti^{3+} are located at the surface of the unit cell (representing 31% of surface Ti cations) and one electron is shared on the RhH_2 unit. After creation of another vacancy by desorption of H_2O (2v + 4H* intermediate on Figure 4.10), one more Ti^{4+} is reduced to Ti^{3+} on the surface and Rh gains further electronic population (charge: −0.50 |e|). This negatively charged Rh can transfer electron to CO_2, and promote the adsorption and activation of CO_2.

The steady-state nature of the catalyst in reaction conditions is given by the most stable intermediate along the profile. For the supported Rh on TiO_2, this corresponds to the coadsorption of CO and H on Rh, with three additional H adsorbates and one O vacancy on the TiO_2 unit cell (Rh(H)(CO) in Fig 4.9). In reaction conditions, it is 0.21 eV (Supplementary Table 1) more stable than the best substitutional site, which in the same conditions bears two H on the Rh and four H adsorbates and two O vacancy on TiO_2. This Rh(H)(CO) structure is supported experimentally by in situ Fourier-transform infrared spectroscopy (FTIR) measurements under the same reaction conditions where a linear CO bonded to Rh appears at 2049 cm^{-1}, close to the calculated value 2044 cm^{-1} (Figure 4.11a). Post-reaction analysis showed that the Rh species retained its SA structure (Figure 4.11b). The catalytic activity (turn over frequency, TOF) was calculated from the pathway (and in the conditions) of Figure 4.10 by using the energetic span approach.[37] The value obtained (0.0056 s^{-1}) is in qualitative agreement with the measured TOF values in similar conditions (~0.01 s−1).[3]. Comparing the theoretical and experimental results obtained here for rutile TiO_2 supported single Rh atoms with reactivity measurements made on P25 mixed-phase TiO_2 supports is justified based on CO IR measurements that suggest single Rh species localized on rutile domains of the P25 TiO_2 support (Figure 4.12). Hence, the experimental

and theoretical analysis agrees on the most stable species under reaction conditions and the TOF. This strongly validates our conclusion that, during RWGS reaction, Rh atoms will tend to move from the substitutional site favored during catalyst synthesis toward the supported site, more stable but also catalytically active.

By a combination of first-principles modeling and experiment, we have shown that single Rh atoms on TiO_2 could dynamically adapt their site to the reaction conditions under reduction condition. This finding is consistent with the stability analyses of SAs on oxide surface that can vary with the site and reaction conditions.[29,38] The allusion of statically anchoring for a stable single metal atom on an oxide support can be misleading under such circumstances. In oxidative conditions, Rh prefers to substitute the six-coordinated Ti atoms in the surface plane of the oxide. In contrast, under a pressure of H_2 or CO, it prefers to be supported on-top on the oxide. The roles of H_2 and CO are however distinct in this scenario. CO efficiently stabilizes the supported site when adsorbed on it, but is unable to interact with the initial saturated substitutional site. In contrast, the stabilization induced by hydrogen is weaker, but it can decrease the Rh cation coordination by creation of O vacancies and hence open a channel for CO adsorption. In addition, the single metal atom is not bare, but covered by H atoms and/or CO molecule(s) in catalytic conditions. FTIR measurements of CO adsorption on SA Rh following varied pretreatment confirms the site change trend obtained from the calculations and show that the transformation is kinetically accessible.

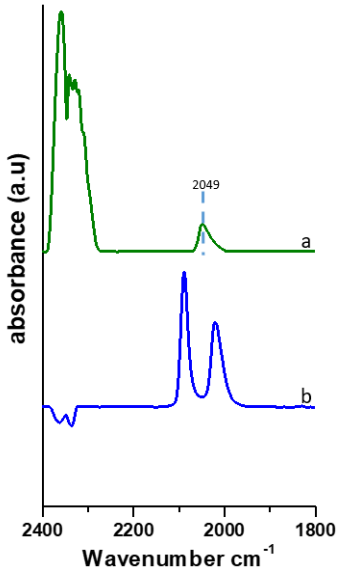

Figure 4.11: In-situ FTIR a) of Rh SAC on TiO_2 after reduced in 10% H_2 in argon for at 200 °C for 1 hour and exposed to reaction conditions (200 °C, $10CO_2$:$1H_2$) for 30 minutes. b) Same Rh SAC on TiO_2 after exposed to reaction conditions, purged in argon at 200 °C, cooled for 1 hour in argon to 20° C, exposed to 10% CO in argon for 10 min, and then purged in argon for 10 min.

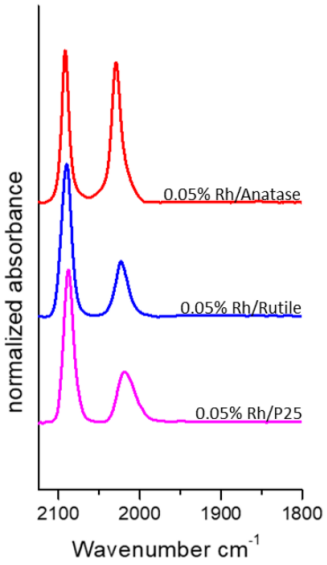

Figure 4.12: CO probe molecule IR spectra of 0.05% Rh SAC using TiO_2 supports with different phases (Anatase, Rutile, and P25) that have undergone the same synthesis and pretreatment conditions (350 C oxidation and 200 C reduction in H_2) and were then exposed to CO at 20 °C. The ratio of the symmetric stretch to the asymmetric stretch of Rutile and P25 are in close agreement, indicating the same Rh SAC site is identified, whereas the Rh SAC on Anatase creates a ratio closer to 1 and thus constitutes a different Rh SAC active site.

This adaptive character of the SA can only be accessed by operando studies and can be crucial for its catalytic reactivity, as illustrated here with the RWGS reaction. The as-prepared SAs, placed in substitution of titanium, are inactive for this reaction even after reduction by hydrogen and vacancy creation around the Rh. Especially noteworthy is the finding that the reductive condition of the reaction promotes the change of the site from substitution toward the supported structure, a situation where the SA is covered by H and CO and becomes catalytically active. FTIR during reaction again confirms the result. The H_2 reactant, further assisted by the CO product, hence in situ switches the inactive as-prepared catalyst precursor into a highly active species. The dual character of the SAC with an off-site and an on-site, switchable through specific chemical interactions, could also explain the controversy in the literature on the inactive or active character of SAC, for example, in the case of Pt for CO oxidation and water gas shift reaction.[24,39,40]

Restructuring under reaction conditions is not a privilege of SAs, but also occurs for catalytic clusters and nanoparticles, as shown by in situ studies.[41] A key difference is that with SAs, the support plays the primary role in driving the reconstruction. In the present case, we showed that the change in oxidation state and coordination environment of Rh is driven by OH formation and O-vacancy formation at the TiO_2 surface. In contrast, the dynamical behavior of a metal cluster in reaction conditions, although affected by the state of the support, is primarily driven by the metal cluster thermodynamics.

Our findings have provided insights on the critical questions of stability of heterogeneously supported SAs under reactive condition and the dynamic position changes of these atoms in redox reactions. The approach, and the proposed link between the transformation of the support and the restructuring of the metal, can in principle be extended to other SAC with similar metals (Rh, Pt, Ni, etc.) on reducible oxides (Fe_3O_4, CoO, CeO_2) in

order to understand how the chemical nature of oxide and metal controls the restructuring process. The message from the present study is that as-prepared catalysts provide structures with the metal at high oxidation state occupying the oxide cation position, and that migration to a more reduced, supported and adequately liganded structure might be required for optimal catalytic activity. Our results provide a detailed understanding of the local structure of SAs on oxide support and their adaptive and dynamic character under realistic catalytic conditions, which are key insights that chemists should have in mind when designing single SACs.

4.4 Appendix

Via Tang, Y.[1,2], Li, J.[1], and Sautet, P.[2] at Department of Chemistry and Key Laboratory of Organic Optoelectronics and Molecular Engineering of the Ministry of Education, Tsinghua University;[1] and Department of Chemical and Biomolecular Engineering, University of California, Los Angeles.[2]

4.4.1 Methods

4.4.1.1 DFT Parameters

All the calculations were performed using periodic DFT method implemented in the Vienna Ab initio simulation package (VASP) code. [42,43] The projector augmented wave[44] method was used for the interaction between the atomic cores and valence electrons. The valence orbitals of Ti (3p, 4s, 3d), Rh (4d, 5s), O (2s, 2p), C (2s, 2p), and H (1s) were described by plane-wave basis sets with cutoff energies of 400 eV. The exchange-correlation energies were calculated by the generalized gradient approximation with the Perdew–Burke–Ernzerhof functional[45]. Spin polarization was considered using unrestricted Kohn–Sham formalism. To correct the strong electron-correlation properties of these oxides, DFT + U calculations[46,47] were performed with U = 4.2 eV for Ti, which is taken from the

literature.[48,49] The force threshold on each relaxed ion was set as 0.02 eV/Å. Monkhorst–Pack (1 × 1 × 1) Γ-centered k-points grid sampling within the Brillouin zones were used because of the large size of the surface models. The location and energy of transition states were calculated with the climbing-image nudged elastic band and dimer methods.[50,51] Vibrational analysis was further used to confirm the transition states with only one imaginary frequency. Computational models. The rutile TiO_2 [110] surface was modeled as periodic slabs with 12 layers (four tri-layers), with a vacuum gap between slabs at ~15 Å. A 4 × 2 surface cell was utilized and the bottom three layers were kept fixed to their bulk position. In this work, we calculated the adsorption energies according to the following equation: Eads = E(slab+adsorbate) − E(slab) − E(adsorbate), where E(slab+ adsorbate), E(slab), and E(adsorbate) are the calculated electronic energy of species adsorbed on the surface, the bare surface, and the gas-phase molecule, respectively. Similarly, the desorption energy is defined as Edes = E(slab+ desorbate)− E(slab)− E(desorbate) and the reaction energy is defined as ΔE = E(products) − E(reactants). The charge density differences were evaluated using the formula Δρ = ρA +B − ρA − ρB, where ρX is the electron density of X. Atomic charges were computed using the atom-in-molecule scheme proposed by Bader.[52]

4.4.1.2 Stability Descriptor.

The system chemical potential μ(system) was used to measure the stability of different models with a consistent reference:

$$\mu(\text{system}) = E(\text{system}) - n(\text{O})\mu(\text{O}) - n(\text{TiO}_2)\mu(\text{TiO}_2) - (E(\text{TiO}_2) + \mu(\text{Rh}))$$

where E(system) is the VASP calculated energy of Rh_1TiO_2 structures, and E(TiO_2) is the energy of the bare TiO_2 surface. The μ(Rh) and μ(TiO_2) represent the chemical potential of bulk Rh and TiO_2, respectively, and μ(O) is the free energy of oxygen atom. Bulk solid

chemical potentials are taken from optimized DFT structures. The n values are set to balance the stoichiometry relative to a standard Rh_1TiO_2 system, namely, the TiO_2 surface slab and bulk Rh. The relative free energy is calculated for each system by subtracting the energy of this standard system.

The chemical potential of oxygen atom, μ(O), is calculated as a function of temperature T and oxygen partial pressure P, using

$$\mu(\mathrm{O}) = 1/2[E(\mathrm{O_2}) + \Delta\mu(\mathrm{O_2}(T,P))]$$

where Δμ(O) is the value of μ(O) when using the half of E(O2) as zero reference.Similar definitions are used to Δμ(H) and Δμ(CO).

When we consider the absorbed species, the chemical potential of system with adsorbed species μ(system-ads) can be estimated by

$$\mu(\mathrm{system-ads}) = \mu(\mathrm{system}) + E_{\mathrm{ads}} - \Delta\mu_{\mathrm{ads}}(T,P).$$

For H_2 reduction, it should be

$$\begin{aligned}\mu(\mathrm{system-H}) = {} & E(\mathrm{system-H}) - n(\mathrm{O})\mu(\mathrm{O}) - n(\mathrm{TiO_2})\mu(\mathrm{TiO_2}) \\ & - (\mathrm{E(TiO_2)} + \mu(\mathrm{Rh})) - n(\mathrm{H})\mu(\mathrm{H}),\end{aligned}$$

where μ(system) is the chemical potential of system without adsorbed species; Eads is the adsorption energy for adsorbed species and μads(T,P) is the chemical potential of adsorbed species. In the case of H_2 reduction, an additional variable μ(H) is introduced, and μ(O) is given by

$$\mu(\mathrm{O}) = \mu(\mathrm{H_2O}) - \mu(\mathrm{H_2})$$

4.4.2 Free Energy Calculations: System Chemical Potential

The system chemical potential μ(system) is calculated, using Eq. 1, for each configuration from the following formulas:

$\mu(Rh1/TiO_2) = E(Rh_1/TiO_2) - (E(TiO_2) + \mu(Rh))$ for supported single-atom Rh1 on TiO_2 surface.

$\mu(Rh_1@TiO_2) = E(Rh_1@TiO_2) - 2\mu(O) + \mu(TiO_2) - (E(TiO_2) + \mu(Rh))$ for substituted single-atom Rh_1 on TiO_2 surface.

$\mu(Rh_1/TiO_2{+}nx) = E(Rh_1/TiO_{2+nx}) - n\mu(O) - (E(TiO_2) + \mu(Rh))$ for supported single-atom Rh_1 on oxidized TiO_2 surface, n means the number of extra O atoms.

$\mu(Rh_1@TiO_{2+nx}) = E(Rh_1@TiO_{2+nx}) - (n+2)\mu(O) + \mu(TiO_2) - (E(TiO_2) + \mu(Rh))$ for substituted single-atom Rh_1 on oxidized TiO_2 surface, n means the number of extra O atoms.

$\mu(Rh_1/TiO_{2-nx}) = E(Rh_1/TiO_{2-nx}) + n\mu(O) - (E(TiO_2) + \mu(Rh))$ for supported single-atom Rh_1 on reduced TiO_2 surface, n means the number of oxygen vacancies.

$\mu(Rh_1@TiO_{2-nx}) = E(Rh_1@TiO_{2-nx}) + (n-2)\mu(O) + \mu(TiO_2) - (E(TiO_2) + \mu(Rh))$ for supported single-atom Rh1 on reduced TiO2 surface, n means the number of oxygen vacancies.

4.4.3 Appendix Figures and Tables

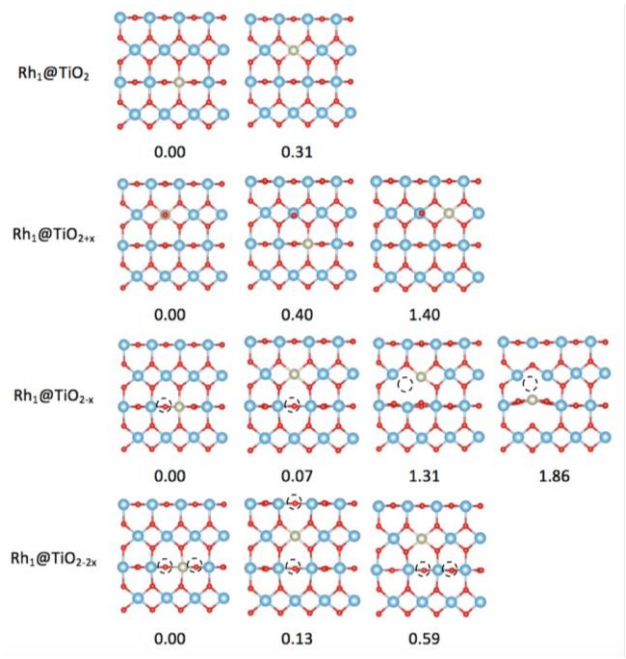

Figure 4.13A: Possible adsorption sites for single-atom Rh in substituted models. The value under each configuration means the relative energy between it and the most stable one. Color code: O-red; Ti-blue; Rh-gray. The dashed circle represents the oxygen vacancy site.

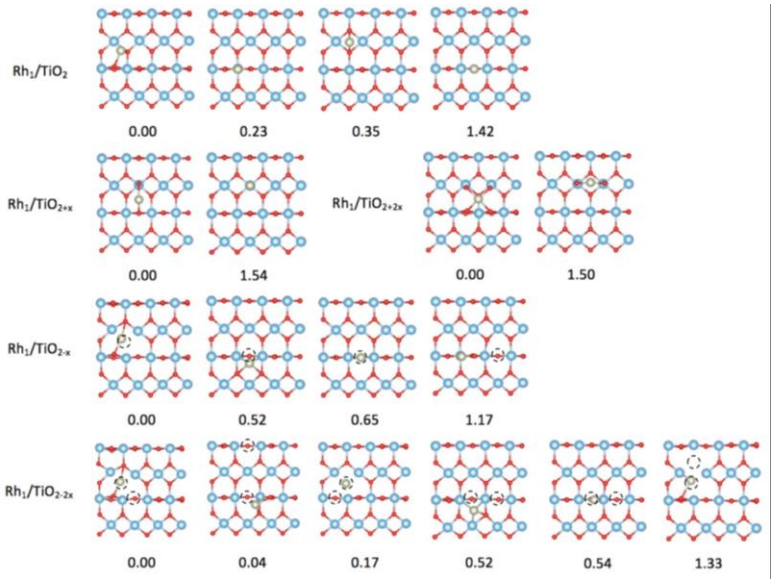

Figure 4.14A: Possible adsorption sites for single-atom Rh in supported models. The value under each configuration means the relative energy between it and the most stable one. Color code: O-red; Ti-blue; Rh-gray. The dashed circle represents the oxygen vacancy site.

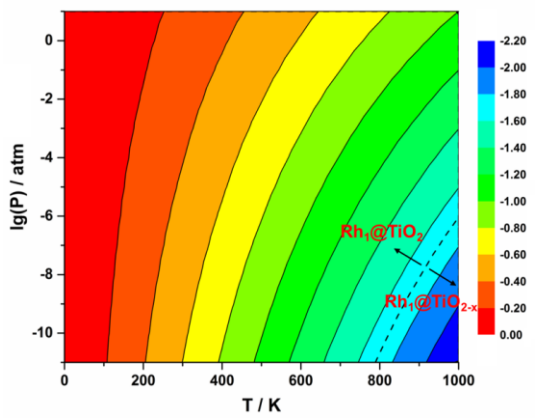

Figure 4.15A: Phase diagram for most stable single-atom Rh states on TiO_2 [110] surface. The color represents the value of chemical potential of oxygen, which depends on pressure and temperature of oxygen molecule. The dashed line means the boundary line between $Rh_1@TiO_2$ and $Rh_1@TiO_{2-x}$.

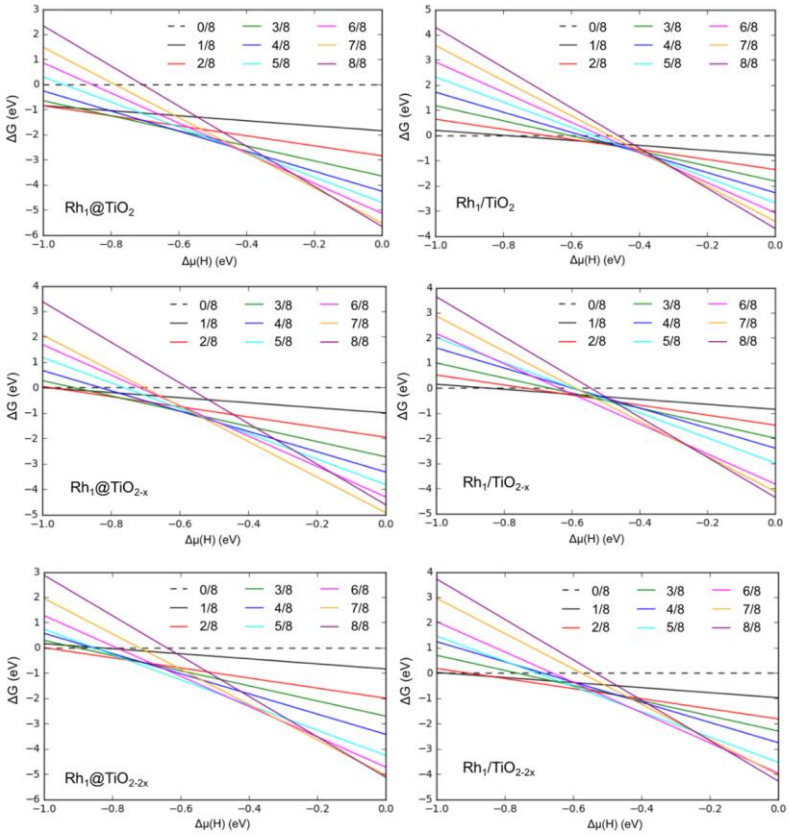

Figure 4.16A: The energy change with different coverages of hydrogen on various Rh_1TiO_2 models as a function of Δμ(H). The ΔG represents the energy difference between the hydrogen-adsorbed system and the initial system without hydrogen atoms on the surface.

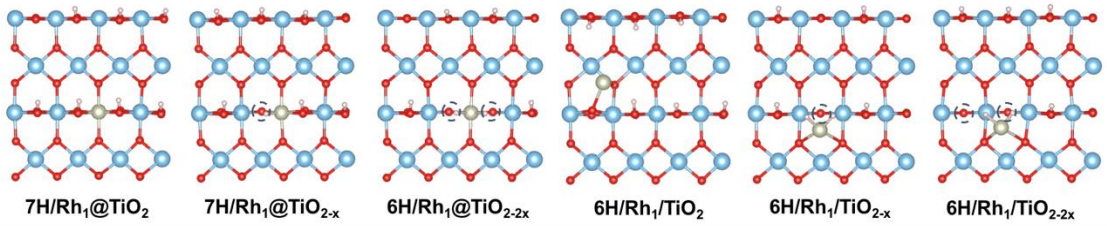

Figure 4.17A: Optimized configurations for hydrogen adsorbed on Rh_1SiO_2 SACs. Color code: O-red; Ti-blue; Rh-gray. The dashed circle represents the oxygen vacancy site.

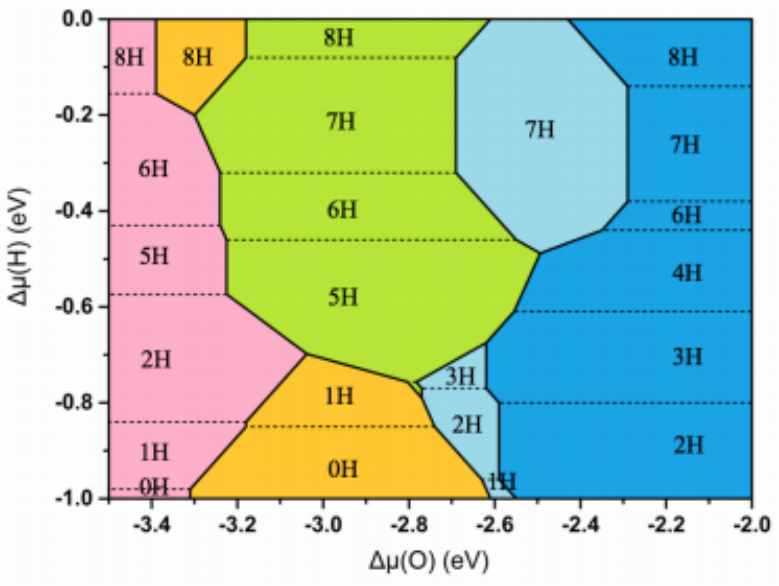

Figure 4.18A: Surface stability diagram for single atom Rh on the TiO_2 [110] surface in the presence of H_2 as a function of H and O chemical potentials (noted $\Delta\mu(H)$ and $\Delta\mu(O)$). The amount of hydrogen adsorbed on the TiO_2 surface and the Rh atom depends on $\Delta\mu(H)$ and dash lines limit the zones corresponding to different hydrogen coverage. Different colors indicate the various configurations for the Rh and the TiO_2 surface, where blue, light blue, green, orange and pink regions denote $Rh_1@TiO_2$, $Rh_1@TiO_{2-x}$, $Rh_1@TiO_{2-2x}$, Rh_1/TiO_{2-x} and Rh_1/TiO_{2-2x}, respectively.

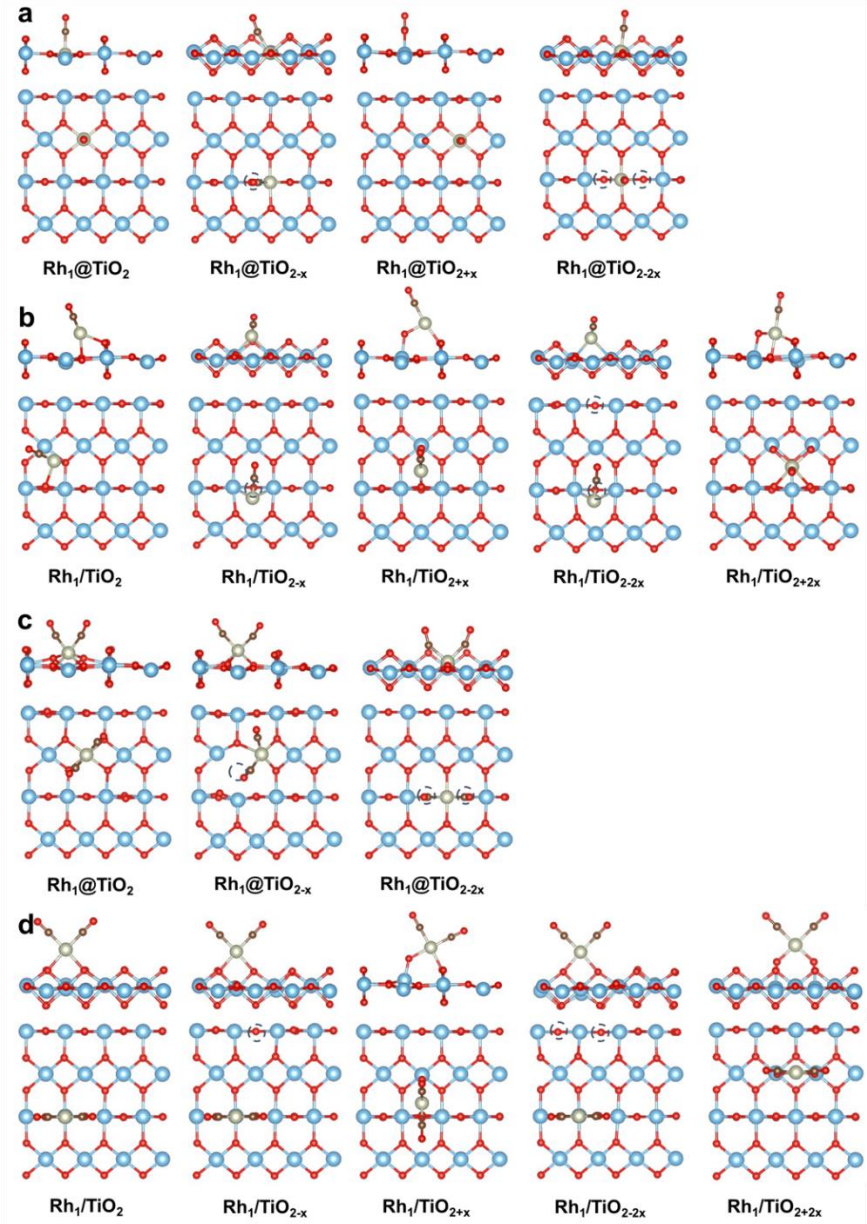

Figure 4.19A: Optimized configurations for CO adsorbed on Rh_1SiO_2 SACs. a,b, one CO adsorption. c,d, 2CO adsorption. Color code: O-red; Ti-blue; Rh-gray. The dashed circle represents the oxygen vacancy site.

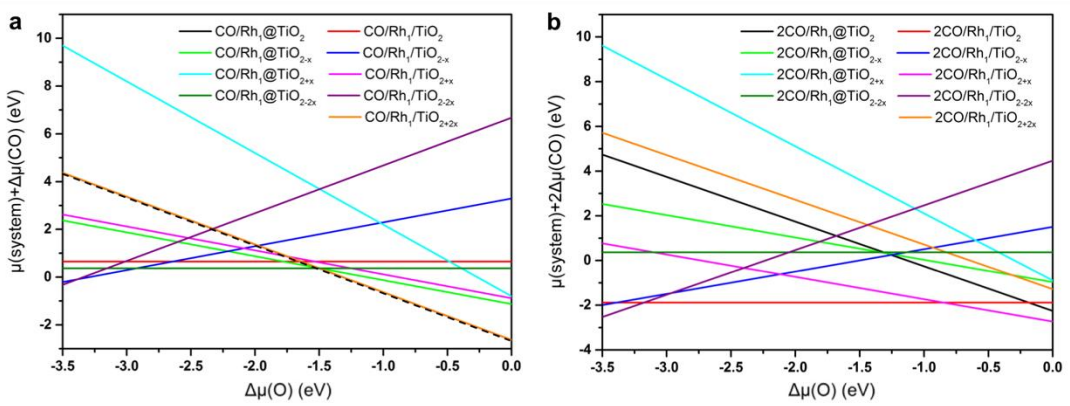

Figure 4.20A: Relative stability of Rh_1TiO_2 with CO adsorbates. a. 1CO adsorption. The most stable site from O rich to O poor conditions (right to left on x axis) is $CO/Rh_1@TiO_2$ (substitutional site for Rh, shown as a black dashed line and very close to $CO/Rh_1/TiO_{2+2x}$ where Rh is in supported site), $CO/Rh_1@TiO_{2-2x}$, $CO/Rh_1/TiO_{2-x}$, $CO/Rh_1/TiO_{2-2x}$. b. 2CO adsorption. The most stable site from O rich to O poor conditions is $2CO/Rh_1/TiO_{2+x}$, $2CO/Rh_1/TiO_2$, $2CO/Rh_1/TiO_{2-2x}$.

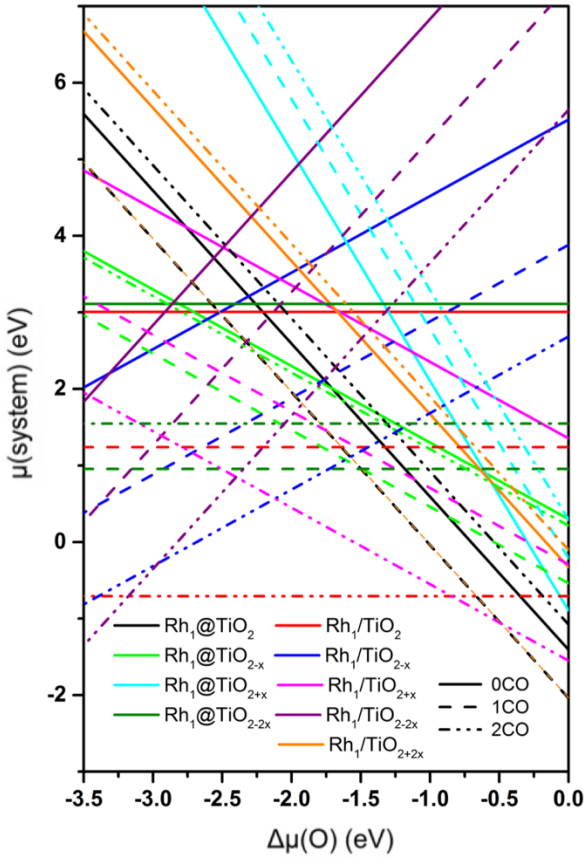

Figure 4.21: Relative stability of all kinds of Rh_1TiO_2 with or without CO as a function of μ(O). The data is calculated under a given condition (Δμ(CO) = -0.59 eV).

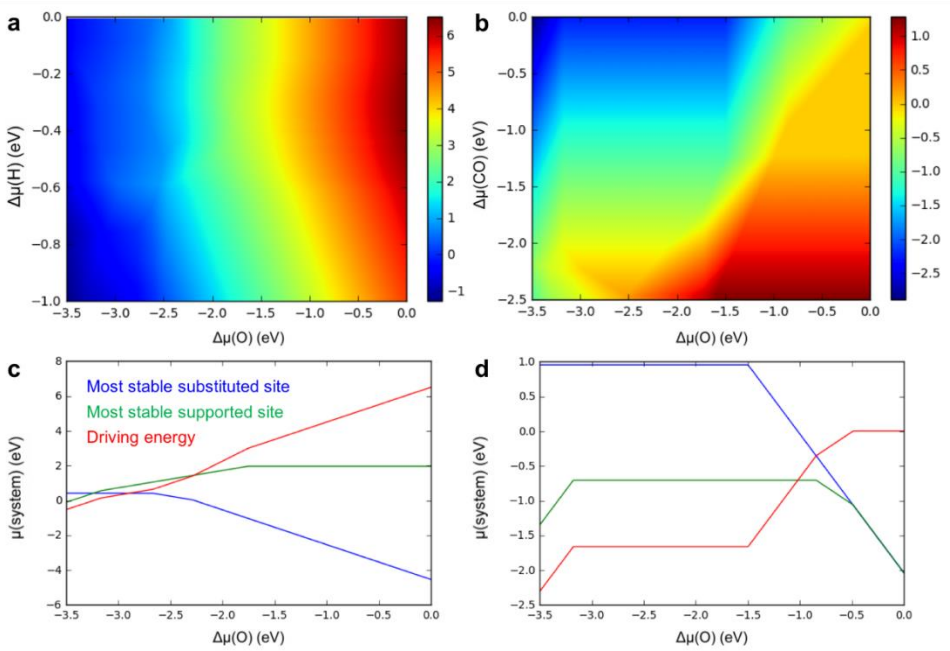

Figure 4.22A: Driving energy. a,c, the calculated driving energy in H_2 reduction. b,d, the calculated driving energy in CO adsorption. The color in a,b represents the value of driving energy. c is a typical condition in a (H_2 at 10% atmospheric pressure at 500 K, i.e. $\Delta\mu(H) = -0.35$ eV). d is a typical condition in b (CO at 10% atmospheric pressure at 300 K, i.e. $\Delta\mu(CO) = -0.59$ eV).

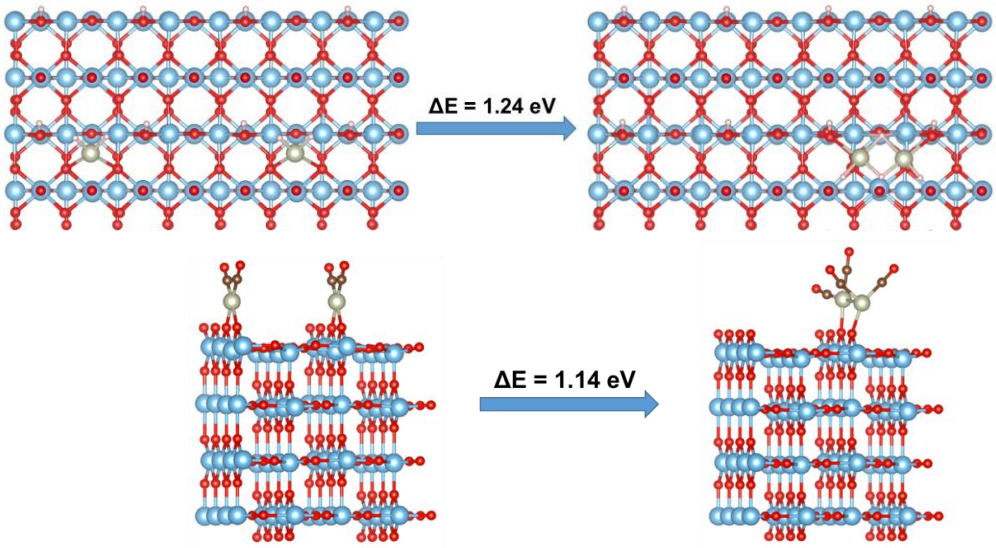

Figure 4.23A: The dimerization of the Rh single atoms is endoenergetic. Top: dimerization of RhH_2 in the conditions of the reduction with hydrogen. Bottom: dimerization of $Rh(CO)_2$ under a pressure of CO. Both reaction energies are endothermic

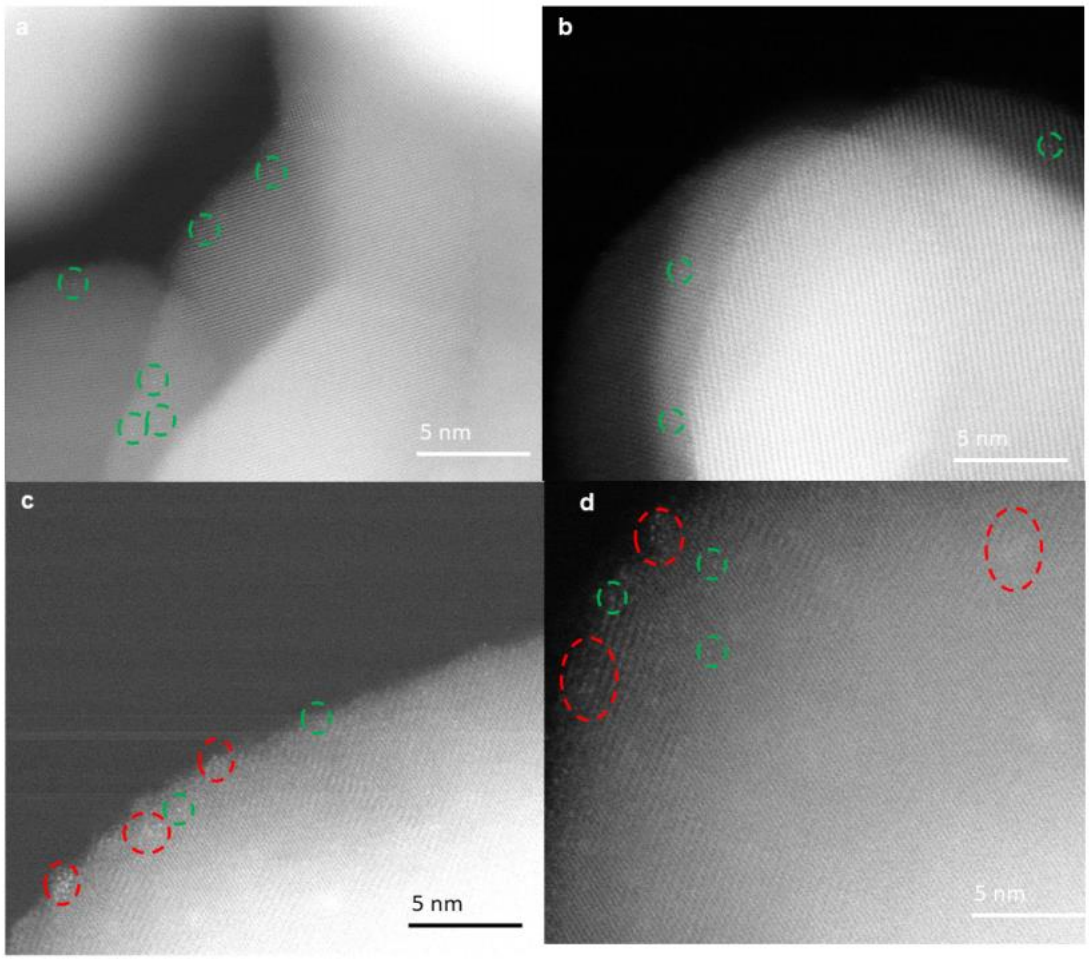

Figure 4.24A: STEM imaging of samples after varying temperature reduction. a, b, Additional HAADF STEM images of 100 °C H_2 reduced sample where only single Rh atoms were observed. c, d, 300 °C H_2 reduced sample in which small Rh clusters and Rh single atoms are observed. Green circles identify the single Rh atoms, while red circles identify Rh clusters.

Table 4.1. Calculated μ(system) of various terminations and positions of the Rh atoms in RWGS reaction conditions (200 °C, $10CO_2$:$1H_2$). Δμ(O) is calculated to be -3.03 eV if we assume the reaction is at chemical equilibrium.

System	μ(system)
$6H/Rh_1@TiO_2$	1.92
$7H/Rh_1@TiO_{2-x}$	1.20
$6H/Rh_1@TiO_{2-2x}$	0.77
$4H/Rh_1/TiO_2$	2.32
$6H/Rh_1/TiO_{2-x}$	1.06
$6H/Rh_1/TiO_{2-2x}$	1.20
$4H/CO/Rh_1/TiO_{2-x}$	0.56

Table 4.2. Calculated reaction energies (ΔE) and activation barriers (E_a) for elementary steps in the RWGS reaction on $6H/Rh_1/TiO_{2-x}$. These elementary steps can be found in Figure 4.9.

	Reaction pathway	Energy		Gibbs Free Energy	
		ΔE (eV)	E_a (eV)	ΔE (eV)	E_a (eV)
1)	$v+6H^* \rightarrow 2v+4H^*+H_2O^*$	0.91	1.05	0.91	1.05
2)	$2v+4H^*+H_2O^* \rightarrow 2v+4H^*+H_2O$	0.81	--	-0.49	--
3)	$2v+4H^*+CO_2 \rightarrow 2v+4H^*+CO_2^*$	-1.70	--	-0.56	--
4)	$2v+4H^*+CO_2^* \rightarrow v+4H^*+CO^*$	-0.33	0.26	-0.33	0.26
5)	$v+4H^*+CO^*+H_2 \rightarrow v+6H^*+CO^*$	-0.34	--	0.47	--
6)	$v+6H^*+CO^* \rightarrow v+6H^*+CO$	1.38	--	0.03	--

Note: The contribution of the entropy term to the free energies of each gas phase were cited from D.R. Stull, H. Propher, JANAF Thermochemical Tables, U. S. National Bureau of Standards, Washington, DC, 1971.

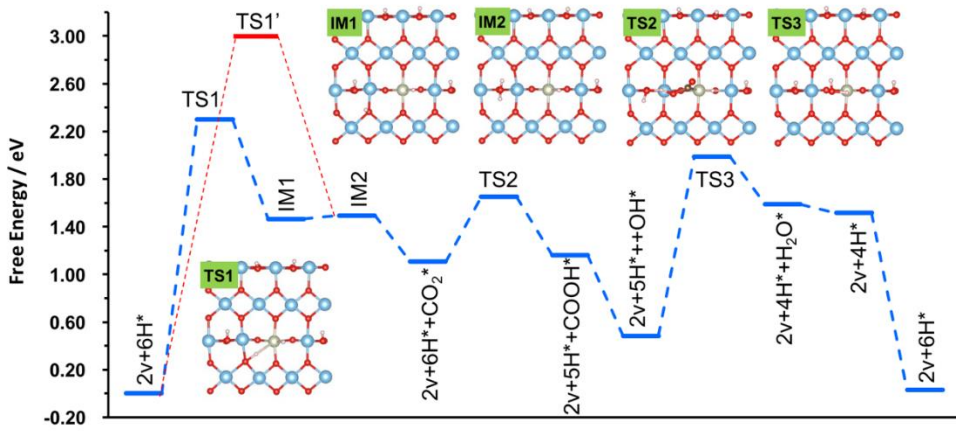

Figure 4.25A: Free energy profile of RWGS reaction on the substitutional site $6H/Rh_1@TiO_{2-2x}$. Color code: O-red; Ti-blue; Rh-gray. Rh is initially liganded by 2 H atoms. The first step is a H transfer from the Rh atom to surface -OH species to form H_2O, with an endothermic energy of 1.49 eV and a barrier of 2.30 eV. Then CO_2 can adsorb on Rh atom with an adsorption energy of -1.53 eV. The dissociation of the C-O bond via the COOH species is more facile than from the CO_2 molecule directly. After the dissociation of the COOH species, the remaining OH species will react with H atom on Rh atom to form H_2O. The formed water can desorb to gas easily at reaction temperature, and H_2 can adsorb on the Rh atom to reform the initial structure.

Table 4.3. Calculated reaction energies (ΔE) and activation barriers (E_a) for elementary steps in the RWGS reaction on $6H/Rh_1@TiO_{2-2x}$. These elementary steps can be found in Figure 4.25A.

	Reaction pathway	Energy		Gibbs Free Energy	
		ΔE (eV)	E_a (eV)	ΔE (eV)	E_a (eV)
1)	2v+6H* → IM1	1.46	2.30	1.46	2.30
2)	IM1 → IM2	0.03	--	0.03	--
3)	IM2 → 2v+6H*+CO_2*	-1.53	--	-0.39	--
4)	2v+6H*+CO_2*→2v+5H*+COOH*	0.06	1.16	0.06	1.16
5)	2v+5H*+COOH*→2v+5H*+CO+OH*	0.67	--	-0.68	--
6)	2v+5H*+OH* → 2v+4H*+H_2O*	1.10	1.50	1.10	1.50
7)	2v+4H*+H_2O* → 2v+4H*+H_2O	1.23	--	-0.07	--
8)	2v+4H*+H_2 → 2v+6H*	-2.30	--	-1.48	--

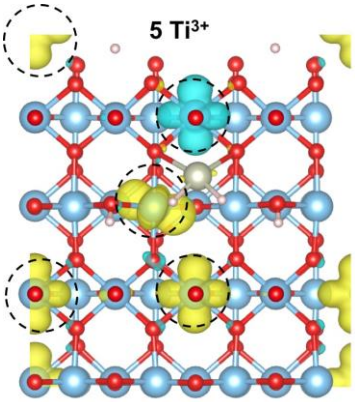

Figure 4.26A: Spin density map for 6H/Rh_1/TiO_{2-x} showing the 5 Ti^{3+} centers. Yellow and blue areas represent charge increase and reduction, respectively. Five black circles indicate the Ti^{3+} centers, and one dashed circle indicates the position of O vacancy.

4.5 References

1. Qiao, B. et al. Single-atom catalysis of CO oxidation using Pt1/FeOx. Nat. Chem. 3, 634 (2011).

2. Flytzani-Stephanopoulos, M. & Gates, B. C. Atomically dispersed supported metal catalysts. Annu. Rev. Chem. Biomol. Eng 3, 545-574 (2012).

3. Yang, X.-F. et al. Single-atom catalysts: a new frontier in heterogeneous catalysis. Acc. Chem. Res. 46, 1740-1748 (2013).

4. Li, T. et al. Maximizing the Number of Interfacial Sites in Single-Atom Catalysts for the Highly Selective, Solvent-Free Oxidation of Primary Alcohols. Angew. Chem. Int. Ed. 57, 7795-7799 (2018).

5. Wang, A., Li, J. & Zhang, T. Heterogeneous single-atom catalysis. Nature Reviews Chemistry, 1 (2018).

6. Thomas, J. M., Raja, R. & Lewis, D. W. Single-site heterogeneous catalysts. Angew. Chem. Int. Ed. 44, 6456-6482 (2005).

7. Flytzani-Stephanopoulos, M. Gold atoms stabilized on various supports catalyze the water–gas shift reaction. Acc. Chem. Res. 47, 783-792 (2013).

8. Bruix, A. et al. Maximum noble-metal efficiency in catalytic materials: atomically dispersed surface platinum. Angew. Chem. Int. Ed. 53, 10525-10530 (2014).

9. Lucci, F. R. et al. Selective hydrogenation of 1, 3-butadiene on platinum–copper alloys at the single-atom limit. Nat. Commun. 6, 8550 (2015).

10. Jones, J. et al. Thermally stable single-atom platinum-on-ceria catalysts via atom trapping. Science 353, 150-154 (2016).

11. Tang, Y., Zhao, S., Long, B., Liu, J.-C. & Li, J. On the nature of support effects of metal dioxides MO2 (M= Ti, Zr, Hf, Ce, Th) in single-atom gold catalysts: Importance of quantum primogenic effect. J. Phys. Chem. C 120, 17514-17526 (2016).

12. Liu, J. Catalysis by supported single metal atoms. ACS Catal. 7, 34-59 (2016).

13. Zhang, S. et al. Catalysis on Singly Dispersed Rh Atoms Anchored on an Inert Support. ACS Catal. 8, 110-121 (2017).

14. Schwarz, H. Ménage-à-trois: single-atom catalysis, mass spectrometry, and computational chemistry. Catalysis Science & Technology 7, 4302-4314 (2017).

15. Wei, S. et al. Direct observation of noble metal nanoparticles transforming to thermally stable single atoms. Nat. Nanotechnol 13, 856 (2018).

16. Matsubu, J. C. et al. Adsorbate-mediated strong metal–support interactions in oxide-supported Rh catalysts. Nat. Chem. 9, 120 (2017).

17. Liu, J.-C., Tang, Y., Wang, Y.-G., Zhang, T. & Li, J. Theoretical understanding of the stability of single-atom catalysts. National Science Review 5, 638-641 (2018).

18. Camellone, M. F. & Fabris, S. Reaction mechanisms for the CO oxidation on Au/CeO2 catalysts: Activity of substitutional Au3+/Au+ cations and deactivation of supported Au+ adatoms. J. Am. Chem. Soc. 131, 10473-10483 (2009).

19. Wang, L. et al. Atomic-level insights in optimizing reaction paths for hydroformylation reaction over Rh/CoO single-atom catalyst. Nat. Commun. 7, 14036 (2016).

20. Zhang, S. et al. Catalysis on singly dispersed bimetallic sites. Nat. Commun. 6, 7938 (2015).

21. Ma, X.-L., Liu, J.-C., Xiao, H. & Li, J. Surface single-cluster catalyst for N2-to-NH3 thermal conversion. J. Am. Chem. Soc. 140, 46-49 (2017).

22. Nie, L. et al. Activation of surface lattice oxygen in single-atom Pt/CeO2 for low-temperature CO oxidation. Science 358, 1419-1423 (2017).

23. Asokan, C., DeRita, L. & Christopher, P. Using probe molecule FTIR spectroscopy to identify and characterize Pt-group metal based single atom catalysts. Chin. J. Catal. 38, 1473-1480 (2017).

24. DeRita, L. et al. Catalyst architecture for stable single atom dispersion enables site-specific spectroscopic and reactivity measurements of CO adsorbed to Pt atoms, oxidized Pt clusters, and metallic Pt clusters on TiO2. J. Am. Chem. Soc. 139, 14150-14165 (2017).

25. Duan, S., Wang, R. & Liu, J. Stability investigation of a high number density Pt1/Fe2O3 single-atom catalyst under different gas environments by HAADF-STEM. Nanotechnology 29, 204002 (2018).

26. Evans, J., Hayden, B., Mosselmans, F. & Murray, A. Rhodium geminal dicarbonyl on TiO2 (110). J. Am. Chem. Soc. 114, 6912-6913 (1992).

27. Berkó, A., Ménesi, G. & Solymosi, F. Scanning tunneling microscopy study of the CO-induced structural changes of Rh crystallites supported by TiO2 (110). J. Phys. Chem 100, 17732-17734 (1996).

28. Wang, Y.-G., Mei, D., Glezakou, V.-A., Li, J. & Rousseau, R. Dynamic formation of single-atom catalytic active sites on ceria-supported gold nanoparticles. Nat. Commun. 6, 6511 (2015).

29. Wang, Y.-G. et al. CO oxidation on Au/TiO2: condition-dependent active sites and mechanistic pathways. J. Am. Chem. Soc. 138, 10467-10476 (2016).

30. He, Y. et al. Size-dependent dynamic structures of supported gold nanoparticles in CO oxidation reaction condition. Proc. Natl. Acad. Sci. U.S.A. 115, 7700-7705 (2018).

31. Lazarus, M. & Sham, T. X-ray photoelectron spectroscopy (XPS) studies of hydrogen reduced rutile (TiO2-x) surfaces. Chem. Phys. Lett 92, 670-674 (1982).

32. Sham, T. & Lazarus, M. X-ray photoelectron spectroscopy (XPS) studies of clean and hydrated TiO2 (rutile) surfaces. Chem. Phys. Lett 68, 426-432 (1979).

33. Van Grieken, R. & Markowicz, A. Handbook of X-ray Spectrometry. (CRC press, 2001).

34. Zhang, S. et al. Dynamical observation and detailed description of catalysts under strong metal–support interaction. Nano. Lett. 16, 4528-4534 (2016).

35. Matsubu, J. C., Yang, V. N. & Christopher, P. Isolated metal active site concentration and stability control catalytic CO2 reduction selectivity. J. Am. Chem. Soc. 137, 3076-3084 (2015).

36. Avanesian, T., Gusmão, G. S. & Christopher, P. Mechanism of CO2 reduction by H2 on Ru (0001) and general selectivity descriptors for late-transition metal catalysts. J. Catal. 343, 86-96 (2016).

37. Kozuch, S. & Shaik, S. How to conceptualize catalytic cycles? The energetic span model. Acc. Chem. Res. 44, 101-110 (2010).

38. Liu, J.-C., Wang, Y.-G. & Li, J. Toward rational design of oxide-supported single-atom catalysts: atomic dispersion of gold on ceria. J. Am. Chem. Soc. 139, 6190-6199 (2017).

39. Ding, K. et al. Identification of active sites in CO oxidation and water-gas shift over supported Pt catalysts. Science 350, 189-192 (2015).

40. Yang, M. et al. A common single-site Pt(II)–O(OH)x–species stabilized by sodium on "active" and "inert" supports catalyzes the water-gas shift reaction. J. Am. Chem. Soc. 137, 3470-3473 (2015).

41. Berkó, A. & Solymosi, F. Adsorption-induced structural changes of Rh supported by TiO2 (110)-(1× 2): an STM study. J. Catal. 183, 91-101 (1999).

42. Kresse, G. & Furthmüller, J. Efficiency of ab-initio total energy calculations for metals and semiconductors using a plane-wave basis set. Comput. Mater. Sci 6, 15-50 (1996).

43. Kresse, G. & Furthmüller, J. Efficient iterative schemes for ab initio total-energy calculations using a plane-wave basis set. Phys. Rev. B 54, 11169 (1996).

44. Kresse, G. & Joubert, D. From ultrasoft pseudopotentials to the projector augmented-wave method. Phys. Rev. B 59, 1758 (1999).

45. Perdew, J. P., Burke, K. & Ernzerhof, M. Generalized gradient approximation made simple. Phys. Rev. Lett. 77, 3865 (1996).

46. Anisimov, V. I., Aryasetiawan, F. & Lichtenstein, A. First-principles calculations of the electronic structure and spectra of strongly correlated systems: the LDA+ U method. J. Phys.: Condens. Matter. 9, 767 (1997).

47. Dudarev, S., Botton, G., Savrasov, S., Humphreys, C. & Sutton, A. Electron-energy-loss spectra and the structural stability of nickel oxide: An LSDA+ U study. Phys. Rev. B 57, 1505 (1998).

48. Deskins, N. A., Rousseau, R. & Dupuis, M. Distribution of Ti3+ surface sites in reduced TiO2. J. Phys. Chem. C 115, 7562-7572 (2011).

49. Yu, Y.-Y. & Gong, X.-Q. CO oxidation at rutile TiO2 (110): role of oxygen vacancies and titanium interstitials. ACS Catal. 5, 2042-2050 (2015).

50. Henkelman, G. & Jónsson, H. A dimer method for finding saddle points on high dimensional potential surfaces using only first derivatives. J. Chem. Phys. 111, 7010-7022 (1999).

51. Henkelman, G., Uberuaga, B. P. & Jónsson, H. A climbing image nudged elastic band method for finding saddle points and minimum energy paths. J. Chem. Phys. 113, 9901-9904 (2000).

52. Bader, R. F. A quantum theory of molecular structure and its applications. Chem. Rev. 91, 893-928 (1991).

Chapter 5:

Low-Temperature Ammonia Production during NO Reduction by CO is due to Atomically Dispersed Rhodium Active Sites

Adapted from *ACS Catalysis* article:
Asokan, C., Yang, Y., Dang, A., Getsoian, A. B., & Christopher, P. "Low-Temperature Ammonia Production during NO Reduction by CO is due to Atomically Dispersed Rhodium Active Sites." *ACS Catalysis*, 10(9), 5217-5222 (2020).

5.1 Introduction

Rhodium plays a key role in three-way catalysts to control NOx emissions in gasoline engines primarily through the reduction of NO by CO. Despite extensive investigation, there remains uncertainty about NO reduction mechanisms. Particularly, it is unknown which sites are responsible for the unselective reduction of NO to NH_3 under light-off conditions or in CO-rich feed. By varying Rh catalyst structure from atomically dispersed species to clusters on Al_2O_3 and CeO_2, we provide evidence that in the reduction of NO by CO with co-fed H_2O, low-temperature NH_3 formation occurs on atomically dispersed Rh sites, whereas high nuclearity Rh clusters are selective to N_2.

5.2 Methods

5.2.1 Catalyst Synthesis

Catalysts were synthesized using incipient wetness impregnation at targeted Rh weight loadings on 1 gram of support by dissolving Rhodium(III) nitrate hydrate precursor $Rh(NO_3)_3 \cdot xH_2O$ (Sigma Aldrich, CAS: 10139-58-9) in 800 µL of high-performance liquid chromatograph (HPLC)-grade water (J.T. Baker, CAS: 7732-18-15) and adding the diluted precursor solution to γ-Al_2O_3 (Sasol, Puralox TH100/150, CAS: 9529248-35-0) or CeO_2 (US Research Nanomaterials, CAS: 1306-38-3). The mixtures were dried overnight in an oven at 60 °C. The catalyst powders were then calcined in dry air in a tube furnace at 350 °C for 4 h.

5.2.2 Probe Molecule CO FTIR

Catalysts were loaded in a Harrick Low Temperature Reaction chamber mounted inside a ThermoScientific Praying Mantis diffuse reflectance adapter set in a Nicolet iS10 FTIR spectrometer with a Mercury Cadmium Telluride (MCT) detector and mass flow controllers (Teledyne Hastings) were used to control the gas flow rates across the reactor

bed. Catalysts were in-situ pretreated for 30 minutes at 350 °C in pure O_2 and subsequently in 10% H_2/Ar at 100 °C. After in situ pretreatment in a Harrick Reaction chamber, the samples were cooled down to room temperature in flowing Ar, exposed to flowing 10% CO in Ar until Rh sites were saturated, and then purged with Ar to take spectra with 32 scans and 0.482 cm^{-1} data spacing.

The relative fraction of atomically dispersed Rh species, Rh_{iso}, was estimated using equation 5.1, using the specific CO:Rh stoichiometries in each adsorption mode, and the extinction coefficients of CO species associated with $Rh(CO)_2$ (Rh_{iso}), Rh-CO (CO linearly bound to Rh nanoparticles), and Rh_2CO (CO bridge bound to Rh nanoparticles). The extinction coefficients, εi, used for the symmetric $Rh(CO)_2$, Rh-CO, and Rh2CO, were 74, 26, and 85 (x10^6 m/mol), respectively.[1–4] The CO:Rh ratios for the symmetric gem-dicarbonyl, linear, and bridge configurations were 2, 1, and 0.5, respectively. The fraction of exposed sites existing as atomically dispersed species was then quantified by integrating the relative intensity of each CO stretch.

(5.1)
$$X_{\text{iso}} = \frac{I_{\text{iso}} / \left(\varepsilon_{\text{iso}} \times \left(\frac{\text{CO}}{\text{Rh}} \right)_{\text{iso}} \right)}{\sum_{i=1}^{3} \left[I_i / \left(\varepsilon_i \times \left(\frac{\text{CO}}{\text{Rh}} \right)_i \right) \right]}$$

Table 5.1 :Site Quantification. The intensities, I_i, are the integrated areas of the fit peaks in absorbance units. X_{iso} and X_{nano} represent the fraction of CO adsorption sites existing as atomically dispersed species and at the surface of Rh nanoparticles, respectively.

Rh wt%	I_{iso}	I_{linear}	I_{bridge}	X_{iso}	X_{nano}
5%	30.8	32.1	46.1	0.08	0.92
2%	26.9	9.9	18.5	0.18	0.82
0.05%	25.2	-	-	1.00	
parameter					
Coefficients ($x10^6$ m^2/mol)	74	26	85		
CO/Rh ratio	2	1	0.5		
Peak locations (cm^1)	2088	2061	1839		

5.2.3 Reactivity Experiments

To test the reactivity of the various structures of Rh, "light off" experiments were performed where the reactor is heated at a constant rate under reactive environments from ambient temperature to test how the catalyst would act during start-up conditions. Catalysts were diluted and thoroughly mixed with purified silicon dioxide (Sigma Aldrich, CAS: 84878) to a total of 0.2 milligram of Rh per 1 g total material, Table 5.2. A home-built, temperature-controlled reactor system with mass flow controllers (Teledyne Hastings) was used to precisely control CO, NO, H_2O and Ar gas flow concentrations.

Table 5.2: Catalyst Loadings				
Total mg Rh	wt% Rh cat	mg catalyst	mg diluent	mg total
0.2	0.05	400	600	1000
0.2	0.1	200	800	1000
0.2	0.2	100	900	1000
0.2	0.5	40	960	1000
0.2	1	20	980	1000
0.2	1	20	980	1000
0.2	2	10	990	1000
0.2	5	4	996	1000

After pretreatment identical to the CO FTIR characterization, catalysts were heated at 5 °C/min while 200 sccm (standard cubic centimeters per minute) of 5000 ppm CO and 1000 ppm NO in Ar gas flown over a packed bed in both dry and wet conditions (with ~2% water). Gas phase product compositions were identified by flowing outlet effluent through a Thermo Scientific Antaris IGS 2-meter Gas Cell set in a Nicolet iS10 FTIR spectrometer with a Mercury Cadmium Telluride (MCT) detector and using OMNIC Series Software to take 5 spectral scans every 10 seconds at high 0.5 resolution, and 0.241 cm^{-1} data spacing. Reactants and products were calibrated with the TQ Analyst Pro Edition Software to identify established spectral signatures of known mixtures of CO, NO, N_2O, NH_3, CO_2, and H_2O in Ar at set pressure and temperature. Because the quantity of N_2 produced from NO reduction over Rh cannot be identified by gas phase FTIR, the product concentration was calculated from mass balance as follows:

(5.2)

$$[N_2\ ppm]_{out} = \frac{1}{2} \times ([NO\ ppm]_{in} - [NO\ ppm]_{out} - [2 \times N_2O\ ppm]_{out} - [NH_3\ ppm]_{out})$$

5.3 Results and Discussion

In gasoline-powered vehicles, a Three-Way Catalyst (TWC) is used to control the emission of criteria pollutants (NO_x, CO, and hydrocarbons). While oxidation of CO and hydrocarbons results in CO_2 and H_2O emissions, simultaneous reduction of NO_x can produce not only N_2 (the desired product), but also NH_3 and N_2O. These products are environmentally detrimental: N_2O is a potent greenhouse gas, and atmospheric NH_3 is linked to particulate formation, ecosystem eutrophication, and decreased resilience of vegetation to exasperation, including parasites and drought.[5–8] To guide the formulation and operation of TWCs to minimize NH_3 and N_2O formation while maintaining maximal control over NO_x emissions, greater understanding of the mechanisms of NO_x reduction in TWCs is required.

Although it is generally observed that richer air-fuel ratios lead to increasing NH_3 selectivity during NO_x reduction, selectivity is also sensitive to catalyst formulation.[9–12] Rh is generally considered to be both more active for NO_x reduction and more selective to N_2 than Pd.[13] However, even Rh-only catalysts can generate NH_3 under light-off conditions or in feeds containing excess reductant or a source of hydrogen.[14] While pathways leading to NH_3 formation on Pd have been investigated in detail, NH_3 formation on Rh has received little attention.[15] Many fundamental studies of NO reduction on Rh model catalysts have been conducted under conditions that avoid NH_3 formation because it adds challenges to elucidating N_2 production pathways.[16–18] Even under simplified conditions, e.g. reduction of NO by CO, mechanistic understanding on single crystals is inconsistent with results obtained

on supported particles (and different investigators obtain different results on the latter), underscoring the need for a new look at structure-function relationships for Rh catalysts.[17–22]

Developing structure-function relationships for heterogeneous Rh catalysts is complicated because Rh is known to speciate between atomically dispersed species and metal clusters, depending on environmental conditions, particularly under environments containing CO, NO, H_2 and H_2O, which are abundant in exhaust streams.[23,24] This is important because TWCs Rh weight loadings are commonly lower than ~0.3%, where a mix of Rh nanoparticles, small clusters, and atomically dispersed species co-exist.[4] While the reduction of NO by CO is well studied for Rh nanoparticles and extended Rh surfaces, the role of atomically dispersed species in this chemistry, particularly under relevant conditions with H_2O in the feed, has not been addressed.[20,25–31] This is a potential key to understanding mechanistic pathways in TWCs because atomically dispersed Rh species on oxide supports are known to exhibit distinct selectivity in catalytic processes compared to Rh clusters.[1,32–34]

Here, we elucidate structure-function relationships for oxide supported Rh catalysts for the reduction of NO by CO under dry conditions and in the presence of H_2O. Under dry conditions atomically dispersed Rh species are less reactive than Rh clusters. The addition of H_2O to the feed significantly promotes the reactivity of atomically dispersed Rh and results in 100% selectivity to NH_3 at temperatures < 200 °C on both Al_2O_3 and CeO_2 supports. Rh clusters are less reactive than atomically dispersed species when H_2O is co-fed and the reaction primarily leads to N_2 formation. This revelation provides a basis for examining impacts of catalyst formulation for minimizing NH_3 production.

To facilitate the development of structure-function relationships, catalysts were synthesized using $Rh(NO_3)_3$ at varied weight loadings on γ-Al_2O_3 (Sasol, Puralox TH100/150, 150 m^2/g), Figure 5.1.[35] The Rh weight loading was varied from 0.05 to 5 wt. %

to control the distribution of Rh species from atomically dispersed to clusters and nanoparticles. Catalysts were ex-situ oxidized at 350 °C for 4 hours and in-situ oxidized at 350 °C for 30 minutes in O_2, purged with inert, and in-situ reduced at 100 °C for 1 hour in H_2 prior to characterization or reactivity measurements.

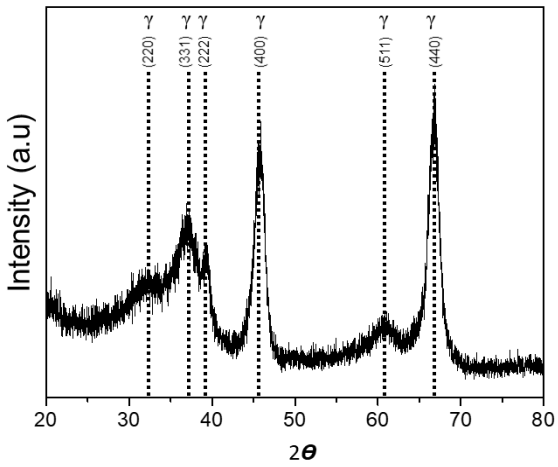

Figure 5.1: X-ray powder diffraction (XRD) of Sasol Puralox TH100/150. The primary peaks show consistency with standards for γ-Al_2O_3.

Characterization of Rh structures present on the catalysts was accomplished by using CO probe molecule FTIR spectroscopy.[1,27,30,36–41] This approach is particularly useful for characterizing supported atomically dispersed Rh species because of their unique vibrational signatures as compared to Rh clusters. In 1957, Garland and Yang first hypothesized that CO adsorption on atomically dispersed Rh resulted in the formation gem-dicarbonyl ($Rh(CO)_2$) species with characteristic symmetric and asymmetric CO stretches at ~2090 and 2020 cm^{-1}, respectively.[42] On Rh nanoparticle and cluster surfaces, CO adsorbs in linear and bridge bound geometries that have characteristic stretches at ~2070-2050 and ~1950-1850 cm^{-1}, respectively.[2,3,42–44] These Rh structural assignments based on CO FTIR have been substantiated by nuclear magnetic resonance (NMR) measurements, X-ray photoelectron spectroscopy (XPS), X-ray absorption spectroscopy (XAS), and high-angle annular dark-

field scanning transmission electron microscopy (HAADF-STEM) imaging.[37,45–48] For example, structure-function relationships for Rh/TiO_2 based catalysts for the reduction of CO_2 developed via characterization based on CO FTIR and reactivity measurements were further supported later based on STEM and XPS analysis.[1,37,48] Thus, while applying a full suite of characterization tools is necessary when studying systems containing new catalyst compositions and structures, CO FTIR is a well-established approach for developing structure-function relationships for supported Rh-based catalysts.[1,37,49,50]

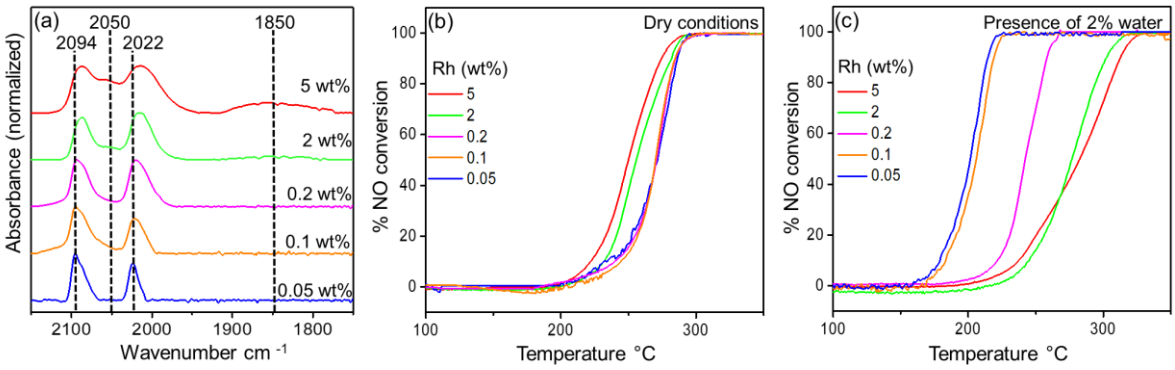

Figure 5.2: a) CO probe molecule FTIR spectra collected for $Rh/\gamma\text{-}Al_2O_3$ with varying Rh wt. % after in-situ 350 °C oxidation for 30 minutes and 100 °C reduction in H_2 for 60 minutes, followed by saturation with 10% CO at 20 °C. The spectra were normalized by the highest intensity feature in this region and vertically separated for clarity. b) NO conversion (%) as a function of temperature for a linear temperature ramp of 5 °C/min in dry conditions (5000 ppm CO/ 1000 ppm NO, and c) wet conditions (5 °C/min in 2% H_2O /5000 ppm CO/ 1000 ppm NO) for the series of catalysts characterized in (a).

Figure 5.2(a) shows CO probe molecule IR spectra for 0.05, 0.01, 0.2, 2, and 5 wt. % Rh/Al_2O_3. At low Rh wt. % (0.05, 0.1 and 0.2%) the IR spectra were dominated by CO stretches at 2094 and 2022 cm^{-1} associated with the atomically dispersed $Rh(CO)_2$ species. The CO stretching bands associated with the $Rh(CO)_2$ species show asymmetry, suggesting the existence of multiple coordination environments to the support (for example based on the proximity to hydroxyl species with varying characteristics).[2,41,42,51,52] Temperature programmed desorption (TPD) measurements of CO from the 0.1 wt. % Rh sample shows

evidence of two distinct $Rh(CO)_2$ species, where CO desorbs at different temperature, Figure 5.3. Thus, while the lowest Rh loading samples contain predominantly atomically dispersed species, these species likely reside in various coordination environments on the support. Future work will aim to understand the influence of atomically dispersed Rh coordination environment on reactivity. Evidence for linearly bound CO to small Rh clusters could also be seen on the 0.1 and 0.2 wt. % samples based on an increase in absorbance between the $Rh(CO)_2$ stretches. The prevalence of Rh clusters increased with increasing Rh loadings, as evidenced by the stronger absorbance associated with CO stretches at 2070 and 1850 cm^{-1} associated with linear and bridge bound CO. The fraction of exposed Rh sites existing as atomically dispersed species was estimated by integrating the peak areas associated with CO on various adsorption sites and accounting for adsorption stoichiometry and extinction coefficients, where $Rh(CO)_2$ species have a ~3-fold larger extinction coefficient than linearly bound CO on Rh clusters.[1–3,53] Based on this approach, it was estimated that on the 5 wt. % Rh sample only ~ 8% of the exposed Rh sites were atomically dispersed species, while 92% of adsorption sites were at the surface of Rh nanoparticles, see Table 5.1. Therefore, this series of catalysts presents a decreasing fraction of exposed atomically dispersed Rh species with increasing weight loading.

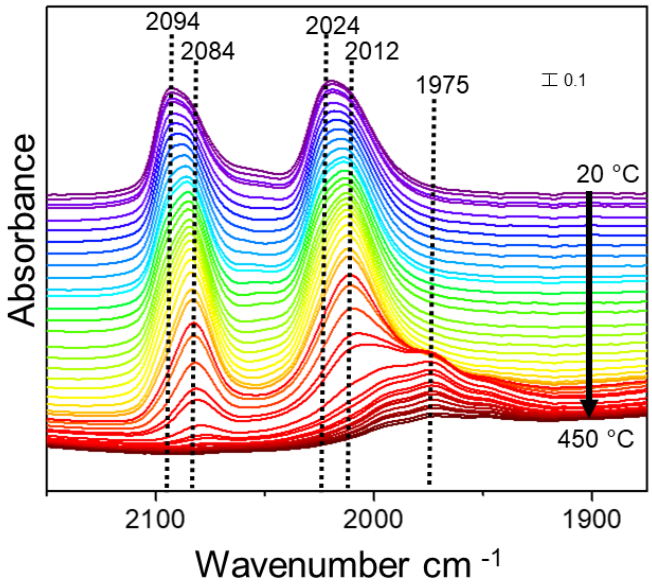

Figure 5.3: Temperature programmed desorption measurements of CO from the 0.1 wt% Rh on Al_2O_3 sample. The data shows evidence that 2 distinct $Rh(CO)_2$ species exist with symmetric (2094 and 2084) and asymmetric (2024 and 2012) stretching frequencies. Interestingly the pair of bands at 2094 and 2024 cm^{-1} disappear together without any new bands emerging, suggesting both COs desorb simultaneously. Alternatively, the bands at 2084 and 2012 cm^{-1} disappear at higher temperature and correlate with the formation of a band at ~1975 cm^{-1}. Recent work from our group on Rh/TiO_2 using CO FTIR and DFT calculations suggested that the emergence of a band at 1975 cm^{-1} was due to $Rh(CO)_2$ species existing near OH species on the support, where 1 CO first desorbs to leave a Rh(CO)(OH) species, with a characteristic stretch at 1975 cm^{-1}. Thus, the asymmetry in the $Rh(CO)_2$ stretching bands likely arises from the existence of $Rh(CO)_2$ species with distinct coordination environments to the support, which is not surprising for Al_2O_3, given the surface complexity. Future efforts will attempt to identify which $Rh(CO)_2$ coordination environments are responsible for catalytic reactivity.

To develop structure-function relationships over the variable Rh catalysts relevant for the start-up regime of TWC operation, “light off” experiments were performed where the reactor was heated at a controlled linear rate from ambient temperature. CO was chosen as reductant for NO because light-offs of CO and NO are known to be coupled on Rh catalysts.[54] In some tests, water was co-fed in order to assess the impact of this important exhaust component on NO_x reduction selectivity. While more complex feeds could also be considered, the $CO+NO+H_2O$ blend was sufficient to achieve the aims of the present study.

Catalysts were diluted with purified silicon dioxide (Sigma Aldrich 84878) to provide a constant loading of 0.2 mg of Rh in the 1 g of total material loaded into the reactor, Table .2. After pretreatment, catalysts were heated at 5 °C/min in a flow of 5000 ppm CO and 1000 ppm NO diluted in Ar both in dry and wet conditions (with ~2% water) at a total flow rate of 200 sccm (standard cubic centimeters per minute).

In dry reaction conditions, all catalysts started converting NO into N_2 at ~210 °C, but samples with a higher fraction of Rh clusters, 2 and 5 wt.% Rh, exhibited increased conversion at lower temperature as compared to samples that contained predominantly atomically dispersed Rh, 0.05, 0.1, and 0.2 wt.% Rh, Figure 2(b). All catalysts produced 1:1 stoichiometric amounts of CO_2 and N_2 with high selectivity, although a small amount of N_2O was observed at low temperatures, which was independent of Rh loading, see Figure 4. Differences in the light off curve shapes suggests different rate laws for NO reduction over Rh clusters compared to atomically dispersed species.[55] However, future steady state measurements are necessary to unravel the underlying kinetics. It is clear that Rh clusters on Al_2O_3 are more effective at catalyzing the reduction of NO by CO under dry conditions, although only by a small amount.

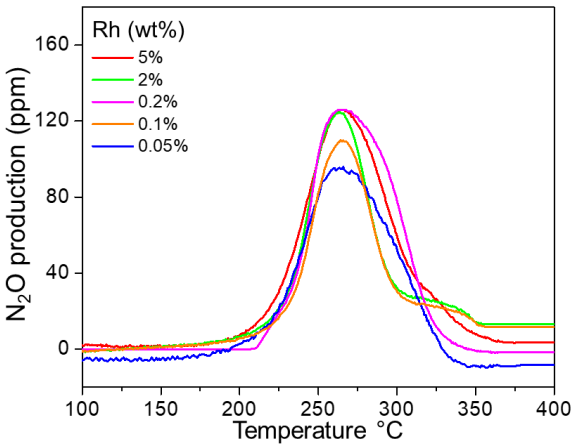

Figure 5.4: N_2O production during temperature programmed reaction at a temperature ramp rate of 5 °C/min in 5000 ppm CO/ 1000 ppm NO over catalysts with varying Rh wt. %.

Light off curves performed in the presence of H_2O exhibited distinct differences as a function of Rh weight loading, see Figure 5.2(c). The addition of H_2O to the feed promoted the reactivity of lower wt. % Rh catalysts, for example decreasing the onset of measurable NO conversion by ~50 °C for the 0.05 and 0.1 wt. % Rh catalysts. While the 0.2 wt.% Rh catalyst exhibited higher light-off temperatures as compared to the 0.05 and 0.1 wt.% catalysts, the shape of the light off curve was similar, suggesting similar kinetic behavior with a fewer number of active sites. For the higher Rh wt. % catalysts (2 and 5%), the addition of H_2O to the feed inhibited the onset of NO conversion by ~10 °C. Thus, while the behavior of all catalysts was similar under dry conditions, stark differences were observed upon the introduction of H_2O to the feed.

Most interestingly, the concentration of NH_3 produced during the wet light off experiments increased with decreasing Rh wt. % and thus with an increase in the relative fraction of atomically dispersed Rh species, Figure 5.5(a). The lowest tested Rh weight loading, 0.05%, exhibited ~100% NH_3 selectivity with complete NO conversion by ~210 °C. The 0.1 wt. % Rh catalyst converted NO to NH_3 with close to 100% selectivity during the light off, but once 100% NO conversion was reached, NH_3 selectivity declined and N_2 production increased. As the Rh wt. % in the catalyst was increased, the selectivity towards N_2 increased and NH_3 production decreased. The amounts of N_2 and N_2O produced during the light off are shown in Figure 5.6.

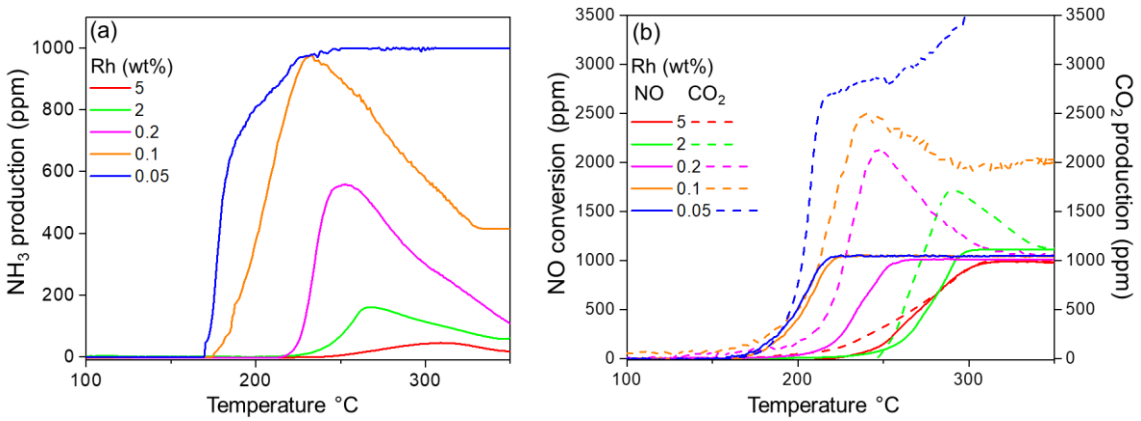

Figure 5.5: a) NH_3 production (ppm), b) NO consumption (solid lines), and CO_2 production (dotted lines) during temperature programmed reaction at a temperature ramp rate of 5 °C/min in 5000 ppm CO/ 1000 ppm NO / 2% H_2O for the series of catalysts characterized in Figure 5.2(a).

We compared NO conversion and CO_2 production to elucidate the stoichiometry of the reactions taking place, see Figure 5.5(b). For the 0.05 and 0.1 Rh wt. % catalysts, at the temperature where 100% conversion of NO to NH_3 was reached, 2.5 times more CO_2 was produced than NO consumed. For the 5 Rh wt.% catalyst, less than 50 ppm of NH_3 was produced and at the temperature where NO conversion reaches 100%, quantitative selectivity toward N_2 was observed, thus CO_2 production occurred at a 1:1 ratio with NO and CO consumption. We can derive site-specific overall reactions for NO reduction by CO in wet environments, where in the case of Rh clusters , $2NO + 2CO \rightarrow N_2 + 2CO_2$ occurs whereas for atomically dispersed Rh $2NO + 3H_2O + 5CO \rightarrow 2NH_3 + 5CO_2$ occurs.

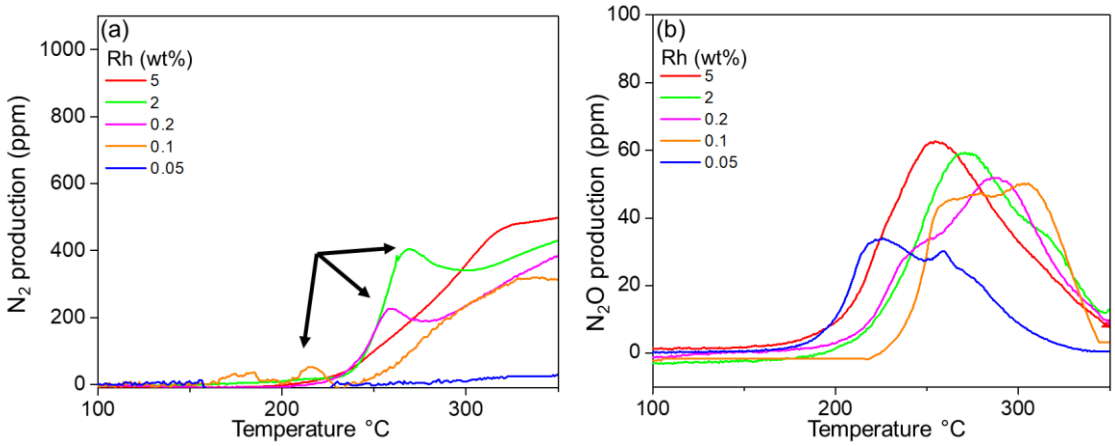

Figure 5.6: a) N_2 production and b) N_2O production during temperature programmed reaction at a temperature ramp rate of 5 °C/min in 5000 ppm CO/ 1000 ppm NO / 2% H_2O over catalysts with varying Rh wt. %. Black arrows in (a) point to apparent excess N_2 spike, which was caused by NH_3 adsorption on Al_2O_3 and the calculation of N_2 amount via N mass balance.

For the 0.05 and 0.1 Rh wt. % cases, there was an excess of CO_2 formed after complete NO conversion that was not accounted for by the reactions proposed above. A plausible source of CO_2 production is through the water-gas shift reaction (, WGS) occurring $H_2O + CO \rightarrow H_2 + CO_2$ over atomically dispersed Rh species. To test this hypothesis, light off curves were obtained with 2% H_2O and at CO levels equivalent to the balance of CO after complete NO consumption, Figure 5.7. For the 0.05 Rh wt. % catalyst, CO_2 started forming at ~275 ºC and gradually increased to ~1000 ppm by the end of run, Figure 5.7. This is consistent with the excess CO_2 formed over atomically dispersed Rh samples at temperatures where NO conversion was complete. This behavior is also consistent with previous work showing that various atomically dispersed metal catalysts, and specifically Rh, are highly active for WGS.[37,48,56–58] The 5 wt. % Rh catalyst did not light off WGS until > 300 °C, accounting for the lack of excess CO_2 on catalysts consisting primarily of Rh clusters.

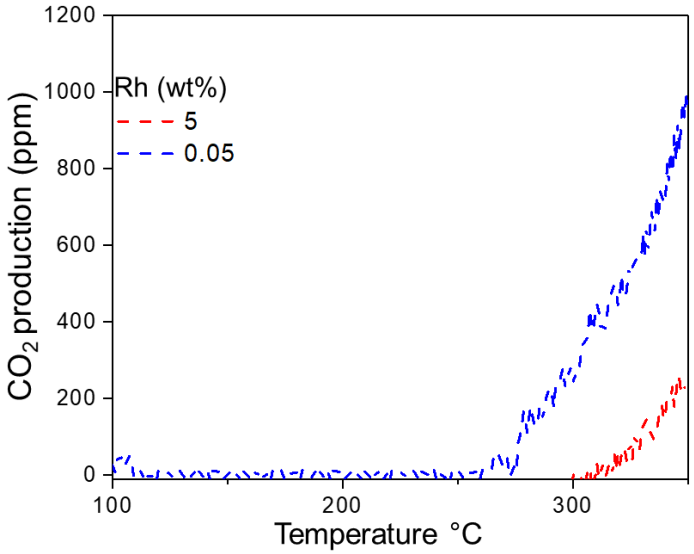

Figure 5.7: CO_2 production during water-gas shift light off experiments with a temperature ramp rate of 5 °C/min and 2% water and 4000 ppm CO (5% Rh) and 2500 ppm CO (0.05% Rh) in the feed.

Including WGS over atomically dispersed Rh closes the mass balance for all products over the tested temperature range. However, in the cases of 0.1, 0.2, and 2 wt. % Rh, there was an apparent spike of excess N_2 produced during the initial NO conversion light off, Figure 5.6(a). The amount of N_2 produced was calculated by mass balance assuming N_2, NO, N_2O, and NH_3 are the only N containing species. It was hypothesized that NH_3 formed during initial light off adsorbs to acidic sites inherent to the Al_2O_3 support, so there was a delay in formed NH_3 exciting the reactor while NO was being consumed until all acidic sites were titrated.[59,60] To test this hypothesis, a steady state experiment was performed where a feed consisting of 1000 ppm NO, 5000 ppm CO, and 2% water was introduced to the 0.1 Rh wt.% catalyst for extended time at 185, 195, 205, and 215 °C (Figure 5.7). The steady state amount of NH_3 reached 2.5:1 stochiometric balance with CO_2 at all temperatures in agreement with the proposed reaction, demonstrating that NH_3 adsorption to the catalyst surface likely was occurring during initial light off.

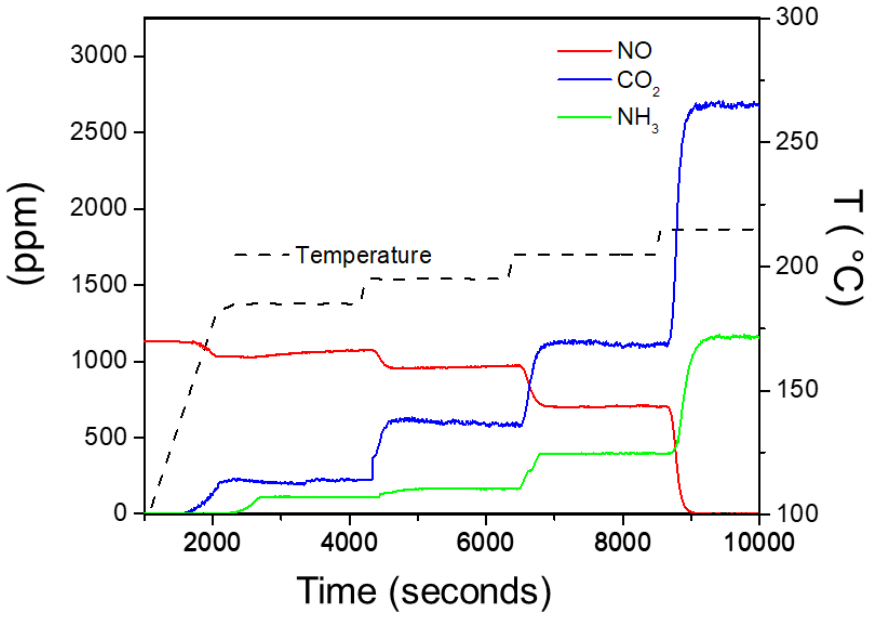

Figure 5.8: Product effluent and temperature during steady state experiments on 0.1%wt Rh/Al_2O_3 conducted at 2% H_2O/ 1000 NO/5000 CO with temperature ramped at rate 5 °C/min until 185 °C held for 2100 seconds (35 minutes) at 185, 195, 205, and 215 °C. The consistent, steady state 2.5:1 CO_2:NH_3 ratio is observed at each temperature.

We also explored whether the structure-function relationship developed for Rh/Al_2O_3 would apply to CeO_2 supports (US-Nano stock #US3037, 70 m^2/g), which are also of relevance to catalytic converters (Figure 5.9).[49] At 0.2 wt.% Rh on CeO_2, where CO FTIR suggested Rh is predominantly atomically dispersed, the catalyst was 100% selective towards NH_3 during the wet light off experiment. The reaction lights off at a lower temperature on atomically dispersed Rh on CeO_2 as compared to Al_2O_3 by ~25 °C, suggesting inherently higher reactivity on the reducible support. At 2 wt. % Rh loading, where the presence of Rh clusters is evidenced in the CO FTIR, selectivity towards N_2 increased suggesting Rh clusters are selective for N_2 on either support.

The strong correlation between the fraction of exposed sites existing as atomically dispersed Rh species in initial characterization and the amount of NH_3 produced during reactivity measurements with co-fed H_2O provides strong evidence that atomically dispersed

Rh species on Al_2O_3 and CeO_2 are active at low temperature for NH_3 formation, and suggests this is a critical active site in TWC. Recent reports of analysis of atomically dispersed Rh and Pt species in TWCs did not identify this active site relationship either due to focus on oxidation reactions, the lack of inclusion of H_2O in the feed, or focus on trends in conversion and stability.[61–63] Within a ~50 °C window we found that NH_3 formation and WGS over atomically dispersed Rh occurred simultaneously with N_2 formation over Rh clusters, making it challenging to understand the catalytic behavior of materials containing a mix of active site types, as portrayed in Figure 5.10.

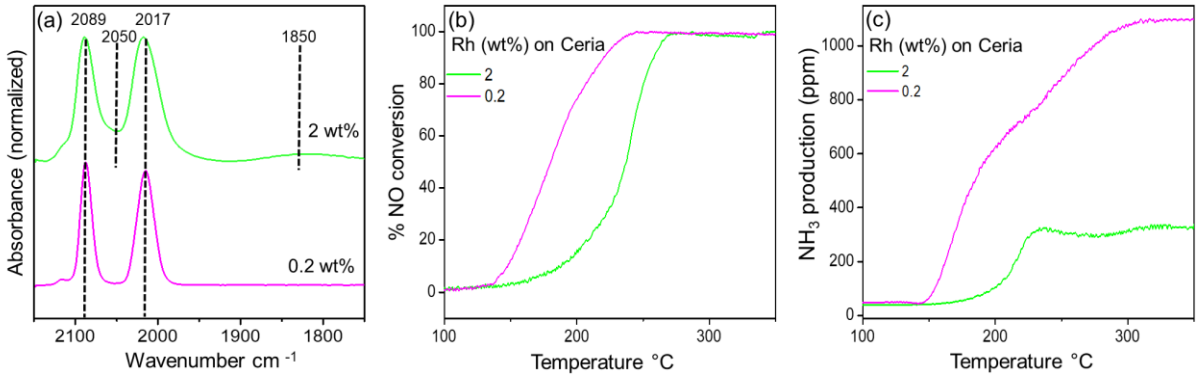

Figure 5.9: a) CO probe molecule FTIR spectra for Rh on CeO_2 (US-Nano stock #US3037, 70 m^2/g) collected at 20 °C after in-situ 350 °C oxidation for 30 minutes and 100 °C reduction in H_2 for 60 minutes, followed by saturation with 1% CO at 20 °C. The lack of stretching intensity between the $Rh(CO)_2$ bands for 0.2 wt.% Rh/CeO_2 suggest the sample consists almost exclusively of atomically dispersed Rh, while the increasing in band intensity in this region for the 2 wt.% Rh/CeO_2 catalyst suggests the existence of Rh clusters. b) NO conversion (%) during 5 °C/min temperature ramp in wet conditions (2% water /5000 ppm CO/ 1000 ppm NO.) c) NH_3 concentration in the effluent for Rh/CeO_2 during 5 °C/min temperature ramp in wet conditions (2% water /5000 ppm CO/ 1000 ppm NO). The data is consistent with the observations for $Rh/\gamma\text{-}Al_2O_3$ where atomically dispersed Rh is more active than Rh clusters under wet conditions and primarily leads to NH_3 production.

The present work demonstrates that even for a simple feed containing only NO, CO, and H_2O, dramatic differences in rate and selectivity on active sites of differing Rh nuclearity are observed. Additional species present in combustion exhaust, including oxygen and hydrocarbons, may also alter selectivity not only by introducing competing reaction pathways or inhibiting kinetically relevant steps in NO reduction, but also potentially by

altering the distribution of active site nuclearity. Thus, while it is not reasonable to hypothesize a complete mechanistic pathway for NH_3 formation over atomically dispersed species, it is likely that the mechanism is distinct from NO reduction pathways on extended Rh surfaces, which proceed through NO dissociation. It is hypothesized that NH_3 formation on atomically dispersed Rh shares mechanistic steps with the water gas shift reaction, which occurs at lower temperatures on atomically dispersed Rh as compared to Rh clusters and is promoted by reducible supports.[64] Further, it is expected that Rh structure and coordination to the support may be quite dynamic under the complex feed conditions of TWC, a consideration that will be critical for future mechanistic analyses.

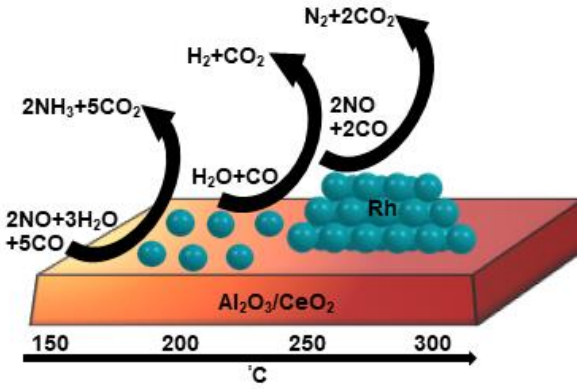

Figure 5.10: Depiction of product formation during NO reduction over different Rh structures on oxide supports at steadily increasing temperature between 150 ºC to 300 ºC. $2NO+3H_2O+5CO \rightarrow 2NH_3+5CO_2$ occurs over atomically dispersed Rh at ~180 ºC, $H_2O+CO > H_2+CO_2$ (WGS) occurs over atomically dispersed Rh at ~250, and $2NO+2CO > N_2+2CO_2$ occurs over Rh clusters at higher temperatures (~250 ºC).

In conclusion, we provide evidence that atomically dispersed Rh species selectively produce NH_3 at low temperature in the reduction of NO by CO when H_2O is present. These conclusions indicate that reformulating the TWC in catalytic converters to prevent the formation of atomically dispersed Rh could reduce NH_3 emissions from gasoline burning automobiles. This study also clearly identifies the important role of minimizing the distribution of active site types in catalytic materials to facilitate structure-function relationship elucidation.

5.4 References

(1) Matsubu, J. C.; Yang, V. N.; Christopher, P. Isolated Metal Active Site Concentration and Stability Control Catalytic CO2 Reduction Selectivity. *J. Am. Chem. Soc.* **2015**, *137* (8), 3076–3084.

(2) Yates, J. T.; Duncan, T. M.; Worley, S. D.; Vaughan, R. W. Infrared Spectra of Chemisorbed CO on Rh. *J. Chem. Phys.* **1979**, *70* (3), 1219.

(3) Duncan, T. M.; Vaughan, R. W. A 13C NMR Study of the Adsorbed States of CO on Rh Dispersed on Al_2O_3. *J. Chem. Phys.* **1980**, *73* (2), 975–985.

(4) Getsoian, A. (Bean); Theis, J. R.; Paxton, W. A.; Lance, M. J.; Lambert, C. K. Remarkable Improvement in Low Temperature Performance of Model Three-Way Catalysts through Solution Atomic Layer Deposition. *Nat. Catal.* **2019**, *2* (7), 614–622.

(5) Behera, S. N.; Sharma, M. Science of the Total Environment Investigating the Potential Role of Ammonia in Ion Chemistry of Fine Particulate Matter Formation for an Urban Environment. *Sci. Total Environ.* **2010**, *408* (17), 3569–3575.

(6) Gong, L.; Lewicki, R.; Griffin, R. J.; Tittel, F. K.; Lonsdale, C. R.; Stevens, R. G.; Pierce, J. R.; Malloy, Q. G. J.; Travis, S. A.; Bobmanuel, L. M.; et al. Role of Atmospheric Ammonia in Particulate Matter Formation in Houston during Summertime. *Atmos. Environ.* **2013**, *77*, 893–900.

(7) Bergstro, A.; Jansson, M. Atmospheric Nitrogen Deposition Has Caused Nitrogen Enrichment and Eutrophication of Lakes in the Northern Hemisphere. *Glob. Chang. Biol.* **2006**, *12* (4), 635–643.

(8) Fangmeierfl, A.; Angelika Hadwiger-Fangmeier, L. V. der E.; Jäger, H.-J. Effects of Atmospheric Ammonia on Vegetation—a Review. *Environ. Pollut.* **1994**, *86* (1), 43–82.

(9) Heeb, N. V; Forss, A.-M.; Brühlmann, S.; Lüscher, R.; Saxer, C. J.; Hug, P. Three-Way Catalyst-Induced Formation of Ammonia—Velocity-and Acceleration-Dependent Emission Factors. *Atmos. Environ.* **2006**, *40* (31), 5986–5997.

(10) Prikhodko, V. Y.; Parks, J. E.; Pihl, J. A.; Toops, T. J. Ammonia Generation and Utilization in a Passive SCR (TWC+SCR) System on Lean Gasoline Engine. *SAE Int. J. Engines* **2016**, *9* (2), 1289–1295.

(11) Macleod, N.; Isaac, J.; Lambert, R. M. A Comparison of Sodium-Modified Rh/γ-Al_2O_3 and Pd/γ-Al_2O_3 Catalysts Operated under Simulated TWC Conditions. *Appl. Catal. B Environ.* **2001**, *33* (4), 335–343.

(12) Wang, C.; Tan, J.; Harle, G.; Gong, H.; Xia, W.; Zheng, T.; Yang, D.; Ge, Y.; Zhao, Y. Ammonia Formation over Pd/Rh Three-Way Catalysts during Lean-to-Rich Fluctuations: The Effect of the Catalyst Aging, Exhaust Temperature, Lambda, and

Duration in Rich Conditions. *Environ. Sci. Technol.* **2019**, *53* (21), 12621–12628.

(13) Shelef, M.; Graham, G. W. Why Rhodium in Automotive Three-Way Catalysts? *Catal. Rev.* **1994**, *36* (3), 433–457.

(14) Digiulio, C. D.; Pihl, J. A.; Parks, J. E.; Amiridis, M. D.; Toops, T. J. Passive-Ammonia Selective Catalytic Reduction (SCR): Understanding NH 3 Formation over Close-Coupled Three Way Catalysts (TWC). *Catal. Today* **2014**, *231* (X), 33–45.

(15) Hibbitts, D. D.; Jiménez, R.; Yoshimura, M.; Weiss, B.; Iglesia, E. Catalytic NO Activation and NO–H2 Reaction Pathways. *J. Catal.* **2014**, *319*, 95–109.

(16) Dümpelmann, R.; Cant, N. W.; Trimm, D. L. The Positive Effect of Hydrogen on the Reaction of Nitric Oxide with Carbon Monoxide over Platinum and Rhodium Catalysts. *Catal. Letters* **1995**, *32* (3–4), 357–369.

(17) Oh, S. H.; Triplett, T. Reaction Pathways and Mechanism for Ammonia Formation and Removal over Palladium-Based Three-Way Catalysts : Multiple Roles of CO. *Catal. Today* **2014**, *231*, 22–32.

(18) Oh, S. H.; Fisher, G. B.; Carpenter, J. E.; Goodman, D. W. Comparative Kinetic Studies of CO-O2 and CO-NO Reactions over Single Crystal and Supported Rhodium Catalysts. *J. Catal* **1986**, *100* (2), 360–376.

(19) Zhdanov, V. P.; Kasemo, B. Mechanism and Kinetics of the NO□ CO Reaction on Rh. *Surf. Sci. Rep.* **1997**, *29* (2), 31–90.

(20) Hecker, W. C.; Bell, A. T. Reduction of NO by CO over Silica-Supported Rhodium: Infrared and Kinetic Studies. *J. Catal.* **1983**, *84* (1), 200–215.

(21) Araya, P.; Gracia, F.; Cortés, J.; Wolf, E. E. FTIR Study of the Reduction Reaction of NO by CO over Rh/SiO2 Catalysts with Different Crystallite Size. *Appl. Catal. B Environ.* **2002**, *38* (2), 77–90.

(22) Hendriksen, D. E.; Meyer, C. D.; Eisenberg, R. Nature of the Active Catalyst in the Rhodium Complex Catalyzed Reduction of Nitric Oxide by Carbon Monoxide. *Inorg. Chem.* **1977**, *16* (4), 970–972.

(23) Goldsmith, B. R.; Sanderson, E. D.; Ouyang, R.; Li, W. X. CO- and NO-Induced Disintegration and Redispersion of Three-Way Catalysts Rhodium, Palladium, and Platinum: An Ab Initio Thermodynamics Study. *J. Phys. Chem. C* **2014**, *118* (18), 9588–9597.

(24) Guzman, J.; Gates, B. C. Supported Molecular Catalysts : Metal Complexes and Clusters on Oxides and Zeolites. *Dalt. Trans.* **2003**, *17*, 3303–3318.

(25) Tan, L.; Huang, L.; Liu, Y.; Wang, Q. Detailed Mechanism of the NO + CO Reaction on Rh(1 0 0) and Rh(1 1 1): A First-Principles Study. *Appl. Surf. Sci.* **2018**, *444*, 276–286.

(26) Deushi, F.; Ishikawa, A.; Nakai, H. Density Functional Theory Analysis of Elementary Reactions in NOxReduction on Rh Surfaces and Rh Clusters. *J. Phys. Chem. C* **2017**, *121* (28), 15272–15281.

(27) Chafik, T.; Kondarides, D. I.; Verykios, X. E. Catalytic Reduction of NO by CO over Rhodium Catalysts: 1. Adsorption and Displacement Characteristics Investigated by In Situ FTIR and Transient-MS Techniques. *J. Catal.* **2000**, *190* (2), 446–459.

(28) McCabe, R. W.; Wong, C. Steady-State Kinetics of the CON2O Reaction over an Alumina-Supported Rhodium Catalyst. *J. Catal.* **1990**, *121* (2), 422–431.

(29) Almusaiteer, K. A.; Chuang, S. S. C. Infrared Characterization of Rh Surface States and Their Adsorbates during the NO-CO Reaction. *J. Phys. Chem. B* **2000**, *104* (10), 2265–2272.

(30) Granger, P.; Dhainaut, F.; Pietrzik, S.; Malfoy, P.; Mamede, A. S.; Leclercq, L.; Leclercq, G. An Overview: Comparative Kinetic Behaviour of Pt, Rh and Pd in the NO+CO and NO+H2 Reactions. *Top. Catal.* **2006**, *39* (1–2), 65–76.

(31) Vityuk, A. D.; Ma, S.; Alexeev, O. S.; Amiridis, M. D. NO Reduction with CO over HY Zeolite-Supported Rhodium Dicarbonyl Complexes: Giving Insight into the Structure Sensitivity. *React. Chem. Eng.* **2019**, *4* (2), 418–426.

(32) Qi, J.; Christopher, P. Atomically Dispersed Rh Active Sites on Oxide Supports with Controlled Acidity for Gas-Phase Halide-Free Methanol Carbonylation to Acetic Acid. *Ind. Eng. Chem. Res.* **2019**, *58* (28), 12632–12641.

(33) Shan, J.; Li, M.; Allard, L. F.; Lee, S.; Flytzani-Stephanopoulos, M. Mild Oxidation of Methane to Methanol or Acetic Acid on Supported Isolated Rhodium Catalysts. *Nature* **2017**, *551* (7682), 605–608.

(34) Serna, P.; Gates, B. C. Zeolite-Supported Rhodium Complexes and Clusters: Switching Catalytic Selectivity by Controlling Structures of Essentially Molecular Species. *J. Am. Chem. Soc.* **2011**, *133* (13), 4714–4717.

(35) Santos, P. S.; Santos, H. S.; Toledo, S. P. Standard Transition Aluminas. Electron Microscopy Studies. *Mater. Res.* **2000**, *3* (4), 104–114.

(36) Asokan, C.; Derita, L.; Christopher, P. Using Probe Molecule FTIR Spectroscopy to Identify and Characterize Pt - Group Metal Based Single Atom Catalysts. *Chinese J. Catal.* **2017**, *38* (9), 1473–1480.

(37) Tang, Y.; Asokan, C.; Xu, M.; Graham, G. W.; Pan, X.; Christopher, P.; Li, J.; Sautet, P. Rh Single Atoms on TiO2 Dynamically Respond to Reaction Conditions by Adapting Their Site. *Nat. Commun.* **2019**, *10* (1), 4488.

(38) Hyde, E. A.; Robert, R.; Rochester, C. H. Infrared Study of the Interactions between NO and CO on Rh / Al2O3 Catalysts. *J. Chem. Soc. Faraday Trans. 1 Phys. Chem. Condens. Phases* **1984**, *80* (3), 531–541.

(39) Granger, P.; Delannoy, L.; Lecomte, J. J.; Dathy, C.; Praliaud, H.; Leclercq, L.; Leclercq, G. Kinetics of the CO + NO Reaction over Bimetallic Platinum-Rhodium on Alumina: Effect of Ceria Incorporation into Noble Metals. *J. Catal.* **2002**, *207* (2), 202–212.

(40) Lamberti, C.; Zecchina, A.; Groppo, E.; Bordiga, S. Probing the Surfaces of Heterogeneous Catalysts by in Situ IR Spectroscopy. *Chem. Soc. Rev.* **2010**, *39* (12), 4951.

(41) Asokan, C.; Thang, H. V.; Pacchioni, G.; Christopher, P. Reductant Composition Influences the Coordination of Atomically Dispersed Rh on Anatase TiO2. *Catal. Sci. Technol.* **2020**, *10* (6), 1597–1601.

(42) Garland, C. W.; Yang, A. Infrared Studies of Carbon Monoxide Chemisorbed on Rhodium. *J. Phys. Chem.* **1957**, *61* (11), 1504–1512.

(43) Goellner, J. F.; Gates, B. C.; Vayssilov, G. N.; Rösch, N. Structure and Bonding of a Site-Isolated Transition Metal Complex: Rhodium Dicarbonyl in Highly Dealuminated Zeolite Y. *J. Am. Chem. Soc.* **2000**, *122* (33), 8056–8066.

(44) Brown, T. L.; Darensbourg, D. J. Intensities of CO Stretching Modes in the Infrared Spectra of Adsorbed CO and Metal Carbonyls. *Inorg. Chem.* **1967**, *6* (5), 971–977.

(45) Van't Blik, H. F. J.; Van Zon, J.; Huizinga, T.; Vis, J. C.; Koningsberger, D. C.; Prins, R. Structure of Rhodium in an Ultradispersed Rhodium/Alumina Catalyst as Studied by EXAFS and Other Techniques. *J. Am. Chem. Soc.* **1985**, *107* (11), 3139–3147.

(46) Robbins, J. L. Rhodium Dicarbonyl Sites on Alumina Surfaces. 1. Preparation and Characterization of a Model System. *J. Phys. Chem.* **1986**, *90* (15), 3381–3386.

(47) Buchanan, D. A.; Hernandez, M. E.; Solymosi, F.; White, J. M. CO-Induced Structural Changes of Rh on TiO2 Support. *J. Catal.* **1990**, *125* (2), 456–466.

(48) Guan, H.; Lin, J.; Qiao, B.; Miao, S.; Wang, A.; Wang, X.; Zhang, T. Enhanced Performance of Rh 1 / TiO 2 Catalyst Without Methanation in Water-Gas Shift Reaction. *AIChE J.* **2017**, *63* (6), 2081–2088.

(49) Resasco, J.; DeRita, L.; Dai, S.; Chada, J. P.; Xu, M.; Yan, X.; Finzel, J.; Hanukovich, S.; Hoffman, A. S.; Graham, G. W. Uniformity Is Key in Defining Structure–Function Relationships for Atomically Dispersed Metal Catalysts: The Case of Pt/CeO2. *J. Am. Chem. Soc.* **2019**, *142* (1), 169–184.

(50) DeRita, L.; Resasco, J.; Dai, S.; Boubnov, A.; Thang, H. V.; Hoffman, A. S.; Ro, I.; Graham, G. W.; Bare, S. R.; Pacchioni, G.; et al. Structural Evolution of Atomically Dispersed Pt Catalysts Dictates Reactivity. *Nat. Mater.* **2019**, *18* (7), 746–751.

(51) Rice, C. A.; Worley, S. D.; Curtis, C. W.; Guin, J. A.; Tarrer, A. R. The Oxidation State of Dispersed Rh on AI2O3. *J. Chem. Phys.* **1981**, *74* (11), 6487–6497.

(52) Yates, J. T.; Duncan, T. M.; Worley, S. D.; Vaughan, R. W. Infrared Spectra of

Chemisorbed CO on Rh. *J. Chem. Phys.* **1979**, *70* (3), 1219.

(53) Cavanagh, R. R., Yates Jr., J. T. Site Distribution Studies of Rh Supported on Al2O3—An Infrared Study of Chemisorbed CO. *J. Chem. Phys.* **1981**, *74* (7), 4150.

(54) Getsoian, A. B.; Theis, J. R.; Lambert, C. K. Sensitivity of Three-Way Catalyst Light-Off Temperature to Air-Fuel Ratio. *Emiss. Control Sci. Technol.* **2018**, *4* (3), 136–142.

(55) Coller, D. H.; Vicente, B. C.; Scott, S. L. Rapid Extraction of Quantitative Kinetic Information from Variable-Temperature Reaction Profiles. *Chem. Eng. J.* **2016**, *303*, 182–193.

(56) Flytzani-stephanopoulos, M. Gold Atoms Stabilized on Various Supports Catalyze the Water À Gas Shift Reaction. *Acc. Chem. Res.* **2014**, *47* (3), 783–792.

(57) Li, J.; Liu, J.; Zhang, T. Remarkable Performance of Ir1/FeOx Single-Atom Catalyst in Water Gas Shift Reaction. *J. Am. Chem. Soc.* **2013**, *135* (41), 15314−15317.

(58) Ghosh, T. K.; Nair, N. N. Rh 1 / g -Al 2 O 3 Single-Atom Catalysis of O 2 Activation and CO Oxidation : Mechanism , Effects of Hydration , Oxidation State , and Cluster Size. *ChemCatChem* **2013**, *016* (5), 1811–1821.

(59) Tamura, M.; Shimizu, K.; Satsuma, A. Applied Catalysis A : General Comprehensive IR Study on Acid / Base Properties of Metal Oxides. *"Applied Catal. A, Gen.* **2012**, *433*, 135–145.

(60) Busca, G. The Surface Acidity of Solid Oxides and Its Characterization by IR Spectroscopic Methods . An Attempt at Systematization. *Phys. Chem. Chem. Phys.* **1999**, *1* (5), 723–736.

(61) Jeong, H.; Kwon, O.; Kim, B.; Bae, J.; Shin, S.; Kim, H.; Kim, J.; Lee, H. Highly Durable Metal Ensemble Catalysts with Full Dispersion for Automotive Applications beyond Single-Atom Catalysts. *Nat. Catal.* **2020**, 1–8.

(62) Jeong, H.; Lee, G.; Kim, B.; Bae, J.; Han, J. W.; Lee, H. Fully Dispersed Rh Ensemble Catalyst To Enhance Low-Temperature Activity. *J. Am. Chem. Soc.* **2018**, *140* (30), 9558–9565.

(63) Liu, L.; Boronat, M.; Arenal, R.; Concepcion, P.; Corma, A. Low-Temperature Catalytic NO Reduction with CO by Subnanometric Pt Clusters. *ACS Catal.* **2019**, *9* (12), 11530–11541.

(64) Li, T.; Chen, F.; Lang, R.; Wang, H.; Su, Y.; Qiao, B.; Wang, A.; Zhang, T. Styrene Hydroformylation with In Situ Hydrogen : Regioselectivity Control by Coupling with the Low-Temperature Water – Gas Shift Reaction. *Angew. Chemie Int. Ed.* **2020**, *59*, 1–6.

Chapter 6:

Conclusions, and Future Perspectives.

6.1 Conclusions

Previously, extensive studies of NO reduction by CO on Rh catalysts have focused on Rh particles and extended surfaces, primarily in dry environments. These studies are inconsistent with realistic automotive conditions in catalytic converters where there are low Rh weight loadings (0.2-0.3 wt%) and high concentrations of H_2O, up to 10%.[30,82,196] Our studies focused on analyzing the role of atomically dispersed Rh species in NO reduction by CO under dry and wet environments.

Our work started by using principles from SEA to optimize interactions between charged Rh precursors in solution and oxide support surfaces, enabling the synthesis of atomically dispersed metal catalysts on various oxide supports. These materials were characterized in detail using probe molecule FTIR spectroscopy, TPD, and HAADF-STEM imaging. The experimental analyses were used to develop and validate theoretical active site models.[169,197,198] The theoretical active site models and extensive DFT calculations and thermodynamic modelling then informed how the local coordination of Rh species adapts to changes in environment.

We then used these series of materials to demonstrate that atomically dispersed Rh species act as distinct active sites in TWC conditions with water as a co-feed and are quantitatively selective to NH_3 formation at low temperatures (< 200 °C). Alternatively, Rh clusters were selective to N_2 and N_2O under identical conditions. Therefore, solely considering a Rh extended surface or larger Rh nanoparticles for NO reduction to understand realistic TWC reactivity in catalytic converters is not practical, because there is a mix of active Rh structures in TWCs. [10,65,82,199–202] Our results provided an important result for industrial researchers to attempt to mitigate NH_3 formation during start up conditions. This implies that the formulation of the TWC or emission control strategies should be targeted to

avoid the formation of atomically dispersed Rh species to mitigate low temperature NH_3 formation. Broadly, this study also clearly identifies the important role of minimizing the distribution of active site types in catalytic materials to facilitate structure-function relationship elucidation.

6.2 Future Work

6.2.1 Support Influence on Atomically Dispersed Metal Activity

Using CO as a probe molecule in FTIR, we show features associated with $Rh(CO)_2$ on CeO_2, TiO_2, and Al_2O_3 (Figure 6.1 a, b, and c) after CO saturation.[95,106,107,117] To compare the adsorption strength of CO to the atomically dispersed Rh catalysts on different supports, TPD at 20 °C/min was employed to track the intensity decrease of the CO stretching bands (Figure 6.1 a, b, and c). The temperature where the CO band intensity decreases the most between regular temperature intervals, indicating the temperature where CO reaches the highest desorption rate from the atomically dispersed Rh, varies with support reducibility. That is, CO desorbs from atomically dispersed Rh on the least reducible support, CeO_2, at the lowest temperature comparatively, by 160 °C. Then subsequently CO desorbs from atomically dispersed Rh on TiO_2 and then Al_2O_3 at increasing temperatures, 300 and 450 °C. The general trend observed is increasing CO adsorption strength with decreasing support reducibility; CeO_2 being the most reducible, then TiO_2, and then Al_2O_3.[203,204] If CO adsorption strength can be inversely related to Rh adsorption strength to the support, this indicates that Rh bonds strongly to reducible supports.

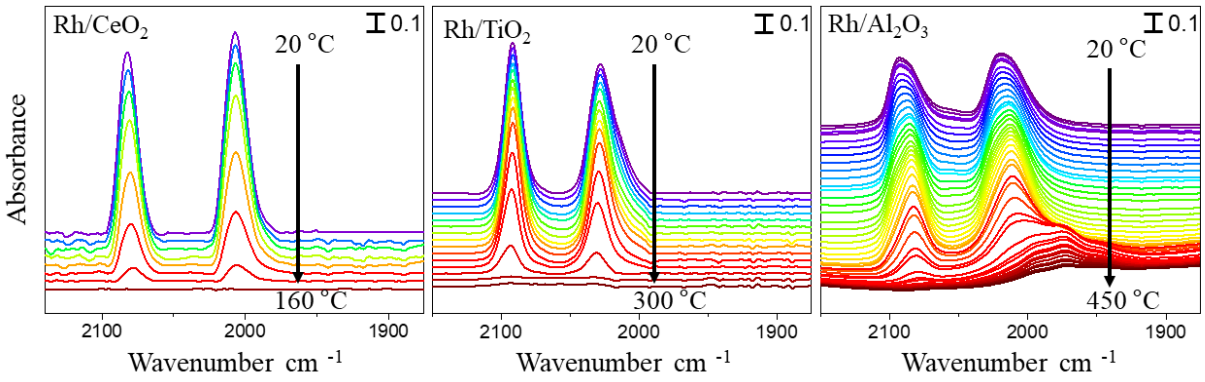

Figure 6.1 FTIR spectra of atomically dispersed Rh after CO saturation to form $Rh(CO)_2$ on oxide supports, indicated by symmetric and asymmetric signatures at ~2090 and 2020 cm^{-1}, and during TPD of CO a rate of 20° C/min after sample was reduced in CO at 300 °C for 60 min a) 0.1% Rh on Ceria, CeO_2 b) 0.1% Rh on anatase Titania, TiO_2 c) 0.1% Rh on γ-Alumina, Al_2O_3

We then look to how support influences on the adsorption energy of CO to atomically dispersed Rh relates to catalytic reactivity. Previous studies have attempted to link trends in reactivity of precious metals to support influence.[204,205] Here, in figure 6.2, we provide evidence that on atomically dispersed Rh, NO reduction by CO in the presence of water and the resulting NH_3 formation light off temperature is correlated to CO adsorption strength on atomically dispersed Rh. As previously seen, atomically dispersed Rh is 100% selective towards NH_3 during NO reduction by CO in the presence of water.[198] Across the three relevant supports we studied, NH_3 formation lights off at the lowest temperature, 155 °C, on atomically dispersed Rh/CeO_2, then at 165 °C on Rh/TiO_2, and then finally at 170 °C on Rh/Al_2O_3. This is consistent with the order of reducibility of these supports: CeO_2> TiO_2> Al_2O_3. Additional work should be done in the future to establish connections between the binding energy of CO to Rh, the interaction of Rh and the oxide support, and the light off temperature for CO reduction by NO. Clearly the support has a significant influence on the chemistry and catalytic properties of atomically dispersed species.

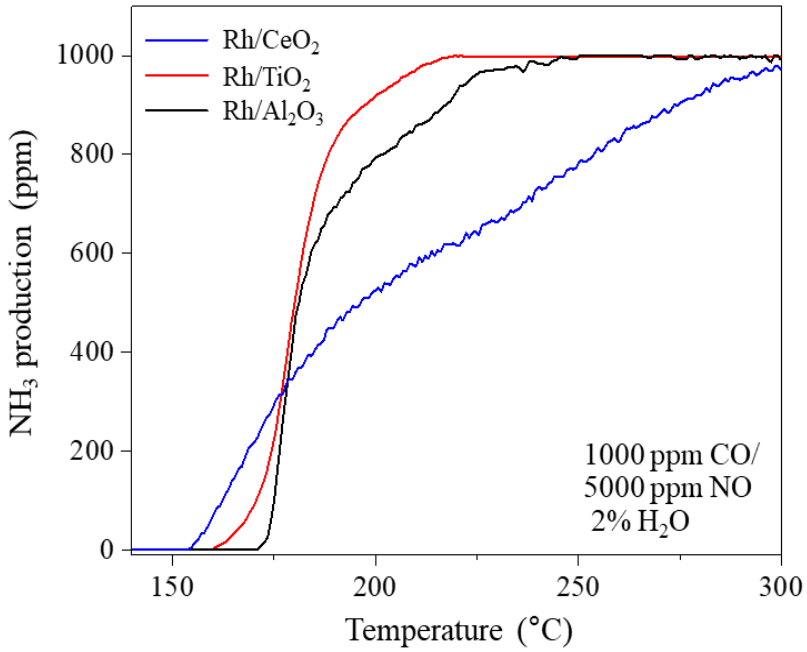

Figure 6.2: NH_3 concentration in the effluent during 5 °C/min temperature ramp in wet NO reduction conditions (2% water /5000 ppm CO/ 1000 ppm NO) over atomically dispersed 0.1% Rh on CeO_2 (blue), 0.1% Rh on TiO_2 (red), and 0.05% Rh on Al_2O_3.

6.2.2 Finding the Active Atomically Dispersed Rh Structure During NO Reduction

In order to provide insights into the mechanism of NH_3 formation through NO reduction by CO in wet environments on atomically dispersed Rh active sites, we are interested in developing a realistic theoretical model of atomically dispersed Rh species on Al_2O_3. By comparing CO probe molecule FTIR to DFT calculations, we were able to observe agreement between experimental and theoretical characteristics of $Rh(CO)_2$, including CO binding energies, stretching frequencies, and influence of surface hydroxylation. We also show through cryogenic FTIR and DFT calculations on our narrowed down selection of model sites that CO preferentially bonds to atomically dispersed Rh over NO and the Rh species does not appear to strongly bond to NO because the highly reactive nature of the Rh site converts NO into N_2O from the $Rh(NO)_2$ form at low temperature.

Symmetric and asymmetric stretching frequencies associated with the $Rh(CO)_2$ species were observed in FTIR measurements at 2094 and 2020 cm^{-1} (see Figure 6.3a) after an atomically dispersed 0.1% Rh/ Al_2O_3 catalyst was insitu pretreated with H_2 at 100 °C, and then saturated by flowing 1% CO.[107,206] The lack of CO bands in the experimental FTIR spectra at frequencies characteristic of linear (~2040-2080 cm^{-1}) and bridge (~1850-1950 cm^{-1}) bound CO on Rh clusters confirms that Rh primarily existed as atomically dispersed species following CO exposure.[207] Extensive DFT calculations of $Rh(CO)_2$ on Al_2O_3 this assignment.[208] The bands are wide and show asymmetry, suggesting the existence of multiple coordination environments, possibly due to proximity to hydroxyls. Rhe large FWHM indicates a lack of homogeneity of the local coordination environment of $Rh(CO)_2$ species.[209–211] TPD measurements of CO from the 0.1 wt. % Rh catalyst provide evidence that 2 distinct $Rh(CO)_2$ species exist with two distinct sets of symmetric and asymmetric frequencies, (2094/2024 and 2084/2012), figure 6.3b. As temperature increases from ambient temperature to 220 °C, the pair of bands at 2094 and 2024 cm^{-1} decrease together while the pair of bands at 2084 and 2012 cm^{-1} grow, suggesting that the first species reconstructs into the second species as temperature increases.[121,127] At 220 °C, the 2084 and 2012 cm^{-1} peaks reach a maximum in area before decreasing as temperature continued to increase, (see Figure 6.3a and Table 6.1). Above 220 °C the loss of intensity of the bands at 2012 and 2084 cm^{-1} coincides with the formation of distinct bands at ~1975-1985 cm^{-1}. Recent work on Rh/TiO_2 suggests that the emergence of these bands are due to the proximity of the $Rh(CO)_2$ species to an OH species on the support, which stabilizes the formation of Rh(CO) species coordinated to OH groups.[169] This species is predicted to characteristically desorb each CO at different temperatures such that 1 CO first desorbs to leave a Rh(CO)(OH) species with a characteristic CO stretches a 1975-1985 cm^{-1}.

The change of peak areas, and thus change in surface adsorbate concentration, was analyzed as a function of temperature. The first CO desorption appears to have a direct correlation to NO reduction over atomically dispersed Rh sites as measured in a temperature programmed reactivity measurement. Seen in figure 6.3c, NO light off conversion by CO coincides with the loss of intensity of the ~2084 cm^{-1} / 2010 cm^{-1} $Rh(CO)_2$ bands, and thus coincides with the loss of the first CO from the $Rh(CO)_2$ species.[198] Combined TPD and light off analysis of atomically dispersed Rh suggests that dry NO conversion by CO occurs on CO poisoned $Rh(CO)_2$ sites and that desorption of the first CO is the rate limiting step specific to this Rh structure. This is in direct contrast to NO reduction over nanoparticles where NO outcompetes CO and directly limits the reaction rate. Therefore, a key difference in modeling NO reduction over atomically dispersed Rh compared to Rh particles it that the reaction would start with a CO saturated Rh atom, rather than an NO saturated Rh particle.

Using Redhead analysis, the adsorption energy of CO for each deconvoluted species can be calculated based on the maximum temperature of desorption, table 6.1.[212,213] The predicted $Rh(OH)(CO)_2$ species has 2 distinct adsorption energies for each CO molecule, hence 2 desorption temperatures. In order to identify the nature of the different Rh species, including the experimentally hypothesized $Rh(OH)(CO)_2$ species, an extensive series of models of Rh species and their computed properties was considered by DFT calculations and compared to experimental characteristics in table 6.1. Given the surface complexity of Al_2O_3, experimental observations will aide in identifying which $Rh(CO)_2$ coordination exists on the hydroxylated oxide surface and the level of surface hydroxylation at specified temperatures.[146,151,152] Specifically, one modeled $Rh(CO)_2$ species would have properties, including frequencies at 2094/2024 cm^{-1}, that are present at room temperature, where there is a high saturation of hydroxyl groups bonded to the oxide surface. The first $Rh(CO)_2$ species

may be mobile on the Al_2O_3 surface and allow the first species to reconstruct into the second identified $Rh(CO)_2$ species (~2084 cm^{-1} / 2010 cm^{-1}). This second species would characteristically desorb 1 CO at a time and is associated with nearby a hydroxyl group.[169] Based on experimentally determined binding energies from redhead analysis, the first Rh-CO would have a binding energy of ~1.6 eV and the 2nd Rh-CO would have a binding energy between ~1.8 -2.1 eV.[125,212]

Table 6.1. Parameters to fit and deconvolute CO vibrational frequencies associated with CO bonding to atomically dispersed Rh species on Al_2O_3 and corresponding enthalpy and entropy values

cm^{-1}	2094/2020	2084/2010	1985	1975
FWHM	11.4/11.6	22/29	49	36
T °C	190	300	360	450
Adsorption Energy [b] (ev)	1.3[a]	1.6	1.8	2.1

[a] Binding energy calculated if separate species desorbs [b]Energies calculated using Redhead analysis, assuming first order desorption, assumed constant assumed to be $10^{13.6}$:

Where: $$\frac{E}{RT_p} = ln\left(\frac{\upsilon T_p}{\beta}\right) - 3.46$$

E= Energy, kJ/mol
T_p= Temperature at peak desorption rate*, K
R= 8.3124 kJ/ K kmol
υ = rate constant= $10^{13.6}$

β = Rate of Temperature, 20 °K/min

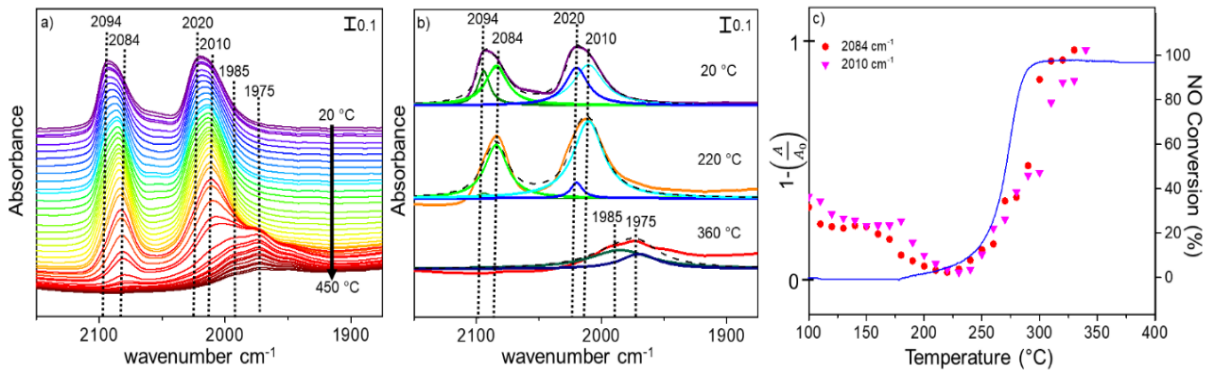

Figure 6.3: a) IR spectra's taken of 0.1% Rh/Al_2O_3 every 10 °C after sample is fully saturated with CO, and as temperature increases 20 °C/min , identifying 2 pairs of $Rh(CO)_2$ symmetric and asymmetric peaks at 2094/2020 and 2084/2010 cm^{-1} and linear CO on atomically dispersed Rh peaks at 1985-1975 b) Deconvolution spectra from (a) at 20 °C, to assign secondary pair of $Rh(CO)_2$ symmetric and asymmetric peak positions, at 220 °C to assign primary pair of $Rh(CO)_2$ symmetric and asymmetric peak positions, and at 360 °C to assign linear CO on atomically dispersed Rh peak positions c) Fraction of deconvoluted symmetric (2084 cm^{-1}) and asymmetric (2010 cm^{-1}) $Rh(CO)_2$ IR peak area loss normalized to the largest respective peak area overlay with NO conversion (%) as a function of temperature at a ramp rate of 5 °C/min in 5000 ppm of CO/1000 ppm of NO of 200 mg of diluted 0.1% Rh/Al_2O_3 catalyst (0.2 mg Rh)

Additionally, via probe molecule FTIR, a NO stretching frequency was not observed when flowing NO over atomically dispersed 0.1% Rh/ Al_2O_3 at 20 °C. When subsequently flowing CO, $Rh(CO)_2$ asymmetric and symmetric bands were observed similarly to what was observed when initially flowing CO, even in the presence of NO (figure 6.4a). NO bands were still not observed as CO desorbs from the species while being heated to 400°C at 20 °C/min and then cooled down to 20 °C in NO. This indicates that once CO adsorbs onto atomically dispersed Rh, it is not easily displaced by NO. Next, we cooled down to -120 °C in NO flow to see if NO adsorbs on atomically dispersed Rh at cryogenic temperatures. While NO was flowing, we observed a ~1900 cm^{-1} feature below -50 °C but only after -100°C did apparent growth of a 1885 cm^{-1} feature and overlapping 1760/1740 stretches at ~1750 cm^{-1} appear, likely associated with $Rh^+(NO)_2$ (figure 6.4a and 6.4b). The initial ~1900 cm^{-1} band was likely due to the presence of $Rh^+(NO)$ species, as seen in previous examples

of cationic Rh on oxide supports. The a combination of overlapping symmetric vibration bands from multiple $Rh^{+}(NO)_2$ species become clear at -120 °C, thus resulting in a center peak value of 1885 cm^{-1}.[36,130,131,214] Warming back to 20 °C in argon showed a loss of stretches associated with $Rh^{+}(NO)_2$. When cooling back down to -120 °C in argon, the ~1885/1750 stretches did not appear, thus proving the stretches were not present as a function of temperature but rather the NO species was created in NO flow at cryogenic temperatures and was not stable when the temperature was increased to 20 °C. Reflowing NO after the environment was stable at -120 °C resulted in readsorption of NO species with characteristic ~1885/1750 cm^{-1} stretches (figure 6.4b).[179,215] During the disappearance of bands at ~1885/1750 cm^{-1}, a notable band increased at 1625 cm^{-1}, overlapping with bands associated with surface adsorbed NO dimers. We hypothesized that this stretch may be associated with N_2O formation.[36,123,216] Shown in figure 6.5, we flowed 1000 ppm N_2O over the plain Al_2O_3 support to provide reference for the N_2O spectral signature at cryogenic temperatures. Stretching frequencies for N_2O on plain Al_2O_3 were observed at -120 °C at 1650 and 2240 cm^{-1}, which were also observed above -100 °C after NO exposed Rh catalyst was warmed in argon to 20 °C (figure 6.4b). This implies that the $Rh(NO)_2$ species is highly reactive, such that it is not detectable at 20 °C and immediately forms N_2O that interacts with the Al_2O_3 surface.[56,57,217] In future studies, we will compare DFT calculations to provide evidence of the low energy barrier of N_2O from $Rh(NO)_2$ based on structures with similar $Rh(CO)_2$ characteristics as what we have seen experimentally. This will give us a basis to understand the mechanism for NO reduction on these species.

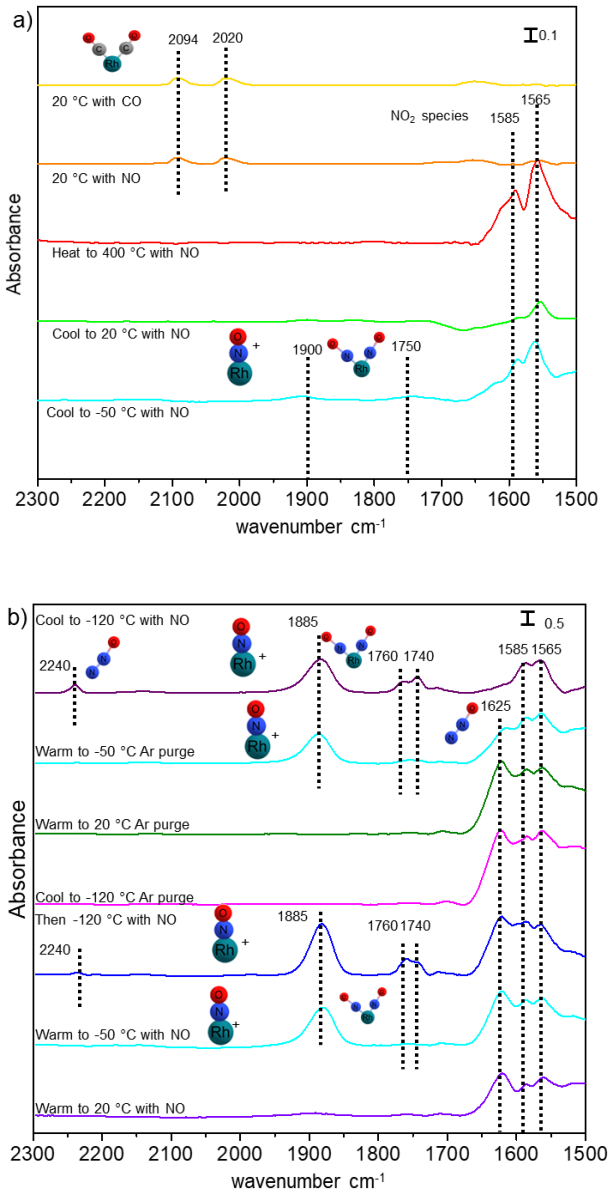

Figure 6.4: (a) 0.1% Rh in 1.0% CO/Ar flow to form $Rh(CO)_2$ (yellow line) and then 1.5% NO/Ar flows over the sample for 15 minutes while $Rh(CO)_2$ remains at ambient (orange line). Sample is heated to 400 °C at 20 °C/min (red line) and cooled back down to 20 °C in 1.5% NO/Ar (light green line). Above 20 °C, there was an absence of NO related stretching frequencies. Cooling down to cryogenic temperature in NO show's growth of a 1900 cm^{-1} feature at -50 °C (light blue line) (b) The 1900 cm^{-1} then grows into a 1885 cm^{-1} stretch and overlapping stretches at 1760/1740 cm^{-1} appear, associated with $Rh(NO)_2$, while NO flows below -100°C (purple line). Warming back to 20 °C shows apparent shrinkage/ disappearance of 1885/1760/1740 cm^{-1} stretches and an apparent increase of stretching frequency at ~1625 cm^{-1} (dark green line). Cooling back down in Ar does not result in the reappearance former bands at -120 °C (pink line). When NO is reposed to the catalyst at -120 °C, features at 1885/1760/1740 cm^{-1} reappear (dark blue line).

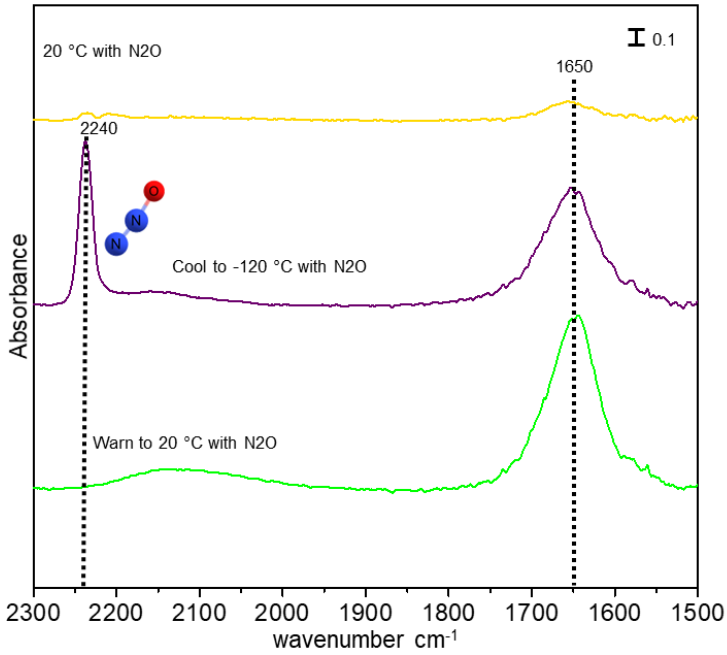

Figure 6.5: N_2O flow over plain Al_2O_3 at 20° C and -120° C, indicating stretches associated with N_2O on Al_2O_3 at 2240 and 1650 cm^{-1}

6.2.3 Rh Reconstruction Effect on NO Reduction by CO Kinetics

Finally, with the insights provided here that different Rh structures have different reactivity and selectivity for NO reduction by CO, it is critical to consider whether various Rh structure interconvert under relevant reaction conditions. Further, in the case of NO reduction by CO in TWCs, kinetic studies are challenging because we have provided evidence that the structure of Rh is dependent on atmospheric conditions.[32,202] We have started initial kinetic studies under differential reaction conditions where the rate of NO reduction varies based on what conditions the catalyst was previously exposed to – the catalyst had memory, which strong suggests reconstruction.

A 0.1 wt% Rh/Al_2O_3 catalyst (starting as predominantly atomically dispersed Rh species) was initially exposed to low CO/NO ratios (0.00025:0.005 PPM) and the NO reduction rate was measured as a function of increasing CO partial pressure. The observed behavior resembled what would be expected from Rh nanoparticle NO reduction chemistry

(figure 6.6a) and selectivity was consistent with Rh nanoparticles, ~60% N_2O/~40 N_2 (figure 6.6b). However, the behavior was distinct the catalyst was initially exposed to high CO/NO ratios (0.0075:0.005) and the NO reduction rate was measured as a function of CO partial pressure decreased. The NO reduction rate was higher overall compared to the former case (figure 6.6a) and the selectivity toward N_2 was higher than the former case (figure 6.6b). This notable change in reactivity was likely due to a change in active site distribution, because Rh is able to reconstruct in variable reactant atmospheres. This simple experiment shows how the structure of supported Rh species are highly dependent on their environmental condition.

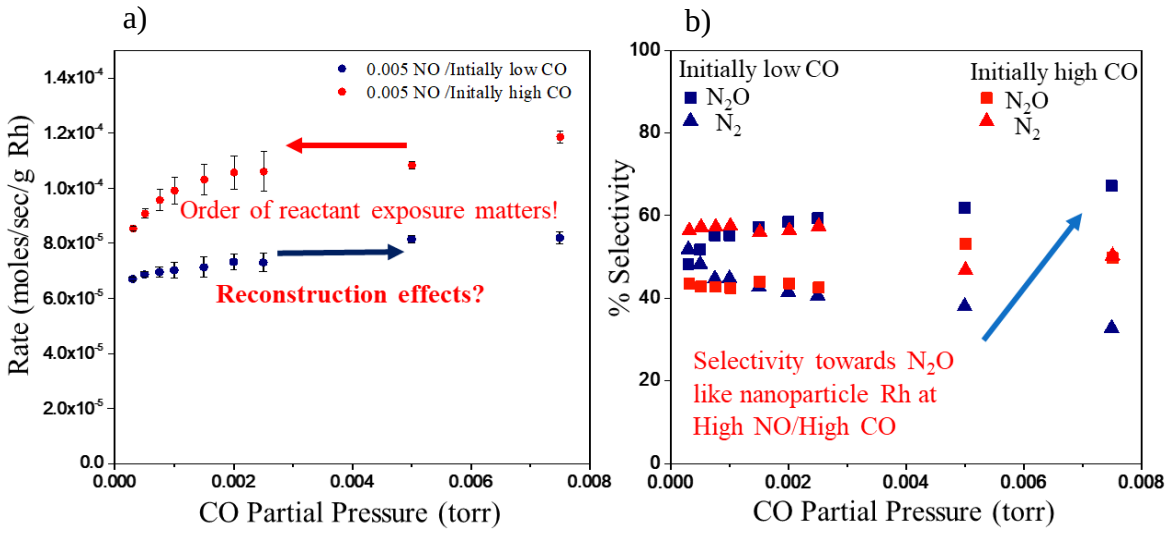

Figure 6.6: Atomically dispersed 0.05% Rh/ Al_2O_3 were diluted with acid purified silica, insitu oxidized at 350 °C for 30 min and reduced at 100 °C for 60 min. Gas concentration after catalyst exposure was collected and reported as an average of data points taken every 10 seconds for 15 min at 205 °C, 250 sccm flow rate, constant 0.005 partial pressure NO at 800 torr, and specified steady state CO partial pressures. a) Rate of NO reduction as a function of variable CO partial pressure at constant 0.005 NO where catalyst was initially exposed to the low CO partial pressure of 0.00025 CO then increased to eventually 0.0075 CO (in blue) vs. catalyst was initially exposed to the high CO partial pressure of 0.0075 CO then eventually decreased to 0.00025 CO (in red). b) Corresponding N_2 and N_2O selectivity of initially low CO partial trial vs. initially high CO partial pressure trial where differences depending on initial CO/NO exposure have correlation to selectivity.

The fact that NO reduction reactivity and selectivity in catalytic converters exhibits unique and dynamic changes with operating conditions suggests that the ensemble of existing active sites may be continuously evolving.[2,51] Future work will focus on how the mobility of Rh may contribute to NO_x reduction performance and selectivity, including the develop of stability phase diagrams, which could potentially be used to inform control systems about which composition spaces may produce unwanted atomically dispersed species. Further, dynamic structure of Rh species under the complex feed conditions of TWCs, is a critical consideration for future mechanistic analyses.

6.3 References

(1) Granger, P.; Delannoy, L.; Lecomte, J. J.; Dathy, C.; Praliaud, H.; Leclercq, L.; Leclercq, G. Kinetics of the CO + NO Reaction over Bimetallic Platinum-Rhodium on Alumina: Effect of Ceria Incorporation into Noble Metals. J. Catal. 2002, 207 (2), 202–212.

(2) Srinivasan, A.; Depcik, C. Review of Chemical Reactions in the NO Reduction by CO on Rhodium/Alumina Catalysts. Catal. Rev. - Sci. Eng. 2010, 52 (4), 462–493.

(3) Nehasil, V.; Stará, I.; Matolín, V. Study of CO Desorption and Dissociation on Rh Surfaces. Surf. Sci. 1995, 331–333 (PART A), 105–109.

(4) Tang, Y.; Asokan, C.; Xu, M.; Graham, G. W.; Pan, X.; Christopher, P.; Li, J.; Sautet, P. Rh Single Atoms on TiO2 Dynamically Respond to Reaction Conditions by Adapting Their Site. Nat. Commun. 2019, 10 (1), 4488.

(5) Asokan, C.; Thang, H. V.; Pacchioni, G.; Christopher, P. Reductant Composition Influences the Coordination of Atomically Dispersed Rh on Anatase TiO2. Catal. Sci. Technol. 2020, 10 (6), 1597–1601.

(6) Asokan, C.; Yang, Y.; Dang, A.; Getsoian, A. “Bean”; Christopher, P. Low-Temperature Ammonia Production during NO Reduction by CO Is Due to Atomically Dispersed Rhodium Active Sites. ACS Catal. 2020, 10 (9), 5217–5222.

(7) Worley, S. D.; Rice, C. A.; Mattson, G. A. The Effect of Rhodium Precursor on Rhl Al2O3 Catalysts. 1982, 76 (1), 20–25.

(8) McCabe, R. W.; Usmen, R. K.; Ober, K.; Gandhi, H. S. The Effect of Alumina Phase-Structure on the Dispersion of Rhodium/Alumina Catalysts. Journal of Catalysis. 1995, pp 385–393.

(9) Miessner, H.; Gutschick, D.; Ewald, H.; Miller, H. The Influence of Support on the Geminal Dicarbonyl Species RhI (CO) 2 on Supported Rhodium Catalysts: An IR Spectroscopic Study. 2000, 36 (1986), 369–373.

(10) Dictor, R.; Roberts, S. Influence of Ceria on Alumina-Supported Rhodium: Observations of Rhodium Morphology Made Using FTIR Spectroscopy. J. Phys. Chem. 1989, 93 (15), 5846–5850.

(11) Burch, R.; Breen, J. P.; Meunier, F. C. A Review of the Selective Reduction of NOxwith Hydrocarbons under Lean-Burn Conditions with Non-Zeolitic Oxide and Platinum Group Metal Catalysts. Appl. Catal. B Environ. 2002, 39 (4), 283–303.

(12) Gandhi, H. S.; Graham, G. W.; McCabe, R. W. Automotive Exhaust Catalysis. J. Catal. 2003, 216 (1–2), 433–442.

(13) Resasco, J.; Dai, S.; Graham, G.; Pan, X.; Christopher, P. Combining In-Situ Transmission Electron Microscopy and Infrared Spectroscopy for Understanding Dynamic and Atomic-Scale Features of Supported Metal Catalysts. J. Phys. Chem. C 2018, 122 (44), 25143–25157.

(14) Jones, J.; Xiong, H.; DeLaRiva, A. T.; Peterson, E. J.; Pham, H.; Challa, S. R.; Qi, G.; Oh, S.; Wiebenga, M. H.; Hernández, X. I. P. Thermally Stable Single-Atom Platinum-on-Ceria Catalysts via Atom Trapping. Science (80-.). 2016, 353 (6295), 150–154.

(15) Nie, L.; Mei, D.; Xiong, H.; Peng, B.; Ren, Z.; Hernandez, X. I. P.; DeLaRiva, A.; Wang, M.; Engelhard, M. H.; Kovarik, L. Activation of Surface Lattice Oxygen in Single-Atom Pt/CeO2 for Low-Temperature CO Oxidation. Science (80-.). 2017, 358 (6369), 1419–1423.

(16) Bruix, A.; Lykhach, Y.; Matolínová, I.; Neitzel, A.; Skála, T.; Tsud, N.; Vorokhta, M.; Stetsovych, V.; Ševčíková, K.; Mysliveček, J. Maximum Noble-metal Efficiency in Catalytic Materials: Atomically Dispersed Surface Platinum. Angew. Chemie Int. Ed. 2014, 53 (39), 10525–10530.

(17) Maurer, F.; Jelic, J.; Wang, J.; Gänzler, A.; Dolcet, P.; Wöll, C.; Wang, Y.; Studt, F.; Casapu, M.; Grunwaldt, J.-D. Tracking the Formation, Fate and Consequence for Catalytic Activity of Pt Single Sites on CeO 2. Nat. Catal. 2020, 3 (10), 824–833.

(18) Yates, J. T.; Duncan, T. M.; Worley, S. D.; Vaughan, R. W. Infrared Spectra of Chemisorbed CO on Rh. J. Chem. Phys. 1979, 70 (3), 1219.

(19) Duncan, T. M.; Vaughan, R. W. A 13C NMR Study of the Adsorbed States of CO on Rh Dispersed on Al2O3. J. Chem. Phys. 1980, 73 (2), 975–985.

(20) Yates, J. T.; Kolasinski, K. Infrared Spectroscopic Investigation of the Rhodium Gem-Dicarbonyl Surface Species. J. Chem. Phys. 1983, 79 (2), 1026.

(21) Garland, C. W.; Yang, A. Infrared Studies of Carbon Monoxide Chemisorbed on

Rhodium. J. Phys. Chem. 1957, 61 (11), 1504–1512.

(22) Campbell, C. T.; Mao, Z. Chemical Potential of Metal Atoms in Supported Nanoparticles: Dependence upon Particle Size and Support. ACS Catal. 2017, 7 (12), 8460–8466.

(23) Lou, Y.; Liu, J. CO Oxidation on Metal Oxide Supported Single Pt Atoms: The Role of the Support. Ind. Eng. Chem. Res. 2017, 56 (24), 6916–6925.

(24) Beyer, H.; Emmerich, J.; Chatziapostolou, K.; Köhler, K. Decomposition of Nitrous Oxide by Rhodium Catalysts: Effect of Rhodium Particle Size and Metal Oxide Support. Appl. Catal. A Gen. 2011, 391 (1), 411–416.

(25) Yates, J. T.; Duncan, T. M.; Worley, S. D.; Vaughan, R. W. Infrared Spectra of Chemisorbed CO on Rh. J. Chem. Phys. 1979, 70 (3), 1219.

(26) Solymosi, F.; Pásztor, M. Infrared Study of the Effect Of. J. Phys. Chem. 1986, 90, 5312–5317.

(27) Roscioni, O. M.; Dyke, J. M.; Evans, J. Structural Characterization of Supported Rh I (CO) 2 /γ-Al 2 O 3 Catalysts by Periodic DFT Calculations. J. Phys. Chem. C 2013, 117 (38), 130911121850001.

(28) Cavanagh, R. R., Yates Jr., J. T. Site Distribution Studies of Rh Supported on Al2O3—An Infrared Study of Chemisorbed CO. J. Chem. Phys. 1981, 74 (7), 4150.

(29) Serna, P.; Gates, B. C. Zeolite-Supported Rhodium Complexes and Clusters: Switching Catalytic Selectivity by Controlling Structures of Essentially Molecular Species. J. Am. Chem. Soc. 2011, 133 (13), 4714–4717.

(30) Hoffman, A. S.; Fang, C.; Gates, B. C. Homogeneity of Surface Sites in Supported Single- Site Metal Catalysts : Assessment with Band Widths of Metal Carbonyl Infrared Spectra. 2016.

(31) Panayotov, P. B.; Yates, J. T. Rhodium-Carbon Monoxide Surface Chemistry: The Involvement of Surface Hydroxyl Groups on A12O3and SiO2Supports. J. Am. Chem. Soc. 1988, 110 (7), 2074–2081.

(32) Hadjiivanov, K. Identification and Characterization of Surface Hydroxyl Groups by Infrared Spectroscopy. In Advances in Catalysis; Academic Press, 2014; Vol. 57, pp 99–318.

(33) Redhead, P. A. Thermal Desorption of Gases. Vacuum 1962, 12 (4), 203–211.

(34) Nehasil, V.; Star, I.; Matolln, V. Study of CO Desorption and Dissociation on Rh Surfaces. 1995, 333, 105–109.

(35) Digne, M.; Sautet, P.; Raybaud, P.; Euzen, P.; Toulhoat, H. Hydroxyl Groups on γ-Alumina Surfaces: A DFT Study. J. Catal. 2002, 211 (1), 1–5.

(36) Chizallet, C.; Digne, M.; Arrouvel, C.; Raybaud, P.; Delbecq, F.; Costentin, G.; Che, M.; Sautet, P.; Toulhoat, H. Insights into the Geometry, Stability and Vibrational Properties of OH Groups on γ-Al2O3, TiO2 -Anatase and MgO from DFT Calculations. Topics in Catalysis. Top. Catal. 2009, 1005–1016.

(37) Digne, M.; Sautet, P.; Raybaud, P.; Euzen, P.; Toulhoat, H. Use of DFT to Achieve a Rational Understanding of Acid-Basic Properties of ??-Alumina Surfaces. J. Catal. 2004, 226 (1), 54–68.

(38) Thiel, P. A.; Williams, E. D.; Yates, J. T.; Weinberg, W. H. The Chemisorption of CO on Rh(111). Surf. Sci. 1979, 84 (1), 54–64.

(39) Chafik, T.; Kondarides, D. I.; Verykios, X. E. Catalytic Reduction of NO by CO over Rhodium Catalysts: 1. Adsorption and Displacement Characteristics Investigated by In Situ FTIR and Transient-MS Techniques. J. Catal. 2000, 190 (2), 446–459.

(40) Anderson, J. A.; Rochester, C. H. Infrared Study of NO 2–CO Reactions over Supported Rhodium and Platinum Catalysts. J. Chem. Soc. Faraday Trans. 1991, 87 (9), 1485–1489.

(41) Hadjiivanov, K. I. Identification of Neutral and Charged N x O y Surface. 2007, 4940.

(42) Hadjiivanov, K.; Avreyska, V.; Klissurski, D.; Marinova, T. Surface Species Formed after NO Adsorption and NO+ O2 Coadsorption on ZrO2 and Sulfated ZrO2: An FTIR Spectroscopic Study. Langmuir 2002, 18 (5), 1619–1625.

(43) Miessner, H.; Burkhardt, I.; Gutschick, D. Coadsorption and Interaction of Nitric Oxide and Carbon Monoxide on Rh Supported on Highly Dealuminated Y Zeolite. Formation of Mixed Rh Carbonyl–Nitrosyls on the Surface. J. Chem. Soc. Faraday Trans. 1990, 86 (12), 2329–2335.

(44) Panayotov, D. A.; Burrows, S.; Mihaylov, M.; Hadjiivanov, K.; Tissue, B. M.; Morris, J. R. Effect of Methanol on the Lewis Acidity of Rutile TiO2 Nanoparticles Probed through Vibrational Spectroscopy of Coadsorbed CO. Langmuir 2010, 26 (11), 8106–8112.

(45) Lamberti, C.; Zecchina, A.; Groppo, E.; Bordiga, S. Probing the Surfaces of Heterogeneous Catalysts by in Situ IR Spectroscopy. Chem. Soc. Rev. 2010, 39 (12), 4951.

(46) Tyson, W. R.; Miller, W. A. Surface Free Energies of Solid Metals: Estimation from Liquid Surface Tension Measurements. Surf. Sci. 1977, 62 (1), 267–276.

(47) Matsushima, T.; Imamura, K.; Horino, H.; Hiratsuka, A.; Ma, Y.-S.; Rzeznicka, I. I.; Nakagoe, O. Inclined N2 Desorption in N2O Decomposition on Rh (1 1 0). Appl. Surf. Sci. 2005, 244 (1–4), 141–144.

(48) Peden, C. H. F.; Goodman, D. W.; Blair, D. S.; Berlowitz, P. J.; Fisher, G. B.; Oh, S. H. Kinetics of Carbon Monoxide Oxidation by Oxygen or Nitric Oxide on Rhodium

(111) and Rhodium (100) Single Crystals. J. Phys. Chem. 1988, 92 (6), 1563–1567.

(49) Peden, C. H. F.; Belton, D. N.; Schmieg, S. J. Structure Sensitive Selectivity of the NO-CO Reaction over Rh (110) and Rh (111). J. Catal. 1995, 155 (2), 204–218.

(50) Goldsmith, B. R.; Sanderson, E. D.; Ouyang, R.; Li, W. X. CO- and NO-Induced Disintegration and Redispersion of Three-Way Catalysts Rhodium, Palladium, and Platinum: An Ab Initio Thermodynamics Study. J. Phys. Chem. C 2014, 118 (18), 9588–9597.

(51) Oh, S. Comparative Kinetic Studies of CO-O2 and CO-NO Reactions over Single Crystal and Supported Rhodium Catalysts. J. Catal. 1986, 100 (2), 360–376.